DEPARTMENT OF MECHANICAL ENGINEERING
INDIAN INSTITUTE OF TECHNOLOGY MADRAS
CHENNAI – 600036

Experimental and Numerical Investigations on the Three Dimensional Slot Film Cooling of an Annular Combustor

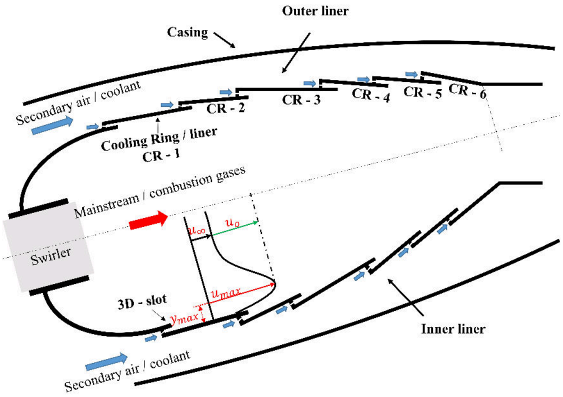

A Thesis

Submitted by

REVULAGADDA ANANDA PRASANNA

For the award of the degree

Of

DOCTOR OF PHILOSOPHY

December 2023

With hard work and dedication, anything is possible.

– Paul Raj

Dedicated to: My Teachers, Family, and Friends

THESIS CERTIFICATE

This is to undertake that the Thesis titled **EXPERIMENTAL AND NUMERICAL INVESTIGATIONS ON THE THREE DIMENSIONAL SLOT FILM COOLING OF AN ANNULAR COMBUSTOR**, submitted by me to the Indian Institute of Technology Madras, for the award of **Doctor of Philosophy**, is a bona fide record of the research work done by me under the supervision of **Dr. Arvind Pattamatta and Dr. Chakravarthy Balaji**. The contents of this Thesis, in full or in parts, have not been submitted to any other Institute or University for the award of any degree or diploma.

Chennai 600036

Date: December 2023

Revulagadda Ananda Prasanna

Dr. Arvind Pattamatta
Research advisor
Professor
Department of Mechanical Engineering
IIT Madras

C.Balaji

Dr. C Balaji
Research Co-advisor
Professor
Department of Mechanical Engineering
IIT Madras

ACKNOWLEDGEMENTS

I wish to extend my heartfelt gratitude to my esteemed research advisors, **Dr. Arvind Pattamatta** and **Dr. C. Balaji**, for their invaluable guidance and mentorship. Their expertise in academic matters, empathetic understanding, and nurturing care have been instrumental in propelling my research forward. Their unwavering support has not only been academically enriching but has also helped me maintain a composed and focused mindset throughout this journey.

I would like to express my profound thanks to the distinguished members of my Doctoral Committee: **Dr. Shamit Bakshi**, **Dr. Balaji S. Srinivasan**, **Dr. Rinku Mukherjee**, and **Dr. Shaligram Tiwari**. Their insightful suggestions at various junctures of my research have been immeasurably valuable.

I am also deeply appreciative of the technical support provided by the dedicated team at the HTTP lab, including **Mr. Sagaya Rajesh**, **Mr. Prabhakaran**, and **Mr. Surendar**. Their assistance played a pivotal role in the successful execution of my research.

I am grateful to **Dr. Sangamesh C. Godi** for generously sharing his expertise in experimental methodology and to my junior colleague, **Buhci Raju Adapa**, for their collaboration on the Hybrid slot cooling study and **Dr. Rajesh Akhula** for the introduction to optimization techniques significantly enriched the depth of my work. A special note of gratitude goes to **Praveen Dhanalakota** for his invaluable assistance in honing my technical writing skills.

Recognizing that a supportive and conducive workplace is pivotal for nurturing innovative ideas, I consider myself fortunate to have had **Dr. Sangamesh C. Godi**, **Dr. Srinivasa Sagar**, **Dr. Tejaswi Josyula**, **Dr. Laxman**, and **Mr. Praveen Dhanalakota** as my research colleague. Their motivation, guidance, and unwavering moral support have been instrumental in sustaining my belief in the research's potential.

I am deeply grateful for the friendships I have experienced during my tenure at IIT Madras. To **Rajesh Akula**, **Prudhvi**, **Abhinav**, **Parinith Ramakrishna**, **Piyush**, and **Rama**, your companionship and unwavering support have been truly cherished. I extend my deepest thanks to my parents, **Shri. Revulagadda John Chandra Prakash Babu**, and **Smt. Vijaya Kumari**, for their steadfast care throughout my life. I would also like to express my heartfelt appreciation to my uncle, **R I V Prasadh Babu**, Aunt **R Kezia**, my brothers **Poorna Chaithanya** and **Sukumar**, my cousin **Susmitha**, and my niece **Ammulu**, as well as my grandparents, **R Paul Raju** and **Sakkubhai**, for their unwavering love and support, which kept me energized throughout my Ph.D. journey.

I extend my sincere gratitude to the **Gas Turbine Research Establishment, DRDO, Govt. of India.** for their generous financial support. Additionally, I am indebted to the **High-Performance Computing Environment, AQUA cluster**, provided by IIT Madras, without which the numerical analysis in this study would not have been possible.

I would like to express my profound thanks to all who have contributed to this research endeavor in various capacities. Your support and assistance have been invaluable, and I am truly appreciative of your contributions.

Revulagadda Ananda prasanna

LIST OF TABLES

LIST OF FIGURES

ABBREVIATIONS

1D One-dimensional.

2D Two-dimensional.

3D Three-dimensional.

BR Blowing Ratio.

CFD Computational Fluid Dynamics.

CRVP Counter Rotating Vortex Pair.

CTA Constant Tempearature Anemometer.

DC Direct Current.

DR Density Ratio.

ewt Enhanced Wall Treatment.

HTTP Heat Transfer and Thermal Power.

IIT Indian Institute of Technology.

MAE Mean Absolute Error.

MFR Mass Flow Ratio.

MSE Mean Square Error.

NSGA Non-dominated Sorting Genetic Algorithm.

RKE Realizable k- epsilon model.

RMS Root Mean Square.

,

NOTATION

A	area, m^2
ad	adiabatic wall
BR	blowing ratio
C_p	specific heat capacity, J/kgK
d	diameter of the film cooling hole
d_e	diameter of effusion jets, mm
D_h	hydraulic diameter, mm
$D_{i,m}$	mass diffusion coefficient
DR	density ratio
E	represents the internal energy
e/L	offset from slot exit
f	objective function
h	enthalpy
i	i-th component
J	diffusion term
k	thermal conductivity, $W/m \cdot k$
k	turbulence kinetic energy, m^2/S^2
L	lip length, mm
L/d	dimensionless lip length

MFR mass flow ratio

N total number of effusion rows

n number of backward effusion rows

n refractive index

p pitch, mm

p/d dimensionless pitch

Re Reynolds number

S slot height, mm

S_h source term

t time, S

T_c coolant temperature, ^oC

T_h mainstream temperature, ^oC

T_w wall temperature, ^oC

TI local turbulence intensity, (%)

u streamwise mean velocity, m/s

u' fluctuating component of the jet velocity in the x direction, m/s

u_h main stream velocity, m/s

u_{max} local maximum velocity, m/s

u_o difference of local maximum velocity and mainstream velocity, m/s

u_s mean velocity coolant at the slot exit, m/s

VR velocity ratio

x distance along the streamwise direction, mm

X/S dimensionless streamwise distance

y normal distance from the wall surface, mm

Y/S dimensionless normal distance from the wall surface

$y_{0.5}$ normal distance from the wall surface, where 0.5 x u_{max} exists, mm

Y_i mass fraction of i^{th} gas

y_{max} normal distance from the wall surface, where u_{max} exists, mm

$\overrightarrow{F}$ volume force vector

$\overrightarrow{r}$ position vector

$\overrightarrow{s}'$ scattering direction vector

Subscripts

ad	adiabatic
$ad.lat$	laterally averaged adiabatic
$ad.avg$	area averaged adiabatic
c	coolant
eff	effusion
h	hot gas
sl	slot
∞	mainstream
w	wall
opt	optimum
ov	overall
$ov.lat$	laterally averaged overall
$ov.avg$	area averaged overall
j	slot jet
i	i-th component

Greek letters

α	thermal diffusivity kg/mS
δ	lateral uniformity index
ε	turbulent dissipation rate, m^2/s^3
η	film cooling effectiveness
ρ	density, kg/m^3
σ_η	standard deviation of local effectiveness
σ_S	scattering coefficient
σ	Stefan-Boltzmann constant
$\bar{\bar{\tau}}$	stress tensor
ϕ	phase function
Ω'	solid angle.
ω	vorticity , $1/s$

CONTENTS

ABSTRACT

KEYWORDS Gas turbine; Annular combustor Liner; Three-dimensional slots ; Effusion cooling; Film Cooling effectiveness; Hotwire anemometry; Infrared thermography; Optimization; Genetic algorithm; Kriging; Neural networks

Aircraft employ gas turbine engines as their principal power source of propulsion. To enhance their thermal efficiency, the combustion temperatures of modern gas turbines have steadily increased. The typical combustion gas temperature in modern gas turbines ranges from 1700 to 2400 K. The combustor liner metals on their own would be unable to withstand these operating conditions and cause the failure of the combustor due to thermal fatigue. Slot film cooling is one of the cooling techniques used in combustors of aviation gas turbines.

In the present work, combined experimental and numerical studies are conducted to investigate the three-dimensional slot film cooling of an annular combustor. Experimental investigation is conducted to understand the fluid flow and heat transfer phenomenon of the film cooling and to validate the numerical study under laboratory conditions (low temperature and pressure). Transient infrared thermography is used to estimate both adiabatic film-cooling effectiveness (η_{ad}) and heat transfer coefficient (h) simultaneously using a semi-infinite approximation method. The blowing ratios considered in the study are in the range of 0.5 to 5. Following this, a parametric study is conducted numerically to understand the effect of flow and geometrical parameters under actual engine conditions (high temperature and pressure). The parameters considered are slot Reynolds number (Re_s), slot jet diameter (d), slot jet pitch (p), lip taper angle (α), lip length (L), and slot jet injection angle (β).

In addition, a combined experimental, numerical investigation and optimization using an evolutionary-based genetic algorithm is implemented to optimize the three-dimensional

slot configuration under actual engine conditions (high temperature and pressure). The primary objective of the optimization is to maximize the area-averaged effectiveness ($\eta_{ad.avg}$) and minimize its standard deviation (σ_η) at a fixed coolant mass flux for a single liner. A design space is created using the Latin hypercube sampling technique and solved using steady-state simulations (RANS) to estimate the $\eta_{ad.avg}$ and σ_η. A surrogate model is developed using the Kriging technique to predict the objective functions, and the optimum configuration is identified using the genetic algorithm. The geometrical parameters are slot jet diameter (d), slot jet pitch (p), lip taper angle (α), and lip length (L). The numerical and experimental results show that the optimum three-dimensional slot configuration outperforms the reference configurations of the baseline combustor. Furthermore, the study on subsequent liner revealed that the optimum slot configuration cools an additional liner length (G/S) of 5.5 compared to the reference-1 slot and results in a reduction of one pair of cooling rings in the combustor, which contributes to a 16.6 % less coolant mass flux for the entire combustor. Subsequently, the benefit of implementing the optimum three-dimensional slot in the hybrid slot configuration is discussed. In conclusion, a numerical analysis is undertaken to explore how gas radiation and the application of thermal barrier coatings influence the effectiveness of three-dimensional slot film cooling. The numerical results showed that gas radiation significantly affects the film cooling performance. In addition, it is observed that the optimized three-dimensional slot outperforms the reference slots, even if the effects of gas radiation are considered.

CHAPTER 1

INTRODUCTION

1.1 GAS TURBINE

A gas turbine is an internal combustion engine in which the rotary components extract energy from high-pressure and temperature combustion gases and are used for thrust, power generation, etc. The schematic of a typical gas turbine is shown in Figure 1.1.

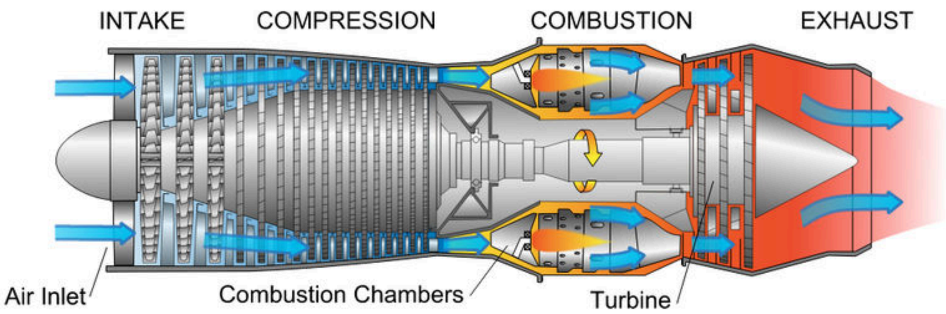

Figure 1.1: Schematic of a typical gas turbine (Wikipedia (2007))

The principal constituents within a conventional gas turbine system comprise the compressor, combustion chamber, and turbine. A standard gas turbine operates in accordance with the principles of the Brayton cycle. As shown in the figure, the ambient air is compressed to high pressure, heat is supplied in the combustion chamber, and work is extracted from high-temperature and high-pressure air using the turbine.

1.2 COOLING OF HOT GAS PATH COMPONENTS

A modern gas turbine demands a high turbine inlet temperature to increase cycle efficiency. Over the last few decades, the demand for the turbine inlet temperature has increased from approximately 1100 K to 2100 K. Figure 1.2 shows the evolution of the turbine inlet temperature attributed to alloy development and advances in cooling technologies and thermal barrier coatings.

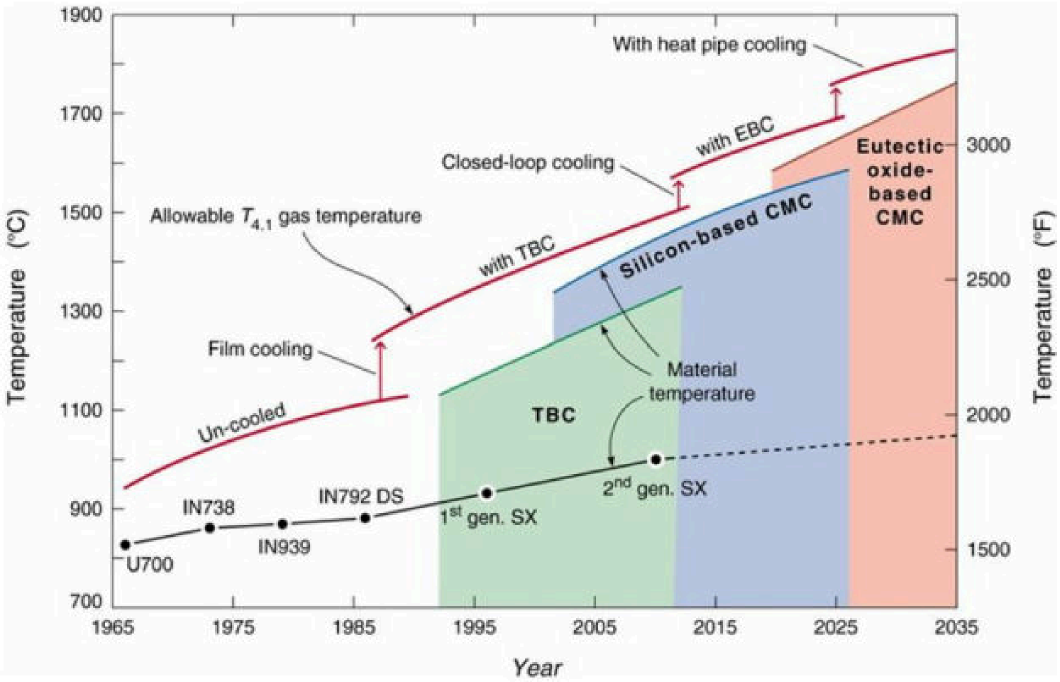

Figure 1.2: Enhancements in gas turbine inlet gas temperature achieved through alloy development and cooling technologies. (Image source: Wadley Research Group, University of Virginia)

The hot-gas path components, such as combustors, guide vanes, and turbine blades, cannot withstand high-temperature combustion gases. From a material perspective, these components would fail due to the thermal load for a prolonged period, known as creep, and also due to cyclic thermal load called thermal fatigue. To overcome these problems, the hot gas path components are cooled to safe temperatures using relatively low-temperature bleed air from the compressor through multiple internal passages. Figure 1.3 shows cracks generated on the combustor liner due to the hotspots and thermal stresses that arise due to inadequate cooling strategies.

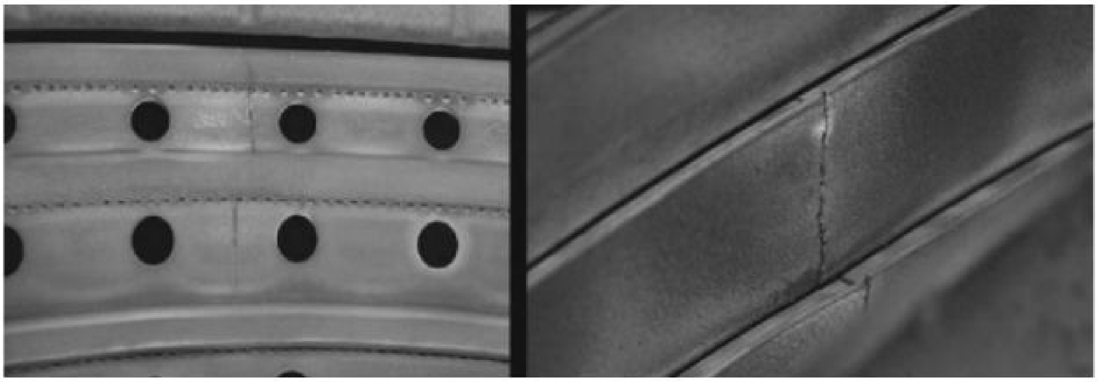

Figure 1.3: Cracks developed on the combustor liner due to the hotspots obtained by the poor cooling techniques (Image source: Tinga *et al.* (2006)

Figure 1.4 shows the hot corrosion or oxidation of the turbine blade due to prolonged usage at high temperatures without cooling.

Figure 1.4: Severe hot corrosion on turbine blades after long-term usage at high temperatures (Image source: Wing (1981)

On the other hand, in modern combustors, premixed lean combustion is implemented to reduce the emissions of exhaust gases. As a result, the air available for cooling purposes is limited. Hence, operating the gas turbine by maintaining the hot gas path components under safe temperatures is challenging. Particularly, protecting the combustor from hot gases is necessary and complex. In the present work, the cooling of a typical annular combustor liner using various three-dimensional film cooling techniques is investigated extensively.

1.3 COMBUSTOR LINER COOLING TECHNIQUES

Figure 1.5 illustrates a three-dimensional model representing a typical annular gas turbine combustor. The combustor comprises essential components such as the outer casing, liner, swirlers, fuel nozzles, and dilution holes. The air from the compressor serves a dual purpose: it is utilized partially for combustion, and the remaining portion is dedicated to cooling the combustor, effectively diluting the combustion gases.

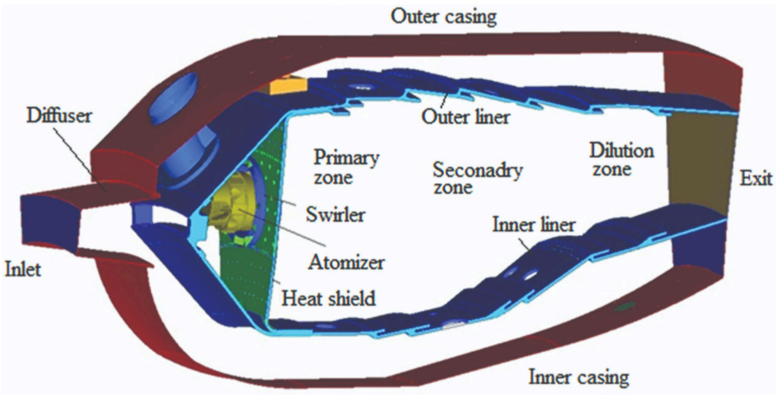

Figure 1.5: Three-dimensional model of a typical annular combustion chamber (Image source Rao *et al.* (2022)

In the combustor, combustion of the fuel takes place in an annular casing known as a liner. The temperature of combustion gases would be in the range of 1700 to 2100K. As discussed earlier, the liner needs to be cooled in order to enhance its life and reduce the risks of failure at these high-temperature combustion gases. The heat transfer mechanisms to the liner are shown in Figure 1.6. The liner experiences heating from both radiation and convection due to hot combustion gases. Simultaneously, it undergoes cooling from the relatively cooler air present in the annular space between the outer casing and the liner. In addition, the annular air is introduced on the gas side of the liner surface to impede heat transfer from the hot gases by utilizing slots or effusion arrays known as film cooling. According to Lefebvre and Ballal (2010), film cooling is one of the promising techniques to protect the combustion chamber from hot combustion gases.

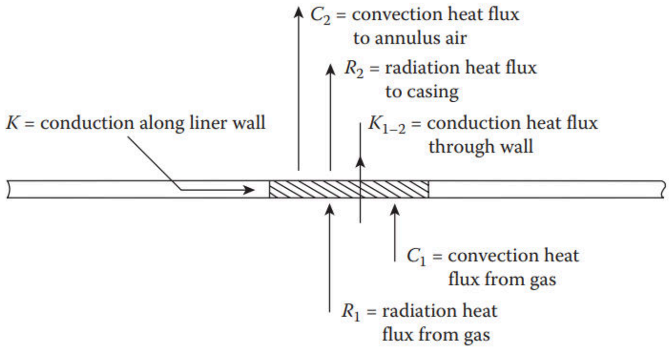

Figure 1.6: Schematic of a heat transfer mechanisms in the combustor liner (Image source Lefebvre and Ballal (2010))

Figure 1.7 depicts the schematic of the cross-section of the baseline annular combustion chamber under consideration.

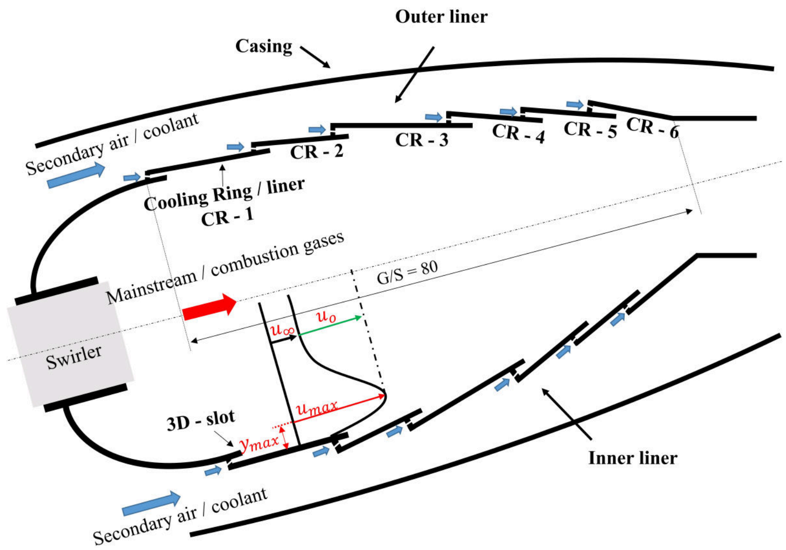

Figure 1.7: Schematic of a typical annular combustor

A typical liner is made up of multiple concentric cooling rings stacked horizontally. The annular gap between the cooling rings provides a provision referred to as a slot for the coolant entry. This enables a low-temperature blanket of coolant on the liner and maintains safe temperatures. The number of cooling rings (CR) of the liner is fixed depending on the efficiency of the slot configuration and desired cooling efficiency. The present baseline combustor consists of six pairs of cooling rings, including the outer and inner liners, to protect the combustor with a length (G/S) equal to 80.

Active cooling techniques for the combustor liner have been evolving over the last four decades. The fundamental principle underlying active cooling approaches involves the utilization of secondary bleed air derived from the compressor, specifically annular air. This air is strategically injected over the surface of the liner using various cooling mechanisms, protecting it against the high temperatures generated by combustion gases and ensuring the maintenance of safe operating temperatures. Typical cooling methods include slot film cooling, effusion film cooling, impingement cooling, hybrid film cooling, and transpiration cooling.

1.3.1 Slot film cooling

In slot film cooling, coolant is introduced over the liner surface through slots to reduce the heat transfer to the liner from combustion gases. The schematic of the slot film cooling in a typical combustor liner is shown in Figure 1.8. Based on the type of coolant injection, the practical film cooling slots are classified into T-type slots and wall jet slots. In the T-type slot (see Figure 1.8a), coolant enters the slot through the jet holes that are made on the liner, impinges under the overhanging part (lip) of the other concentric liner, and spreads over the liner surface. T-type slots have been extensively investigated by Wei *et al.* (2015), Li and Mongia (July, 2001).

In the wall jet slot (see Figure 1.8 b), the coolant enters through the jet holes placed in an annular gap between two consecutive and concentric liners, impinges under the lip, mixes within the slot, and spreads over the liner surface. In slot film cooling, the coolant interacts with the mainstream in the streamwise direction. As a result, its temperature increases in the streamwise direction, and film cooling performance reduces. The zone where the mainstream and cold stream interact is called the mixing zone and is highlighted in Figure 1.8 b.

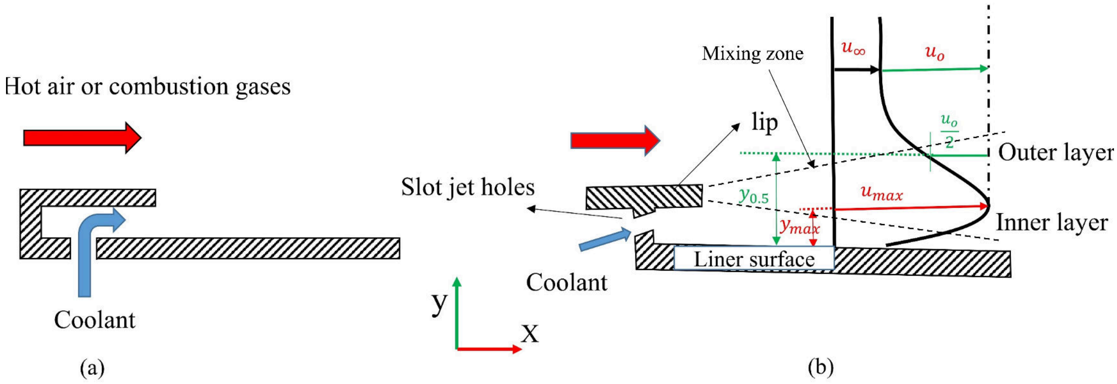

Figure 1.8: Schematic of three-dimensional film cooling slots (a) T-type slot (b) wall jet slot

In addition, a schematic of the velocity profile of slot film cooling is shown in Figure 1.8 b. The region between the maximum velocity of the velocity profile and the wall surface is called the inner layer, and the region above the maximum velocity of the profile is called the outer layer. In the far field of the outer layer, the influence of the coolant is negligible, and the velocity is equal to the mainstream velocity (u_∞). In film cooling, the velocity profile obtained is the superimposition of both the mainstream and cold streams. According to Zhou and Wygnanski (1993), in the presence of mainstream in a wall jet (co-flow), the velocity scale is corrected to $u_o = (u - u_\infty)$. The normal distance from the surface at which the maximum coolant velocity u_{max} attains is called y_{max}. In addition, the normal distance from the wall surface where the velocity in the outer layer is half of the maximum corrected velocity ($\frac{u_o}{2}$) is called y-half, and it is denoted as $y_{0.5}$.

1.3.2 Effusion cooling

Figure 1.9 shows the schematic of the effusion cooling. In effusion cooling, the coolant is introduced over the liner surface through the perforated holes on the liner. As a result, a low-temperature film is developed over the surface and protects from the combustion gases. In this case, the full coverage of the coolant film is not generated at the start of the effusion array. However, the coolant interacts laterally along the streamwise direction and forms a full coverage of the film. As a result, the film cooling performance increases in the streamwise direction.

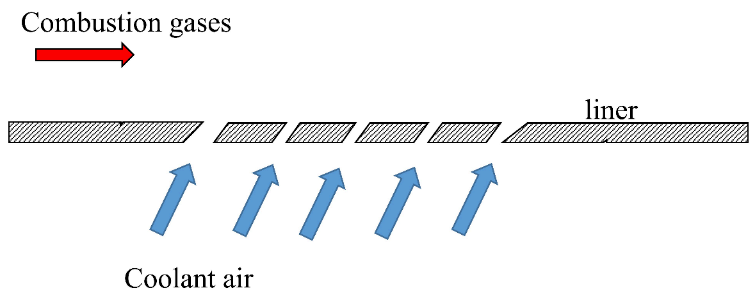

Figure 1.9: Schematic of effusion cooling

1.3.3 Hybrid film cooling

As explained before, the film cooling performance decays along the streamwise direction for slot film cooling. Whereas in effusion cooing, it increases along the streamwise direction. The drawbacks of these two configurations are reduced by combining the three-dimensional slot and effusion cooing, called hybrid film cooling. A typical hybrid cooling configuration is shown in Figure 1.10.

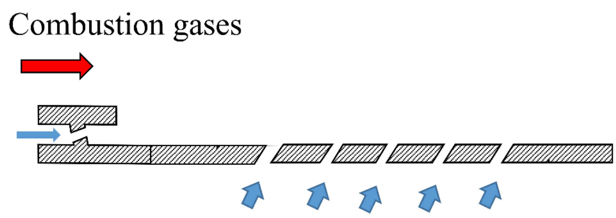

Figure 1.10: Schematic of hybrid cooling

1.3.4 Impingement cooling

In impinging cooling, the heat conducted in the liner is removed by the impingement of the coolant. In addition, a low-temperature film is enveloped on the gas side of the liner to reduce further increase in heat transfer from the combustion gases. As a result, this technique outperforms other cooling techniques. The schematic of the impingement cooling is shown in Figure 1.11. However, the fabrication complexities due to the double-walled configuration become a bottleneck for implementing this technique.

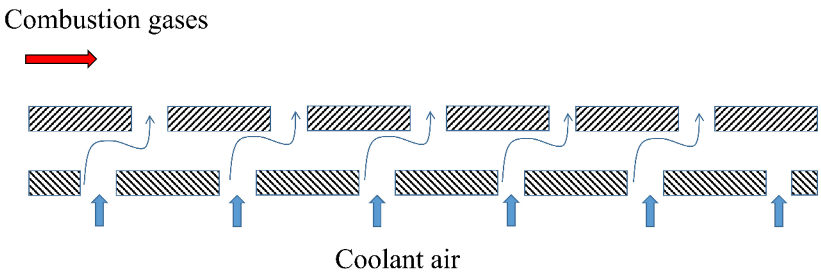

Figure 1.11: Schematic of impingement cooling

1.3.5 Transpiration cooling

In transpiration cooling, as illustrated in Figure 1.12, the surface to be cooled is made porous, and the coolant is driven through the wall due to the pressure difference. The liner material has a wide surface area inside the wall, allowing for efficient heat removal. However, the liner wall is subjected to thermal oxidation, thermal stress, and intense radiation from the combustion flame. In addition, the porous wall is prone to plugging with the soot particles.

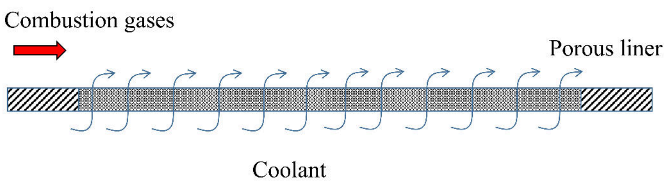

Figure 1.12: Schematic of transpiration cooling

1.3.6 Organization of the thesis

The thesis is organized into nine chapters, including this chapter. A summary of each chapter is discussed as follows.

Chapter 1 briefly describes the working of a typical gas turbine, combustor and the necessity of cooling the hot gas path components. In addition, various combustor liner cooling techniques and their advantages and demerits are discussed. Finally, an outline of the thesis organization is provided in this chapter.

Chapter 2 provides an overview of the literature on film cooling. These studies provide a basis for the problem formulation of the present study. The studies on experimental techniques, numerical studies, and optimization using machine learning algorithms to solve the present problem are discussed. In addition, studies on the effect of gas radiation on the film cooling performance are discussed. Further, at the end of the chapter, a synopsis of the entire literature review is provided for ease of understanding.

Chapter 3 presents the details of the experimental facility fabricated for conducting the film cooling studies, experimental methodology, and the uncertainty of the experimental results are discussed. In addition, it presents the details of the numerical methodology and turbulence closure employed, the numerical domain, imposed boundary conditions, and the results of the grid independence study are highlighted.

Chapter 4 presents the experimental investigations on fluid flow and heat transfer characteristics, and the validation of the numerical study under laboratory conditions (low temperature and pressure) are discussed.

Chapter 5 presents numerical investigations on film cooling performance under actual engine conditions (high pressure and temperature) and accompanying results are presented. In addition, a detailed parametric study conducted under actual engine conditions to obtain further insights into the effects of flow and geometrical parameters on the film cooling performance is elucidated. Finally, the details of an Artificial Neural Network (ANN) based mathematical model developed to predict the film cooling effectiveness is reported.

Chapter 6 presents the sensitivity of the geometrical parameters and optimization of a three-dimensional slot under actual engine conditions (high temperature and pressure). The robustness of optimum geometry by testing at various flow conditions is discussed in detail. In addition, the experimental testing of the optimum slot configuration under laboratory conditions is discussed. Furthermore, the results of the numerical investigation conducted on the two rows of subsequent liners to understand the effect of film cooling of the first cooling ring on the film cooling effectiveness of the subsequent cooling ring are discussed. The experimental investigation of the subsequent liner configuration is reported. Finally, the enhancement of film cooling performance by implementing the optimum slot in a hybrid configuration is analyzed.

Chapter 7 presents the numerical investigations carried out to study the effect of radiation from the combustion gases on the film cooling performance. Following this, the effects of the equivalence ratio and liner surface emissivity on the film cooling effectiveness are reported. In addition, the benefits of thermal barrier coating (TBC) on film cooling performance are evaluated. Finally, the robustness of the optimum three-dimensional slot configuration by considering the effects of gas radiation is reported.

Chapter 8 summarizes the major conclusions of the entire study. A grand overview of the entire work is delineated, followed by suggestions and future scope work.

1.4 CLOSURE

In this chapter, the importance of cooling a combustor liner was emphasized, and a concise overview of different liner cooling methods was presented. Furthermore, the advantages and disadvantages of commonly practiced cooling techniques were examined. Following this discussion, a brief overview of the thesis structure was provided. The next chapter presents a critical review of the state of the art on film cooling techniques.

CHAPTER 2

REVIEW OF LITERATURE

In this chapter, details of the previous studies related to combustor cooling techniques are discussed briefly. The present study deals with a detailed investigation of three-dimensional slot film cooling of an annular combustor. It involves fundamental investigations of slot film cooling and geometrical optimization of the three-dimensional slot configuration using machine learning algorithms. In addition, the three-dimensional slot is combined with an effusion configuration, known as a hybrid slot, and is investigated in order to fully utilize the benefit of film cooling. Finally, the effect of gas radiation and thermal barrier coating on the film cooling performance will also be studied. In view of the above, the most relevant literature is reviewed based on the following categories.

- Studies on slot film cooling
- Studies on effusion film cooling
- Studies on hybrid film cooling
- Studies on optimization of the film cooling configuration
- Studies on mathematical modeling approaches related to film cooling
- Studies on effects of gas radiation and thermal barrier coating
- Studies on experimental methodology

2.1 STUDIES ON SLOT FILM COOLING

This section presents studies on the fluid flow and heat transfer characteristics of slot film cooling. Most studies are based on the effect of slot geometry, such as two-dimensional and three-dimensional slots. Hence, the studies are classified based on the type of geometries, such as two-dimensional slots and three-dimensional slots. In addition, investigations on the effect of blowing ratio and flow characteristics such as mean velocity and turbulence profiles, are discussed.

Figure 2.1 shows a comparison of two-dimensional and three-dimensional film cooling slots. A two-dimensional slot is an ideal type in which coolant exits with uniform velocity throughout the cross-section. The cooling effectiveness obtained with the two-dimensional slot is the maximum. A two-dimensional slot is mimicked in experiments by arranging two parallel plates for a certain width (See Figure 2.1 a).

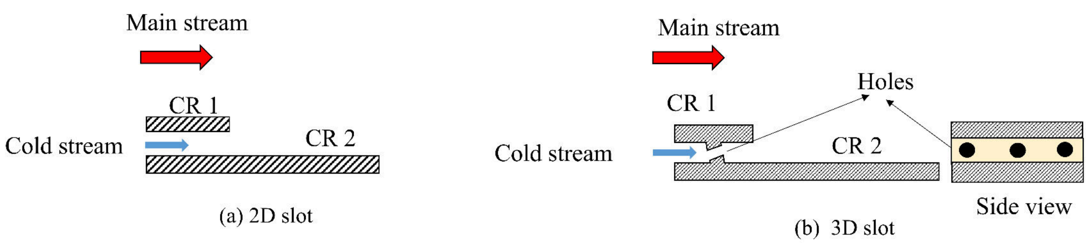

Figure 2.1: Types of film cooling slots (a) two-dimensional slot (b) three-dimensional slot

However, it is not feasible to implement the two-dimensional slots in a combustor due to a lack of structural integrity. In practice, two concentric cooling rings (CR 1 and CR 2) are stacked horizontally, and a supporting frame is provided with holes for the coolant entry (See Figure 2.1 b). In this case, the flow of the coolant is three-dimensional due to the metering port or holes. As a result, the practical slot is called a three-dimensional slot.

Sivasegaram and Whitelaw (1969) investigated two-dimensional slots experimentally and identified that the film cooling effectiveness is reduced when the lip thickness ratio to slot height(t/s) is greater than 0.25. In addition, with the increase in the injection angle, the effectiveness is reduced, and for all the injection angles, the optimum blowing ratio is identified as 1.

Bittlinger *et al.* (1994) conducted an experimental investigation on two-dimensional slots and identified that the blowing ratio greater than unity results in the film cooling flow behaving like a wall jet with a superimposed mainstream flow. Increasing the blowing ratio beyond 1.6 results in increased heat transfer coefficients, particularly near the slot. Additionally, it was noted that the heat transfer coefficient is increased by 200 percent in comparison to the case where there is no blowing.

In practice, two-dimensional slots cannot be used in the combustor. Hence, the following investigations were conducted on three-dimensional slots in the literature.

Sturgess (1968) studied the practical combustor cooling slots for high film cooling effectiveness with a view to designing them. He stated that the prediction of film cooling effectiveness using phenomenological models developed for two-dimensional film cooling is incorrect as the flow is three-dimensional in the actual combustor. In three-dimensional flow, the average film cooling effectiveness depends on the circumferential or lateral uniformity of the film coming out of the slot. The geometrical mixing parameter for different slot designs was developed and examined, and it was concluded that it could differentiate good and poor film cooling slots.

Sturgess (1980) conducted experiments with three-dimensional film cooling slots and reported that the streamwise decay of film cooling effectiveness is due to small-scale turbulence generated at the metering ports and large-scale entrainment of the mainstream.

Nina and Whitelaw (1971) conducted experiments on three-dimensional slots and showed that a slot with a large open area ratio, small lip thickness, and long lip length had a high cooling performance. Practically, the region where an insufficient supply of coolant through the tangential injection can be supplied by normal injection or splash cooling. They also investigated splash cooling and compared it with tangential film cooling. Experiments showed that tangential injection is better than splash cooling for the considered geometry.

Rastogi and Whitelaw (1973) conducted experiments on tangential three-dimensional film cooling slots and investigated the impact of velocity ratio (VR), open area ratio, and density ratio (DR) on film cooling performance. They observed an undulating nature of cooling effectiveness on the liner surface up to at least 30 diameters in the streamwise direction. Further, a higher film cooling effectiveness is observed for a smaller value of the pitch-to-diameter ratio.

Li and Mongia (July, 2001) conducted an experimental and numerical investigation on machined cooling ring liners and developed an improved method for film cooling effectiveness correlation based on the geometrical parameters of the slot. In addition, they identified that at low blowing ratios, the secondary air with low velocity is entrained into the mainstream, and more portion of the lip edge is covered by secondary air (coolant). However, with the increase in the blowing ratio, mainstream is entrained into secondary air at high velocity. It is also observed that the sudden expansion of the main and cold streams generates vortices at the lip edge.

Mongia (2012) developed a three-dimensional radiative heat transfer model based on finite volume techniques to predict the film cooling effectiveness of machined cooling rings. Subsequently, the model was rigorously validated using experimental data. He highlighted that numerical algorithms could provide highly reliable predictions of film performance when all heat transfer mechanisms were considered simultaneously. Notably, this method achieved a closer match to the experimental data obtained from the actual engine pre-test.

Cho and Ham (2001) conducted an experimental study to examine the impact of coolant injection types and the arrangement of the injection feed on the fluid flow and heat transfer characteristics within the injection slot. The findings revealed that both parallel and vertical injection types exhibited relatively weak flow patterns at the slot exit. Moreover, the heat transfer is higher for the vertical injection method at the slot exit compared to parallel injection and the combined injection techniques.

Park *et al.* (2009) carried out an experimental study to explore the impact of injection type on slot film cooling in a ramjet combustor. They observed that increasing the slot injection had a notable adverse effect on the film cooling effectiveness. Furthermore, they observed that the implementation of wiggle strips led to the generation of three-dimensional flow patterns, which, in turn, enhanced the mixing between the hot and cold streams.

Yang and Zhang (2012) conducted an experimental investigation on heat transfer characteristics of film cooling using single and two rows of parallel inlet holes. Results showed that the blowing ratio significantly affects the film cooling effectiveness, and the staggered arrangement of two rows generated a high heat transfer coefficient.

Song *et al.* (2012) experimentally investigated the slot film cooling performance in a ram jet combustor with flame holders. Liquid crystal thermography was used to measure adiabatic cooling effectiveness. In the first slot, the blockage due to the flame holder accelerated the mainstream flow and suppressed the coolant, resulting in better cooling. However, the cooling was reduced in the second slot due to distributed flow. The results reveal that it was crucial to consider the effect of flame holders on practical ram jet combustors.

Wei *et al.* (2015) conducted a numerical study on the effect of various slot geometries on impinging–film hybrid cooling. The critical aspects of various geometries are the cross-section of induction slap, convergent or divergent slots, and jet injection angles. They identified that the triangular slab outperformed other geometries. However, its superiority was reduced with an increase in the blowing ratio. They also observed that the convergent slot was better than the divergent slot, and the best performance was obtained for the coolant injection angle of 60^o for all the configurations.

Zhang *et al.* (2018) conducted an experimental investigation on the overall film cooling performance of the t-type slot impinging film cooling. They investigated the effect of the blowing ratio and geometrical parameters such as jet-to-plate pitch, hole-to-hole pitch, and hole diameter. The results showed that the increase in the jet-to-plate pitch and the decline in the hole pitch enhances the effectiveness. In addition, the hole diameter had minimal influence on the film cooling performance.

Wang *et al.* (2000) conducted an experimental study to examine how various factors influence the mixing of air within slots. These factors included the orientation angle, injection angle, slot width, and slot depth. The results demonstrated that increasing the orientation angle from 0^0 to 60^o improved the uniformity of the coolant flow at the slot exit. However, Wider slots resulted in non-uniform flow. Additionally, the optimal slot depth was found to be 2 to 2.8 times the diameter of the holes.

Alongside heat transfer studies on geometrical parameters of slot film cooling, flow studies have also been under focus to gain more insights into the flow characteristics.

Zhou and Wygnanski (1993) investigated the effect of parameters governing two-dimensional turbulent wall jets in an external stream. They measured the mean velocity profiles and observed self-similarity in the velocity profiles for the cases where the maximum jet velocity was twice that of the free stream velocity.

Ben Haj Ayech *et al.* (2016) conducted a numerical study of a turbulent wall jet in a co-flow stream to determine the dynamic, thermal, and turbulent characteristics of the flow. The study was conducted for a velocity ratio ranging from 0 to 0.2. The results showed that the potential core length decreases with an increase in velocity ratio. They observed that the u-component velocity and maximum turbulent kinetic energy converge to a single curve at different velocity ratios. In addition, they concluded that the effect of the co-flow stream on the dynamic, thermal, and turbulence characteristics is negligible and similar to the case of a jet without co-flow.

Godi *et al.* (2019) investigated the effect of the inlet geometry of wall jets (without external flow) on flow and heat transfer characteristics. A self-similarity in the mean velocity and RMS intensity profiles was observed beyond $X/S > 20$. They also concluded that the circular jets performed better than the other shapes under consideration.

2.2 STUDIES ON EFFUSION COOLING

Studies on effusion cooling of annular combustors are limited in the literature. However, the effusion cooling mechanism is similar to the turbine blade and other hot components of the gas turbine. As a result, the studies related to effusion film cooling in combustors as well as other hot gas path components, are discussed in this section.

Andrews and Bazdidi-Tehrani (1989); Andrews *et al.* (1991, 1995) conducted a series of experiments focused on multi-row effusion film cooling. These experiments explored various porosities of the holes and coolant injection angles. The findings revealed that the length of the effusion hole and the approach area of the hole play a significant role in the overall heat transfer process. The overall performance of the effusion cooling was notably influenced by conduction heat transfer in the plate and also along the lateral contact surfaces of the holes.

Sinha *et al.* (1991) conducted an investigation to analyze the impact of density ratio on the performance of the effusion cooling. The authors noted that a decrease in the density ratio and an increase in the momentum flux ratio lead to reduced coolant dispersion and, consequently, diminished cooling effectiveness.

Scrittore *et al.* (2007) employed Laser Doppler velocimetry to investigate the fluid flow characteristics of effusion cooling. Their observations revealed a self-similarity in both the streamwise velocity and turbulence profiles when scaled with a blowing ratio. Furthermore, it was noted that, as blowing ratios increased, there was a point at which the jet lifted off, and this led to the streamwise velocity showing its two highest values at a point below Y/D = 12.

Huang *et al.* (2015) investigated the cooling performance of a perforated plate effusion cooling system with a hole diameter of 0.5 mm. Their observations revealed that effusion cooling, using densely packed cooling holes with a 0.5 mm diameter, closely resembles sintered porous wall or transpiration cooling. This study lends support to the assertion that as the pitch-to-effusion hole diameter ratio approaches zero, effusion cooling takes on characteristics similar to transpiration cooling.

Venkatesh *et al.* (2018) conducted an investigation on the cooling effectiveness of effusion cooling configurations by varying geometric parameters. Additionally, they explored the impact of variable hole diameter in the effusion configuration to reduce coolant consumption in the far field. This strategy was driven by the fact that far-field rows typically have a fully established coolant layer, leading to optimal cooling efficiency. Consequently, the downstream regions necessitate a reduced amount of coolant to maintain performance at an acceptable level in comparison to the upstream regions.

Singh *et al.* (2017) conducted experimental and numerical investigations on film cooling involving both forward and reverse coolant injection methods. By implementing reverse injection, they effectively eliminated the kidney vortices typically associated with conventional forward coolant injection. The results of their study revealed significant improvements in film cooling effectiveness, particularly at a blowing ratio of 1. The film cooling effectiveness is enhanced by 170, 78, and 186% for injection angles of 30^o, 45^o and 60^o, respectively.

Pu *et al.* (2022) conducted a combined experimental and numerical investigation on the performance of backward film cooling by including the thermal barrier coatings (TBC). The major parameters considered were jet orientation, thickness of the TBC, and wall curvature. They identified that the backward jet increases the cooling air coverage and reduces the potential of the thermal barrier coating. The effect of wall curvature was found to be insignificant on the film cooling performance. The trench-induced increase in the overall effectiveness was reduced by 50% for a TBC coating thickness of 1.0d.

Sakai *et al.* (2014) performed Large Eddy Simulations (LES) on a single row of effusion holes and observed the emergence of coherent vortex structures. The authors also examined the impact of vortex shapes on the performance of film cooling and revealed that the effusion cooling method exhibits distinct vortex structures, including horseshoe vortices that facilitate the distribution of coolant and counter-rotating vortex pairs that diminish cooling effectiveness by inducing mixing between the main and cold streams. Li (2010) examined the benefits of a backward-injected effusion jet compared to a forward-injected effusion jet. They revealed that the backward injection of coolant eliminates CRVPs, resulting in enhanced cooling effectiveness and reduction in its non-uniformity.

2.3 STUDIES ON HYBRID FILM COOLING

Few studies have also been conducted on combined slot and effusion film cooling, called hybrid slot film cooling, to enhance film cooling performance.

A study conducted by Ceccherini *et al.* (2009) examined the performance of film cooling configuration which included a slot, effusion holes, and dilution holes. The authors made an observation that the penetration of the effusion jet is dependent on the velocity ratio. Subsequently, they conducted a quantitative investigation and revealed that the presence of counter-rotating vortex pairs (CRVP) within the effusion flow is likewise associated with diminished film cooling effectiveness.

Facchini *et al.* (2010) investigated the impact of the slot and effusion configurations combined dilution holes on the cooling effectiveness and heat transfer coefficient. The authors examined this effect at various blowing ratios ranging from 3 to 7. They concluded that an increase in the blowing ratio of the effusion configuration leads to an increase in the heat transfer coefficient. Moreover, it was observed that the presence of the dilution hole does not have an impact on the heat transfer.

Andreini *et al.* (2012) investigated the impact of density ratio on the performance of a combined slot and effusion cooling configuration. According to their research, the influence of the density ratio was shown to be insignificant in the penetration regime. However, in the downstream, it was observed that the effectiveness was enhanced under constant velocity ratio conditions with higher density ratios.

Hong Qu *et al.* (2017) investigated combined two-dimensional slot and effusion film cooling and reported that combining both cooling techniques mitigates the low effectiveness in the far field for slot film cooling and the beginning of effusion cooling. They observed that for a given slot blowing ratio, the combined film cooling improves significantly at low blowing ratios and very marginally at high effusion blowing ratios.

Click *et al.* (2021) proposed the utilization of a louver slot in conjunction with a double wall configuration with effusion and impingement cooling. The implementation of a louver slot structure resulted in a decrease in the heat transfer coefficient downstream while simultaneously enhancing the efficiency upstream.

2.4 STUDIES ON OPTIMIZATION OF FILM COOLING CONFIGURATION

To obtain the maximum benefit of film cooling, the geometrical parameters of the cooling configuration need to be optimized. In this section, studies related to geometrical optimization and optimization strategies are discussed.

In a study conducted by Lee and Kim (2011), an optimization analysis was performed on a fan-shaped film cooling hole. The researchers utilized the Kriging approach to construct a surrogate model for the purpose of the study. The findings indicate that the optimized shaped effusion hole exhibits superior performance as compared to a reference design, resulting in a significant improvement in the film cooling performance.

Wang *et al.* (2019) conducted a multi-objective optimization of a turbine end wall cooling. The optimization process involved using Latin Hypercube Sampling for the design space and Kriging to construct a surrogate model, which was then integrated with a genetic algorithm to find the optimum configuration. The optimized configuration resulted in a marginal enhancement of the objective functions. Nevertheless, it has been found that the local improvement is considerably more prominent in comparison to the mean values.

Wang *et al.* (2020) performed an optimization analysis of impingement cooling, in which the mass flow rate of the coolant remained constant. They stated that the optimized geometry exhibits geometric dimensions that closely correspond with the upper or lower limits of the design space. The primary factor contributing to this phenomenon is the linear correlation between the size of the holes and the pitch with the film cooling effectiveness. The utilization of an optimization technique facilitates the exploration of the correlation between various geometric characteristics and film cooling effectiveness.

Tu *et al.* (2017) investigated the film-cooling effectiveness of effusion plates with isotropic and anisotropic thermal conductivity. The standard deviation of cooling effectiveness is used as the uniformity index in their study. They reported that evaluating cooling uniformity is a crucial aspect of liner design, as it indicates the severity of thermal stresses.

Dávalos *et al.* (2018) implemented artificial neural networks to predict the film cooling effectiveness on the leading edge of a gas turbine blade and optimized the cooling using the differential Evolution technique. They used hole diameter, injection angle, blowing ratio, hole pitch, and column pitch as input parameters. The results showed that there is an increment of film cooling effectiveness by 36 % and a mass flow reduction by 66 %.

2.5 STUDIES ON MATHEMATICAL MODELING APPROACHES RELATED TO FILM COOLING

Investigating the film cooling under various operating conditions and geometrical configurations implies a high computational cost. Multi-nonlinear regression techniques and surrogate methods such as Artificial Neural Networks (ANN), Kriging, and Support Vector Machines (SVM) have been generally implemented to predict film cooling effectiveness.

Lefebvre and Ballal (2010) studied film cooling effectiveness in the near-slot region.

The earlier studies have developed models by assuming an idealized turbulent boundary layer which is not valid in the near slot region. As a result, they considered skin friction coefficients obtained by direct measurement near the slot region in developing the correlation. A theoretical model was derived that predicts two-dimensional film cooling effectiveness with ± 5 percent accuracy.

Kumar *et al.* (1998) developed an automated cooling design methodology for combustor walls. The methodology has a converged fluid flow solver, which generates a detailed temperature distribution of the combustor liner and dome. The automated code can provide the temperature and heat flux distribution, effusion cooling holes, starter slots, and impinging hole arrangement.

Li and Mongia (July, 2001) developed an improved method for a correlation of film cooling effectiveness of gas turbine combustor liners. Mass transfer analogy was used for measuring the effectiveness. Design of experiments was adopted to investigate the injection angle of coolant, slot lip shape, the shape of the slot lip exit, and the thickness of the slot on the cooling performance. Numerical simulations were conducted based on configurations determined by the design of experiments. Based on experimental and numerical results, an accurate correlation for effectiveness was developed.

Wang *et al.* (2023) developed a surrogate model using artificial neural networks to understand the effect of semi-sphere vortex generator (SVG) parameters. They predicted the averaged film cooling effectiveness based on the SVG input parameters such as compound angle, size, and location.

Wang *et al.* (2015) used a support vector machine (SVM) to predict the film cooling effectiveness using the input parameters such as dimensionless downstream distance, pitch, hole incline angle, hole compound angle, length-to-diameter ratio, blowing ratio, density ratio, and mainstream turbulence intensity.

2.6 STUDIES ON EFFECTS OF GAS RADIATION AND THERMAL BARRIER COATING ON THE FILM COOLING PERFORMANCE

In actual engine conditions, the combustion temperatures would be approximately 2100 K, and at these high combustion temperatures, the radiative heat transfer which increases as the difference in the fourth power of temperature between the body and surroundings cannot be neglected. Although studies on the effect of slot geometry on film cooling performance have been prioritized in literature, very few studies have investigated the effects of radiation and are primarily available for turbine blade cooling. In this section, a brief overview of studies related to the effects of gas radiation and thermal barrier coating is presented.

Wang *et al.* (2011) conducted an investigation on the effect of gas radiation in a highly thermally loaded film cooling system experimentally and numerically. The results showed that the temperature of the test surface increased significantly with radiation effects, thereby decreasing the film cooling effectiveness.

Shan *et al.* (2013) investigated the characteristics of the infrared radiation in a turbofan engine exhaust system with a film-cooling central body numerically and experimentally. They found that the central body with film cooling could reduce the infrared radiation of the interior enclosure by 40 – 70% in comparison to the main body without film cooling.

Singh *et al.* (2018) conducted a numerical investigation to examine the impact of thermal barrier coating (TBC) and gas radiation on the film cooling performance of corrugated surfaces. The application of TBC was found to enhance the overall film cooling efficiency, resulting in an increase ranging from 0.10 to 0.15. Additionally, gas radiation was observed to elevate the temperature of the metal wall by 100 to 150^oC.

Vassen *et al.* (2004) investigated the use of Zirconites with high melting temperatures for application as thermal barrier coating at operating temperatures 1300^oC. $SrZrO_3$, $BaZrO_3$, $La_2Zr_2O_7$ powders are sintered to compacts at various porosities. They observed that the thermal expansion of these Zirconites was lower than Y_2O_3-stabilized-ZrO_2 (YSZ). The thermal conductivity was lowest for $La_2Zr_2O_7$. The results of the thermal cycling test at 1200^oC showed that $La_2Zr_2O_7$ is more stable compared to $BaZrO_3$.

Maurente and Alves (2019) conducted studies on radiation heat transfer in a gas slab with the properties characteristics of a jet engine combustor. The radiative transfer was accurately solved line-by-line with temperature, pressure, and mole fractions of the exhaust gases encountered in the combustor of a jet engine. The results helped to estimate the radiative heat load from each component of combustion species and identify that the H_2O dominates the radiative heat transfer, with CO_2 having a minor contribution.

Asok Kumar and Kale (2002) conducted a numerical simulation of steady-state heat transfer in a ceramic-coated gas turbine. The results showed that at the turbine inlet temperature of 1500 K, the radiative heat transfer is 8.4% of total heat transfer and reduced to 3.4% in the presence of a thermal barrier coating. They also identified that the uncertainties in the convection heat transfer coefficient do not significantly affect the temperatures of the metal.

Akwaboa *et al.* (2010) conducted a numerical investigation on the effects of thermal radiation on air plasma spray-coated gas turbine blades. The results indicate that the metal temperature is reduced to 100K because of the thermal barrier coating. They also reported that the temperature drops with the TBC, reduces the thermal oxidation of the bond coat in the TBC, and also delays its failure by oxidation. In addition, they recommended considering the effects of gas radiation, which contributes to an increase in metal temperatures, for accurate predictions.

2.7 STUDIES ON EXPERIMENTAL METHODOLOGIES

In this section, the studies related to experimental methodologies and calibration techniques are discussed.

Ekkad *et al.* (2004) introduced an innovative approach using transient infrared thermography to simultaneously measure film cooling effectiveness and heat transfer coefficient in a single test. In this technique, the heat transfer coefficient and cooling effectiveness are estimated in a single transient test. The methodology assumes the test surface is a semi-infinite body, and the one-dimensional heat conduction equation is solved on the surface of the test surface. The mainstream and coolant are exposed to the test surface, the surface temperature is taken at two instants, and the heat transfer coefficient and film cooling effectiveness are estimated.

Hayes *et al.* (2017) conducted an experimental investigation of the influence of free-stream turbulence on anti-vortex film cooling. They reported the application of the in-situ calibration using thermocouples to correct the measured temperatures using the IR thermal camera. They also implemented the approach for calculating the uncertainty of the experimental results obtained using the transient methodology.

Sargent *et al.* (1998) worked on an infrared thermography imaging system for convective heat transfer measurements in complex flows. The system involves the measurement of spatially resolved heat transfer coefficient in conjunction with the thermocouples, digital image processing, and IR window. A unique in-situ calibration was employed in this system. The advantages of this technique were articulated by conducting experiments on two complex flows. One was the variation of Nusselt number in swirl chamber surfaces, and the second was film cooling effectiveness on the turbine blade.

Schulz (2000) used Infrared thermography to study the film cooling of gas turbine components. A quantitative analysis of film cooling was described using the in-situ calibration. Shaped single-hole injection film cooling and full-coverage effusion cooling is taken to describe the in-situ calibration process.

For convenience and ease, the above review of literature is presented in a tabular form in Table 2.1.

Table 2.1: Summary of literature related to the present study

Sl No	Authors	year	Remarks
(a) Studies on Slot cooling			
1	Sivasegaram and Whitelaw	1969	Experimentally investigated the effect of lip thickness and injection angle on film cooling effectiveness for two-dimensional slots and observed a reduction of effectiveness when the lip thickness ratio to slot height(t/s) is greater than 0.25 and also with an increase in injection angle.
2	Bittlinger et al.	1994	Experimentally investigated two-dimensional slots and identified that the blowing ratio greater than unity results in the film cooling flow behaving like a wall jet with a superimposed mainstream flow.
3	Sturgess	1968	Stated that the prediction of film cooling effectiveness using phenomenological models developed for two-dimensional film cooling was incorrect as the flow is three-dimensional in the actual combustor. The geometrical mixing parameter for different slot designs was developed, examined, and concluded that it could differentiate good and poor film cooling slots

Continued on next page

Table 2.1 – continued from previous page

Sl No	Authors	year	Remarks
4	Sturgess	1980	Conducted experiments on three-dimensional film cooling slots and reported that the streamwise decay of film cooling effectiveness is due to small-scale turbulence generated at the metering ports and large-scale entrainment of the mainstream.
5	Nina and Whitelaw	1971	Conducted experiments with three dimensional film cooling slots and showed that a slot with a large open area ratio, small lip thickness, and long lip length has a high cooling. Experimental results also showed that tangential injection is better than splash cooling for the considered geometry.
6	Rastogi and Whitelaw	1973	Conducted experiments with three-dimensional film cooling slots to examine the impact of velocity ratio (VR), density ratio (DR), and open area on the film cooling characteristics. The authors noted that the undulating character of the effectiveness was found to be effective up to a ratio of $X/S = 30D$.

Continued on next page

Table 2.1 – continued from previous page

Sl No	Authors	year	Remarks
7	Li and Mongia	2001	Conducted experimental and numerical investigations on machined cooling ring liners and developed an improved film cooling effectiveness correlation method. In addition, they identified that at low blowing ratios, the secondary air, which has a low velocity, was entrained into the mainstream and vice-versa.
8	Mongia	2012	Developed a three-dimensional radiative heat transfer model based on finite volume techniques to predict the film cooling effectiveness of machined cooling rings. Subsequently, the model was rigorously validated using experimental data. He highlighted that numerical algorithms could provide highly reliable predictions of film performance when all heat transfer mechanisms were considered simultaneously.

Continued on next page

Table 2.1 – continued from previous page

Sl No	Authors	year	Remarks
9	Cho and Ham	2001	Conducted an experimental study to examine the impact of coolant injection types and the arrangement of the injection feed on the fluid flow and heat transfer characteristics and revealed that both parallel and vertical injection types exhibited relatively weak flow patterns at the slot exit. Moreover, the heat transfer is found to be higher for the vertical injection method.
11	Park et al.	2009	Conducted an experimental study to investigate the effect of injection type on slot film cooling for a ramjet combustor. They identified that the increase in the slot injection reduced the film cooling effectiveness significantly, and the wiggle strips induced the three-dimensional flow and enhanced the mixing.

Continued on next page

Table 2.1 – continued from previous page

Sl No	Authors	year	Remarks
12	Yang et al.	2012	Conducted an experimental investigation on heat transfer characteristics of film cooling using single and two rows of parallel inlet holes. Results showed that the blowing ratio significantly affects the effectiveness, and the staggered arrangement of two rows generated a high heat transfer coefficient.
13	Song et al.	2012	Experimentally investigated the slot film cooling performance in a ram jet combustor with flame holders. In the first slot, the blockage due to the flame holder accelerated the mainstream flow and suppressed the coolant, resulting in better cooling. However, the cooling was reduced in the second slot due to distributed flow.
14	Wei et al.	2015	Conducted a numerical study on the effect of various slot geometries on impinging–film hybrid cooling. They identified that the triangular slab outperformed other geometries. It was also observed that the convergent slot is better than the divergent slot.

Continued on next page

Table 2.1 – continued from previous page

Sl No	Authors	year	Remarks
15	Zang et al.	2018	Conducted an experimental investigation on the overall film cooling performance of the t-type slot impinging film cooling. They investigated the effect of the blowing ratio and geometrical parameters such as jet-to-plate pitch, hole-to-hole pitch, and hole diameter. The results showed that the increase in the jet-to-plate pitch and the decline in the hole pitch enhances the effectiveness.
16	Wang et al.	2018	Conducted an experimental study to examine how various factors influence the mixing of air within slots. These factors included the orientation angle, injection angle, slot width, and slot depth. The results demonstrated that increasing the orientation angle from 0^0 to 60^0 improved the uniformity of the coolant flow at the slot exit. However, Wider slots resulted in non-uniform flow. Additionally, the optimal slot depth was found to be 2 to 2.8 times the diameter of the holes.

Continued on next page

Table 2.1 – continued from previous page

Sl No	Authors	year	Remarks
17	Zhou and Wygnanski	1993	Investigated the effect of parameters governing two-dimensional turbulent wall jets in an external stream. They measured the mean velocity profiles and observed self-similarity in the velocity profiles for the cases where the maximum jet velocity was twice that of the free stream velocity.
18	Ben Haj Ayech et al.	2016	Conducted a numerical study of a turbulent wall jet in a co-flow stream to determine the flow's dynamic, thermal, and turbulent characteristics. The study was conducted for a velocity ratio ranging from 0 to 0.2. The findings indicate that there is a negative correlation between the velocity ratio and the potential core length and also observed a self-similarity in velocity and turbulence profiles.
19	Godi et al.	2019	Investigated the effect of the inlet geometry of wall jets (without external flow) on flow and heat transfer characteristics. Self-similarity in the mean velocity and RMS intensity profiles was observed beyond X/S = 20.
(b) Studies on effusion film cooling			
Continued on next page			

Table 2.1 – continued from previous page

Sl No	Authors	year	Remarks
1	Andrews et al.	1989	Conducted experiments on multi-row effusion film cooling with various hole porosities and coolant injection angles and revealed that the length of the effusion hole and the approach area of the hole play a significant role in the overall heat transfer phenomenon.
2	Sinha et al.	1991	Investigated the impact of density ratio on film cooling performance and reported that a decrease in the density ratio and an increase in the momentum flux ratio leads to a deterioration of cooling performance.
3	Scrittore et al.	2007	Laser Doppler velocimetry was employed to investigate the fluid flow characteristics of effusion cooling and observed a self-similarity in both the velocity and turbulence profiles when scaled with a blowing ratio.
4	Huang et al.	2015	Investigated the cooling performance of effusion cooling with a hole diameter of 0.5 mm and revealed that effusion cooling, using compactly packed cooling holes with a 0.5 mm diameter, closely resembles transpiration cooling.

Continued on next page

Table 2.1 – continued from previous page

Sl No	Authors	year	Remarks
5	Venkatesh et al.	2018	Investigated the impact of variable hole diameter on the performance of the effusion configuration to reduce coolant consumption in the far field. This strategy was driven by the fact that far-field rows typically have a fully established coolant layer, leading to optimal cooling efficiency. Consequently, the downstream regions necessitate a reduced amount of coolant to maintain performance at an acceptable level in comparison to the upstream regions.
6	Singh et al.	2017	Investigated the impact of coolant injection in forward and reverse directions on film cooling performance and reported that the performance is enhanced by eliminating the kidney vortices in the conventional forward coolant injection using reverse injection.

Continued on next page

Table 2.1 – continued from previous page

Sl No	Authors	year	Remarks
7	Pu et al.	2022	Conducted experimental and numerical studies on the thermal performance of backward film cooling with simulated thermal barrier coatings (TBC) at various walls. They identified that the backward jet increases the cooling air coverage and reduces the potential of the thermal barrier coating.
8	Sakai et al.	2014	Large Eddy Simulations are Conducted on a single row of effusion holes and observed coherent vortex structures in the flow. They also investigated how vortex shapes affect film cooling performance and identified that the horseshoe vortices aid in the distribution of coolant, and counter-rotating vortex pairs reduce the cooling efficiency.
9	Li et al.	2010	examined the benefits of a backward-injected effusion jet compared to a forward-injected effusion jet. They revealed that the backward injection of coolant eliminates CRVPs, resulting in enhanced cooling effectiveness and reduction in its non-uniformity.
(c)Studies on hybrid film cooling			

Continued on next page

Table 2.1 – continued from previous page

Sl No	Authors	year	Remarks
1	Ceccherini et al.	2009	Examined the performance of film cooling configuration, which included a slot, effusion holes, and dilution hole. They observed that the penetration of the effusion jet is dependent on the velocity ratio, and the presence of counter-rotating vortex pairs (CRVP) within the effusion flow is likewise associated with diminished film cooling effectiveness.
2	Facchini et al.	2010	Investigated the impact of the slot and effusion configurations combined with dilution holes on the cooling effectiveness and heat transfer coefficient and revealed that an increase in the blowing ratio of the effusion configuration leads to an increase in the heat transfer coefficient. Moreover, it was observed that the presence of the dilution hole does not have an impact on the heat transfer.
3	Andreini et al.	2012	Investigated the impact of density ratio on the performance of a combined slot and effusion cooling configuration and revealed that the effectiveness was enhanced under constant velocity ratio conditions with higher density ratios.

Continued on next page

Table 2.1 – continued from previous page

Sl No	Authors	year	Remarks
4	Hong Qu et al.	2017	Investigated combined two-dimensional slot and effusion film cooling and reported that combining both cooling techniques mitigates the low effectiveness in the far field for slot film cooling and the beginning of effusion cooling. For a given BR_{slot}, the combined film cooling improves significantly at low blowing ratios compared to high blowing ratios.
5	Click et al.	2021	proposed the utilization of a louver slot in conjunction with a double wall configuration with effusion and impingement cooling. The implementation of a louver slot structure resulted in a decrease in the heat transfer coefficient downstream while simultaneously enhancing the efficiency upstream.
(d) Studies on optimization of the film cooling configuration			

Continued on next page

Table 2.1 – continued from previous page

Sl No	Authors	year	Remarks
1	Lee and Kim et al.	2011	Conducted an optimization analysis on a fan-shaped film cooling hole by utilizing the Kriging approach to construct a surrogate model for the study. The findings indicate that the optimized configuration exhibits superior performance as compared to a baseline design, resulting in a significant improvement in the film cooling performance.
2	Wang et al.	2019	Conducted a multi-objective optimization of a turbine end wall cooling using Latin Hypercube Sampling for the design space and Kriging to construct a surrogate model, which was then integrated with a genetic algorithm to find the optimum configuration. The results showed that the optimum configuration showed a local improvement in film cooling effectiveness considerably more prominent in comparison to the mean values.

Continued on next page

Table 2.1 – continued from previous page

Sl No	Authors	year	Remarks
3	Wang et al.	2020	performed an optimization analysis of impingement cooling, in which the mass flow rate of the coolant remained constant. They stated that the optimized geometry exhibits geometric dimensions that closely correspond with the upper or lower limits specified in the design of space. The primary factor contributing to this phenomenon is the linear correlation between the size of the holes and the pitch with the film cooling effectiveness
4	Tu et al.	2017	This study examined the film-cooling efficiency of effusion test plates and employed the standard deviation of cooling efficiency to measure the uniformity of the effectiveness. The assessment of cooling uniformity holds significant importance in the design of liners, as it serves as an indicator of the magnitude of thermal strains. They identified that the effusion hole with 35^0 at low BR shows better cooling.

Continued on next page

Table 2.1 – continued from previous page

Sl No	Authors	year	Remarks
5	Davalos et al.	2018	Implemented artificial neural networks to predict the film cooling effectiveness on the leading edge of a gas turbine blade and optimized the cooling configuration using the differential Evolution technique.
(e) Studies on mathematical modeling approaches related to film cooling			
1	Kumar et al.	1998	Developed an automated cooling design methodology for combustor walls. The methodology has a converged fluid flow solver, which generates a detailed temperature distribution of the combustor liner and dome having effusion holes, starter slots, and impinging hole arrangement.
2	Li and Mongia	2001	Developed an improved method for a correlation of film cooling effectiveness. The design of experiments was adopted to investigate the injection angle of coolant, slot lip shape, and the thickness of the slot. An accurate correlation for effectiveness was developed based on experimental and numerical results.

Continued on next page

Table 2.1 – continued from previous page

Sl No	Authors	year	Remarks
3	Wang et al.	2023	Developed a surrogate model using artificial neural networks to understand the effect of semi-sphere vortex generator (SVG) parameters. They predicted the averaged film cooling effectiveness based on the SVG input parameters, such as compound angle, size, and location.
4	Wang et al.	2015	Used a support vector machine (SVM) to predict the film cooling effectiveness using the input parameters such as dimensionless downstream distance, pitch, hole incline angle, hole compound angle, length-to-diameter ratio, blowing ratio, density ratio, mainstream turbulence intensity.
(f) Studies on the effect of gas radiation and thermal barrier coating			
1	Wang et al.	2011	Conducted combined experimental and numerical investigations on radiation effects in a highly thermally loaded film cooling system. The results showed that the temperature of the plate increased significantly with radiation effects.

Continued on next page

Table 2.1 – continued from previous page

Sl No	Authors	year	Remarks
2	Shan et al.	2013	Investigated the infrared radiation characteristics of a turbofan engine exhaust system with a film-cooling central body numerically and experimentally. They found that the central body with film cooling could reduce the infrared radiation of the interior enclosure by 40 – 70 % in comparison to the main body without film cooling.
3	Singh et al.	2018	Carried out a numerical investigation of the influence of thermal barrier coating and gas radiation on the film cooling of corrugated surfaces. The application of TBC enhanced the overall film cooling efficiency by a value ranging from 0.10 to 0.15, and gas radiation raises the hot side metal wall temperature from 100 to 150^oC.

Continued on next page

Table 2.1 – continued from previous page

Sl No	Authors	year	Remarks
4	Vassen et al.	2004	Investigated the use of Zirconites with high melting temperatures for application as thermal barrier coating at operating temperatures 1300^oC. $SrZrO_3$, $BaZrO_3$, $La_2Zr_2O_7$ powders are sintered to compacts at various porosities. They observed that the thermal expansion of these Zirconites was lower than Y_2O_3-stabilized-ZrO_2 (YSZ). The thermal conductivity was lowest for $La_2Zr_2O_7$.
5	Maurente and Alves	2019	Conducted studies on radiation heat transfer in a gas slab with the properties characteristics of a jet engine combustor. The radiative transfer was accurately solved line-by-line with temperature, pressure, and mole fractions of the exhaust gases encountered in the combustor of a jet engine. The results helped to estimate the radiative heat load from each component of combustion species and identify that the H_2O dominates the radiative heat transfer, with CO_2 having a minor contribution.

Continued on next page

Table 2.1 – continued from previous page

Sl No	Authors	year	Remarks
6	Asok Kumar and Kale	2002	Conducted a numerical simulation of steady-state heat transfer in a ceramic-coated gas turbine. The results showed that at the turbine inlet temperature of 1500 K, the radiative heat transfer is 8.4% of total heat transfer and reduced to 3.4% in the presence of a thermal barrier coating.
7	Akwaboa et al.	2010	Conducted a numerical investigation on the effects of thermal radiation on air plasma spray-coated gas turbine blades. The results indicate that the metal temperature is reduced to 100K because of the thermal barrier coating.
(g) Studies on experimental methodology			
1	Ekkad et al.	2004	Introduced an innovative approach using transient infrared thermography to simultaneously measure film cooling effectiveness and heat transfer coefficient in a single test by assuming the test surface is a semi-infinite body.

Continued on next page

Table 2.1 – continued from previous page

Sl No	Authors	year	Remarks
2	Hayes et al.	2017	Conducted experiments to investigate the impact of free-stream turbulence on anti-vortex film cooling. They reported the application of the in-situ calibration using thermocouples to correct the measured temperatures using the IR thermal camera.
3	Sargent et al.	1998	Worked on an infrared thermography imaging system for convective heat transfer measurements in complex flows. The system integrates the measurement of spatially resolved heat transfer coefficients, employing a combination of thermocouples, infrared (IR) window, and digital image processing. A unique in-situ calibration was employed, and the advantages of this technique were articulated by conducting experiments.
4	Suhulz et al.	2000	Implemented infrared thermography to study the film cooling in gas turbine components. A quantitative analysis of film cooling was described using the in-situ calibration. Shaped hole injection film cooling and effusion cooling were considered to describe the in-situ calibration process.

2.8 OBJECTIVES OF THE PRESENT STUDY

From the above review of literature, it is evident that film cooling is a promising technique for maintaining the combustor liner at safe temperatures. Although several studies have been conducted in the past, studies on the practical film cooling slot configuration of a combustor liner are scarce in the literature. Studies have been generally reported under laboratory operating conditions (low pressure and low temperature). Most investigations have been devoted to fundamental studies such as validating numerical studies, two-dimensional slots, and non-practical slot configurations. In addition, the prediction of film cooling effectiveness using a mathematical model together with optimization and the inclusion effects of gas radiation for practical slots are very limited in the literature. In consideration of the above reasons, the primary objective of the present study is to investigate a practical three-dimensional slot film cooling of an annular combustor liner and optimize its performance under actual engine conditions. The present work focuses on comprehensive experimental and numerical parametric studies to get insights into the practical three-dimensional slot film cooling (with lip, inclined holes, and realistic configuration) under laboratory as well as actual engine conditions. The three-dimensional slot configuration is optimized using machine learning algorithms such as kriging and genetic algorithms. In addition, a numerical investigation is conducted under actual engine conditions on two rows of subsequent liners to identify the effect of film cooling of the first cooling ring (CR) on the performance of the subsequent cooling ring, and the pitch between the liners is also optimized. Furthermore, the baseline three-dimensional slot of an improvised hybrid slot configuration is replaced with the optimized three-dimensional slot configuration to get the complete benefit of film cooling. The cooling performance of the optimal configuration of the three-dimensional slot and subsequent rows of liners is validated by testing experimentally under laboratory conditions. Finally, a numerical investigation is conducted to estimate the effect of the combustion gas radiation and thermal barrier coating on the film cooling performance. The objectives of the present study are:

- To study the fluid flow and heat transfer characteristics of the three-dimensional slot film cooling under laboratory conditions experimentally and numerically.

- To study the influence of the flow and geometrical parameters on the film cooling performance and develop a mathematical model for predicting the film cooling effectiveness under actual engine conditions.

- To conduct the sensitivity of the geometrical parameters numerically and optimize the three-dimensional slot configuration under actual engine conditions to enhance film cooling effectiveness and its uniformity on the liner.

- To conduct a numerical study on two rows of subsequent liners to identify the effect of film cooling of the first cooling ring (CR) on the performance of the subsequent cooling ring and also to optimize the liner length to reduce the number of cooling rings for the entire combustor.

- To estimate the complete benefit of film cooling performance by replacing the baseline three-dimensional slot with the optimized three-dimensional slot configuration in an improvised hybrid slot configuration obtained from the studies of Adapa (2022).

- To test and validate the cooling performance of optimum three-dimensional slot and optimum subsequent rows using experiments under laboratory conditions.

- To conduct a numerical investigation for estimating the effect of the combustion gas radiation and thermal barrier coating on the film cooling performance.

- To test the robustness of the optimum slot configuration under the effects of gas radiation by comparing it with the reference slot configurations of the baseline combustor.

CHAPTER 3

EXPERIMENTAL AND NUMERICAL METHODOLOGY

3.1 INTRODUCTION

In this chapter, the details of the experimental test facility and the methodology used to estimate the film cooling performance are discussed. In addition, a brief description of each equipment used in the test facility and the uncertainty of the experimental results are discussed. Furthermore, the numerical methodology, domain used, and results of the grid-independence study are highlighted.

3.1.1 Details of the experimental facility

The objective of the experimental facility is to investigate the film cooling performance of the three-dimensional slot film cooling and validate the numerical study under laboratory conditions (low temperature and pressure). A low-speed wind tunnel experimental rig is developed that mimics the three-dimensional slot film cooling of an annular combustor. Figure 3.1a shows the experimental setup with the mainstream and coolant sections. Here, the mainstream and the coldstream represent the hot gases and the bypassed coolant from the compressor for the film cooling in the actual engine. The photograph of the experimental facility developed for these film cooling studies is shown in Figure 3.2. A centrifugal blower is employed to supply the mainstream air, which is heated by using three consecutive mesh heaters connected in series. A low-voltage, high-current DC source is used to supply electrical power to the mesh heater. Further, the air is mixed in a static mixing chamber to obtain temperature uniformity throughout the cross-section. The mixing chamber comprises two converging and diverging sections with an area ratio of 14, and these are oriented in opposite directions (see Figure 3.1a). This method offers better air mixing at a very low expense of total pressure.

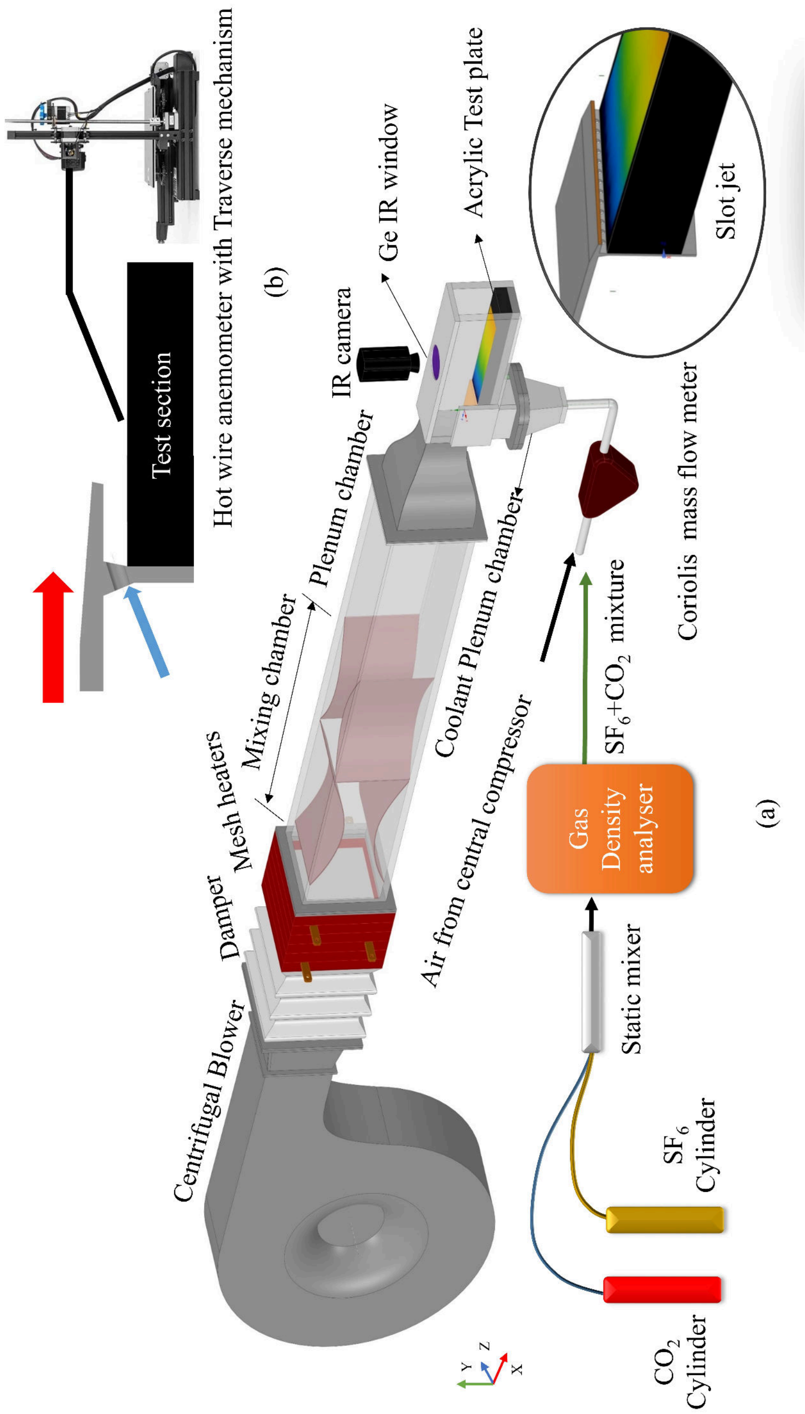

Figure 3.1: Schematic of the experimental layout used in the present study

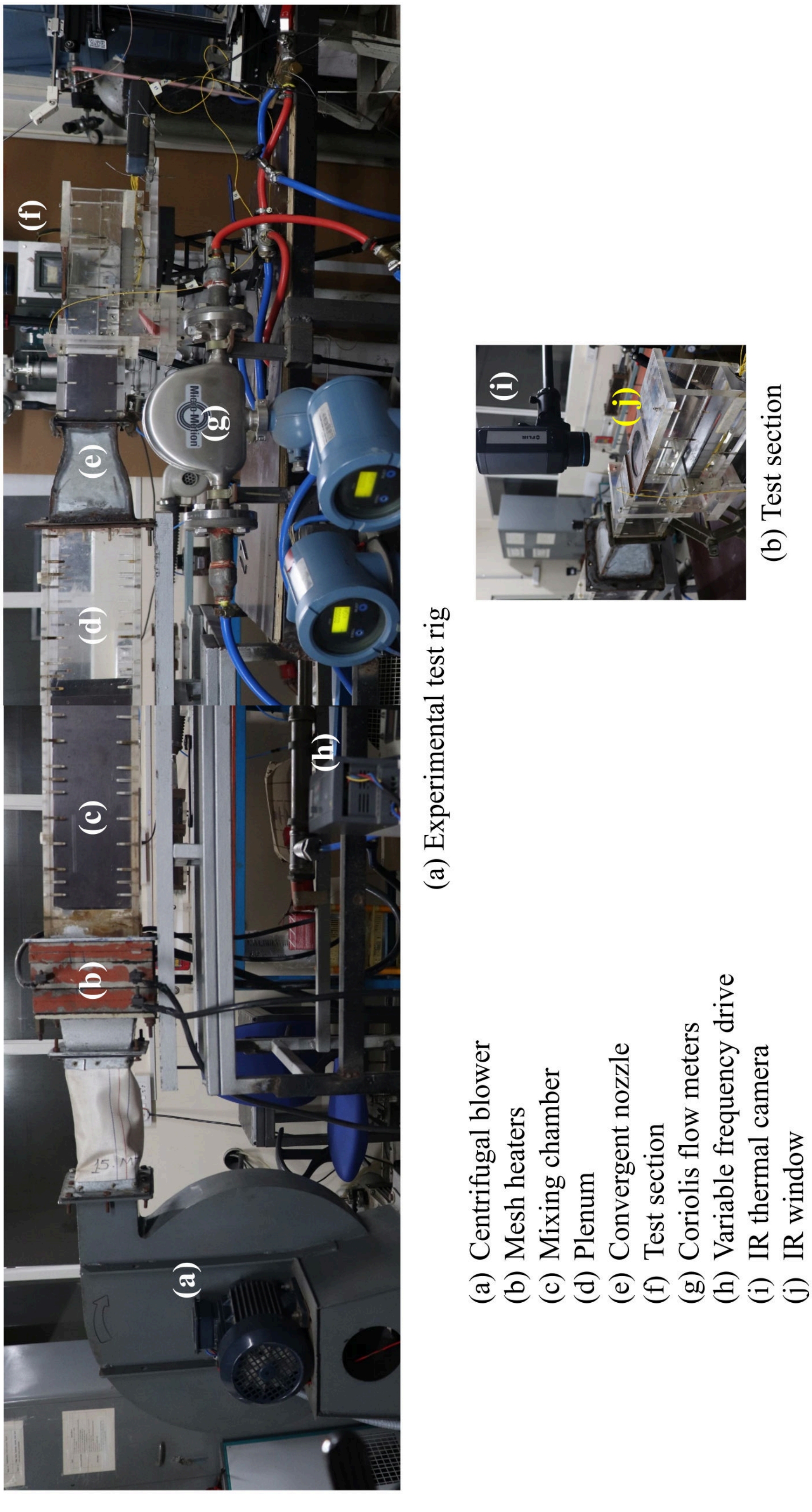

(a) Experimental test rig

(b) Test section

Figure 3.2: Experimental test rig used in the present study

Further, the air is allowed to settle in the plenum chamber to attenuate non-uniformities in the flow and to provide a uniform static pressure. Finally, the plenum chamber and test section are connected by a De-Laval nozzle to attain the required air velocity. The temperature and velocity of the mainstream air at the test section entrance are maintained approximately at 60^oC and 5.4 m/s, respectively.

Ambient air is used as a coolant for low-density ratio (DR) experiments and is supplied by a 6-bar centralized air compressor. Additionally, the density ratio (DR) is increased using a foreign gas to mimic the density ratio of actual engine conditions in the experiments under laboratory conditions (low pressure and temperature). Here, the density ratio (DR) is defined as the ratio of the density of the coolant to the density of the mainstream. A high-density sulfur hexafluoride (SF_6) is diluted using carbon dioxide (CO_2) gas, mixed in a static mixer, and used as the coolant. Two Coriolis flow meters are used to measure the mass flow rate for each gas. Additionally, the density of the gas mixture is dynamically measured using a Yokogawa gas density analyzer (see Figure 3.1 and 3.12). The gas mixture is diverted into the test section when the density and blowing ratios reach the required levels.

The test section and test plate are made of acrylic material, with an extremely low thermal conductivity of k = 0.19 W/mK. The thickness of the test plate is 25 mm. A one-inch layer of glass wool insulation is added to the bottom of the test surface to minimize thermal losses.

The test section has the following dimensions: width (W) = 60 mm, height (H) = 80 mm, and length (l) = 250 mm. The temperature of the test surface is obtained from the IR camera through a germanium infrared window having 90% of transmissivity. As shown in Figure 3.2b, FLIR A655sc IR camera with a 25^o field of view and a spectral range of 8 to 14 μm is used to obtain the temperature field. In the transient experiments, the camera is set to 50 frames per second, and video with a maximum resolution of 640X480 pixels is captured at two frames per second. As described in the study conducted by Godi *et al.* (2020*b*), to capture the temperature field, the test surface is coated with matte black paint to achieve an emissivity of up to 0.97.

Further, using in-situ calibration, the temperatures measured by the IR camera are corrected to the actual temperatures using surface thermocouples. For calibration, seven high-response Omega micro thermocouples of 0.2 *mm* bead size are embedded onto the test surface along the streamwise direction to resolve the entire range of temperatures. The correction approach entails minimizing the temperature difference between the surface thermocouple and the IR camera readings at the same location on the test surface. With a view to minimizing the temperature difference and correcting the entire thermal image, the reflection temperature, atmospheric temperature, and IR glass transmissivity are tuned in the data acquisition software.

Figure 3.3 (a) shows the thermocouple locations on the test surface, and Figure 3.3 (b) shows a comparison of raw IR and calibrated IR measurements with the thermocouple readings. It is apparent from the figure that the calibrated IR measurements are seen to be in good agreement with the thermocouple data.

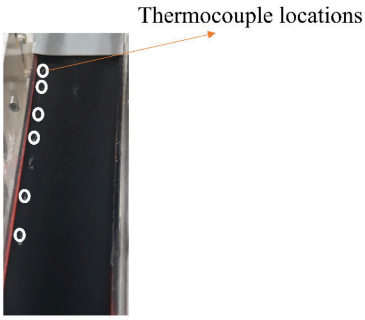

(a)

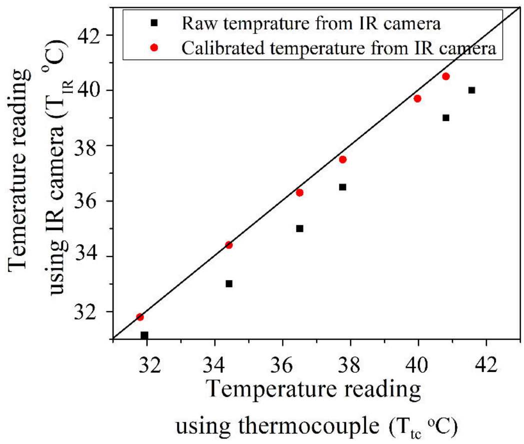

(b)

Figure 3.3: (a) Thermocouple locations on the test plate (b) Comparison of Raw IR measurements and calibrated IR measurements

The flow field is measured using a DANTEC constant-temperature hot wire anemometer.

A single wire boundary layer probe is used to measure the u-component of velocity in the flow field. The probe is made of platinum-coated tungsten wire with a diameter of 5μm and a wire length of 1.2 mm. The schematic of the anemometer arrangement used to measure the flow field is shown in Figure 3.1b. An automated traverse mechanism is fabricated to precisely locate the probe at a required position in the flow field.

3.1.2 Details of jet plate

The jet plate is fabricated using the Digital light processing (DLP) 3D printing technique. In this technique, the resin turns into plastic when applied with a low-powered and high-intensity UV light. A commercially available standard resin that can withstand up to $90^{O}C$ is used for 3D printing. The maximum tolerance of each dimension is 0.1mm. The nomenclature and dimensions of the practical three-dimensional slot under consideration are shown in Figure 3.4 and Table 3.1, respectively. The jet plate used in the experiments consists of 13 slot jet holes. The influence of parameters such as slot Reynolds number (Re_s), slot jet diameter (d), dimensionless slot jet pitch (p/d), lip taper angle (α), dimensionless lip length (L/d) and slot jet injection angle (β) on the flow and heat transfer characteristics and optimization for maximum film cooling performance are reported in the subsequent chapters.

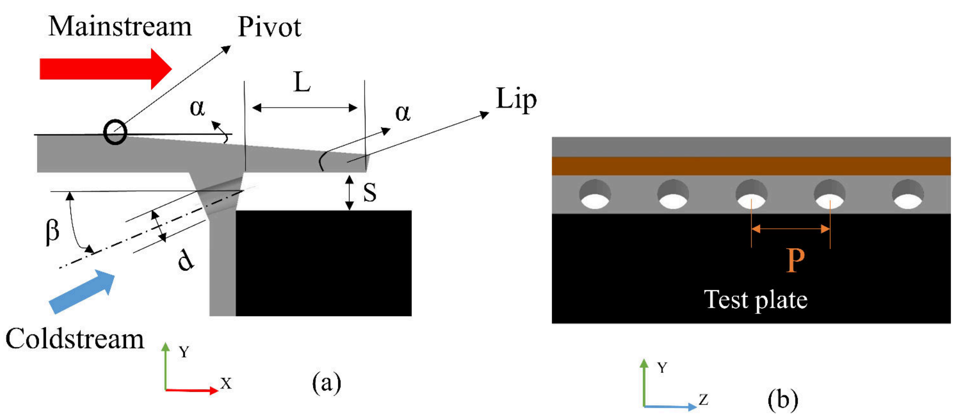

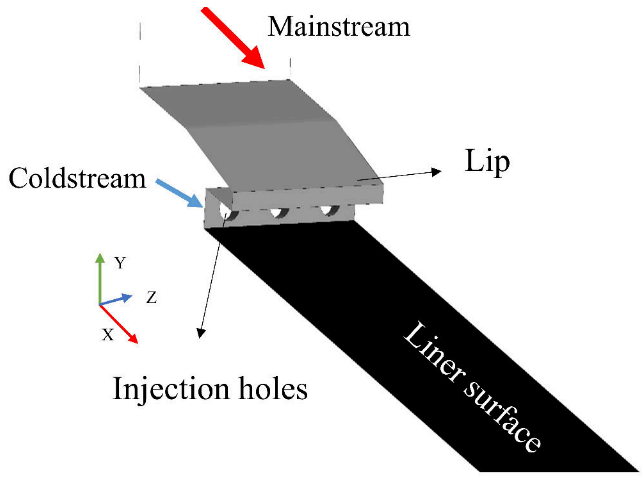

(c)

Figure 3.4: Schematic of the three-dimensional slot: (a) Side view (b) Front view (c) Three-dimensional view

where, S = slot height,

d = Slot jet diameter,

p = Slot jet pitch,

L = lip length,

α = Lip taper angle,

β = Slot jet injection angle

Table 3.1: Dimensions of the practical three-dimensional slot considered in the present study

S (mm)	d (mm)	p/d	L/d	α	β
2.5	1.7	2.45	4.4	5^o	20^o

3.2 INSTRUMENTATION

In this section, the details of the equipment used in the experimental setup are discussed.

3.2.1 Centrifugal blower

A centrifugal blower with a capacity of 800 CFM is used to send the air as a mainstream. The blower is connected to the downstream of the setup using flexible silicon bellows to reduce the propagation of vibrations to the entire setup. The impeller of the blower is rotated by an electrical 3-phase motor, and it is controlled by a variable frequency drive (VFD). The VFD is manually varied and fixed to a certain level as per the flow rate or velocity requirement at the test section. The photograph of the centrifugal blower is shown in Figure 3.5. The non-uniformities of flow are attenuated while flowing in a long wind tunnel. The long wind tunnel consists of a mixing chamber that offers high-pressure drop and a plenum chamber to settle the flow.

Figure 3.5: Centrifugal blower (Image source: KPT Blowers)

3.2.2 Mesh heaters and DC power source

Mesh heaters are used to heat the mainstream air from the blower that works on the principle of Joule heating, where thermal energy is generated when current flows through an electrical conductor. Details of the mesh heater are shown in Figure 3.6a. The heater is made of stainless steel mesh as a heating element, and the size of each cell is 0.3×0.3 mm^2 with 70% open area. The mesh is clamped to a copper bus bar (Width = 15 mm width and thickness = 5 mm), and these copper bus bars are connected to the DC power supply. Three mesh heaters are connected electrically in series to raise the air temperature to 60^oC. A high-current and low-voltage DC transformer is used to supply power to the mesh heater. The input of the transformer is a 3-phase 240 V AC supply, and the output is a DC supply with a maximum power of 8400 KW (25 V and 350 amp). A photograph of the DC power supply used in the study is shown in Figure 3.6b. The DC power supply is controlled to maintain the mainstream at the required temperature.

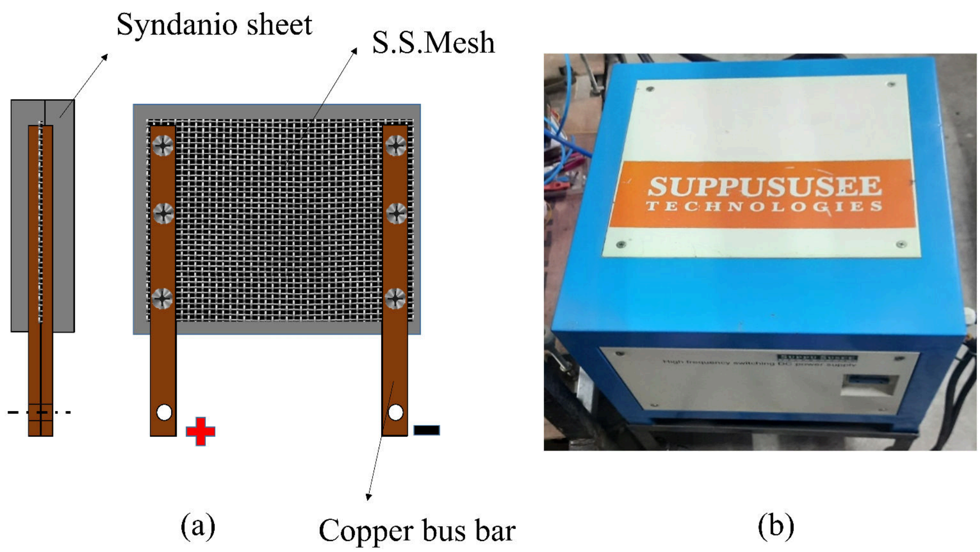

Figure 3.6: (a) Mesh heater (b) DC power source

3.2.3 Infrared thermal camera

The temperature of the test place surface is measured using FLIR A655SC Infrared thermal camera. The heat flux sensor in the IR camera is a microbolometer. A microbolometer is a specific type of bolometer that absorbs radiant heat energy with a wavelength range between 8 to 14 μm from the surface and converts it into voltage. A photograph of the IR camera used in the present study is shown in Figure 3.7. Specifications of the present thermal camera are given in Table 3.2.

Figure 3.7: Infrared Thermal camera (Image source: FLIR)

Table 3.2: Specifications of the infrared thermal camera

Parameters	**Details**
Object temperature range	-40 to 150^0C,100 to 650^0C,300 to 2000^0C
Time constant	8 ms
Resolution	640×480
Thermal sensitivity	0.05 $^0C/Pixel$
Sensitivity	0.03^0C
Frame rate	50 fps @ 640×480

3.2.4 Infrared transparent window

In the experimental test rig, the top plate of the test section is provided with an IR transparent window, allowing the IR camera to measure the temperatures on the test surface. Infrared transparent windows are made of special materials which allow thermal radiation to pass through them. These windows are usually made of germanium, zinc-selenide (Zn-Se), sodium chloride (NaCl), and calcium fluoride (CaF_2). They are selected based on the application, temperature range, cost, and transmissivity. In the present study, a circular IR window made of Germanium crystal with anti-reflection coating is used. The diameter of the windows is 101.6 mm, and the thickness is 5 mm. The average transmissivity of the Ge IR window is 0.9 in the IR wavelength range of 8-14 μm. A photograph of the Germanium IR window and its installation in the test section are shown in Figure 3.8 a and b, respectively.

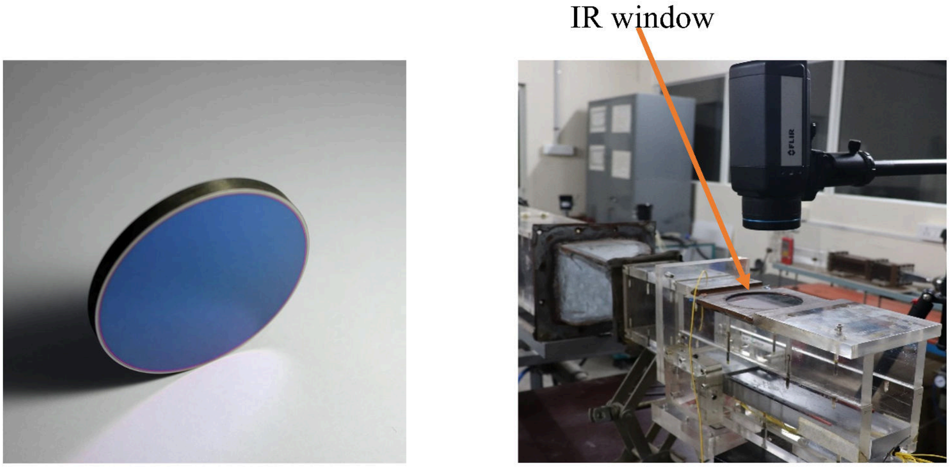

(a) (b)

Figure 3.8: (a)IR window (Image source: VY Optoelectronics Co., Ltd.) (b) IR window in the top plate of the test section

3.2.5 Thermocouples and calibration unit

The mainstream, coldstream, and ambient temperatures are measured using thermocouples. For this purpose, K-type thermocouples made of Chromel-Alumel with a gauge of 34 AWG are used. In addition, Omega micro thermocouples with a bead size of 0.2 mm are used as surface thermocouples for in-situ calibration of the IR camera. In all, seven thermocouples are embedded on the test surface along the streamwise direction and used as reference values to correct the IR camera readings. The details of thermocouples and the location of micro thermocouples on the test surface are shown in Figure 3.9.

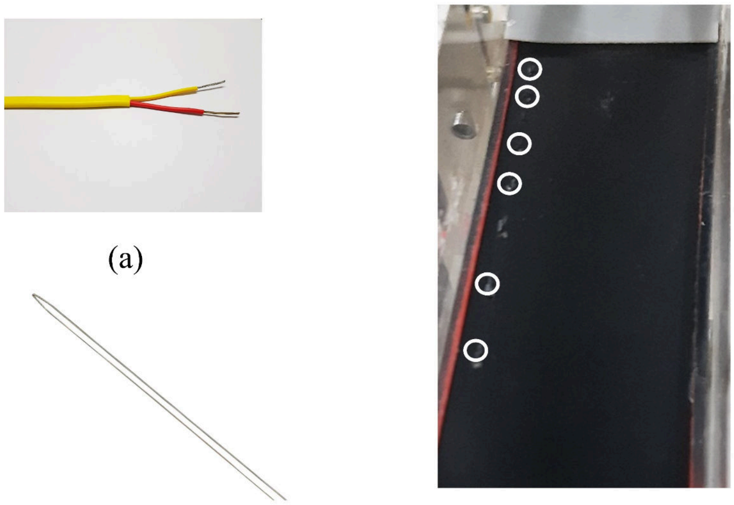

(a)

(b)

(c)

Figure 3.9: (a) K-type thermocouple (34 AWG) (b) K-type micro thermocouple (C) location of mico thermocouple on test surface for In-Situ calibration

Thermocouples used in the present experiments are calibrated using a dry-well calibrator (Model: Fluke 9142). The photograph of the apparatus used for the calibration is shown in Figure 3.10.

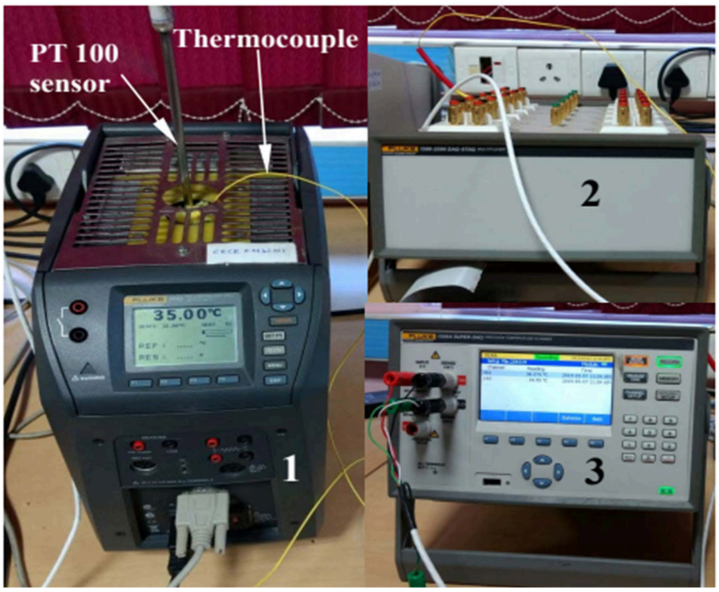

Figure 3.10: Dry-well calibrator integrated with Data acquisition system (Image source: Central Electronics Centre (CEC), IIT Madras)

For this purpose, a highly accurate platinum resistance temperature detector (PT 100) is used as a reference sensor. PT 100 and the thermocouples to be calibrated are placed in the drywall, and temperature data is measured every $5S$ and monitored until a steady state is reached. The calibration is carried out from 20^oC to 100^oC with a resolution of 5^oC.

3.2.6 Coriolis mass flow meter

The mass flow rate of the coolant required for various blowing ratios is monitored using an Emerson - CMFS015M Coriolis mass flow meter. The flow meter works on the principle of motion mechanics. When the fluid enters, the flow splits into two U-tubes. An electrical coil drive simulates the tubes oscillating with a frequency opposite to the natural resonant frequency. As a result, the voltage in each pickoff generates a sine wave. The delay time in each sinewave is proportional to the mass flow rate. The indicator of the flow meter, a schematic of the sensor, and its outlook are depicted in Figure 3.11.

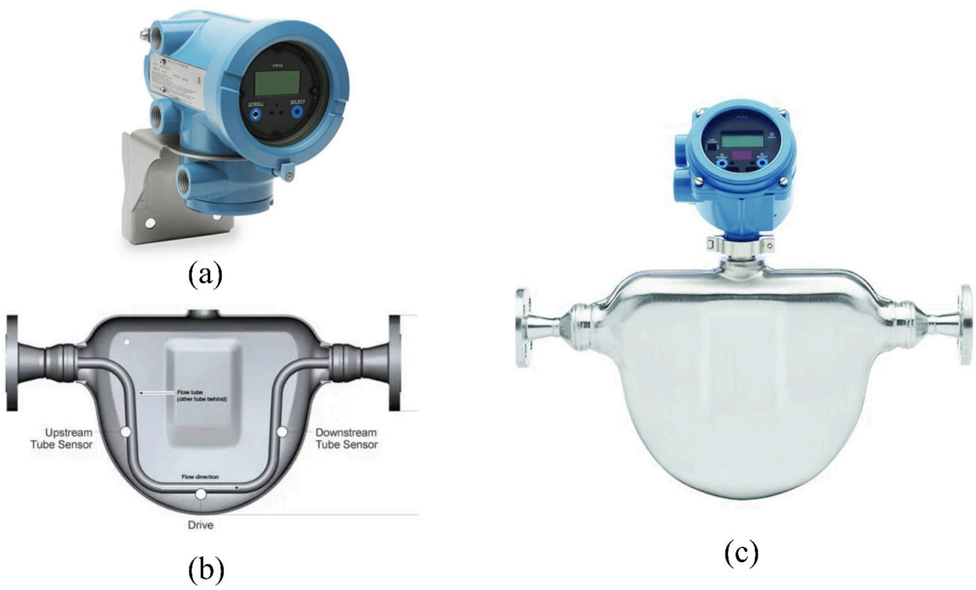

Figure 3.11: Coriolis mass flow meter components (a) Indicator (b) Schematic of the sensor (c) Sensor outlook

3.2.7 Gas density analyser

Film cooling experiments are also conducted at high-density ratios in the laboratory using high-density foreign gas to mimic density ratios under engine conditions. For this purpose, a density analyzer is used to measure the density of the coolant ($SF_6 + CO_2$). After conditioning the density ratio and blowing ratio, the coolant is diverted into the test section. The gas density analyzer works on a similar principle to the working of the Coriolis flow meter. However, here, the density is proportional to the delay in the time in each sine wave. The picture of the density analyzer (Make: YOKOGAWA) used in the present study is shown in Figure 3.12.

Figure 3.12: Gas density analyzer

3.2.8 Pitot tube and digital differential pressure gauge

In the present study, the calibration of the hotwire anemometer is carried out using a micro pitot tube having a 90^o bend. The pitot tube and a digital differential pressure gauge are used to measure the dynamic pressure and to calculate the velocities. A photograph of the differential pressure transducer and micro pitot used in this study is shown in Fig. 3.13. The device is capable of measuring the pressure in the range of -100 to +7000 pa with a resolution of 1 Pa.

(a) (b)

Figure 3.13: Pitot tube and digital differential pressure gauge

3.2.9 Hot wire anemometer and calibration

Fluid flow characteristics of the film cooling are measured using a mini constant temperature anemometer (Make: Dantec Dynamics, Model: MiniCTA 54T42). A photograph of the hot wire anemometer unit, arrangement for measurement, and probes used in the present study are shown in Figure 3.14(a-e). A boundary layer probe is used to measure velocities very close to the test surface. The hot-wire anemometer works on the principle that the heat dissipated from the hot wire by the fluid is proportional to the voltage change in the circuit. The change in voltage depends on the fluid velocity.

The hot-wire anemometer is calibrated using a micro wind tunnel, which consists of a blower, a settling chamber, and a developing test section. The flow rate of the air is controlled using a rheostat. The hotwire probe and pitot tube are placed precisely equidistant on either side of the center at the exit of the test section. Here, the change in voltage in the hotwire anemometer is correlated with the velocity obtained from the pitot tube. A photograph of the micro wind tunnel used in the present study is shown in Figure 3.14 (e).

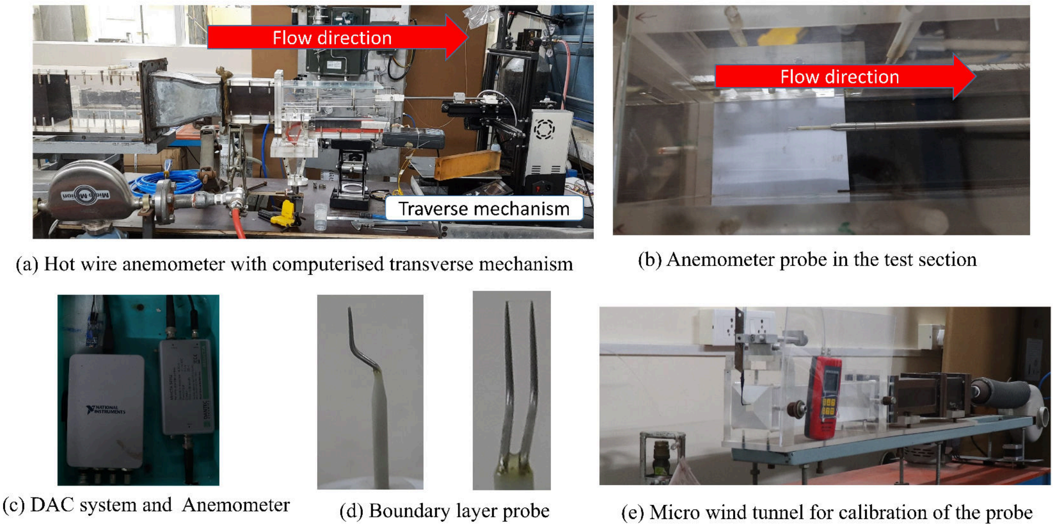

(a) Hot wire anemometer with computerised transverse mechanism

(b) Anemometer probe in the test section

(c) DAC system and Anemometer

(d) Boundary layer probe

(e) Micro wind tunnel for calibration of the probe

Figure 3.14: Details of hotwire anemometer arrangement

3.2.10 Automated traverse mechanism

An automated tri-axial traverse mechanism is developed to measure the velocity at a precise location in the test section. The traverse mechanism is built by modifying an open-source CREALITY ENDER 3 3D printer. An additional arm, slider, and hot wire probe holder are installed on the printer. The probe is controlled in the x,y, and z axes using stepped motors. The stepped motors are controlled using an Arduino UNO board. Arduino is a user-interactive open-source microcontroller board that controls devices digitally. In addition, to change the position and to keep track of the location of the probe, a user interface is developed using a JAVA-based open-source software called PROCESSING. The traverse is also automated in the y-axis (normal to the surface) by coupling a light-detecting sensor(LDR) with the data acquisition system (DAQ). A photograph of the traverse mechanism and user interface developed for the study are shown in Figure 3.15.

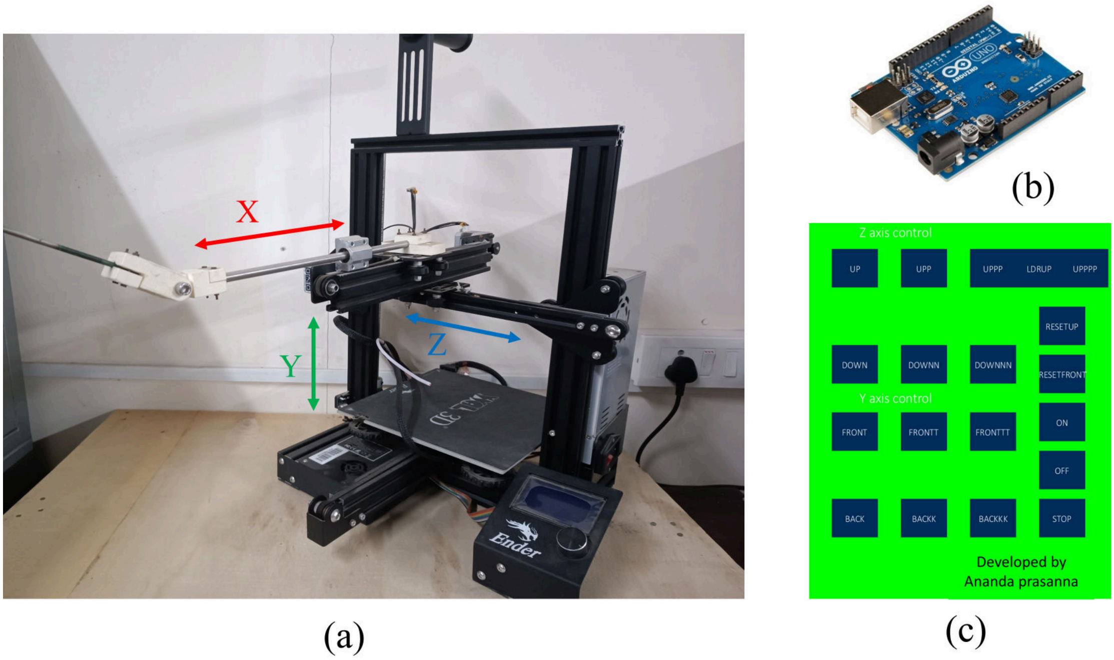

Figure 3.15: (a) Automated tri-axial traverse mechanism (b) Arduino UNO board (c) User interface to control traverse

The mainstream velocity profile measured with the anemometer assisted with the traverse mechanism is shown in Figure 3.16. One can observe the velocity profile in which the velocity is zero at the wall and increases along the y-direction. In the present study, under laboratory conditions, the average mainstream velocity is fixed at 5.4 m/s.

3.3 EXPERIMENTAL METHODOLOGY

In the present experimental study, the film cooling performance is estimated using the transient and steady-state methodologies. The details of experimental methodologies, uncertainty, and adoption of these methods for various operating conditions are discussed in this section.

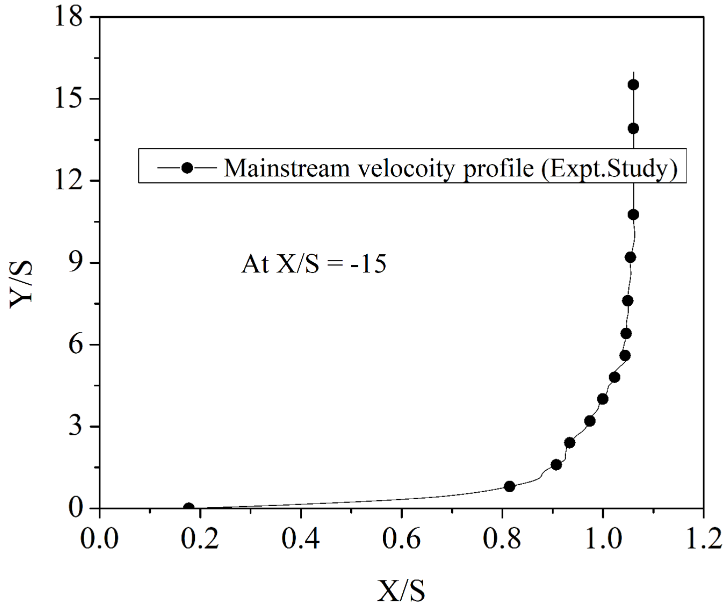

Figure 3.16: Non-dimensional velocity profile of the mainstream obtained from experiments

3.4 TRANSIENT METHODOLOGY

Transient infrared thermography is used to estimate the adiabatic film cooling effectiveness (η_{ad}) and the heat transfer coefficient (h) on the test surface. This technique has been successfully implemented in studies conducted by Ekkad *et al.* (2004) and Godi *et al.* (2020*a*). In this method, a low thermal conductive test plate is modeled as a semi-infinite body with transient one-dimensional heat conduction. Figure 3.17 shows the test surface where a convective boundary condition is imposed by the sudden exposure of the hot and cold streams. The semi-infinite approximation is valid until the thermal perturbation reaches the opposite side of the test plate. In practice, the duration of the experiment depends on the thickness (b) and thermal diffusivity (α) of the test surface and is calculated using Equation 3.1.

$$t = 0.1\frac{b^2}{\alpha} \tag{3.1}$$

The heat conduction in the test plate is assumed to be one-dimensional, and the governing equation for the same is shown in Equation 3.2.

$$\frac{\partial^2 T}{\partial y^2} = \frac{1}{\alpha}\frac{\partial T}{\partial t} \tag{3.2}$$

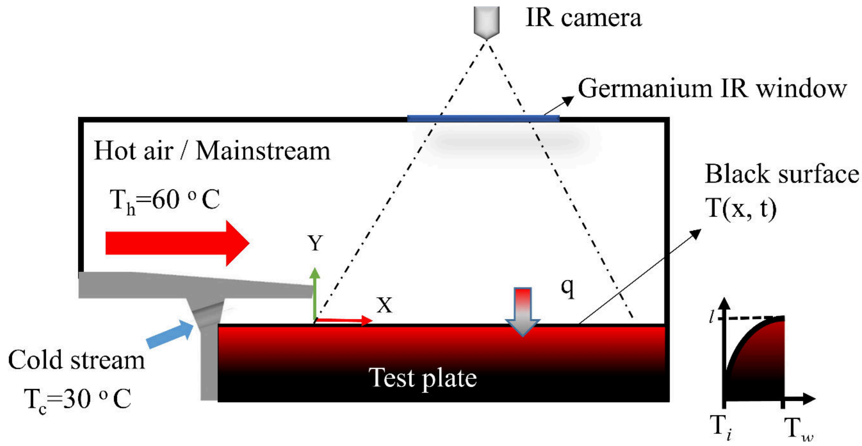

Figure 3.17: Schematic of the one-dimensional transient heat conduction model

The initial and boundary conditions used to solve the above partial differential equation are:

1. Initial condition :

$$at\ t = 0, T = T_i\ for\ all\ x \tag{3.3}$$

2. Boundary conditions:

$$For\ t \geq 0,\ at\ y = -\infty,\ T = T_i \tag{3.4}$$

$$For\ t > 0,\ and\ y = 0, -k\frac{\partial T}{\partial y} = h(T_r - T(x,t)) \tag{3.5}$$

At time t = 0 s, the test plate is at room temperature, and at t > 0, the surface (at y = 0) is exposed to a convective environment with the main and cold streams. The solution to Equation 3.2 at y = 0 subjected to the initial and boundary conditions given by Equations 3.3 - 3.5 is shown in Equation 3.6.

$$\frac{T(x,t) - T_i}{T_r - T_i} = 1 - \exp\left[\left(\frac{h^2 \alpha t}{k^2}\right)\right]\left[c\left(\frac{h\sqrt{\alpha t}}{k}\right)\right] \tag{3.6}$$

In film cooling, three important temperatures are mainstream, cold steam, and test-surface temperatures. The heat transfer from the mainstream to the test surface depends on the average temperature of mainstream and cold streams, which is known as reference temperature. Following Ekkad *et al.* (2004) and Godi *et al.* (2020*b*), the reference temperature (T_r) in Equation 3.6 is considered as film temperature (T_f) which is also assumed as adiabatic surface temperature (T_{ad}). However, it is an unknown temperature. Consequently, Equation 3.6 is represented as Equations 3.7 and 3.8 at two different time instants t_1 and t_2 respectively, which are solved iteratively to estimate the film temperature (T_f) and heat transfer coefficient (h) simultaneously.

$$\frac{T(x,t_1) - T_i}{T_f - T_i} = 1 - \exp\left[\left(\frac{h^2 \alpha t_1}{k^2}\right)\right]\left[c\left(\frac{h\sqrt{\alpha t_1}}{k}\right)\right] \tag{3.7}$$

$$\frac{T(x,t_2) - T_i}{T_f - T_i} = 1 - \exp\left[\left(\frac{h^2 \alpha t_2}{k^2}\right)\right]\left[c\left(\frac{h\sqrt{\alpha t_2}}{k}\right)\right] \tag{3.8}$$

The transient experiment starts by allowing the mainstream and cold streams into the test section. Initially, the test plate is at room temperature. The mainstream and cold streams are conditioned to the required blowing ratio and temperatures and diverted into the test section using the bypass valve. As a result, heat penetrates into the test plate, and its surface temperature increases with time. As described earlier, the surface temperature is measured at two-time instants and used to solve equations 3.7 and 3.8. In the present study, the surface temperatures are measured at 30 s and 80 s, and the equations are solved to obtain the film cooling effectiveness and heat transfer coefficient. The temperature change between these instants is more than the uncertainty of the thermocouple and results in an accurate estimate of η_{ad} and h. During the experiment, surface thermocouple readings are used to correct the IR camera measurements. Finally, the adiabatic effectiveness is estimated at every pixel on the test surface using Equation 3.9.

$$\eta_{ad}(x,z) = \frac{T_h - T_{ad}(x,z)}{T_h - T_c} \tag{3.9}$$

The laterally averaged effectiveness is estimated over the lateral lines on the test surface as shown in Figure 3.18 and it is given as :

$$\eta_{lat}(x) = \frac{1}{2z}\int_{-z}^{z} \eta_{ad}(x,z)dz \tag{3.10}$$

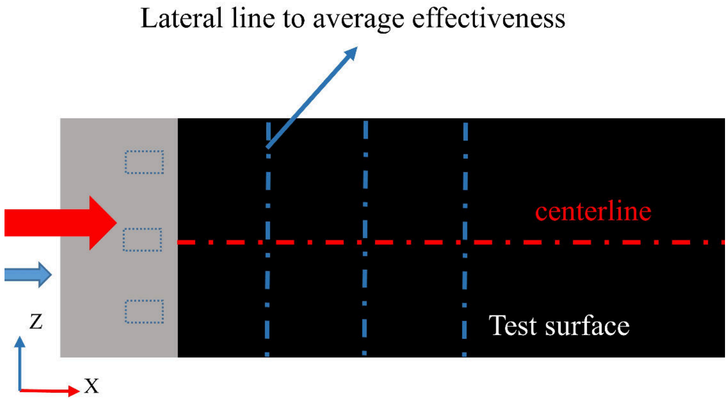

Figure 3.18: Temperature measurement locations on the test surface

3.4.1 Uncertainty analysis

The uncertainty in the measurements is evaluated using the method proposed by Moffat Moffat (1988). This method measures the uncertainty of η_{ad} and h by introducing bias and precision uncertainties. Measured parameters and the range of uncertainties specified by the manufacturer are shown in Table 3.4. Each measured value is perturbed on the positive and the negative sides, and the code is executed to obtain the change in η_{ad}. The absolute changes in η_{ad} from the negative and positive perturbations are averaged and taken as the uncertainty of η_{ad} with respect to the particular measured quantity. The total bias uncertainty is calculated using the quadrature sum of uncertainties for all measured quantities. The same methodology is employed for measuring uncertainty for

Table 3.3: Uncertainties involved in the primary measured quantities

S.No	Measured quantity	Uncertainty
1	T_h	± 0.5^oC
2	T_c	± 0.5^oC
3	T_w	± 0.9^oC
4	T_i	± 0.5^oC
5	t	± 0.125 s
6	k	± 0.01 W/mK

the heat transfer coefficient (h) as well. Further, the second uncertainty involved in the measurements is precision uncertainty. This is the uncertainty involved in the repeatability of the experiment. Four tests are conducted. The precision uncertainty shown in Equation 3.11 is estimated using the student's-t distribution with a 90% confidence level.

$$\eta_{precision} = tS/\sqrt{(}n) \tag{3.11}$$

where, t = 2.353, n = N-1, and N = 4 (no of tests)

Finally, the total uncertainty is calculated as

$$\eta_{uncertainty} = \sqrt{\eta_{bias}^2 + \eta_{precision}^2} \tag{3.12}$$

The maximum uncertainties in the estimated effectiveness and heat transfer coefficient are 7% and 24%, respectively. The uncertainty of the heat transfer coefficient is high as it is obtained by solving the semi-infinite equations (Equation. 3.7 and 3.8) iteratively rather than being measured experimentally. A similar range of uncertainty for the heat transfer coefficient (h) was reported in the investigation carried out by Hayes *et al.* (2017). Hence, the estimated heat transfer coefficient values in the present study are found to be reasonable.

3.5 STEADY STATE METHODOLOGY

In the experiments, the film cooling effectiveness is also measured using a steady-state methodology. In this method, the mainstream and cold stream are sent over the test surface until the change in temperature of the test surface with time is negligible (steady state). The time for each experiment to reach a steady state is approximately 3 hours. The temperature of the test surface is measured using the IR thermal camera. The adiabatic film cooling effectiveness (η_{ad}) on the test surface is determined using Equation 3.13.

$$\eta_{ad}(x,z) = \frac{T_h - T_{ad}(x,z)}{T_h - T_c} \tag{3.13}$$

In the subsequent chapters, the sensitivity and optimization study is conducted at a blowing ratio (BR) of 1 to identify a configuration having maximum area-averaged adiabatic effectiveness ($\eta_{ad.avg}$) and minimum standard deviation (σ_η). Here, the standard deviation indicates the non-uniformity of the adiabatic effectiveness on the liner surface. The definitions of $\eta_{ad.avg}$ and σ_η are given in Equations 6.1 and 6.2.

$$\eta_{ad.avg} = \frac{1}{A}\int_0^{40}\int_{-2.4}^{2.4} \eta_{ad}(x,z)d(Z/S)d(X/S) \tag{3.14}$$

$$\sigma_\eta = \sqrt{\frac{1}{N}\sum_{i=1}^{N}(\eta_i - \eta_{ad.avg})^2} \tag{3.15}$$

The origin of the plane used for calculating the η_{avg} starts at the lip exit of baseline reference 1 slot geometry of the combustor, at which X/S = 0, and it is fixed for all the configurations in the study. The adiabatic film cooling effectiveness accounts only for the film cooling obtained by coolant emerging from the slot and mixing characteristics of the mainstream and cold stream. As a result, it represents the lowest possible case of effectiveness. To obtain favorable mainstream and coldstream mixing characteristics, the slot configuration is optimized based on adiabatic effectiveness. However, in the actual engine, the liner is cooled additionally by the secondary air in the annular space. In this case, the cooling effectiveness obtained is called overall film cooling effectiveness which is defined in the equation 3.16.

$$\eta_{ov}(x, z) = \frac{T_h - T_s(x, z)}{T_h - T_c} \tag{3.16}$$

where T_s is the overall surface temperature of the liner or test surface.

In the study, the film cooling performance is estimated at various blowing ratios. The study conducted by Li and Mongia (July, 2001) defines the blowing ratio based on the slot exit area. The blowing ratio (BR) is defined as the ratio of coolant mass flux at the slot to the mainstream mass flux and is given as Equation 3.17.

$$\text{Blowing ratio } (BR) = \frac{(\text{mass flux})_{\text{coolant}}}{(\text{mass flux})_{\text{mainstream}}} = \frac{\frac{\dot{m}_c}{A_s}}{\rho_h U_h} \tag{3.17}$$

The blowing ratio is also written as the product of density ratio (DR) and velocity ratio (VR) and is given in Equation 3.18.

$$BR = (DR)(VR) \tag{3.18}$$

Where, the density ratio (DR) is defined as the ratio of the cold stream to the mainstream density, and the velocity ratio is defined as the ratio of the cold stream velocity at the slot exit to the mainstream velocity and is given in Equation 3.19.

$$DR = \frac{\rho_s}{\rho_h} \text{ and } VR = \frac{u_s}{u_h} \tag{3.19}$$

The Reynolds number of the film cooling stream and mainstream are given in Equations 3.20 and 3.21.

$$Re_s = \frac{\rho_s u_s S}{\mu_s} \tag{3.20}$$

$$Re_h = \frac{\rho_h u_h D_h}{\mu_h} \tag{3.21}$$

3.5.1 Uncertainty analysis

The uncertainty in the steady-state experimental studies is calculated by the methodology outlined by Kline and Mcclintock (1953). The uncertainty of the effectiveness (η_{ad}) arises due to the temperature measurement of mainstream (T_h) and coldstream (T_c) using thermocouples and surface temperature (T_w) using infrared thermography. The range of uncertainties specified by the manufacturer for the measured parameters is shown in Table 3.4. The uncertainty of the η_{ad} is calculated using the quadrature sum of the individual uncertainties and is given in Equation 3.22. The uncertainty in the η_{ad} is 5.2 %.

$$\sqrt{(\frac{\partial \eta}{\partial T_h}\Delta T_h)^2 + (\frac{\partial \eta}{\partial T_c}\Delta T_c)^2 + (\frac{\partial \eta}{\partial T_w}\Delta T_w)^2} \tag{3.22}$$

Table 3.4: Uncertainties involved in the measured quantities

S.No	Measured quantity	Uncertainty
1	T_h	$\pm$ 0.5^oC
2	T_c	$\pm$ 0.5^oC
3	T_w	$\pm$ 0.9^oC

3.6 ADOPTION OF EXPERIMENTAL METHODOLOGIES

In the present experimental studies, the film cooling performance is estimated using the transient and steady-state methodologies.

The transient methodology is implemented where the semi-infinite approximation is valid. In the transient method, the experiment is conducted in a short time. This method is beneficial in the case of experiments with high-density coolant where the coolant availability is a significant concern. In addition, the heat transfer coefficient can also be measured simultaneously with the film cooling effectiveness. This method is used to obtain film cooling performance of the baseline configuration under laboratory conditions for density ratios 1.1 and 2.63.

Another method used in the experimental study is the steady-state method, which is employed where the semi-infinite approximation is not applicable. This method is used for testing optimum configurations and subsequent rows of film cooling studies. In subsequent rows, the thickness of the test plate is small, and the semi-infinite approximation is invalid. In addition, in the present study, only study state simulations are conducted due to the computationally less expensive compared to transient simulations. Hence, for the purpose of validating the steady-state numerical results, steady-state experiments are conducted.

3.7 NUMERICAL METHODOLOGY AND ITS VALIDATION

3.7.1 Numerical Methodology

Experiments are time-consuming and challenging to mimic actual engine conditions. In view of this, the numerical study is validated using in-house experiments under laboratory conditions (low temperature and pressure). Following this, the validated numerical model is then employed to investigate the film cooling under actual engine conditions (high pressure and temperature).

Governing equations

Three-dimensional, incompressible, steady, and turbulent flow is considered in the problem. The turbulent flow is modeled using the Reynolds averaged Navier Stokes equations (RANS) with an appropriate turbulence model for closure and solved using ANSYS Fluent V20. The governing equations in the solution procedure expressed in the cartesian coordinate system using the indical form are as follows :

Continuity equation:

$$\frac{\partial u_i}{\partial x_i} = 0 \tag{3.23}$$

Momentum equation:

$$\rho \frac{\partial}{\partial x_j}(u_i u_j) = -\frac{\partial P}{\partial x_i} + \frac{\partial}{\partial x_j}\left[\mu\left(\frac{\partial u_i}{\partial x_j} + \frac{\partial u_j}{\partial x_i} - \frac{2}{3}\delta_{ij}\frac{\partial u_i}{\partial x_j}\right)\right] + \frac{\partial}{\partial x_j}\left(-\rho\overline{(u_i' u_j')}\right) \quad (3.24)$$

In the above equation, the Reynolds stresses are modeled using the Boussinesq hypothesis, and it is given as:

$$-\rho\overline{(u_i' u_j')} = \mu_t\left(\frac{\partial u_i}{\partial x_j} + \frac{\partial u_j}{\partial x_i}\right) - \frac{2}{3}\left(\rho k + \mu_t \frac{\partial u_k}{\partial x_k}\right)\delta_{ij} \quad (3.25)$$

The turbulent heat transport (Energy) equation is given as:

$$\frac{\partial}{\partial x_i}(u_i(\rho E + p) = \frac{\partial}{\partial x_j}\left(k_{eff}\frac{\partial T}{\partial x_j} + u_i\left(\tau_{ij}\right)_{eff}\right) \quad (3.26)$$

Where E is the total energy, given as:

$$E = h - \frac{p}{\rho} + \frac{v^2}{2} \quad (3.27)$$

and k_{eff} is the sum of the molecular (k) and turbulent (k_t) thermal conductivities called effective thermal conductivity is given as,

$$K_{eff} = k + k_t = k + \frac{c_p \mu_t}{Pr_t} \quad (3.28)$$

The value of the turbulent Prandtl number Pr_t is constant and is equal to 0.85.

and $(\tau_{ij})_{eff}$ is the deviatoric tensor given in Equation 3.29.

$$(\tau_{ij})_{eff} = \mu_{eff}\left(\frac{\partial u_j}{\partial x_i} + \frac{\partial u_i}{\partial x_j}\right) - \frac{2}{3}\mu_{eff}\frac{\partial u_k}{\partial x_k}\delta_{ij} \quad (3.29)$$

The term involving $(\tau_{ij})_{eff}$ represents the viscous heating.

The governing equations are discretized with second-order upwind interpolation, and a coupled solver is used for pressure-velocity coupling. As described in ANSYS Fluent

(2013), the coupled solver is more efficient than the segregated solvers in which momentum and pressure equations are solved together. Realizable k-ϵ turbulence model with enhanced wall treatment (RKE-ewt) is employed for the turbulence closure. This model was successfully implemented in previous studies Godi *et al.* (2020*b*), Wei *et al.* (2015), Pattamatta and Singh (2012), which are similar to the present study. The transport equations in this model for turbulent kinetic energy (k) and turbulence dissipation rate (ϵ) are given in Equations 3.30 and 3.31.

$$\frac{\partial(\rho k u_j)}{\partial x_j} = \frac{\partial}{\partial x_j}\left[(\mu + \frac{\mu_t}{\sigma_k})\frac{\partial k}{\partial x_j}\right] - \rho\varepsilon + G_k \tag{3.30}$$

$$\frac{\partial(\rho \varepsilon u_j)}{\partial x_j} = \frac{\partial}{\partial x_j}\left[(\mu + \frac{\mu_t}{\sigma_\varepsilon})\frac{\partial \varepsilon}{\partial x_j}\right] + \rho C_1 S\varepsilon - \rho C_2 \frac{\varepsilon^2}{k + \sqrt{\nu\varepsilon}} \tag{3.31}$$

where the turbulent viscosity is given by:

$$\mu_t = \rho C_\mu \frac{k^2}{\varepsilon} \tag{3.32}$$

The model constants are $C_{1\varepsilon}$ = 1.44, C_2 = 1.9, σ_k = 1.0, σ_ε =1.2. For further details of the numerical methodology, refer to ANSYS Fluent (2013).

In order to calculate the near-wall region, the Enhanced Wall Treatment (ewt) is imposed where the assumptions of the high Reynolds number k-ϵ model are no longer valid. If the near-wall mesh is fine enough to be able to resolve the viscous sub layer, then the enhanced wall treatment is identical to the two-layer zonal model. This method divides the computational domain into two zones, which are a viscosity-affected region and a fully-turbulence region. These regions are distinguished by the turbulence Reynolds number Re_y defined based on the normal distance (y) from the wall. The turbulent

Reynolds number Re_y is given as:

$$Re_y = \frac{\rho y \sqrt{k}}{\mu} \tag{3.33}$$

The $k - \epsilon$ model is employed in the fully turbulence zone where the $Re_y > 200$; ($Re_y^* = 200$), and the one equation model of Wolfshtein (1969) is employed in the viscous dominant region $Re_y < 200$. In the one-equation model, the momentum and turbulence kinetic energy (k) equation are retained the same, and the turbulent viscosity is modeled as:

$$\mu_{t,2layer} = \rho C_\mu l_\mu \sqrt{k} \tag{3.34}$$

where the length scale in the above equation is computed from

$$l_\mu = y C_l^* \left(1 - e^{-\frac{Re_y}{A_\mu}}\right) \tag{3.35}$$

The ϵ field is calculated as:

$$\epsilon = \frac{k^{\frac{3}{2}}}{l_\epsilon} \tag{3.36}$$

The length scale appeared in Equation 3.7.1 is given as:

$$l_\epsilon = y C_l^* \left(1 - e^{-\frac{Re_y}{A_\epsilon}}\right) \tag{3.37}$$

Where,

$$C_l^* = \kappa C_\mu^{-3/4}, A_\mu = 70, A_\epsilon = 2C_l^* \tag{3.38}$$

The two-layer formulation for the turbulent viscosity described in Equation 3.34 is blended with the high-Reynolds μ_t of the outer region using a blending function, in which the viscosity is calculated as follows:

$$\mu_{t,ewt} = \theta\mu_t + (1-\theta)\mu_{t,2layer} \tag{3.39}$$

where μ_t and $\mu_{t,1}$ are the viscosity values obtained from the high Reynolds number k-ϵ model and the near-wall one-equation model, respectively. The blending function takes a value of 0 near the walls and 1 in the fully turbulent region.

$$\theta = 0.5\left[1 + tanh\left(\frac{Re_y - Re_y^*}{A}\right)\right] \tag{3.40}$$

Maintaining a fine grid near the wall is essential to capture the viscous region. Usually, the dimensionless first grid distance from the wall (Y^+) should be less than 5, in which the first node is within the viscous sub-layer. In the present study, utmost care is taken to resolve the cells such that the Y^+ is less than 5 in the near-wall region. Additionally, viscous dissipation effects are considered for accurate predictions. Thermal radiation is neglected. The working fluid is air, and the thermo-physical properties of air are acquired from the engineering equation solver (EES).

The simulations are solved until the scaled residuals for the energy equation reach 10^{-10}, and for the remaining equations is 10^{-5}. All the simulations are carried out on HP Apollo servers with Intel Xeon Gold, 2.16 GHz processors available at the high-performance computational environment (HPCE), IIT Madras. Sixteen processors are assigned to each simulation, and the time taken to solve each simulation is approximately 32 hours.

3.7.2 Computational domain and grid independence Study

Figure 3.19a shows the computational domain used in the studies conducted under actual engine conditions (high pressure and temperature). Three holes and periodic boundary conditions are considered to reduce the computational cost. On the basis of preliminary domain independence studies, the domain length (l) from the slot exit and height (H) are chosen to be 89 times and 40 times the slot jet diameter (d), respectively. Velocity inlet boundary condition is used at the mainstream and the cold stream inlets. All the walls

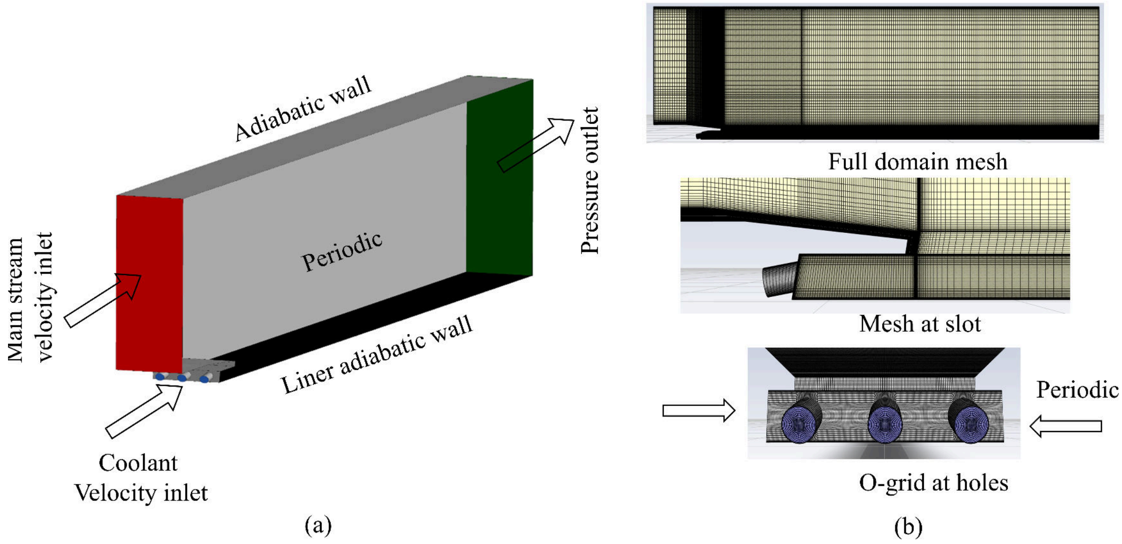

Figure 3.19: (a) Computational domain with boundary conditions (b) Computational grid

are adiabatic, and zero static pressure is imposed at the pressure outlet.

The computational grid is generated using the commercially available software ANSYS ICEM CFD (see Figure 3.19b). A grid-independence test is conducted to identify the optimum mesh for accurate results. Figure 3.20 shows the centerline adiabatic effectiveness (η_{ad}) along the liner length (X/S) for various grid nodes. The range of grid resolution considered in the study is 1.8 to 8 million.

The test shows that there is no significant change in η_{ad} beyond 7 million nodes. Hence, the mesh with 7 million nodes is found to be optimum and used in the subsequent simulations.

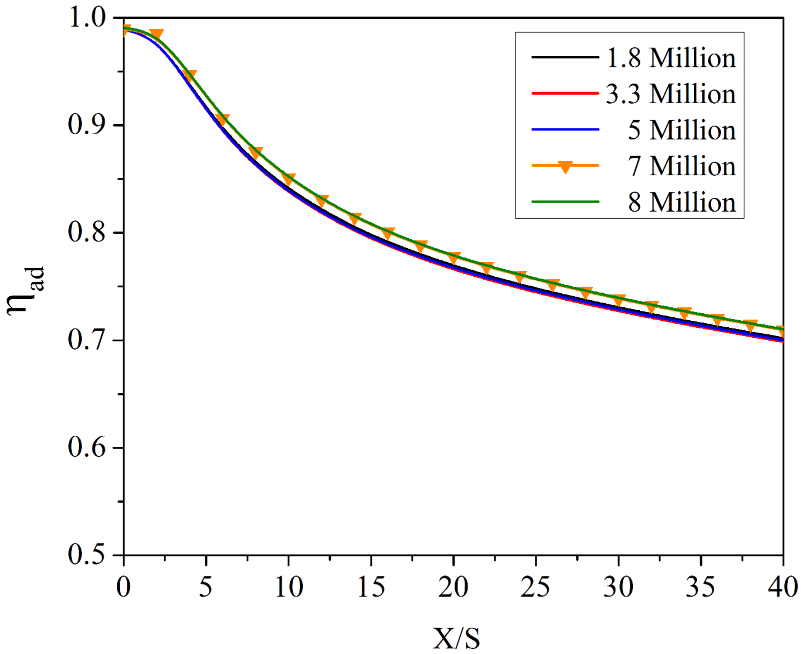

Figure 3.20: Grid independence study for *BR*=1

3.7.3 Effect of the curved surface of the annular combustor liner on film cooling effectiveness

In the present study, the curvature of the combustor is neglected and taken as a flat surface. To understand the impact of this simplification, a study is conducted to identify the curvature effects on the film cooling performance of slot cooling configuration. For this purpose, the cooling ring-2, having the maximum curvature, is selected. The geometric details are of the selected cooling configuration are slot jet diameter d = 2 mm, radius of curvature = 191.6 mm, lip taper angle = 0^o and slot height = 2.5 mm.

The lateral average film cooling effectiveness for the curved and the flat liner are compared and shown in Figure 3.21. From the figure, it is evident that the difference in cooling effectiveness is negligible. The cooling effectiveness is unchanged due to the very small wall curvature, and the simplification of geometry to the flat plate is found to be acceptable.

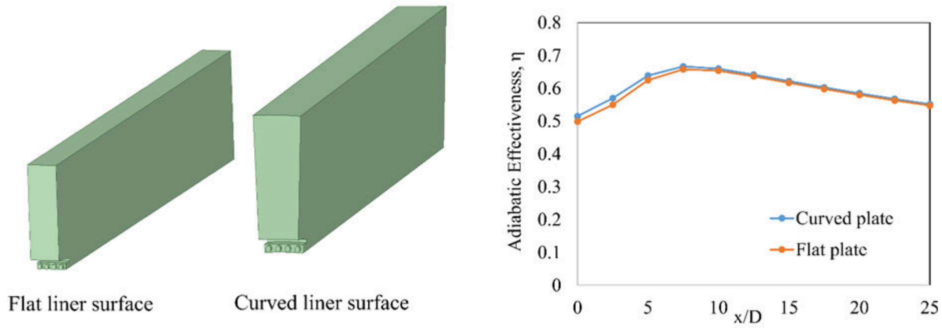

Figure 3.21: (a) Geometry of the liner (b) Comparison of lateral average effectiveness for the flat and curved liner surfaces

3.8 CLOSURE

In this chapter, the details of the experimental facility were discussed extensively. In addition, experimental methods and their adoption in experiments and numerical methodology were discussed. In the next chapter, the validation of the numerical studies, followed by experimental investigations of the film cooling performance of the baseline three-dimensional slot under laboratory conditions is discussed.

1

[1]This chapter is drawn from the following publication: **Revulagadda A.P**, Adapa B.R., Balaji C, Pattamatta A, “Fluid Flow and Heat Transfer Characteristics of Three-Dimensional Slot Film Cooling in an Annular Combustor”, International Journal of Heat and Mass Transfer ,211(2023),p.(124211), doi.org/10.1016/j.ijheatmasstransfer.2023.124211.

CHAPTER 4

EXPERIMENTAL AND NUMERICAL INVESTIGATION OF THREE-DIMENSIONAL SLOT FILM COOLING UNDER LABORATORY CONDITIONS

4.1 INTRODUCTION

This chapter details the results of experimental investigations of the fluid flow and heat transfer characteristics of three-dimensional slot film cooling. Along with the fluid flow and heat transfer characteristics, the validation of the numerical study under laboratory conditions (low pressure and temperature) is also presented.

4.2 VALIDATION OF THE NUMERICAL METHODOLOGY

This section outlines an inter-comparison of the present experimental research and validation of the computational study with the literature for density ratio (DR) of 1.1. In addition, the numerical study is validated with the in-house experimental study under laboratory conditions (DR = 1.1).

The following are the laboratory conditions under which experiments are carried out:

(a) The operating pressure is equivalent to the atmospheric pressure (i.e., 101325 pa).

(b) The inlet temperatures of the mainstream and coldstream are approximately 60^oC and 30^oC, respectively.

Ambient air is used as the mainstream, and the turbulence intensity of the mainstream at the inlet of the test section obtained from in-house flow measurements is 9.5%. Air is used as a coolant for a low-density ratio of 1.1, and a foreign gas is used for a high-density ratio of 2.6. A mixture of SF_6 and CO_2 is used as a high-density foreign gas to reproduce the density ratio of 2.6, similar to actual engine conditions. The blowing ratios are varied by increasing the coolant mass flux for a fixed mainstream mass flux. The corresponding flow conditions are given in Table 4.1.

As mentioned in the previous section (3.7.1) of chapter 3, in the numerical study, the Realizable $k - \epsilon$ turbulence model with Enhanced Wall Treatment (ewt) is used for the turbulence closure. The turbulence model is validated at a low-density ratio (DR) of 1.1, in which only air is used as the coolant.

Table 4.1: Operating conditions for laboratory studies

	DR	BR	u_h (m/s)	u_s (slot exit) (m/s)	Re_s	Re_h
Air as coolant	1.1	0.5 - 5	5.4	2.46 - 24.6	385 - 3846	13735
Foreign gas as coolant	2.6	1 - 2	5.4	2.05 - 4.1	920 - 1840	13735

For purposes of validation, the numerical domain mimics the test section of the experimental setup by including the plenum chamber and test plate. In addition, to reduce the computational cost, the domain is reduced to have three slot jet holes and defined with periodic boundary conditions on the side faces of the domain. Figure 4.1 shows the numerical domain and the corresponding boundary conditions.

4.2.1 Flow characteristics

This section discusses the validation of the numerical model by comparing the numerically obtained flow field (velocity and turbulence profiles) with those flow experiments conducted under laboratory conditions for DR = 1.1. In addition, fluid flow behavior is discussed in detail at various blowing ratios and locations. As mentioned in Chapter 3, a hot wire anemometer assisted with the tri-axial traverse mechanism is used to measure the flow characteristics.

The centerline streamwise mean velocity profiles and the respective turbulence intensity profiles in the normal direction (Y/S) to the liner surface for various blowing ratios at a

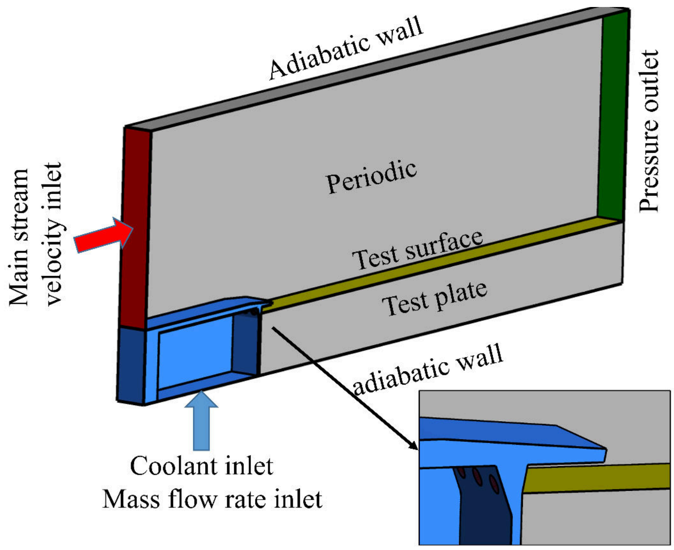

Figure 4.1: Numerical domain used for the validation with in-house experiments

fixed location ($X/S = 27$) are shown in Figure 4.2. It can be observed that there is a reasonably good agreement between the numerical and the experimental studies.

One can observe from Figure 4.2a that the effect of the jet emerging out of the slot is insignificant for BR equal to 1. However, as BR increases from 2 to 5, the effect of the jet turns out to be significant, with a maximum velocity ratio of 5.4 at $BR = 5$. The boundary layer imposed by the liner surface causes an inflection point in the velocity profile near the wall ($Y/S = 0$). In addition, the high velocity of the jet causes an additional inflection in the mixing zone of mainstream and coolant (approximately Y/S from 2 to 4).

The local turbulence intensities (TI) of the velocity profiles are shown in Figure 4.2b. In the experiments, the local streamwise turbulence intensity (TI_{loc}) is defined as $\frac{\sqrt{u'^2}}{\overline{u_{mean}}}$. In the numerical simulations, the normal turbulent stress components such as $-\rho\overline{u'u'}$, $-\rho\overline{v'v'}$ and $-\rho\overline{w'w'}$ are calculated at various locations in the film cooling region and found to be equal in magnitude. As a result, the turbulence is considered isotropic, and the local streamwise turbulence intensity is calculated from Equation 4.1.

$$TI_{loc} = \frac{\sqrt{\frac{2}{3}k}}{u_{mean}} \tag{4.1}$$

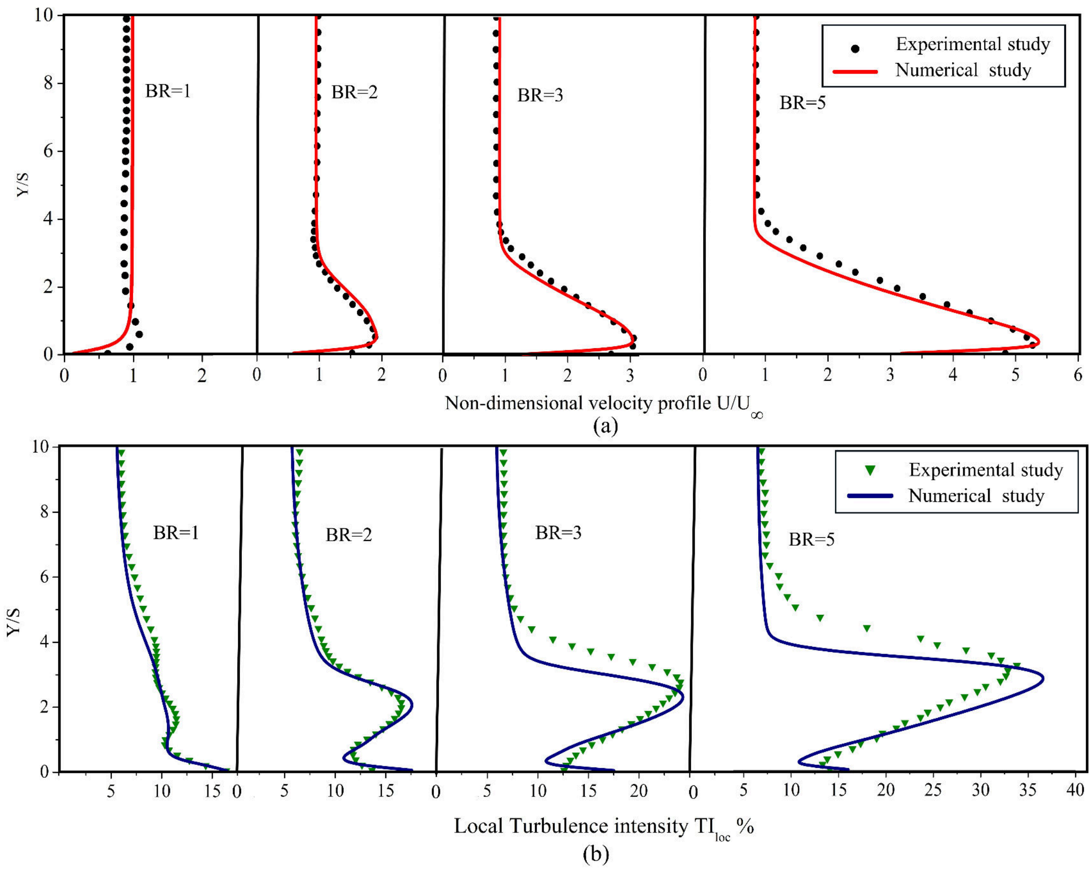

Figure 4.2: Comparison between experimentally and numerically obtained flow field for DR = 1.1 and blowing ratios ranging from 1 to 5 at X/S = 27 (a) velocity profiles (b) local turbulence intensity profiles

where, k is the turbulence kinetic energy and u_{mean} is the local mean streamwise velocity. The maximum turbulence intensity (TI_{max}) is observed in the mixing zone, where both streams shear and impute large-scale eddy generation. With the increase in the blowing ratio, the velocity ratio between the cold stream and mainstream increases and results in more shearing of the streams. As a result, it is observed from Figure 4.2b that the increase in BR from 2 to 5 increases TI_{max} significantly from 18 to 33 %. The increase in TI enhances the mixing of the mainstream and coolant and this results in an adverse effect on film cooling.

In addition, the centerline streamwise mean velocity profiles and the respective turbulence intensity profiles at various locations for a fixed blowing ratio (BR = 2) are shown in Figure 4.3. The locations under consideration are X/S = 10, 30, and 70. From the figure, it is observed that the maximum velocity ratio $\left(\frac{u}{u_\infty}\right)$ is reduced in the streamwise direction because of a decay in the coolant velocity. As a result, shearing between main and cold streams reduces, and so does the turbulence intensity in the streamwise direction.

Further, an appropriate scaling of velocity and the normal distance (y) is considered to verify the self-similarity of velocity profiles. Based on the previous studies of Zhou and Wygnanski (1993), in the present co-flow studies, the local velocity scale is corrected to $u_o = (u - u_\infty)$, and is normalized as $\left(u_o^* = \frac{u - u_\infty}{u_{max} - u_\infty}\right)$ in the outer layer of the velocity profile. In addition, the velocity scale is normalized to $\left(u_i^* = \frac{u}{u_{max}}\right)$ in the inner layer of the velocity profile.

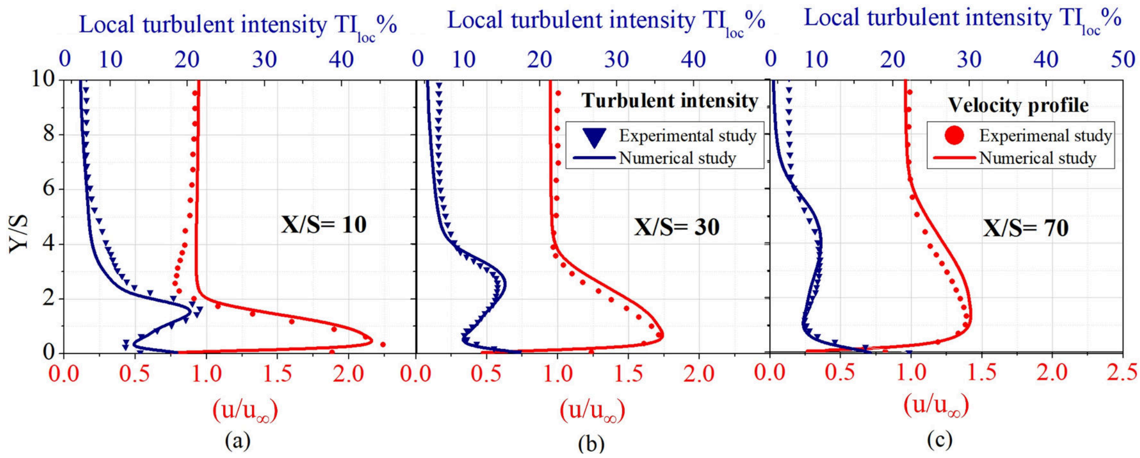

Figure 4.3: Comparison between experimentally and numerically obtained flow field at various locations for DR = 1.1 and BR = 2 (a) at X/S = 10 (b) at X/S = 30 (b) at X/S = 70

When one plots u_i^* in the inner layer and u_o^* in the outer layer against the $y/y_{0.5}$, all the mean velocity profiles of various locations (X/S) in the streamwise direction collapses into a single profile. Figure 4.4 shows the self-similarity of velocity profiles measured from X/S = 5 to 80 at various blowing ratios (BR = 2 to 5).

From Figure 4.4, it is observed that the velocity profiles are self-similar, and the self-similarity is more precise with an increase in the blowing ratio from 2 to 5. However, the self-similarity is not obtained for case (BR = 1) where the jet velocity is less than or equal to the mainstream velocity.

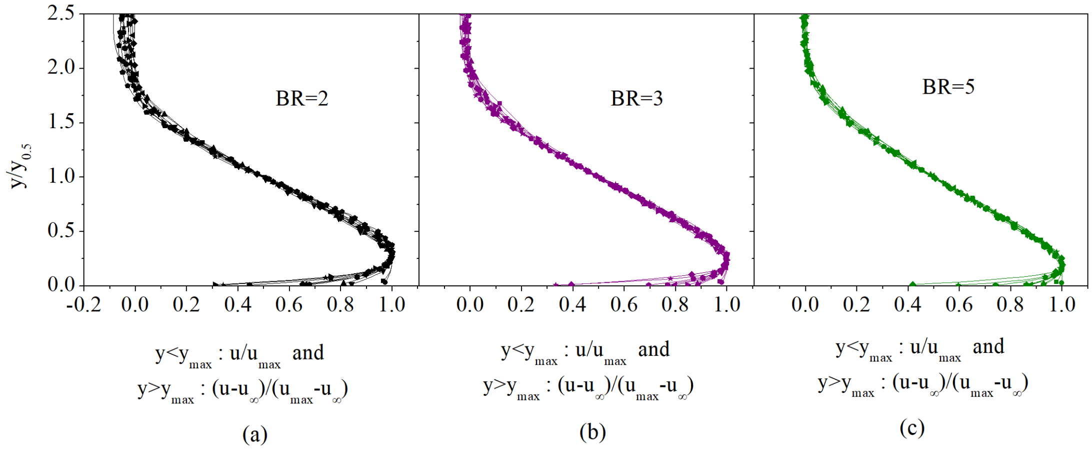

Figure 4.4: Self-similarity of velocity profiles measured between (X/S = 5 to 80) for (a) BR = 2 (b) BR = 3 (c) BR = 5

4.2.2 Heat transfer studies

In this section, first, the experimental setup is validated by comparing the adiabatic film cooling effectiveness obtained using transient experiments with the correlation developed by Lefebvre and Ballal (2010) on two-dimensional slots. Figure 4.5 shows results of the variation of centerline adiabatic effectiveness (η_{ad}) along the liner length X/S for DR = 1.1 and BR = 1. One can observe that there is a good agreement between the in-house experiments and the literature.

In the subsequent chapters, studies are performed using steady-state RANS simulations to investigate the three-dimensional slot film cooling. Hence, to verify the accuracy of the selected turbulence model (RKE-ewt), a steady-state numerical study is conducted and compared with the experimental results of Yang *et al.* (2012) on the three-dimensional slots. Figure 4.6 shows the present numerically obtained film cooling effectiveness along the streamwise distance with the experimental study (Yang *et al.* (2012)) conducted at DR = 1.1 and BR = 1.6. One can observe that there is a good agreement between the present numerical study and the experimental study of Yang *et al.* (2012).

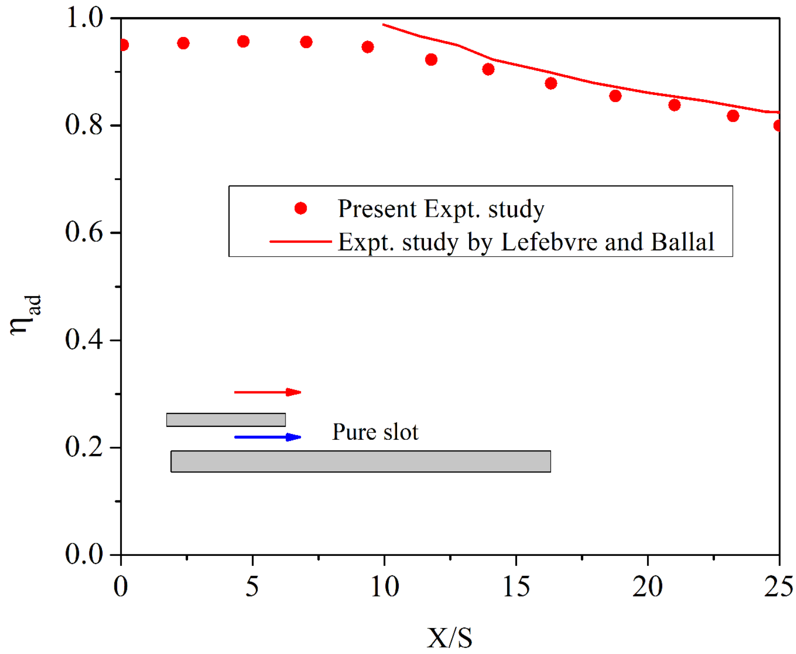

Figure 4.5: Validation of the present in-house experimental result with Lefebvre and Ballal (2010)

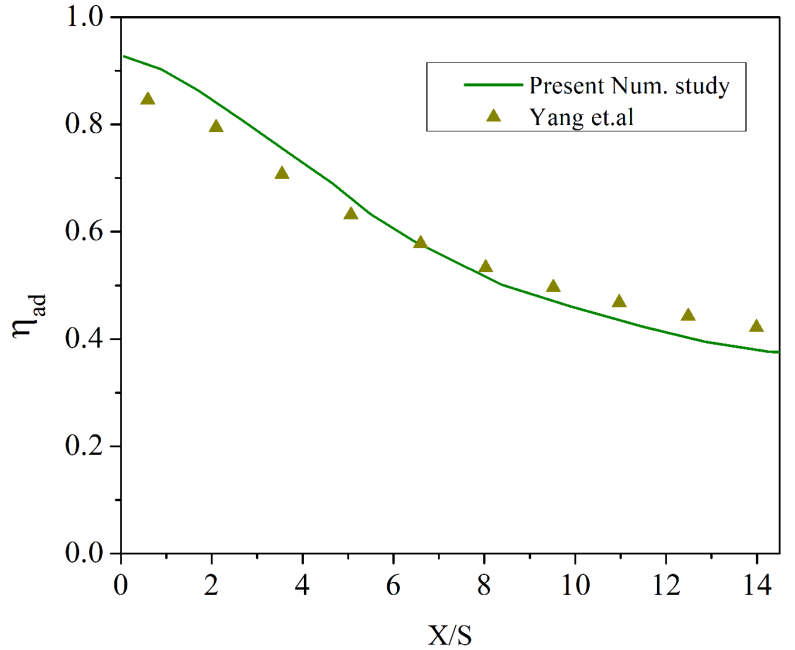

Figure 4.6: Validation of the present numerical study with experimental study by Yang *et al.* (2012)

From the above investigation, it is seen that the results of the present studies and those from the literature agree with each other reasonably well.

In addition to the above validations, the numerical model is validated with the results of in-house experiments on the three-dimensional slot under consideration (Figure 3.4 of chapter 3).

Figures 4.7 and 4.8 show the laterally averaged effectiveness ($\eta_{ad.lat}$) along the dimensionless streamwise distance (X/S) for density ratio (DR) of 1.1 and blowing ratios (BR) of 1 and 2, respectively. The figure compares the film cooling effectiveness obtained from transient experiment, steady-state experiment, and steady-state numerical study. One can observe from the figure that the film cooling effectiveness is nearly 0.95 at the slot exit ($X/S = 0$) and reduces along the streamwise direction due to the entrainment of the mainstream with the cold stream in both the blowing ratios.

In the present work, only steady-state numerical studies are carried out because they are computationally less expensive as compared to transient simulations. Hence, steady-state in-house experiments are conducted to validate the steady-state numerical results. The adiabatic effectiveness obtained experimentally and numerically with steady-state methodology is in reasonably good agreement and within uncertainty.

Another interesting point to be noted here is that the adiabatic effectiveness obtained using the transient experiment is also in good agreement with the steady-state experimental and numerical results. The reason for this behavior is that the measured film temperature is the same in both methodologies. The transient method iteratively solves the semi-infinite equations for the film temperature, and the steady state method measures surface temperature, which is the film temperature after reaching a steady state. Hence, the film temperature is fundamentally independent of the methodologies.

Hence, based on the above validations, it is observed that the RKE-ewt turbulence model predicts the film cooling characteristics reasonably accurately and is used in subsequent studies conducted under actual engine conditions.

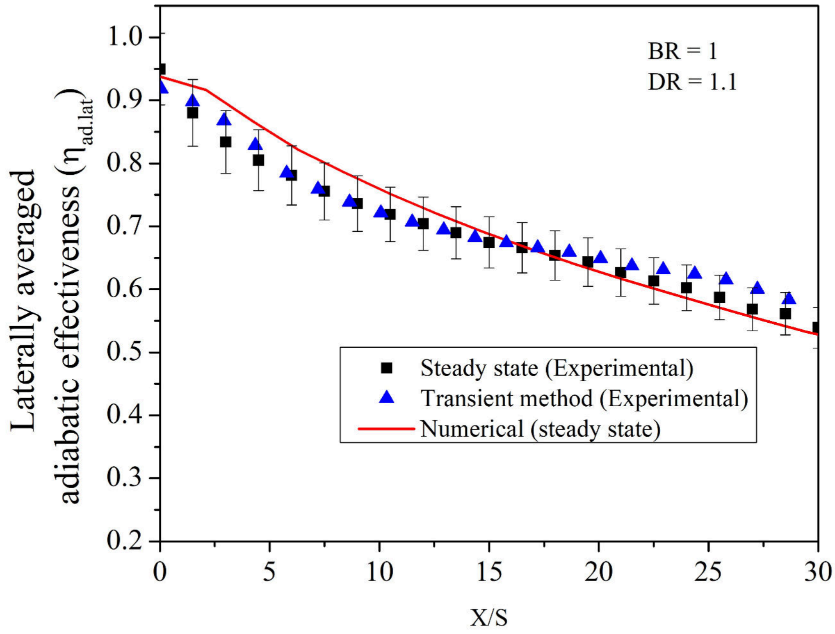

Figure 4.7: Comparison of numerical and in-house experimental results for adiabatic effectiveness at $BR = 1$

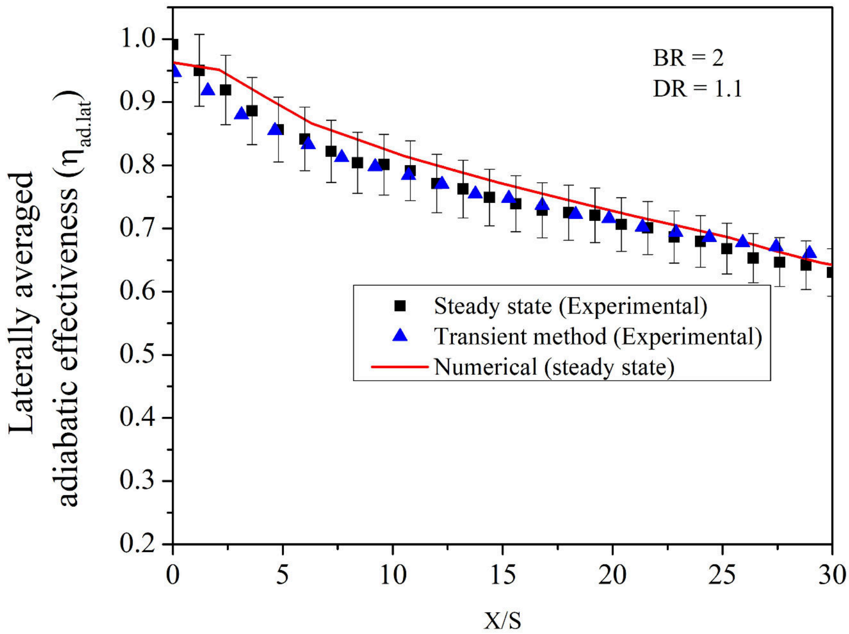

Figure 4.8: Comparison of numerical and in-house experimental results for adiabatic effectiveness at $BR = 2$

4.3 FILM COOLING PERFORMANCE UNDER LABORATORY CONDITIONS

This section reports the results of experimental investigations of film cooling performance for various blowing ratios and density ratios under laboratory conditions (low temperature and pressure). The transient infrared methodology is implemented for this investigation. Figure 4.9 displays the variation of centerline adiabatic effectiveness (η_{ad}) for the full range of blowing ratios from 0.5 to 5 and for a density ratio (DR) of 1.1, at various locations (X/S = 5 to 30). From the figure, it is seen that the η_{ad} reduces in the streamwise direction (X/S) for all the blowing ratios (BR) due to mainstream and cold stream interactions. Another interesting point to be noted here is that the η_{ad} enhances with an increase in blowing ratio (BR) from 0.5 to 2 due to an increase in coolant mass flux and reaches a maximum η_{ad} of 0.85 for the BR of 2 at X/S = 5. Additionally, η_{ad} in the far field is improved as the momentum of the coolant increases with BR. As a result, at X/S = 30 for BR = 2, a maximum effectiveness of 0.65 is noted. However, η_{ad} is reduced from blowing ratio 2 to 5 for all the locations.

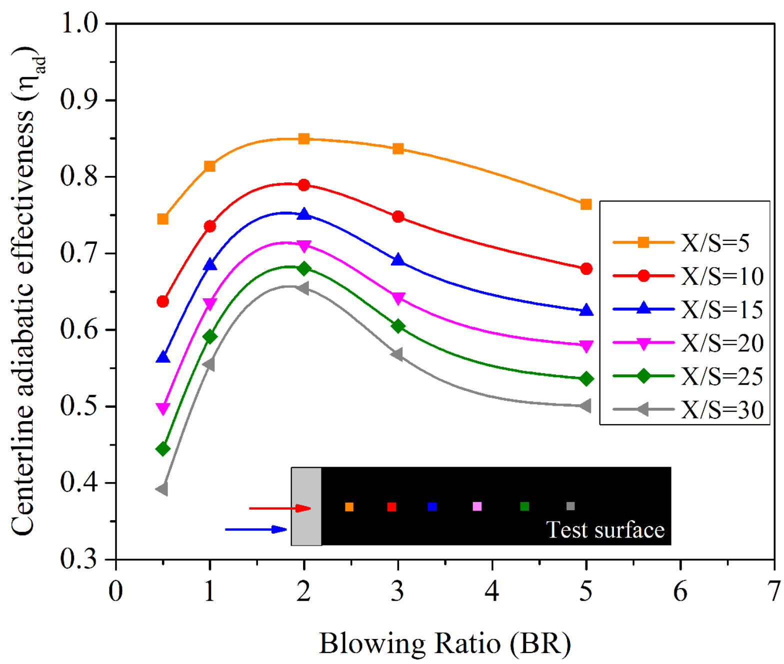

Figure 4.9: Variation of centerline film cooling adiabatic effectiveness with various blowing ratios (BR) under laboratory conditions (DR = 1.1)

The reason behind this is explained using the basis of flow studies elucidated in the previous section (4.2.1). Figure 4.2(b) shows the behavior of turbulence intensity (TI) against the blowing ratio (BR). The TI_{max} increases from 18 to 33 %, when the blowing ratio increases from 2 to 5. As a result, the mixing of the main and cold streams increases, and this adversely affects film cooling effectiveness.

Figure 4.10 shows the contour plots of the adiabatic film cooling effectiveness measured over the liner surface for X/S = 0 to 30 and Z/S = -4 to 4. One can observe that the undulating behavior of the effectiveness is because of the coolant entry through the discrete holes. As a result, the effectiveness is not distributed uniformly near the slot exit. However, due to entrainment and jet spread in the lateral direction, the undulating behavior of the effectiveness reduces in the streamwise distance. From the figure, it is further observed that the effectiveness is enhanced from BR = 0.5 to 2 and reduced at BR = 5 due to high turbulence intensity.

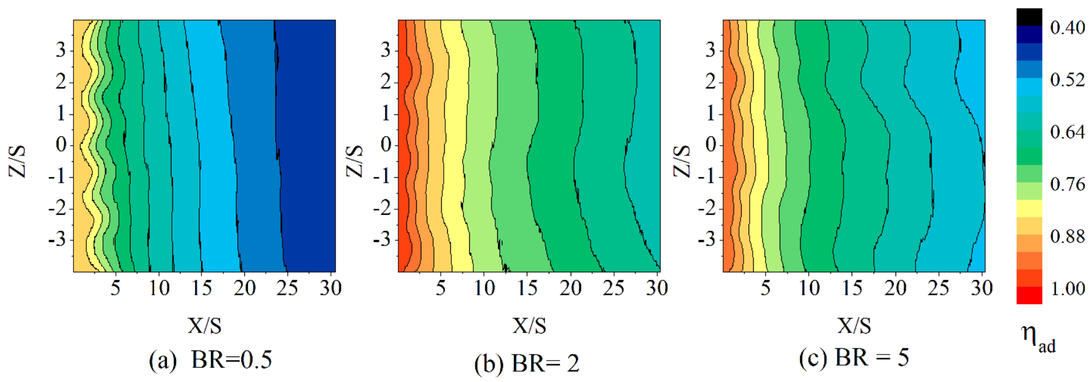

Figure 4.10: Effectiveness contours on the liner surface at (a) BR = 0.5 (b) BR = 2 (c) BR = 5

Furthermore, Figure 4.11 displays the variation of the heat transfer coefficient along the centerline at various blowing ratios ranging from 0.5 to 5. Since the heat transfer coefficient is proportional to the Reynolds number, it increases with the blowing ratio. Additionally, the mainstream suddenly expands and impinges on the liner over the region of X/S = 2 to 5. As a result, the shear stress is significant in that region, and this leads to a sharp increase in the heat transfer coefficient.

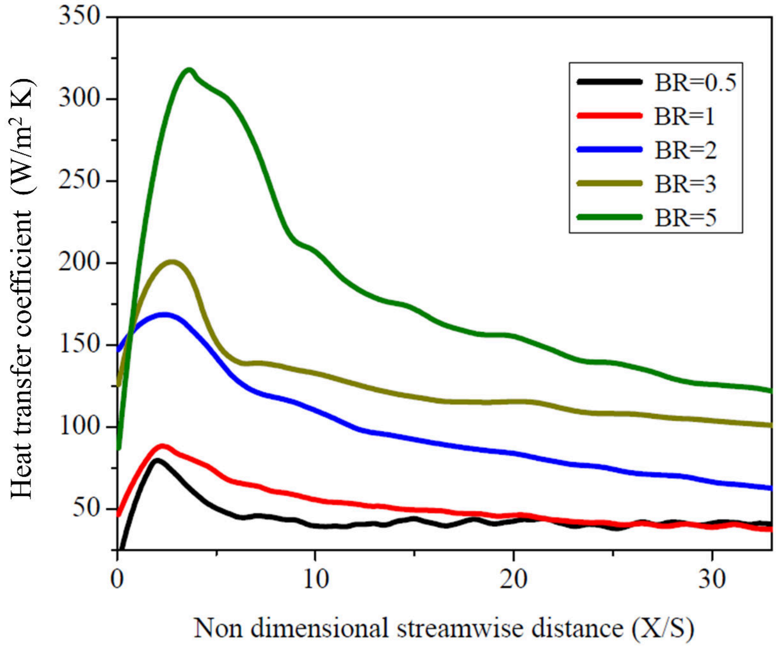

Figure 4.11: Variation of centerline Heat transfer coefficient in the dimensionless streamwise direction (X/S)

The effect of density ratio (DR = 1.1 and 2.6) on the film cooling effectiveness for blowing ratios 1 and 2 is shown in Figures 4.12a and b, respectively. Here, it is instructive to reiterate that the air is used as a coolant for the low-density ratio of 1.1, and foreign gas is used as the coolant for the high-density (DR) ratio of 2.6.

From Figures 4.12a and b, it is observed that the adiabatic effectiveness (η_{ad}) obtained in the case of DR = 1.1 is lower than DR = 2.6. In addition, there is a sudden drop in η_{ad} along the streamwise direction (X/S) for DR of 1.1 compared to 2.6. A study conducted by Rastogi and Whitelaw (1973) on three-dimensional slots also showed a similar effect of density ratio on film cooling effectiveness. The significant difference in the trends of adiabatic effectiveness variation along the streamwise direction for DR = 1.1 and 2.6 is attributed to the physical properties of the coolant. Hence, the density ratio (DR) significantly affects film cooling effectiveness.

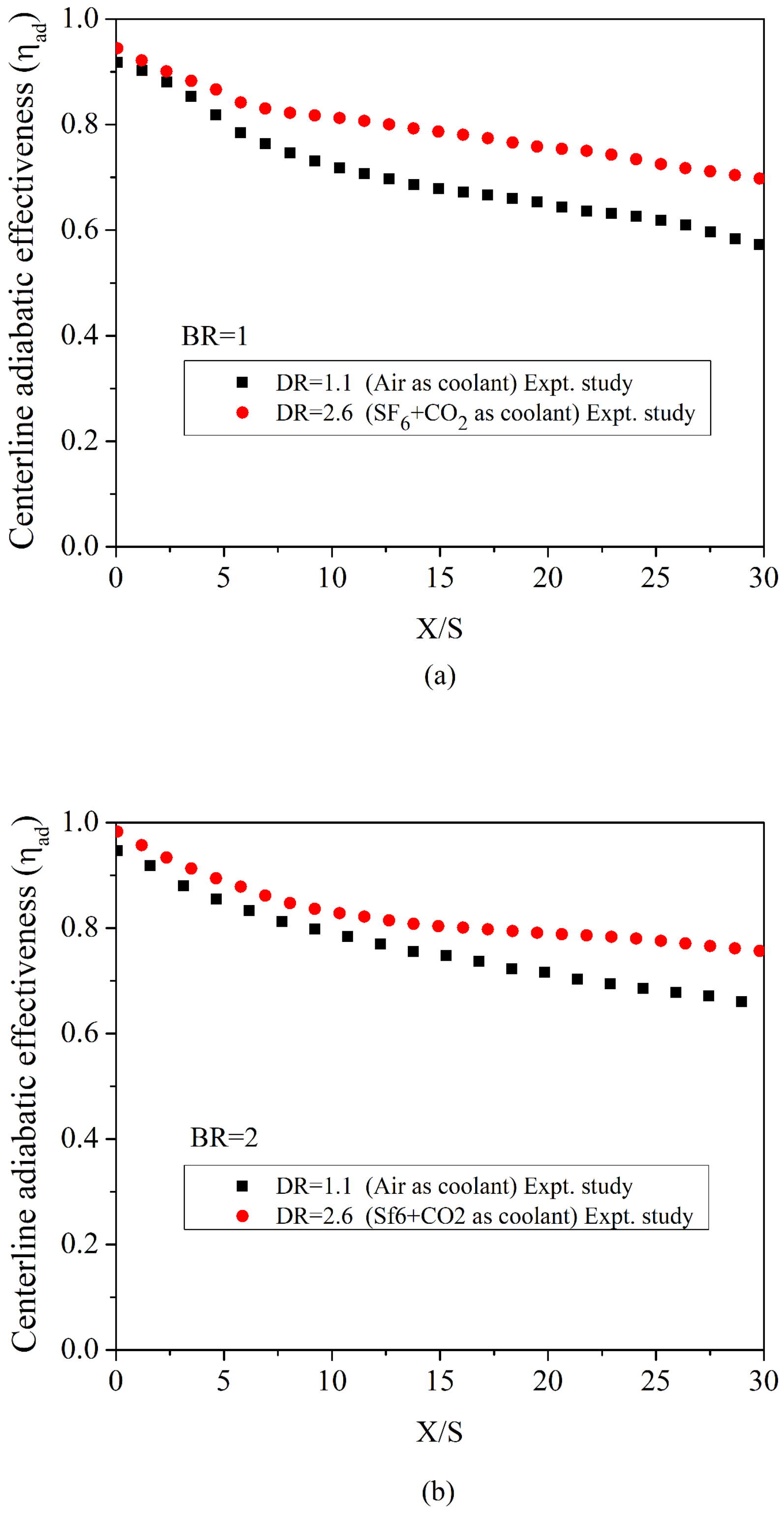

Figure 4.12: Effect of density ratio (DR) on centerline adiabatic effectiveness (η_{ad}) along streamwise distance (X/S) (a) $BR = 1$ (b) $BR = 2$

4.4 CONCLUSIONS

In this study, fluid flow and heat transfer characteristics in three-dimensional slot film cooling were investigated experimentally and numerically. The flow characteristics of the film cooling at various blowing ratios are measured using hot-wire anemometer. The experimental results were used to validate the RANS-based numerical study. In addition, the film cooling performance was investigated experimentally at laboratory conditions (low temperature and pressure) for various blowing ratios and for a density ratio of 1.1. The effect of density ratio on the film cooling performance is also investigated using a high-density foreign gas as a coolant.

The salient conclusions are:

1. In practical three-dimensional slot film cooling, velocity profiles along the streamwise direction exhibit self-similar behavior for blowing ratio (BR) ≥ 2.

2. At laboratory conditions ($DR = 1.1$), the film cooling effectiveness increases for $0.5 \leq BR \leq 2$. However, the effectiveness reduces for $3 \leq BR \leq 5$ due to a significant increase in turbulence intensity caused by the shearing of main and cold streams in the mixing zone. Hence, to save the amount of coolant, it is not recommended to operate the film cooling beyond $BR = 2$.

3. In practical slots, the density ratio shows a significant effect on film cooling effectiveness. For a fixed blowing ratio (BR), film cooling effectiveness obtained for a DR of 2.6 is higher than that obtained for a DR of 1.1.

4. The validation study shows a reasonably good agreement with the literature and in-house experiments. Hence, the Realizable $k - \epsilon$ turbulence model with enhanced wall treatment is considered reliable and can be used in further studies under actual engine conditions.

4.5 CLOSURE

In this chapter, the performance of the three-dimensional baseline slot was investigated under laboratory conditions. The fluid flow and heat transfer characteristics were investigated experimentally at various blowing ratios. In addition, a RANS-based numerical model was validated with the literature and in-house experimental results. In the next chapter, the performance of the present three-dimensional slot under actual engine conditions is numerically investigated using the validated model. In addition, a geometrical parametric study is conducted numerically to obtain further insights into fluid flow and heat transfer characteristics.

[1]

[1]This chapter is drawn from the following publications:
Revulagadda A.P, Adapa B.R., Balaji C, Pattamatta A, "Fluid Flow and Heat Transfer Characteristics of Three-Dimensional Slot Film Cooling in an Annular Combustor", International Journal of Heat and Mass Transfer,211(2023),p. (124211), doi.org/10.1016/j.ijheatmasstransfer.2023.124211.
and
Revulagadda A.P, Ramapada Rana, Batchu Suresh, Balaji C, Pattamatta A, "A Multiobjective Optimization of 3D - Slot Jet Configuration for Enhancement of Film Cooling in an Annular Combustor Liner", International Journal of Heat and Mass Transfer, 218(2024), p.(124745), doi.org/10.1016/j.ijheatmasstransfer.2023.124745.

CHAPTER 5

NUMERICAL INVESTIGATION OF THREE-DIMENSIONAL SLOT FILM COOLING UNDER ACTUAL ENGINE CONDITIONS

5.1 INTRODUCTION

This chapter reports the results of a comprehensive numerical study using the validated numerical model (in Chapter 4) to obtain further insights into the practical three-dimensional slot film cooling (with lip, inclined holes, and realistic configuration) under actual engine conditions (high-pressure and temperature). The schematic of the three-dimensional slot is shown in 5.1 for ease of understanding.

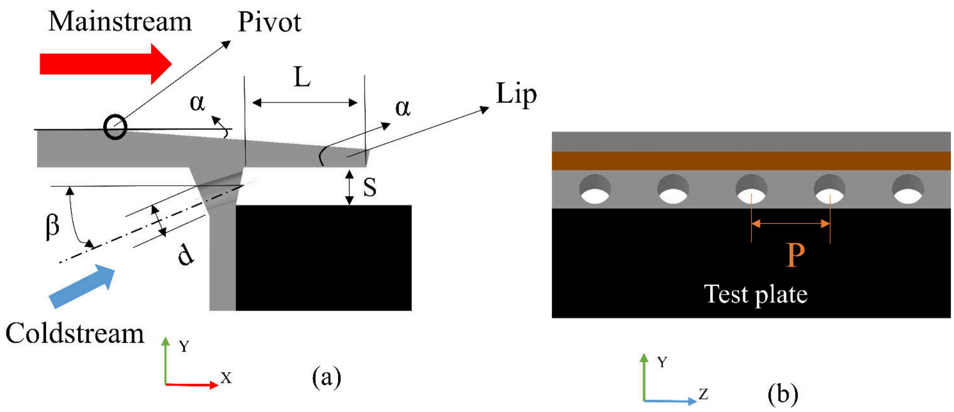

Figure 5.1: Schematic of the three-dimensional slot: (a) Side view (b) Front view

where, S = slot height, d = Slot jet diameter, p = Slot jet pitch,L = lip length, α = Lip taper angle, β = Slot jet injection angle

A detailed parametric study is conducted numerically to understand the influence of flow and geometrical parameters on the film cooling effectiveness. The parameters under consideration are slot Reynolds number (Re_s), slot jet diameter (d), dimensionless slot jet pitch (p/d), lip taper angle (α), dimensionless lip length (L/d), and slot jet injection angle (β). Finally, an artificial neural network-based mathematical model is developed to predict the film cooling effectiveness, using blowing ratio and geometrical parameters.

5.2 THREE-DIMENSIONAL SLOT FILM COOLING PERFORMANCE UNDER ACTUAL ENGINE CONDITIONS

The flow and heat transfer characteristics of film cooling for various blowing ratios (BR) under laboratory conditions were discussed in the previous chapter. Performing the experiments at actual engine conditions is challenging, expensive, and time-consuming. In view of this, the validated numerical model reported in Chapter 4 is taken into consideration for the simulations of the actual engine conditions.

The following are the actual engine conditions under which simulations are carried out:

(a) The operating pressure is 2000000 Pa or 20 Bar.

(b) The inlet temperatures for the main and cold streams are 2100 K and 799 K, respectively.

Air is considered as a working fluid for main and cold streams. The density ratio is 2.6 due to the significant difference in operating temperatures between the main and cold streams. The coolant slot jet Reynolds number (Re_s) is fixed at 20500. Based on a study conducted by Wang and Li (2008) on mist cooling at gas turbine operating conditions, the turbulence intensity of the mainstream is adopted to be 1% in the present study.

Various blowing ratios are attained by altering the mainstream velocities (u_h) at a fixed coolant mass flux. The blowing ratios are varied from 0.5 to 5, with the respective flow conditions given in Table 5.1. The variation of centerline adiabatic effectiveness (η_{ad}) in the streamwise direction (X/S) and laterally averaged adiabatic effectiveness ($\eta_{ad.lat}$) against various blowing ratios (BR) are shown in Figures 5.2a and b, respectively.

Table 5.1: Actual engine operating conditions

DR	BR	u_h (m/s)	u_c (slot exit) (m/s)	Re_s	Re_h
2.6	0.5 - 5	184 - 18.4	34.1	20500	450174 - 45017

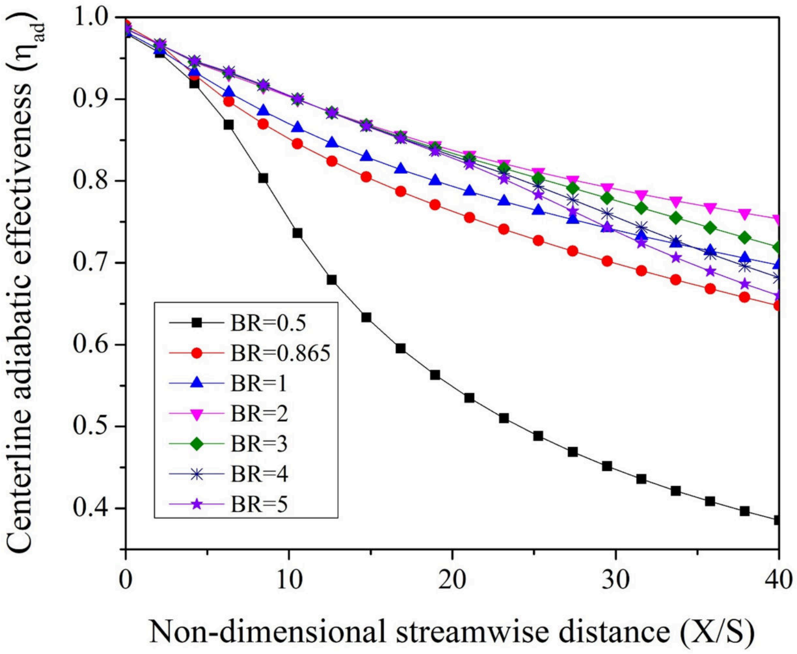

(a)

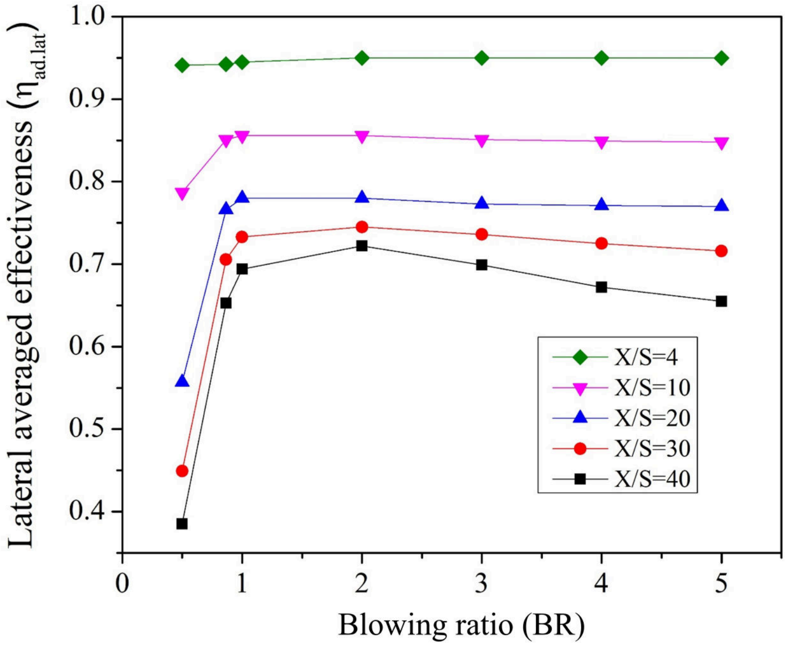

(b)

Figure 5.2: Film cooling performance at actual engine conditions (a) variation of centerline adiabatic effectiveness (η_{ad}) along X/S (b) variation of laterally averaged effectiveness (η_{lat}) with blowing ratio (BR)

From Figure 5.2a it is clear that for all the blowing ratios, the film cooling effectiveness is maximum at the slot exit (X/S = 0), and because of mainstream entrainment with coolant, the effectiveness is reduced in the streamwise direction.

Furthermore, it is observed that the profiles of effectiveness for various blowing ratios (BR) obtained for the present actual engine conditions (DR = 2.6) are similar to the tests conducted under laboratory conditions (DR = 1.1). The film cooling effectiveness is enhanced with an increase in the blowing ratio from BR = 0.5 to 2 (see Figure 5.2 a and b). Further, there is no significant change in η_{lat} form BR = 2 to 5. As explained in the previous section (4.3), the negative impact on the effectiveness beyond the blowing ratio of 2 is attributed to the high turbulence intensities and entrainment. Hence, it is recommended to maintain the blowing ratios (BR) less than 2.

To understand the influence of operating conditions, the film cooling effectiveness (η_{ad}) obtained numerically at actual engine conditions is compared with that obtained from the experimental study (DR = 2.6) under laboratory conditions. Figure 5.3 compares film cooling effectiveness (η_{ad}) in the streamwise distance (X/S) between actual engine conditions (DR = 2.6) and the laboratory conditions for DR = 1.1 and 2.6. For the density ratio (DR) of 1.1, one can observe from the figure that the film cooling effectiveness obtained experimentally under laboratory conditions is less than that obtained numerically under actual engine conditions (DR = 2.6). However, for the case of DR = 2.6 (foreign gas as coolant), an interesting point is noted that the adiabatic effectiveness obtained under the laboratory conditions (Foreign gas experiments) is very close to that obtained from actual engine conditions. Although there are differences in operating pressure, Reynolds number, and properties of gases, the agreement is due to the similar flow phenomena in both cases for fixed BR and DR.

5.3 NUMERICAL PARAMETRIC STUDY

A parametric study is carried out numerically to assess the influence of flow and geometrical parameters on the laterally averaged adiabatic effectiveness ($\eta_{ad.lat}$) under

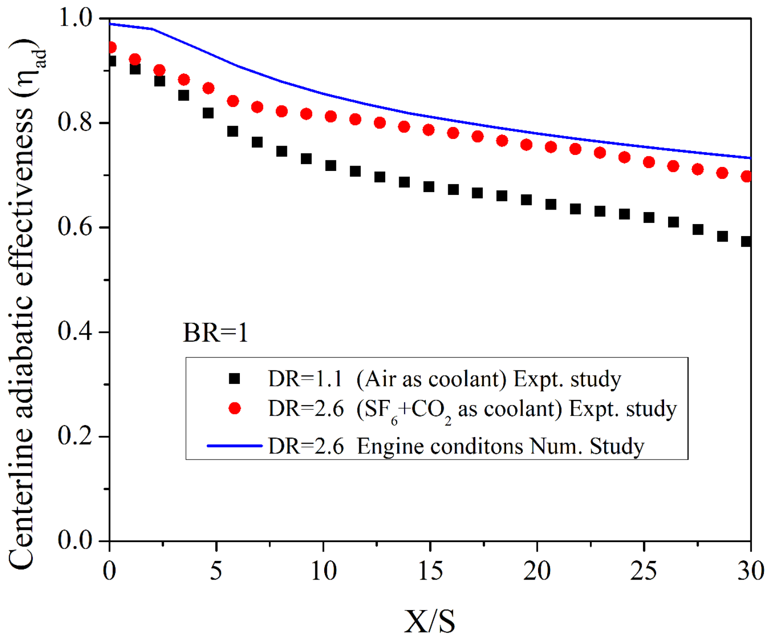

Figure 5.3: Comparison of centerline adiabatic effectiveness between laboratory and actual engine conditions at $BR = 1$

actual engine conditions (high pressure and temperature). The parameters considered are slot Reynolds number (Re_s), slot jet diameter (d), dimensionless slot jet pitch (p/d), lip taper angle (α), dimensionless, lip length (L/d) and slot jet injection angle (β). The range of parameters is shown in Table 5.2. Because of the similar trends in effectiveness observed for $BR > 1$, parametric studies are reported only for BR values of 0.5 and 1.

Table 5.2: Range of the parameters considered in the present parametric study

S.No	Paramter	Units	Minimum	Baseline	Maximum
1	Slot Reynolds number (Re_s)	-	2600	-	20500
2	Slot jet hole diameter (d)	mm	1.5	1.7	2
3	Dimensionless slot jet pitch (p/d)	^{o}	2	2.45	3.5
4	Lip taper angle (α)	-	0	5	7
5	Dimensionless lip length (L/d)	-	2.9	4.4	5.9
6	Slot jet injection angle (β)	^{o}	0	10	20

5.3.1 Effect of the slot Reynolds number

In both experiments and simulations, it is always challenging to mimic the unpredictable flow conditions that exist in the combustor. As a result, evaluating the influence of the slot Reynolds number (Re_s) on film cooling effectiveness is necessary.

Figure 5.4 depicts the effect of slot Reynolds number (Re_s) on laterally averaged film cooling effectiveness $\eta_{ad.lat}$ along the streamwise direction (X/S). The BR and DR are fixed at 0.9 and 2.6, respectively. The slot Reynolds numbers (Re_s) range from 2600 to 20500 and are obtained by scaling the velocity ratio. The η_{lat} is enhanced with an increase in slot Reynolds number (Re_s) up to = 7800. Thereafter, the effect of Re_s is insignificant, and the $\eta_{ad.lat}$ is constant because of the unchanged velocity profiles and turbulence intensity at the slot exit.

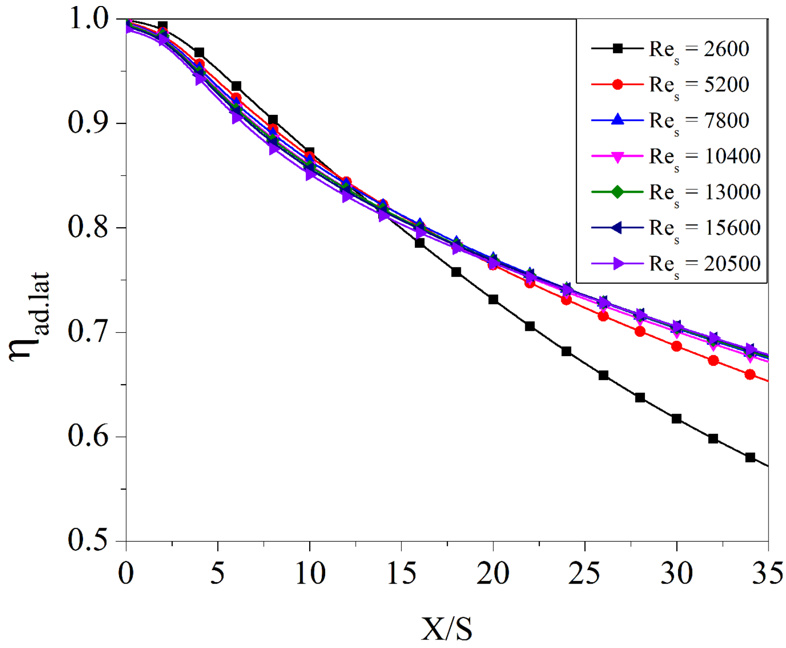

Figure 5.4: Effect of slot Reynolds number on lateral averaged effectiveness ($\eta_{ad.lat}$)

5.3.2 Effect of the slot jet diameter

In this section, the results of the studies on the effect of the slot jet diameter (d) on laterally averaged effectiveness ($\eta_{ad.lat}$) are reported. The slot jet diameters (d) considered in the study are 1.5, 1.7, and 2 mm. Figure 5.5a shows the effect of d on laterally averaged effectiveness ($\eta_{ad.lat}$) in the streamwise distance (X/S).

For BR of 0.5, the influence of the slot jet diameter (d) on the $\eta_{ad.lat}$ is minimal. However, the jet with $d = 2$ mm performs better up to $X/S = 25$. In the case, BR of 1, $\eta_{ad.lat}$ is enhanced for all the slot jet diameters due to the availability of more coolant. One can observe from the figure that there is a reduction in $\eta_{ad.lat}$ from $X/S = 3$ for $BR = 1$, and this adverse effect is reduced as d increases from 1.5 to 2 mm.

The reason behind this could be explained using the turbulent kinetic energy (TKE) contours in the slot. Figure 5.5b shows the contours of TKE in the slot at $BR = 1$ for the slot jet diameters under consideration. For the smaller $d = 1.5$ mm, the maximum TKE is 2200 m^2/s^2, which is high, whereas for the larger $d = 2$ mm, the TKE is only 600 m^2/s^2. The coolant velocity at a fixed mass flux is significantly higher for a smaller jet diameter (d) of 1.5 mm compared to 2 mm. For the case of $d = 1.5$mm, the jet escapes the slot without proper mixing, and this is seen as an increase in TKE. Hence, the slot jet diameter (d) should be large to enhance the effectiveness by attenuating the turbulence at the slot exit.

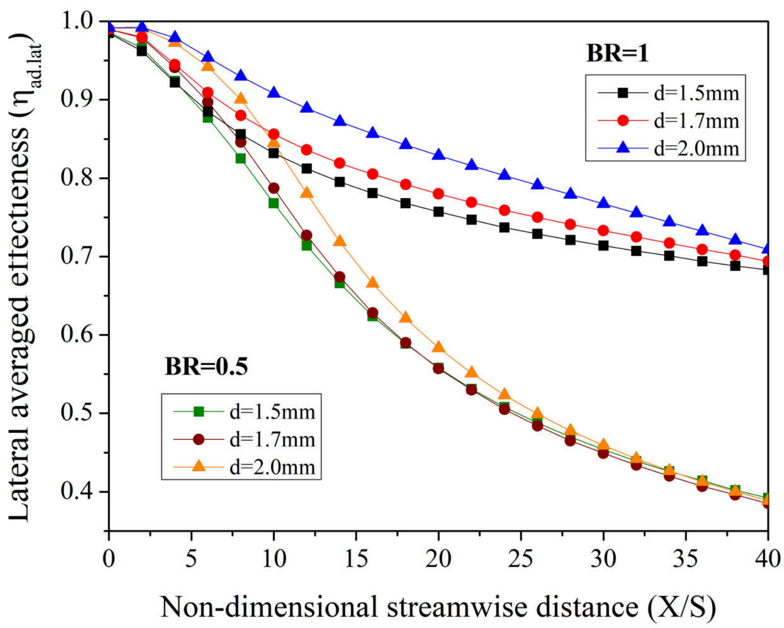

(a)

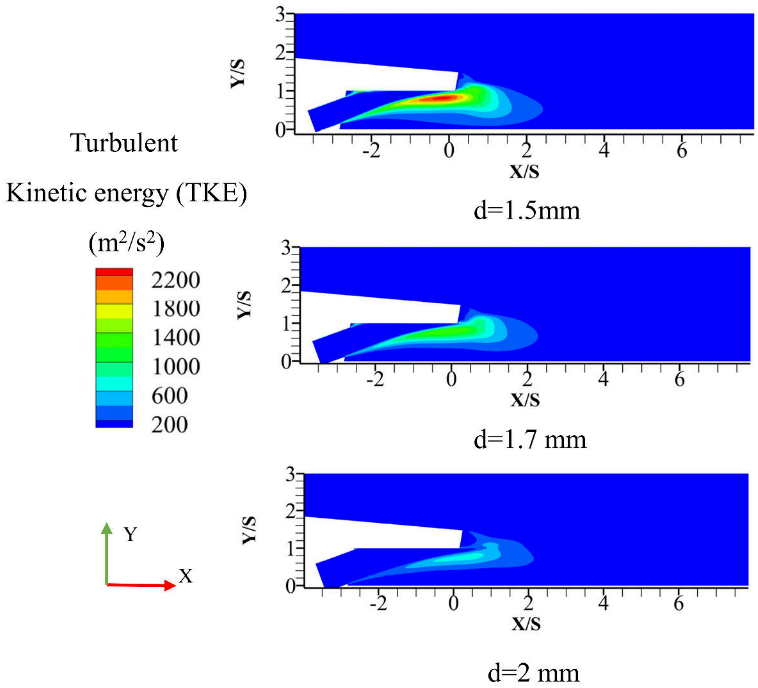

(b)

Figure 5.5: Effect of slot jet diameter (d) on (a) lateral averaged effectiveness ($\eta_{ad.lat}$) in the streamwise distance (X/S) for $BR = 0.5$ and 1 (b) Turbulence kinetic energy (TKE) contours for $BR = 1$

5.3.3 Effect of the slot jet pitch

This section reports results on the influence of dimensionless slot jet pitch (p/d) on the laterally averaged film cooling effectiveness ($\eta_{ad.lat}$). The values of dimensionless slot jet pitch (p/d) considered are 2, 2.45, and 3.5. Figure 5.6 shows the effect of p/d on η_{lat} for blowing ratios of 0.5 and 1.

For all blowing ratios (BR), the slot with a smaller pitch ($p/d = 2$) outperforms the other geometries. For BR of 1 and at $X/S = 10$, a maximum $\eta_{ad.lat}$ of 0.9 is obtained for $p/d = 2$, whereas for $p/d = 3.5$ is only 0.8. The enhancement in $\eta_{ad.lat}$ for $p/d = 2$ is because of the coolant uniformity at the slot exit obtained by the closely spaced slot jets. Figure 5.7a illustrates the contours of adiabatic film cooling effectiveness (η_{ad}) on the liner surface for BR of 1. The contours of effectiveness have undulating behavior due to coolant entry through discrete holes. In addition, the contour appears elongated along the streamwise and spanwise directions due to entrainment. Invoking the concepts of wavelength and amplitude, the pitch of the jets can be considered the wavelength, and the peaks of the contours can be thought of as representing the amplitude. Because of higher coolant uniformity, the amplitude and wavelength of the η_{ad} contours for $p/d = 2$ are smaller than those for $p/d = 3.5$.

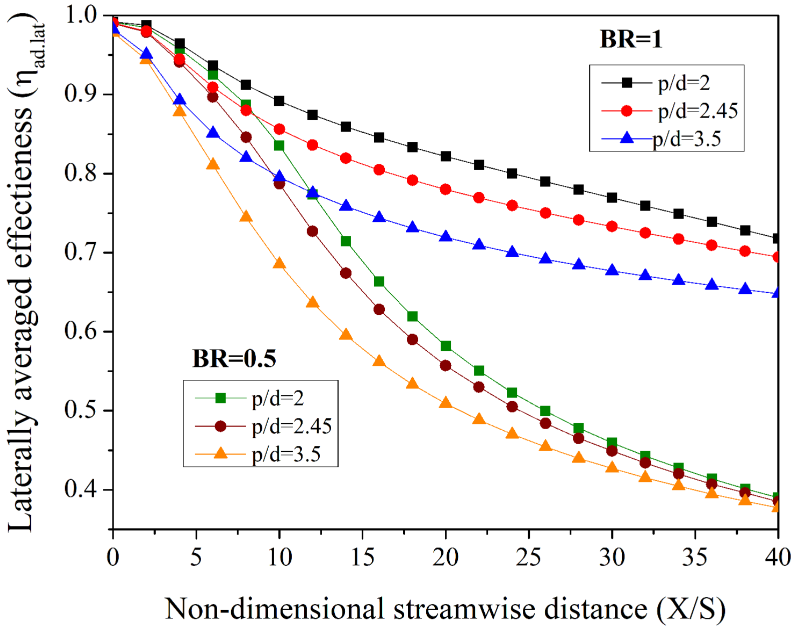

Figure 5.6: Effect of dimensionless slot jet pitch (p/d) on lateral averaged effectiveness (η_{ad}) in the streamwise distance (X/S)

A lateral uniformity index can be defined to visualize the uniformity of the coolant coming out of the slot as follows:

$$\delta = \frac{u_o - u_{p/2}}{(u_o - u_{p/2})_{max}} \tag{5.1}$$

Where u_o and $u_{p/2}$ are velocities on the centerline and along the line at half of the pitch between the two jets, respectively. The variation of the lateral uniformity index (δ) along the liner length (X/S) at height y = $S/2$ is shown in Figure 5.7b.

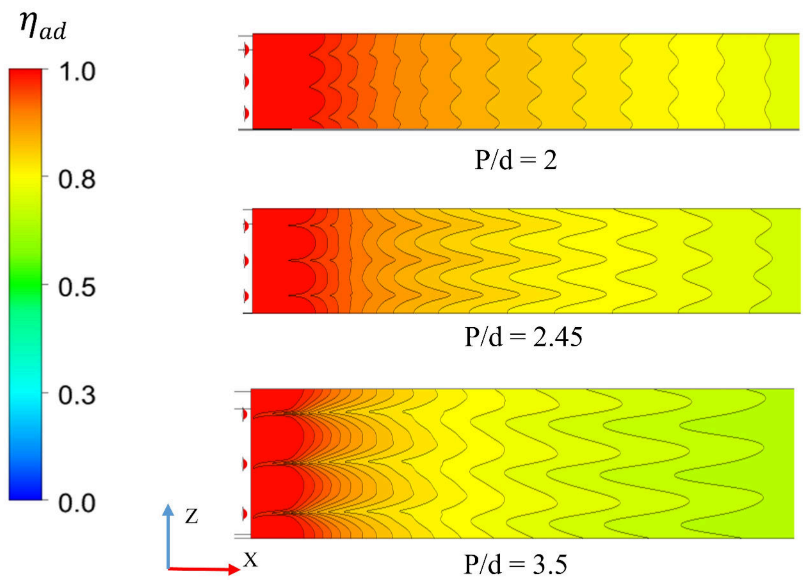

(a)

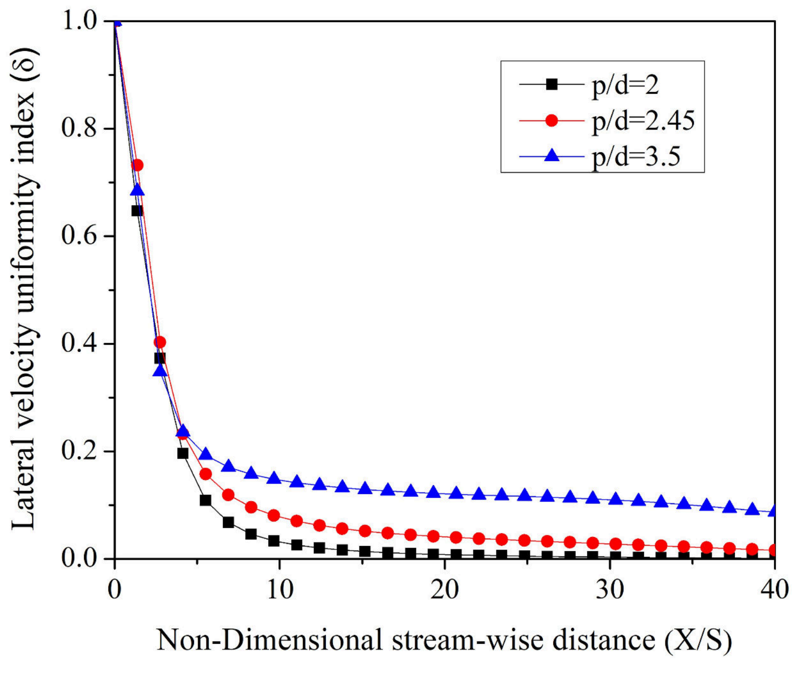

(b)

Figure 5.7: Effect of slot jet pitch (a) adiabatic effectiveness distribution (η_{ad}) on the liner surface (b) variation of lateral uniformity index (δ) along X/S

When the lateral uniformity index (δ) reduces rapidly in the streamwise direction, the coolant emerging out of the slot is more uniform, and vice versa. From Figure 5.7b, it is observed that at X/S = 10, the δ for pitch p/d = 2 is only 0.02 whereas, for p/d = 3.5, it is 0.18, which indicates that coolant is more uniform for p/d = 2. As a result, a higher η_{lat} is obtained with small-pitched jets.

5.3.4 Effect of the lip taper angle

The lip is an overhanging slab that guides the mainstream into the cold stream with a smooth interaction. The lip taper angle is varied based on the pivot shown in the nomenclature of the slot (see Figure 5.1) to understand the influence on laterally averaged adiabatic effectiveness ($\eta_{ad.lat}$). The lip taper angles (α) considered in the study are 0^o, 5^o, and 7^o. Figure 5.8 depicts the effect of α on $\eta_{ad.lat}$ for BR of 0.5 and 1. For a blowing ratio (BR) of 0.5, the lip with α = 0^o performs well up to X/S = 18 compared to other configurations.

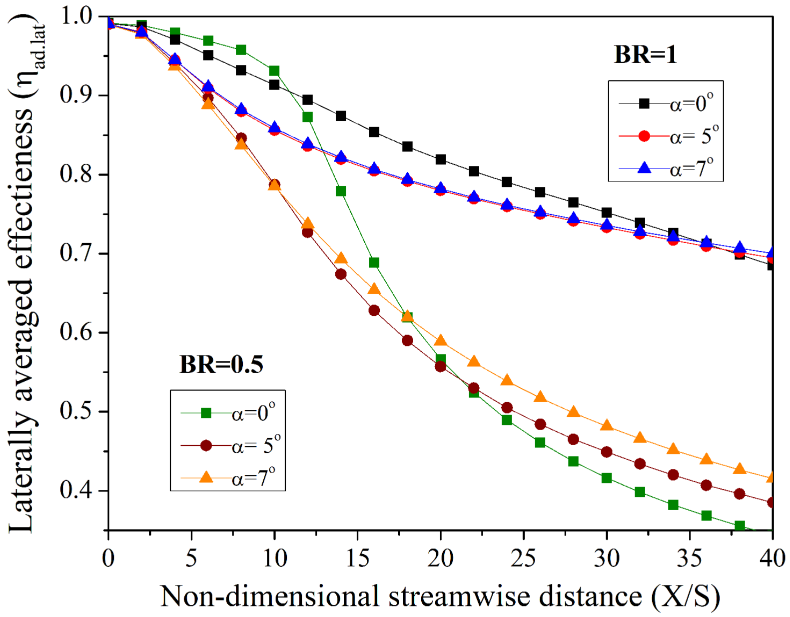

Figure 5.8: Effect of lip taper angle (α) on lateral averaged effectiveness ($\eta_{ad.lat}$) in the streamwise distance (X/S)

However, the $\eta_{ad.lat}$ drops significantly in the far-field ($X/S > 18$). Consequently, in the far field, the lip of the successive liner would burn off due to high temperatures. This reduction in the $\eta_{ad.lat}$ is attributed to the low blowing ratio and a recirculation zone generated at the lip exit.

From Figure 5.8, it is further observed that the film cooling performance of $\alpha = 0^o$ is better than other configurations for BR = 1, compared to the case of $BR = 0.5$.

This behavior can be well explained using Figure 5.9 which compares streamlines and velocity profiles between $\alpha = 0^o$ and 7^o. In the case of $\alpha = 0^o$, the sudden expansion of the main and cold streams creates a recirculation zone at the lip exit. However, the large lip thickness for $\alpha = 0^o$ shifts the interaction of streams away from the slot exit (nearly $X/S = 5$). As a result, the mixing of the mainstream with the cold stream is reduced, which contributes to high film cooling effectiveness even with the recirculation zone.

In contrast, for $\alpha > 0^o$, the mainstream smoothly interacts with the coolant due to the Coanda effect. However, the mainstream has an impinging behavior on the liner surface and interacts with the coldstream immediately at the slot exit (see Figure. 5.9b). As a result, the film cooling performance for $\alpha = 7^o$ is reduced.

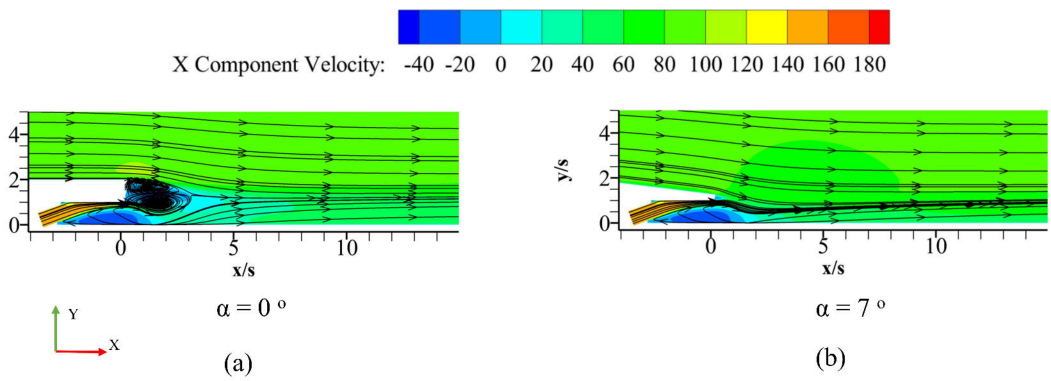

Figure 5.9: Streamlines and velocity profiles at $BR = 1$ (a) $\alpha = 0^o$ (b) $\alpha = 7^o$

5.3.5 Effect of the lip length

This section discusses the influence of dimensionless lip length (L/d) on the laterally averaged effectiveness ($\eta_{ad.lat}$). The values of L/d considered in the study are 2.9, 4.4, and 5.9. Figure 5.10 depicts the influence of lip length on the η_{lat} along streamwise distance (X/S). For blowing ratios (BR) 0.5 and 1, the $\eta_{ad.lat}$ for the long lip with L/d of 5.9 is superior to other configurations. Even at a low BR of 0.5, the $\eta_{ad.lat}$ is significantly enhanced in the far field. This can be attributed to the turbulent kinetic energy (TKE) at

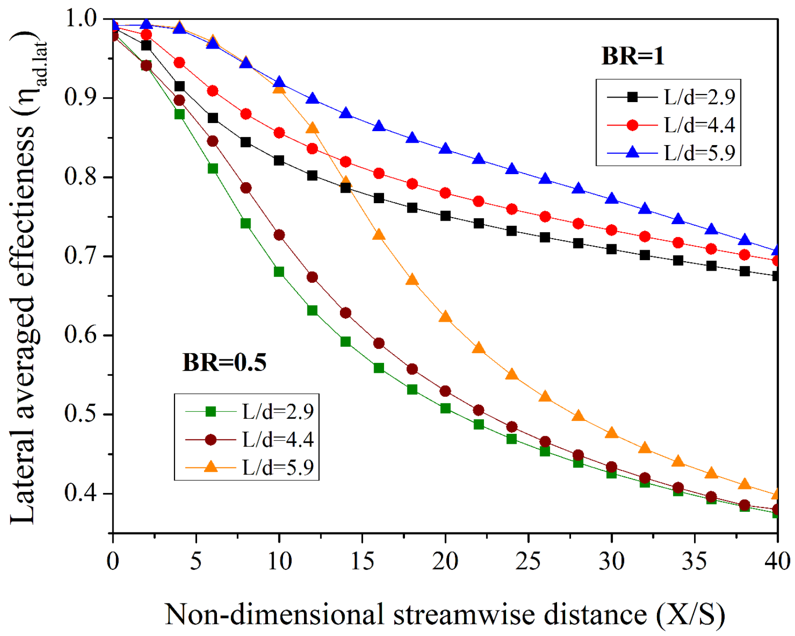

Figure 5.10: Effect of lip length (L/d) on lateral averaged effectiveness (η_{ad}) in the streamwise distance (X/S)

the slot exit. Figure 5.11a shows the TKE contours at BR = 0.5 for the values of L/d considered in the study. It is observed that the TKE is substantially dampened within the slot for the long lip (L/d = 5.9). As a result, the TKE_{max} at the slot exit is only 1200 m^2/s^2. On the other hand, the slot with a L/d of 2.9 has a relatively high TKE_{max} of 2500 m^2/s^2, which adversely affects the performance.

Further, at BR = 0.5, the velocity contours at the slot exit for the above-mentioned values of L/d are shown in Figure 5.11b. In the case of the short lip (L/d = 2.9), some part of the jet penetrates the mainstream right at the slot exit and creates a strong mixing zone. This event affects the film cooling adversely. On the other hand, there is no significant mixing immediately at the slot exit for L/d equal to 5.9, which results in better film cooling performance.

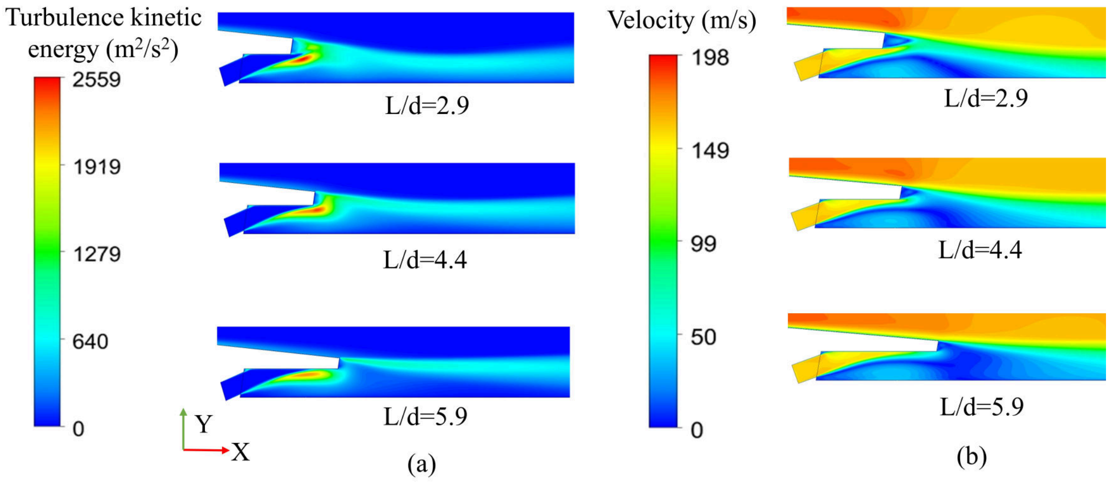

Figure 5.11: Comparison of the flow field for various lip length (L/d) geometries at BR = 0.5 (a) turbulence kinetic energy profiles (b) velocity profiles

5.3.6 Effect of slot jet injection angle

The effect of the blowing ratio on the laterally averaged adiabatic effectiveness ($\eta_{ad.lat}$) for a slot jet injection angle (β) of 0^o is investigated next. For $\beta = 0^o$, parallel slot jet holes allow coolant to flow tangentially to the liner surface. Figure 5.12a, shows the variation of $\eta_{ad.lat}$ for the case of $\beta = 0^o$ along the streamwise distance (X/S). From the figure, it is observed that the film cooling effectiveness ($\eta_{ad.lat}$) is reduced in the near field ($X/S < 10$) with an increase in the blowing ratio (BR) from 0.5 to 2.

Furthermore, the effect of slot jet injection angle (β) on $\eta_{ad.lat}$ is investigated for various blowing ratios(BR). Figure 5.12b shows the variation of $\eta_{ad.lat}$ along the streamwise distance (X/S) for BR of 0.5 and 1.

For a BR of 0.5, the slot injection angle β has a minimal influence on $\eta_{ad.lat}$. However, at BR = 1, the tangential coolant injection ($\beta = 0^o$) underperforms compared to $\beta = 10^o$ and 20^o.

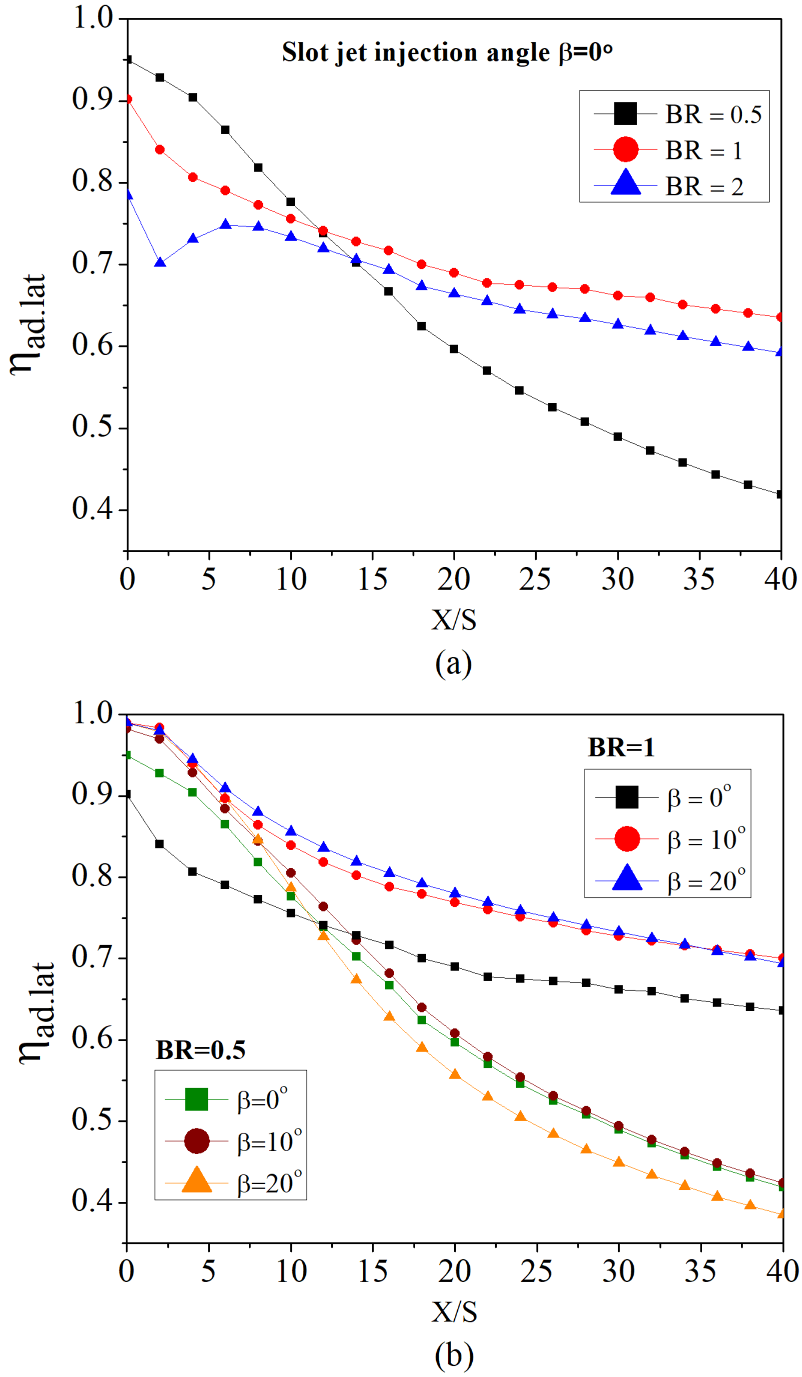

Figure 5.12: (a) Effect of blowing ratio on the effectiveness ($\eta_{ad.lat}$) for $\beta = 0^o$ (b) Effect of injection angle (β) on effectiveness ($\eta_{ad.lat}$) at various blowing ratios

The underperformance of the slot with β of 0^o compared to $\beta = 10^0$ and 20^0 can be explained using the temperature distribution on the liner surface depicted in Figure 5.13a. One can observe the localized hot spots in the temperature distribution near the slot exit. The high-temperature gradients at the hot spots result in high thermal stresses in the liner. The vortex motion of the jets develops a low-pressure region at the slot exit. As a result, the mainstream bleeds into the low-pressure zone, mixes with coolant, and creates hotspots (see Figure 5.13b). Furthermore, as the blowing ratio increases, so does the intensity of the hot spot due to higher vorticity.

Figure 5.13c shows the coolant streamlines in the slot for β of 0^o. The coolant enters the slot through the jet holes and creates a film on the liner. However, one can observe that there is no significant interaction between the jets, leading to low-pressure zones and hotspots.

In contrast, there are no hotspots when $\beta = 20^o$, and the liner is significantly cooled to low temperatures (see Figure 5.13d). In this case, the jets impinge under the lip, interact laterally, and generate stagnation zones (see Figure 5.13e and f). The stagnation zone

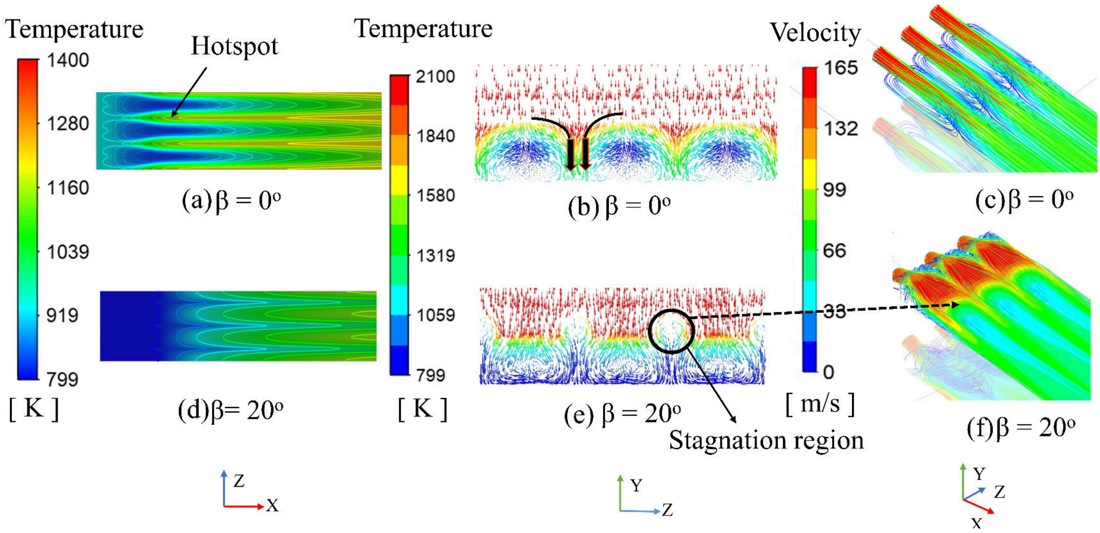

Figure 5.13: Effect of coolant injection angle (β) on (a,d) Temperature distribution on liner surface (b,e) Temperature coloured streamlines (c,f) Coolant streamlines

restricts fluid flow in the y-z plane and only allows it in the x-direction. As a result, the bleeding of the mainstream into the coolant jets is reduced. Hence, the geometry with a slot jet injection angle of $\beta = 20^o$ performs better than $\beta = 0^o$.

5.4 MATHEMATICAL MODEL FOR FILM COOLING EFFECTIVENESS

The ability to predict the effectiveness quickly and swiftly without having to perform numerical simulations would be very useful from an engineering perspective. Hence, the objective of the present section is to formulate an Artificial Neural Network (ANN)-based mathematical model for predicting the effectiveness ($\eta_{ad.lat}$) along the streamwise distance (X/S) at various blowing ratios and various geometries. ANN is a powerful tool to approximate a mathematical model for highly non-linear complex problems. Unlike classical techniques, ANN does not require prior knowledge of the relationship between input and output variables. Mathematically, an ANN is a combination of linear and non-linear transformation of input data Lawal and Idris (2020). A general schematic for a single objective ANN and the mathematical operations in the network is illustrated in Figure 5.14a and b, respectively.

In each perceptron or neuron, linear and non-linear transformations of input variables are carried out with optimum weights and biases obtained from backpropagation (see Figure 5.14 (b)). Finally, the output of the ANN can be represented as a simple formula based on the non-linear tan-sigmoid and linear transfer functions in hidden and output layers, respectively. The ANN is trained by feeding the input data randomly for training, validation, and testing. Based on the relative importance of each variable, five input variables are considered, namely dimensionless streamwise distance (X/S), blowing ratio (BR), slot jet diameter (d), slot jet pitch (p), lip length (L). The current model is valid between $BR = 0.5$ to 2, and the range of geometrical parameters is the same as that shown in Table 5.2. An optimal network of seven neurons is identified based on a neuron-independence carried out for a range of 2 to 15 neurons. A mathematical model can be generated from a trained ANN using the weights and biases of the corresponding neuron in conjunction with the transfer functions. The generic equation of the output for

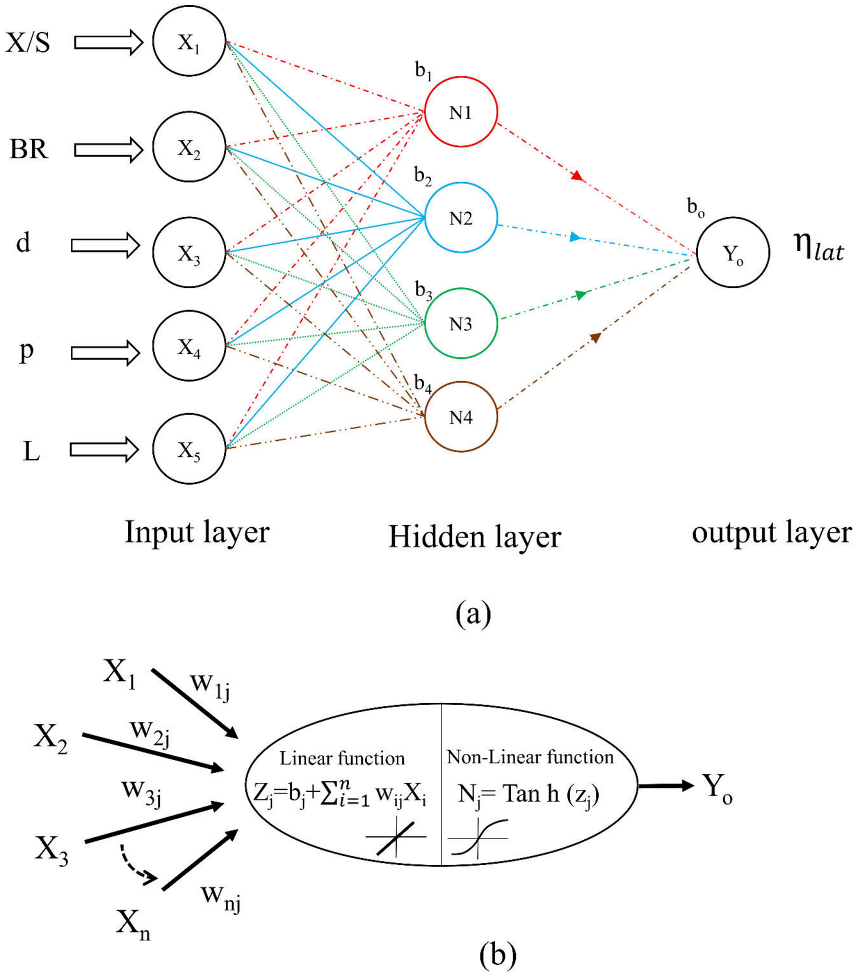

Figure 5.14: Details of ANN (a) Schematic of single objective ANN (b) Mathematical operations in ANN

the single objective ANN is

$$Y_o = b_o + \sum_{j=1}^{n} w_{oj} N_j \tag{5.2}$$

Where

b_o: bias of the output layer

w_{oj}: Connection weight between the hidden layer neurons and output variable

N_j = tanh (Z_j): Non-linear transfer function of each neuron in the hidden layer

$$Z_j = b_j + \sum_{i=1}^{n} w_{ij} X_i \tag{5.3}$$

Table 5.3: Weights and biases generated after training ANN

weights						biases	
w_{1j}	w_{2j}	w_{3j}	w_{4j}	w_{5j}	W_o	b_j	b_o
0.449	-1.916	‘ -0.566	1.031	-0.754	-0.4163	2.326	0.6708
4.255	0.3	-0.413	0.537	-0.744	-0.1766	2.733	
-1.256	2.552	0.075	-0.213	0.267	0.9374	2.075	
-1.348	-5.116	0.195	-0.322	0.405	-0.9516	-0.2531	
0.182	3.668	-0.148	0.188	-0.165	-1.4622	0.5245	
0.671	-0.379	0.261	-1.068	0.445	-1.1857	1.6316	
-0.795	0.527	0.814	2.465	0.826	-0.5411	-2.310	

Z_j : linear transformation of input variables in each neuron

b_j : bias of each neuron in the hidden layer

w_{ij}: Connection weights between the input variables and hidden neurons

The input and output variables are normalized between -1 and 1 to ensure transfer function compatibility and to avoid under or over-fitting issues. To estimate the normalized laterally averaged effectiveness, Equation 5.2 is written as Equation 5.4.

$$\eta_{ad.lat,norm} = 0.6708 + O_1 + O_2 + O_3 + O_4 + O_5 + O_6 + O_7 \tag{5.4}$$

Unknowns O_1 to O_7 are determined using Equations 5.5 to 5.18 and the weights shown in Table 5.3. The Equations are:

$$O_1 = -0.416tanh(Z_1) \tag{5.5}$$

$$O_2 = -0.177tanh(Z_2) \tag{5.6}$$

$$O_3 = 0.937tanh(Z_3) \tag{5.7}$$

$$O_4 = -0.952tanh(Z_4) \tag{5.8}$$

$$O_5 = -1.462tanh(Z_5) \tag{5.9}$$

$$O_6 = -1.186tanh(Z_6) \tag{5.10}$$

$$O_7 = -0.541tanh(Z_7) \tag{5.11}$$

$$Z_1 = 7.474 + 0.0220X/S - 2.5490BR - 2.2640d + 0.8080p - 0.2980L \tag{5.12}$$

$$Z_2 = 1.092 + 0.2130X/S + 0.3990BR - 1.6530d + 0.4210p - 0.2930L \quad (5.13)$$

$$Z_3 = -1.449 - 0.0630X/S + 3.3950BR + 0.2980d - 0.1670p + 0.1050L \quad (5.14)$$

$$Z_4 = 8.241 - 0.0670X/S - 6.8050BR + 0.7810d - 0.2530p + 0.1600L \quad (5.15)$$

$$Z_5 = -4.931 + 0.0090X/S + 4.8780BR - 0.5930d + 0.1470p - 0.0650L \quad (5.16)$$

$$Z_6 = 2.365 + 0.034X/S - 0.5040BR + 1.046d - 0.8370p + 0.1760L \quad (5.17)$$

$$Z_7 = -19.560 - 0.0400X/S + 0.7010BR + 3.256d + 1.933p + 0.3260L \quad (5.18)$$

As the input variables are normalized between -1 to 1, the output Equation 5.4 needs to be denormalized to get actual effectiveness. Hence, Equation 5.4 is denormalized to Equation.5.19 to estimate the actual laterally averaged effectiveness.

$$\eta_{ad.lat} = 0.30895\eta_{lat,norm} + 0.68385 \quad (5.19)$$

Figure 5.15 shows a comparison between predictions of η_{lat} obtained from Equation 5.19 (ANN) with the actual values from numerical simulations. It can be observed that there is reasonably good agreement between numerical results and their corresponding ANN prediction with a maximum error of 5%. Additionally, there is no noticeable bias in the ANN predictions.

5.5 CONCLUSIONS

In this chapter, the results of fluid flow and heat transfer characteristics in three-dimensional slot film cooling based on extensive numerical studies were reported and discussed. Film cooling performance was investigated numerically at actual engine conditions (high temperature and pressure) to understand the influence of the blowing ratio. Furthermore, a detailed parametric study was conducted numerically to evaluate the influence of flow and geometrical parameters. The parameters under consideration were slot Reynolds number (Re_s), slot jet diameter (d), dimensionless slot jet pitch (p/d), lip taper angle (α), dimensionless lip length (L/d), and slot jet injection angle

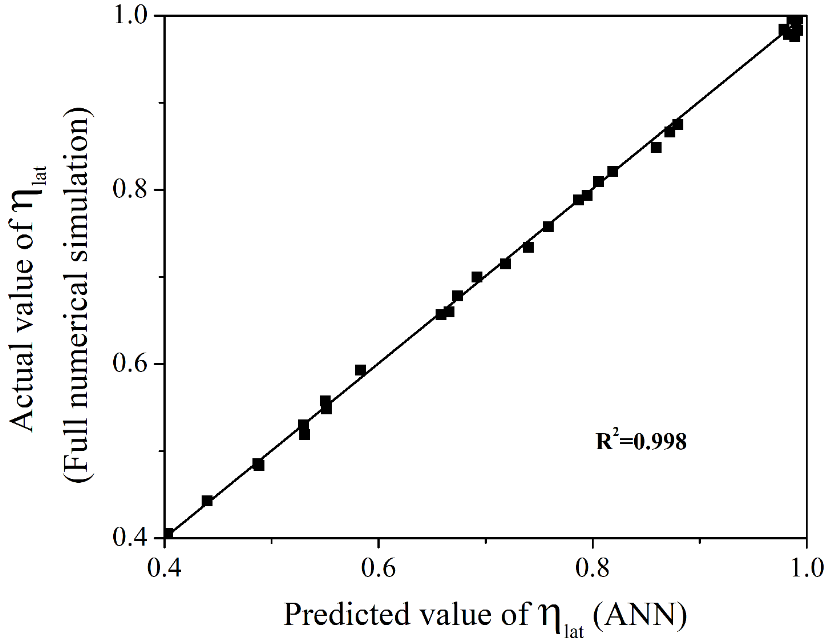

Figure 5.15: Validation of ANN with numerical simulations

(β). Finally, an Artificial Neural Network-based mathematical model was developed for predicting the film cooling effectiveness as a function of the blowing ratio (BR), non-dimensional streamwise distance (X/S), slot jet diameter (d), slot jet pitch (p), lip length (L).

The salient conclusions of the study are:

1. At actual engine conditions (DR = 2.6), the film cooling effectiveness increases for $0.5 \leq BR \leq 2$. However, the effectiveness becomes stagnant for $3 \leq BR \leq 5$ due to a significant increase in turbulence intensity caused by the shearing of main and cold streams in the mixing zone. Moreover, similar trends of effectiveness are observed under laboratory conditions (DR = 1.1). Hence, to save the amount of coolant, it is not recommended to operate the film cooling beyond BR = 2.

2. For a constant blowing ratio and under an incompressible flow regime, film cooling effectiveness increases with an increase in slot Reynolds number Re_s and becomes constant after Re_s = 7800.

3. With the increase in the slot jet diameter, the film cooling effectiveness is increased

due to relatively low-velocity gradients and turbulence intensity in the mixing zone. In addition, a decrease in the pitch (p/d) shows higher film cooling effectiveness due to the coolant uniformity with closely spaced slot jets.

4. The lip with $\alpha = 0^o$ performed well due to the shifting mixing of both streams. In contrast, lips with $\alpha = 5^o$ and 7^o underperformed due to the impinging behavior of mainstream on the liner surface.

5. The slot with a long lip performed well due to the dampening of the turbulent kinetic energy. In contrast, the smaller lip length shows an adverse effect on efficiency because of the insufficient impinging surface and entertainment at the slot exit.

6. High vorticity of the counter-rotating vortices at the slot exit adversely affects the performance of the slot configuration with coolant injection tangential to the liner ($\beta = 0$). In contrast, the lateral interaction of the coolant jets enhances the performance of the slot with $\beta > 0$.

5.6 CLOSURE

In this chapter, the results of the performance of the three-dimensional baseline slot investigated numerically under actual engine conditions were reported. Based on the parametric studies, the effect of key parameters in the problem on the cooling performance was delineated. Finally, an artificial neural network-based mathematical model is developed to predict film cooling effectiveness as a function of five parameters namely dimensionless streamwise distance (X/S), blowing ratio (BR), slot jet diameter (d), slot jet pitch (p), lip length (L). In the next chapter, the results of optimization studies on three-dimensional slot configurations are reported.

[1]

[1]This chapter is drawn from the following publication:**Revulagadda A.P**, Adapa B.R., Balaji C, Pattamatta A, "Fluid Flow and Heat Transfer Characteristics of Three-Dimensional Slot Film Cooling in an Annular Combustor", International Journal of Heat and Mass Transfer ,211(2023),p.(124211), doi.org/10.1016/j.ijheatmasstransfer.2023.124211.

CHAPTER 6

OPTIMIZATION OF THREE-DIMENSIONAL SLOT FILM COOLING CONFIGURATION

In this chapter, the results of the sensitivity studies of the film cooling performance with respect to the geometrical parameters of a three-dimensional slot and optimization using machine learning algorithms under actual engine conditions (high temperature and pressure) are presented. For simulating the actual engine conditions, the validated numerical model outlined in Chapter 4 is considered.

Figure 6.1 depicts a schematic of the cross-section of the baseline combustion chamber in a typical annular gas turbine.

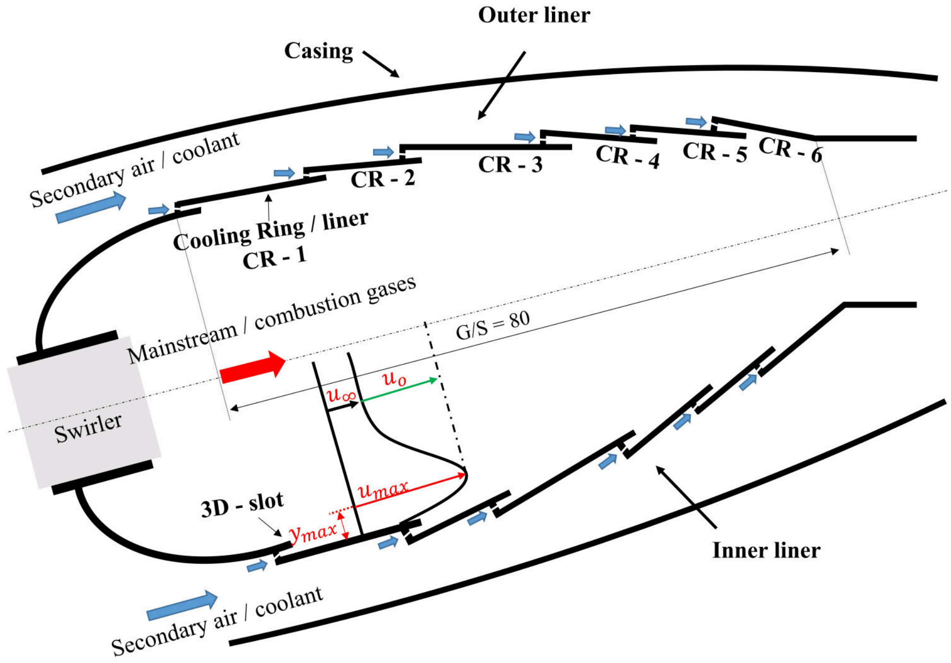

Figure 6.1: Schematic of a typical annular combustor

The liner is made up of multiple concentric cooling rings stacked horizontally. The annular gap between the cooling rings provides a provision for the coolant entry. The baseline combustor consists of six pairs of cooling rings including outer and inner liners, to protect the combustor with a length (G/S) equal to 80.

In the present optimization study, the cooling rings 5 and 6 of the outer liner are considered reference 1 and reference 2 configurations, respectively, in order to compare their film cooling performance to that of the optimal configuration. Reference 1 is the configuration that was investigated in the previous chapters. In the optimization procedure, the design space is generated using the Latin hypercube sampling, and each design point is solved numerically at a blowing ratio (BR) of 1. A surrogate model is developed to predict the reciprocal of area-averaged effectiveness ($1/\eta_{ad.avg}$) and its standard deviation (σ_η) as a function of the geometrical parameters of the slot. An optimum configuration having a maximum $\eta_{ad.avg}$ and a minimum σ_η is identified using a genetic algorithm. Furthermore, a numerical study is conducted on a subsequent row of liners to identify the reduction of coolant mass flux for the entire combustor. The optimum configurations are tested experimentally under laboratory conditions (low temperature and pressure). In view of obtaining the complete benefit of film cooling, the baseline three-dimensional slot is replaced with the optimum slot in an improvised hybrid slot configuration, and the enhancement of film cooling performance is reported.

6.1 SENSITIVITY OF THE FILM COOLING PERFORMANCE TO THE SLOT CONFIGURATION

In this section, the sensitivity of the film cooling effectiveness ($\eta_{ad.avg}$) and its standard deviation (σ_η) to the geometrical parameters of the slot are investigated numerically for a blowing ratio (BR) of 1 under actual engine conditions. For this study, reference 1 slot configuration is considered.

The standard deviation indicates the non-uniformity of the effectiveness on the liner surface. The definitions of $\eta_{ad.avg}$ and σ_η are given in Equations 6.1 and 6.2.

$$\eta_{ad.avg} = \frac{1}{A}\int_0^{40}\int_{-2.4}^{2.4}\eta_{ad}(x,z)d(Z/S)d(X/S) \tag{6.1}$$

$$\sigma_\eta = \sqrt{\frac{1}{N}\sum_{i=1}^{N}(\eta_i - \eta_{ad.avg})^2} \tag{6.2}$$

Based on the parametric study in the previous chapter, it was evident that the configuration with coolant injection angle (β) < 20^o under-performed compared to the case $\beta = 20^o$. In addition, in actual engines, it is not recommended to implement the configuration with $\beta < 20^o$. Hence, the coolant injection angle (β) is fixed to 20^o, the same as the baseline reference configuration. The geometrical parameters under consideration for sensitivity and optimization are slot jet diameter (d), dimensionless slot jet pitch (p/d), lip taper angle (α), and dimensionless lip length (L/d).

6.1.1 Effect of slot jet diameter and slot jet pitch

Figure 6.2a shows the effect of slot jet diameter (d) on area-averaged effectiveness ($\eta_{ad.avg}$) and its standard deviation (σ_η). From the figure, it is observed that the film cooling effectiveness increases with an increase in slot jet diameter (d) from 1.5 to 2 mm. This behavior is attributed to a reduction of turbulence intensity in the mixing zone of the mainstream and coldstream. A study on practical slots by Sturgess (1980) identified that the film cooling effectiveness is maximum when the velocity ratio is unity because of the low turbulence intensity in the mixing zone. Hence, in the present case, the diameter of the slot jet needs to be optimized to obtain low turbulence intensity, thereby maximizing film cooling performance. The effect of dimensionless slot jet pitch (p/d) on the area-averaged effectiveness ($\eta_{ad.avg}$) and its standard deviation (σ_η) is shown in Figure 6.2b. One can observe that the $\eta_{ad.lat}$ reduces with the increase in the dimensionless slot jet pitch (p/d) from 2 to 3.5.

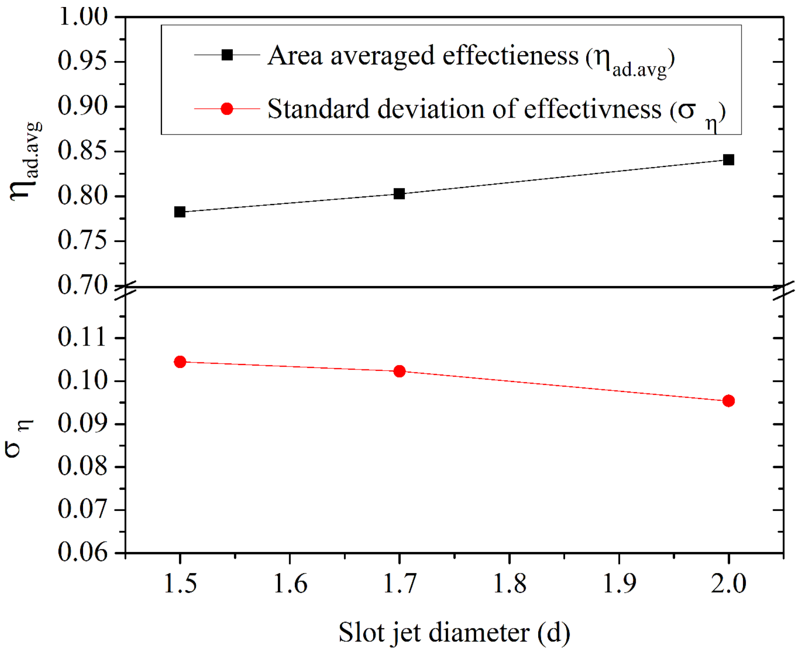

(a)

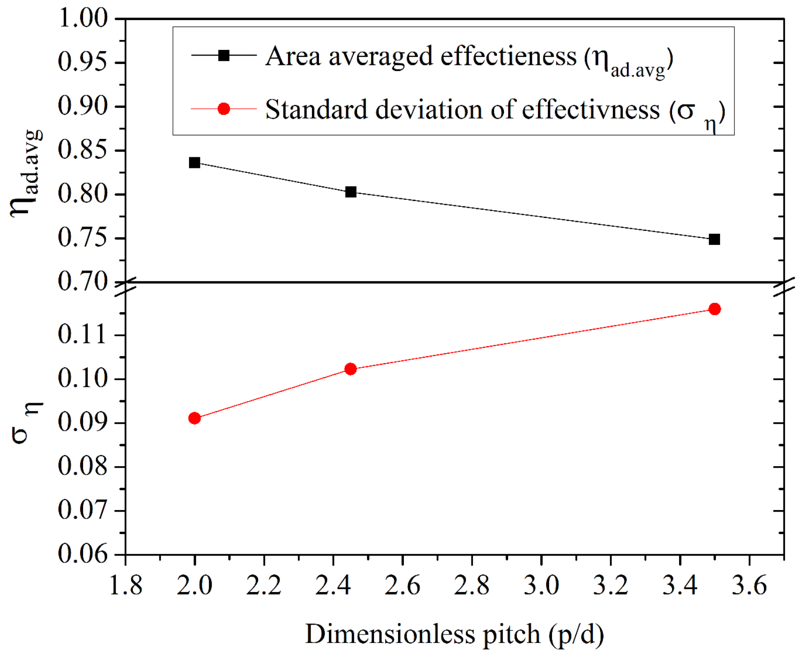

(b)

Figure 6.2: Effect of slot configuration on the film cooling performance (a) slot jet diameter (d), (b) dimensionless slot jet pitch (p/d)

Another observation is that the standard deviation (σ_{η}) is reduced with an increase in the slot jet diameter(d) and with a decrease in slot jet pitch (p/d). The reduction of σ_η is an indication of uniform film cooling effectiveness, and this behavior is attributed to closely spaced jets allowing for proper mixing within the slot.

6.1.2 Effect of lip taper angle and lip length

The effect of lip taper angle (α) on the area-averaged film cooling effectiveness ($\eta_{ad.avg}$) and its respective standard deviation (σ_η) are shown in Figure 6.3a. It is observed that the $\eta_{ad.avg}$ reduces as the lip taper angle (α) increases from 0^o to 7^o, though the decrease is mild.

In the case of $\alpha > 0^o$, the impinging behavior of the mainstream on the liner surface increases the mixing with cold stream and reduces the $\eta_{ad.avg}$. In addition, the standard deviation (σ_η) is reduced with an increase in α from 0^o to 7^o.

The effect of dimensionless lip length (L/d) on the $\eta_{ad.avg}$ and σ_η is shown in Figure 6.3b. From the figure, it is observed that $\eta_{ad.avg}$ increases with an increase in L/d from 3.9 to 5.9 due to the enhanced mixing of jets within the slot. The standard deviation increases with an increase of L/d from 3.9 to 4.5 and reduces thereafter.

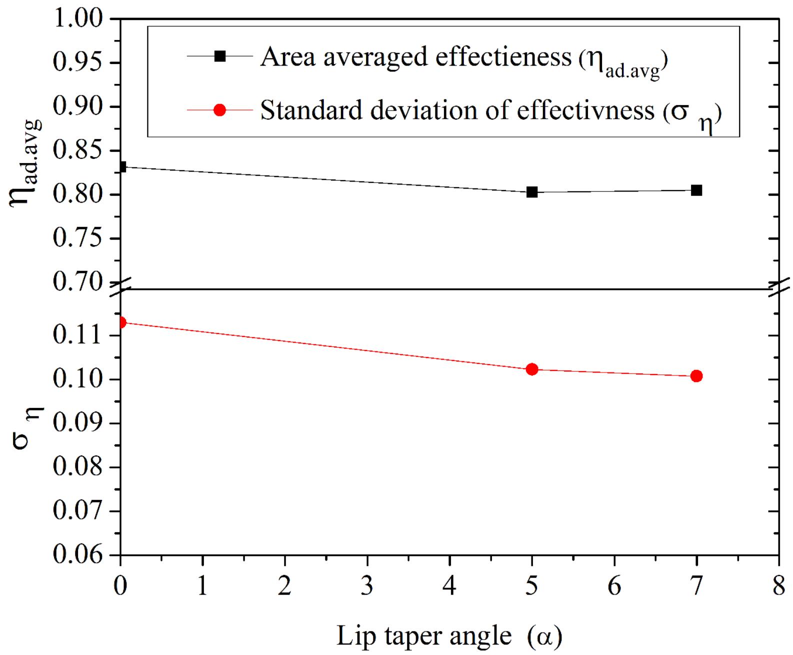

(a)

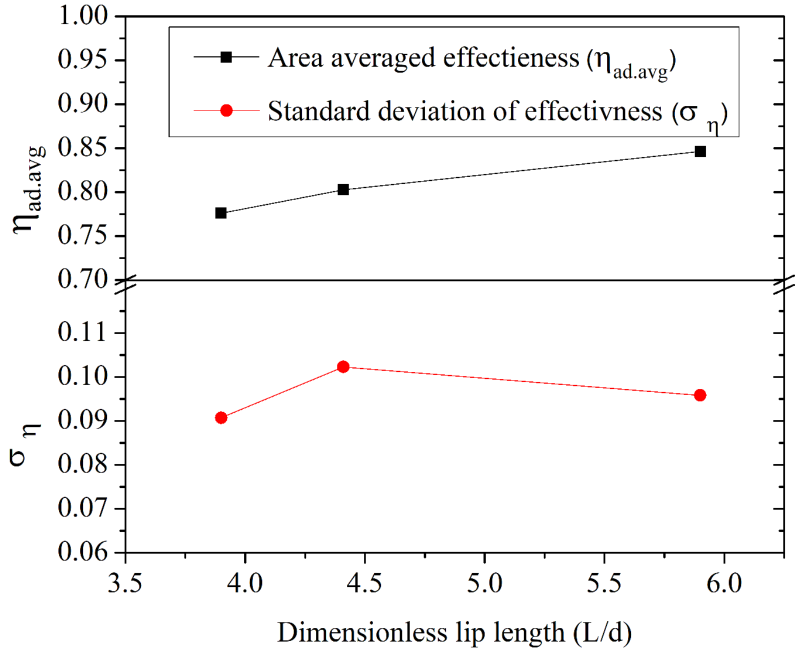

(b)

Figure 6.3: Effect of slot configuration on the film cooling performance (a) lip taper angle (α), (b) dimensionless lip length (L/d)

6.2 OPTIMIZATION OF THREE-DIMENSIONAL FILM COOLING SLOT

From the above sensitivity study, it is evident that the parameters considered influence the film cooling performance significantly and non-linearly in some cases, for example, the effect of L/d on σ_η. The influence of each geometrical parameter is evaluated when other geometrical parameters are fixed.

However, high-resolution data for each parameter and the influence of parameter interactions are required for optimizing the configuration of the film cooling slot. Solving a highly resolved parametric set with full numerical simulations is often extremely time-consuming.

Hence, a surrogate model is developed using a Kriging technique to replace the simulations, followed by optimization using the genetic algorithm. The detailed optimization procedure of the three-dimensional film cooling slot configuration is shown in Figure 6.4. The optimization of the three-dimensional slot configuration is conducted at a fixed blowing ratio BR of 1.

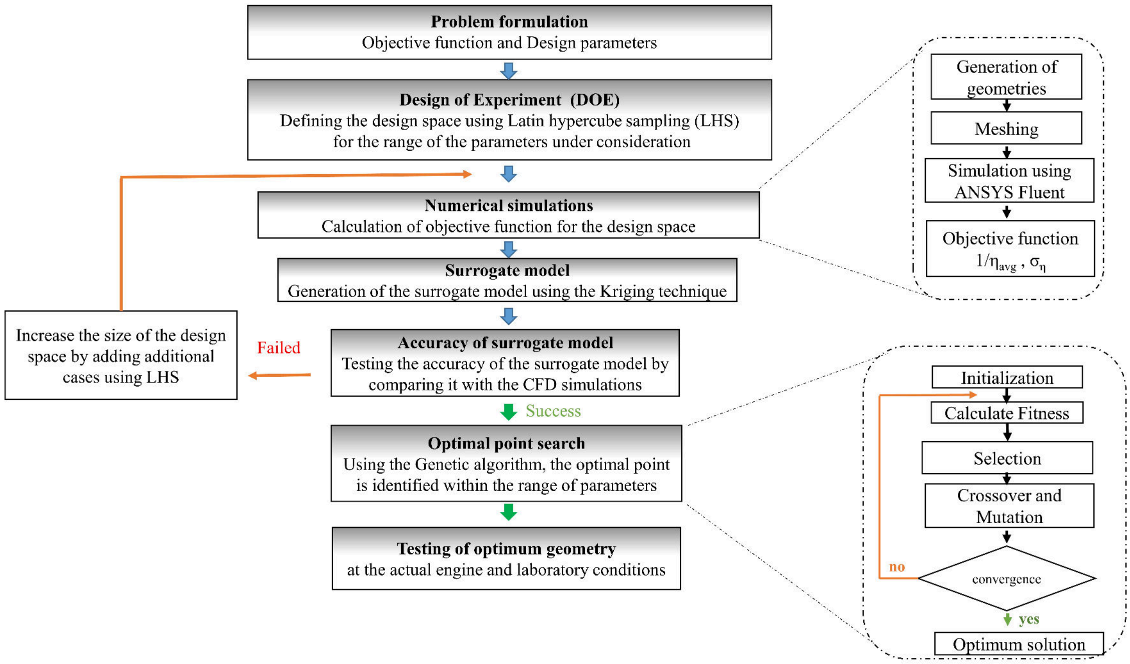

Figure 6.4: Optimization procedure in the present study

The aerothermal conditions under which optimization is carried out are given in Table 6.1.

Table 6.1: Actual engine operating conditions used in optimization

DR	BR	T_h (K)	T_c (K)	u_h (m/s)	u_c (slot exit) (m/s)
2.6	1	2100	799	57	29.7

6.2.1 Objective function and design parameters

A multi-objective optimization of the slot configuration is implemented to enhance the performance of the three–dimensional film cooling slot. The aim of this exercise is to maximize the adiabatic film cooling effectiveness and minimize its non-uniformity on the liner surface. The optimization is conducted at a fixed blowing ratio (BR) of 1, where coolant mass flux is constant. The first objective function is the reciprocal of area-weighted averaged effectiveness ($1/\eta_{ad.avg}$). This is obtained by averaging the film cooling effectiveness (η_{ad}) on the liner surface for the range of X/S from 0 to 40 and $-2.4 \leq Z/S \leq 2.4$. According to the study conducted by Li (2010), the second objective function is the standard deviation (σ_η) of the $\eta_{ad.avg}$, which evaluates the non-uniformity of the η_{ad} on the liner surface.

A Latin hypercube sampling (LHS) technique proposed by McKay *et al.* (1979) is used to generate a design space of 70 samples for developing the surrogate model. LHS is a type of stratified Monte Carlo sampling method where the range of variables is divided into N number of non-overlapping intervals with an equal probability size of 1/N. LHS is being widely used lately as it can significantly reduce the number of samples required to obtain reasonably accurate results.

The parameters and their ranges considered for optimizing the slot configuration are slot jet diameter (d), slot jet pitch (p), lip taper angle (α), and lip length (L). In this study, Matlab inbuilt functions available for the LHS are used to generate the design space, which is subjected to a practical range of parameters given in Table 6.2.

Table 6.2: Range of the parameters considered in the optimization study

S.No	Paramter	Units	Minimum	Maximum
1	Slot jet hole diameter (d)	mm	1.5	2
2	Slot jet pitch (p)	mm	4	6.5
3	Lip taper angle (α)	^{o}	0	7
4	Lip length (L)	mm	4.5	11.5

6.2.2 Surrogate model and genetic algorithm-based optimization

The surrogate model, as the name already implies, serves as a replacement for numerical simulations in the current investigation. The Kriging technique, also known as Gaussian process regression, is used in the present study to develop the surrogate model. This technique has been employed in previous studies on the design of shaped effusion holes and turbine blade cooling by Lee and Kim (2011), Seo *et al.* (2019), and Zhang *et al.*

(2020).

Kriging is a statistical method that fits a model for the higher-order design points using random variables and predicts the non-design points with high accuracy. The generic form of the model is given in Equation 6.3.

$$y = f(x) + Z(x) \tag{6.3}$$

Where

x: denotes the vector representing the parameters,

f(x): is a global function formulated using the design points

Z(x): represents the Gaussian process model with an average of zero and a covariance.

Further details of the Gaussian process regression are referred to work reported by Seo *et al.* (2019). The mathematical representation of the objective functions subjected to the design parameters (see Table 6.2) is given in the following Equations.

$$\begin{aligned}
\text{(a) Minimize,} \quad f_1(d, p, \alpha, L) &= \frac{1}{\eta_{ad.avg}} \\
\text{(b) Minimize,} \quad f_2(d, p, \alpha, L) &= \sigma_\eta
\end{aligned}$$

The surrogate model is developed using the Matlab inbuilt function called ”fitrgp”. In addition, the surrogate model is validated by comparing the predictions of an additional 20 samples with their corresponding numerical study. Figure 6.5 shows the comparison between numerical results and surrogate model predictions for $1/\eta_{ad.avg}$ and σ_η.

From Figure 6.5a and 6.5b, it is evident that the surrogate model is predicting very close to the corresponding numerical results. The performance metrics of the surrogate model compared to numerical results are given in Table 6.3.

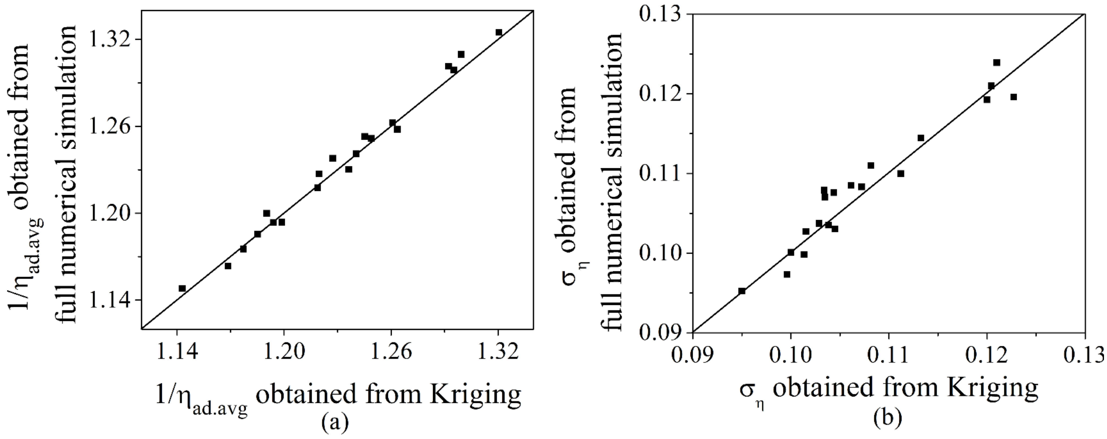

Figure 6.5: Validation of surrogate model with numerical study for (a) Area averaged effectiveness (b) Standard deviation

Table 6.3: Performance metrics of the surrogate model

Objective function	MAE	MSE	RMS
$1/\eta_{ad.avg}$	-3.92×10^{-03}	7.86×10^{-05}	8.86×10^{-03}
σ_η	6.65×10^{-04}	8.02×10^{-06}	2.83×10^{-03}

An evolutionary-based genetic algorithm (GA) is used to identify the optimum configuration within the design space. This method has been successfully implemented in previous studies conducted by other investigators as for example, Moeini and Zargarabadi (2018); Johnson *et al.* (2013). The main objective of the GA is to identify the individual that minimizes the objective functions. The major steps involved in the algorithm are selection, crossover, and mutation. The surrogate model is initialized with a random population, and the population having a good fitness value is retained for crossover and mutation. The population obtained for every iteration is called a generation. The optimal solution is sought until the change in fitness values for each generation is minimal.

The non-dominated sorting genetic algorithm (NSGA-II) available in the Matlab toolbox is used to identify the optimal solution. Further details of NSGA–II are referred to optimization studies by Srikanth *et al.* (2015).

6.2.3 Pareto front

The NSGA-II identifies the global minimum of the objective functions within the design space. This algorithm provides a set of non-dominated solutions for each objective with equal importance. Figure 6.6 depicts the Pareto front providing the set of non-dominated solutions for the minimum reciprocal of area-averaged film cooling effectiveness ($1/\eta_{ad.avg}$) (i.e., maximum of $\eta_{ad.avg}$) and the minimum standard deviation (σ_η) of the area-averaged film cooling effectiveness ($\eta_{ad.avg}$).

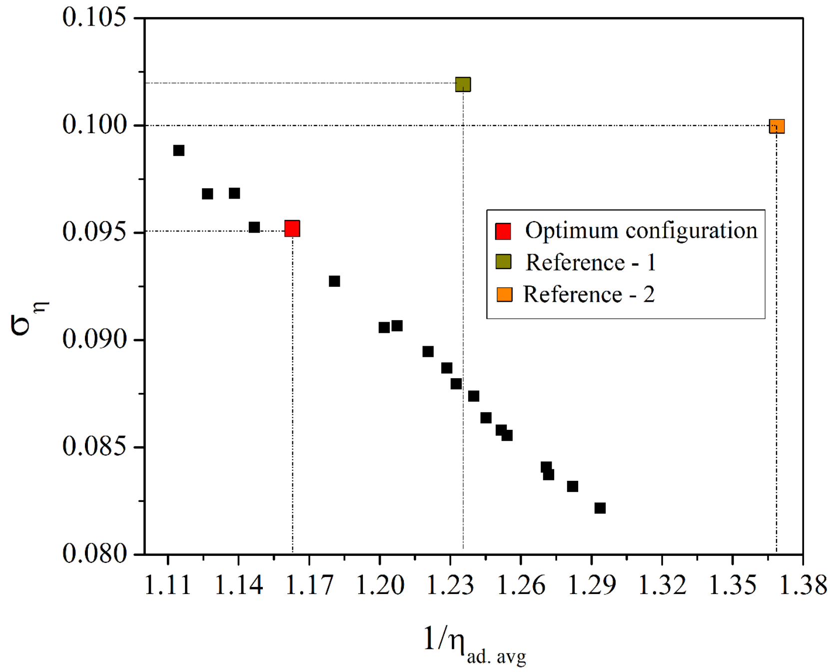

Figure 6.6: Pareto front

One of these optimal points is selected with a better trade-off using a method called Technique for Order of Preference (TOPSIS). This is based on the fundamental notion that the best solution is the one that is closest to the positive-ideal solution and farthest from the negative-ideal one. The solution having the smaller value of $1/\eta_{ad.avg}$ and σ_η, and also which is the farthest from the reference 1 and reference 2 configurations, is considered as optimum configuration and highlighted in the Pareto front. The selected optimal point is farthest from both reference configurations and also close to the positive ideal solution with some compromise on σ_η by giving a weightage of 0.7 and 0.3 to $1/\eta_{ad.avg}$ and σ_η, respectively.

The details of the reference and optimized configurations are given in Table 6.4. The slot jet diameter (d), slot jet pitch (p), and lip length (L) of the optimum configuration are close to the extreme points of the design space. The reason behind this is that a larger slot jet diameter, smaller slot jet pitch, and longer lip length provide a uniform coolant at the slot exit and smooth interaction of main and cold streams. As a result, the film cooling performance is enhanced for the optimum configuration. The fluid flow and heat transfer characteristics of film cooling with the optimum configuration are explained comprehensively in the ensuing sections.

Table 6.4: Dimensions of reference and optimum configurations

Parameter	unit	Reference 1	Reference 2	Optimum configuration
slot jet diameter (d)	mm	1.7	1.5	1.99
Slot jet pitch (p)	mm	4.19	4.19	4
Lip taper angle (α)	^{o}	5	0	4.8
Lip length (L)	mm	7.5	5.1	11.3

At a fixed BR of 1, the adiabatic film cooling performance for the optimum and reference configurations are compared and presented in Table 6.5. There is an 8 % enhancement in area-averaged film cooling effectiveness ($\eta_{ad.avg}$) and a 6.63 % reduction of its standard deviation (σ_η) compared to the reference-1 configuration. Similarly, there is a 19.8 % enhancement in $\eta_{ad.avg}$ and a 5.2 % reduction in σ_η compared to the reference-2 configuration.

Table 6.5: Comparison of adiabatic film cooling performance between reference and optimum configurations

Parameter	Optimum config.	Reference 1	Reference 2
$\eta_{ad.avg}$	0.875	0.81	0.73
σ_η	0.095	0.102	0.1
Enhancement of $\eta_{ad.avg}$ compared to reference	-	8%	19.8%
Reduction of σ_η compared to reference	-	6.63%	5.2%

As already discussed, in the optimization procedure, the slot configuration is optimized based on only the adiabatic film cooling effectiveness. This accounts only for the film cooling obtained by coolant emerging out of the slot and mixing characteristics of the mainstream and cold stream. However, in the actual engine, the liner is not only cooled by the coolant emerging out of the slot but also cooled by the secondary air in the annular space of the combustor (See Figure 6.1). Hence, a study is conducted to verify the overall performance of the optimum configuration under these conditions. The film cooling effectiveness obtained from this study is considered as overall film effectiveness (η_{ov}). The overall film cooling performance of the optimum slot is verified by conducting a conjugate numerical study. In this study, the liner is cooled by the coolant from the slot as well as the secondary air in the annular space of the combustor. To reduce the computational cost, the number of slot jet holes in the numerical domain is reduced to one, and a detailed description of the numerical domain is provided in Chapter 7. The inlet of the secondary flow is defined as a velocity boundary condition with a magnitude of 40 m/s and a back pressure is defined at the outlet of the secondary flow to split the mass flow rate of air for film cooling. The material of the liner is considered a Nickel-based superalloy. The thermophysical properties of the Nickel-based superalloy are taken from Li *et al.* (2023) and given in Table 6.6.

Table 6.6: Thermo-physical properties of liner

Property	Units	Liner
Density	Kg/m^3	8100
Specific heat (C_p)	J/kg K	550
Thermal conductivity	W/mK	16

Table 6.7: Comparison of the overall film cooling performance between reference and optimum configurations

Parameter	Optimum config.	Reference 1	Reference 2
$\eta_{ov.avg}$	0.935	0.894	0.84
$\sigma_{\eta_{ov}}$	3.73×10^{-2}	4.88×10^{-2}	4.13×10^{-2}
Enhancement of $\eta_{ov.ad.avg}$ compared to ref.	-	4.63%	11.34%
Reduction of σ_{η} compared to ref.	-	23.6%	9.73%

The numerical results show that the optimum configuration outperformed both the reference configurations and the enhancement of overall the film cooling performance is given in Table 6.7.

In order to quantify the film cooling performance, a new parameter called performance index (ψ) is introduced. This is defined as the ratio of $(\eta_{ad.avg}/\sigma_{\eta})_{optimum}$ and $(\eta_{ad.avg}/\sigma_{\eta})_{reference}$. If $\psi > 1$, then the optimum configuration outperforms the reference configuration and vice-versa. Figure 6.7 shows the adiabatic and overall performance index (ψ)of the optimum configuration compared to the reference configurations. From the figure, it is observed that the performance index (ψ) of the optimum configuration is found to be greater than 1 for both the adiabatic and overall performances. Hence, it is concluded that the optimum configuration is performing well and is also robust.

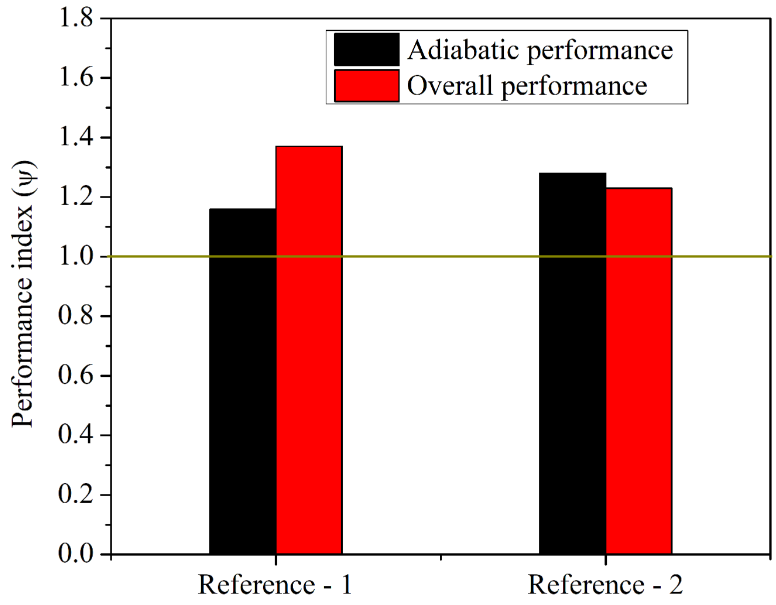

Figure 6.7: Performance index of optimum configuration under adiabatic and conjugate conditions with respect to reference configurations 1 and 2

6.2.4 Reduction of coolant mass flux

In the previous sections, the film cooling performance of the reference and optimum configurations were compared at a fixed blowing ratio (BR) of 1, and it was found that the optimum configuration performed better than the reference configurations. One can now estimate the amount of coolant mass flux that can be reduced with the optimum configuration compared to reference configurations when operated at $BR = 1$ for the same film cooling effectiveness and standard deviation. For the optimum configuration, Figure 6.8 shows the area-averaged adiabatic effectiveness ($\eta_{ad.avg}$) and its corresponding standard deviation σ_η against the blowing ratio ranging for $0.5 \leq BR \leq 1$.

In addition, the performance of the reference configurations when operated at a blowing ratio (BR) of 1 is highlighted in the figure. One can observe that at BR of 0.76, the optimum configuration has a similar effectiveness as the reference 1 configuration operated at $BR = 1$. Since the required blowing ratio is reduced to 0.76 for the optimum configuration, 24 % of coolant mass flux can be reduced to have the same $\eta_{ad.avg}$ as the reference 1 configuration.

Similarly, the optimum configuration has a similar standard deviation (σ_η) as the reference 1 at a blowing ratio (BR) of 0.96. Here, a coolant mass flux of 4 % can be reduced to have the exact σ_η as the reference 1 operated at BR = 1.

Hence, using the optimum slot configuration and the proper trade-off between $\eta_{ad.avg}$ and σ_η, the coolant mass flux ranging from 4 to 24 % could be saved with a similar performance obtained as reference 1 operated at BR = 1. Similarly, 4 to 40 % of coolant mass flux can be saved by comparing with the reference 2 slot configuration.

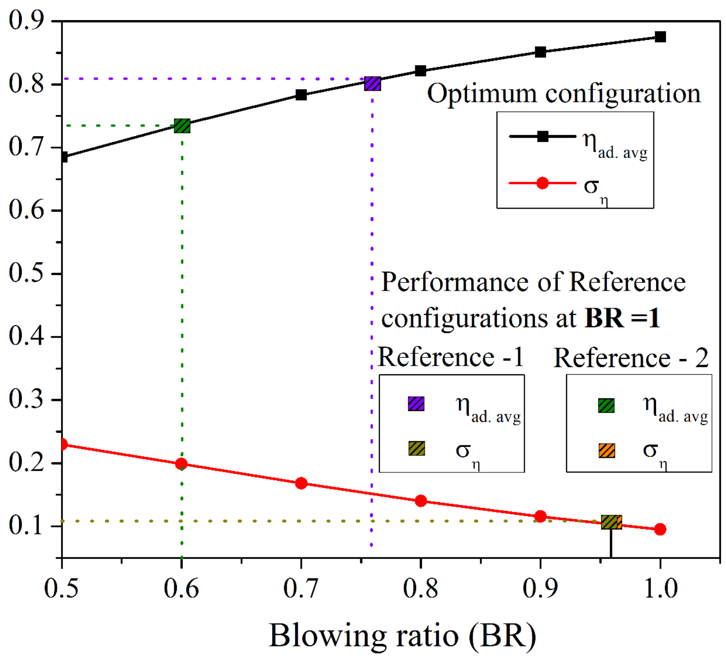

Figure 6.8: Comparison of film cooling performance between optimum and reference configurations to estimate the reduction of coolant mass flux

6.2.5 Comparison of reference and optimum configurations

In this section, the fluid flow and heat transfer characteristics of the optimum and baseline slot configurations are investigated to understand why the optimum configuration is performing well.

Figures 6.9 (a-c) show a comparison of velocity contours in the x-y plane between reference and optimized slot configurations. From the figure, it is evident that for a fixed coolant mass flux, the coolant jet velocity is significantly higher in references 1 and 2 (see Figures 6.9 a and b) compared to the optimum configuration. As a result, the coolant jet joins the mainstream and creates a strong mixing zone at the slot exit. In contrast, the large slot jet diameter and the long lip length of the optimum slot configuration allow the coolant to mix in the slot and emerge out of the slot uniformly.

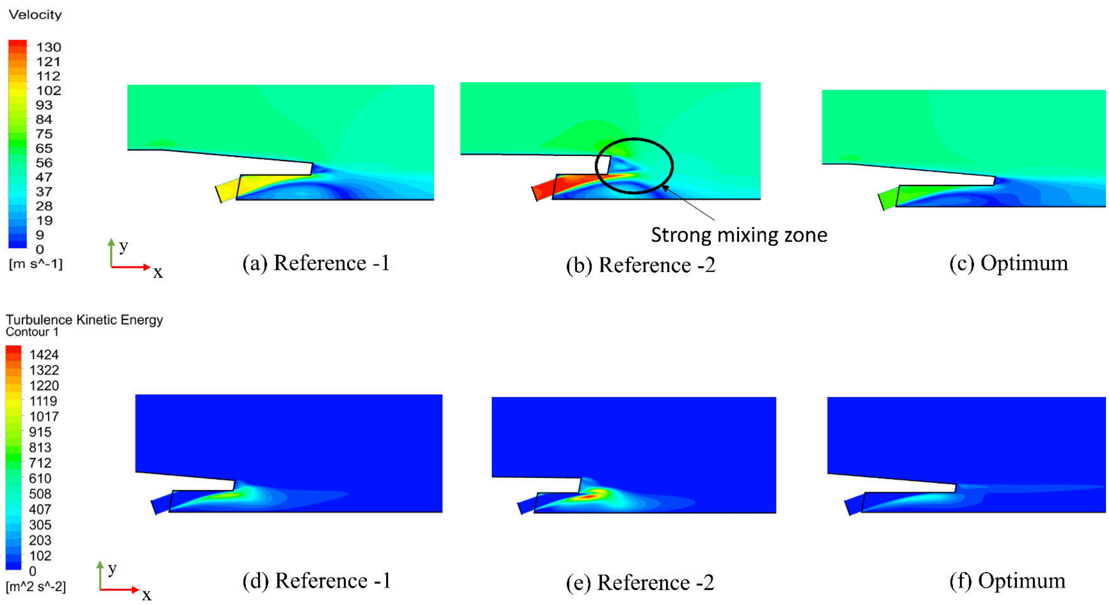

Figure 6.9: Comparison of reference and optimum configurations (a,b,c) Velocity contours (d,e,f) Turbulence Kinetic Energy contours

In addition, the contours of turbulence kinetic energy (TKE) are shown in Figure 6.9 (d-f). In Chapter 5, it was observed that the large slot jet diameter and long slot lip would reduce the TKE. In the present case, it is revealed that the optimum configuration has minimal TKE due to the more uniform flow. As a result, the mixing of main and cold streams is reduced, and film cooling effectiveness is enhanced. Figure 6.10 compares coolant streamlines and velocity contours at $X/S = 8$ between reference and optimum configurations. As mentioned above, it is evident from the streamlines that the coolant is more evenly distributed at the slot exit for the optimum configuration compared to baseline configurations. Another observation is that the size of the mixing zone is larger in the baseline cases because of the vigorous mixing of main and cold streams at the slot exit. The mixing zone is the region where the main and cold streams get entrained and mixed. This region can be identified by the velocity gradients in the flow (as illustrated in Figure 6.10). The larger mixing zone leads to more thermal penetration into the cold stream within the short span of streamwise distance. From the figure, it is apparent that the mixing zone is smaller for the optimum configuration because of the uniform coolant distribution and smooth interaction of main and cold streams at the slot exit.

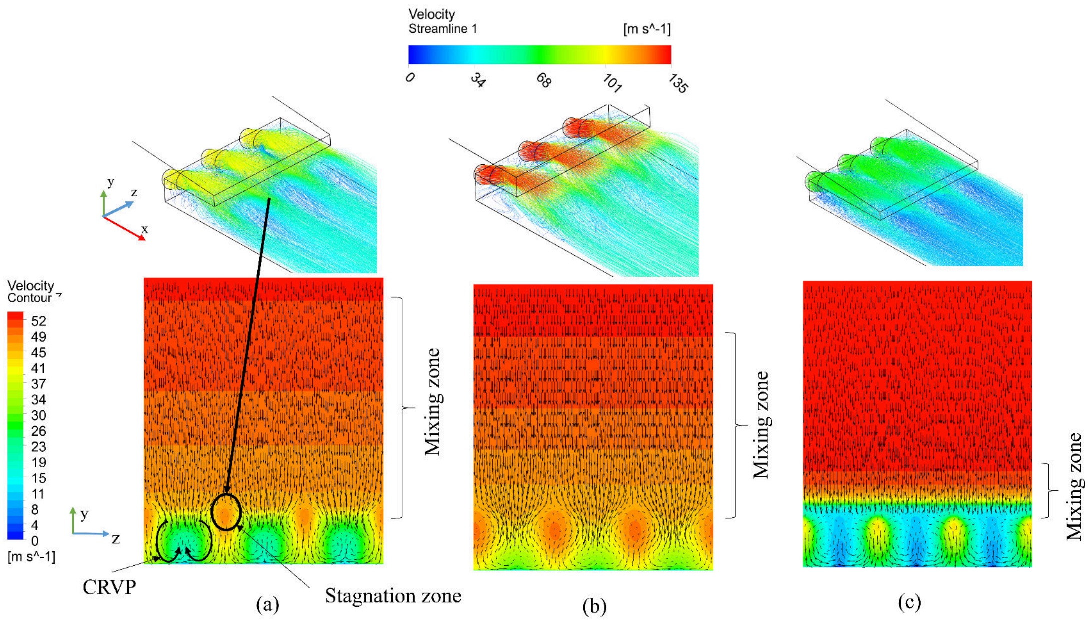

Figure 6.10: Comparison of streamlines and velocity contours between (a) reference 1 configuration (b) reference 2 configuration (c) optimum slot configuration

Furthermore, an additional noteworthy observation from the streamlines is that the coolant impinges the bottom surface of the lip, interacts laterally, and forms a stagnation zone (see Figure 6.10 a). In this zone, the fluid flow in the y and z directions is significantly reduced, and most of the flow occurs primarily in the x-direction (streamwise). As a result, mainstream entrainment is reduced in the stagnation zone. However, the mainstream is bled into the coldstream because of the counter-rotating vortices pairs (CRVP) between the stagnation zones. The local high velocities of the coolant at the slot exit in the baseline configurations lead to high CRVP vorticity, thereby resulting in mainstream entrainment compared to the optimum configuration. In order to get insights into the thermal penetration from the mainstream, the temperature contours on the y-z plane for reference 1 and optimal configurations at different streamwise locations (X/S) ranging from X/S = 6 to 30 are depicted in Figures 6.11 a and b, respectively.

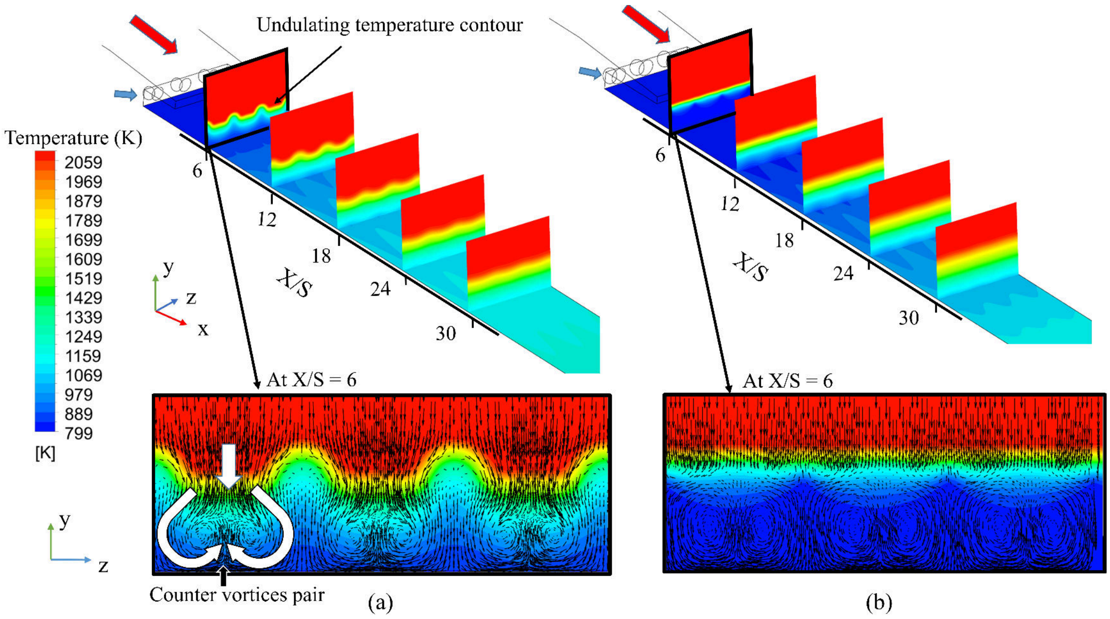

Figure 6.11: Temperature distribution on a y-z plane at various streamwise locations (X/S) (a) reference 1 configuration (b) optimum configuration

In the colored contours, it is evident that red represents the mainstream temperature (T_h = 2100 K), and blue represents the coolant temperature (T_c = 799 K). The main and the cold stream interaction at the slot exit (X/S = 0) results in a steep temperature gradient observed in the mixing zone. For the reference 1 configuration and at X/S = 6, it is apparent from Figure 6.11a that the temperature is significantly penetrating into the coldstream and is undulating. On the other hand, in the case of optimum configuration (see Figure 18b), the thermal penetration is reduced, and it also observed that the coolant temperature rise is insignificant up to X/S = 12. As discussed above, from the vector plots highlighted in Figure 6.11 a, it is evident that the non-uniform coolant velocities and high vorticity of CRVP in the baseline configuration bleed the mainstream into the core of the jet. As a result, the thermal penetration into the coolant increases within the short span of liner length. In contrast, evenly distributed coolant, lower vorticity, and smooth interaction of the main and cold streams for the optimum configuration reduce the mainstream entrainment and thermal penetration (Figure 6.11b). A larger slot jet diameter (d) and a smaller slot jet pitch (p) decrease the coolant non-uniformities and vorticity at the slot exit. A long lip (L) and optimum lip angle (α) enable a smooth interaction of main and cold streams. Hence, the optimum configuration cools a large span of the liner length efficiently compared to the baseline configurations.

Figure 6.12 shows a comparison of the temperature contours on the liner surface between the reference and the optimum configurations at BR = 1. It is apparent from the figure that the temperatures on the liner with the optimum slot are more uniform and lower than the reference configurations.

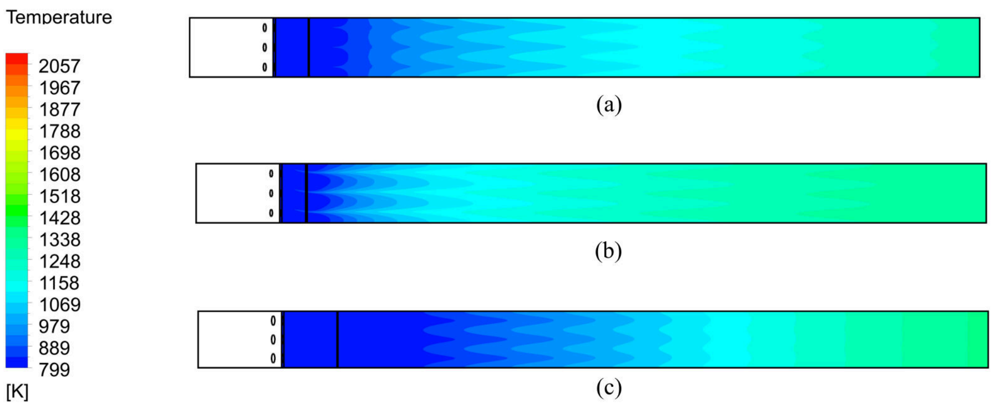

Figure 6.12: Comparison of temperature contours on the liner surface between reference and optimum slot configurations for blowing ratio of 1 (a) reference 1 (b) reference 2 (c) optimum slot configuration

6.2.6 Numerical study on the optimum slot performance at off-design flow conditions

In this section, the optimum configuration is tested numerically under actual engine conditions to check the robustness at off-design flow conditions. The blowing ratios considered vary from 0.5 to 5.

Figure 6.13 shows the variation of laterally averaged adiabatic effectiveness ($\eta_{ad.lat}$) along the dimensionless streamwise direction (X/S) for various blowing ratios (BR) ranges from 0.5 to 5. One can observe from the figure that the optimum configuration performs significantly better than both reference configurations.

In the case of the blowing ratio (BR) equal to 0.5, $\eta_{ad.lat}$ is very close to one in the near field ($X/S < 12$). However, the $\eta_{ad.lat}$ from $X/S = 12$ to 40 reduces significantly due to the low coolant mass flux.

Unlike BR of 0.5, the sudden reduction of effectiveness ($\eta_{ad.lat}$) is reduced in the streamwise direction for the case of $BR = 1$ because of the significant amount of coolant from the slot.

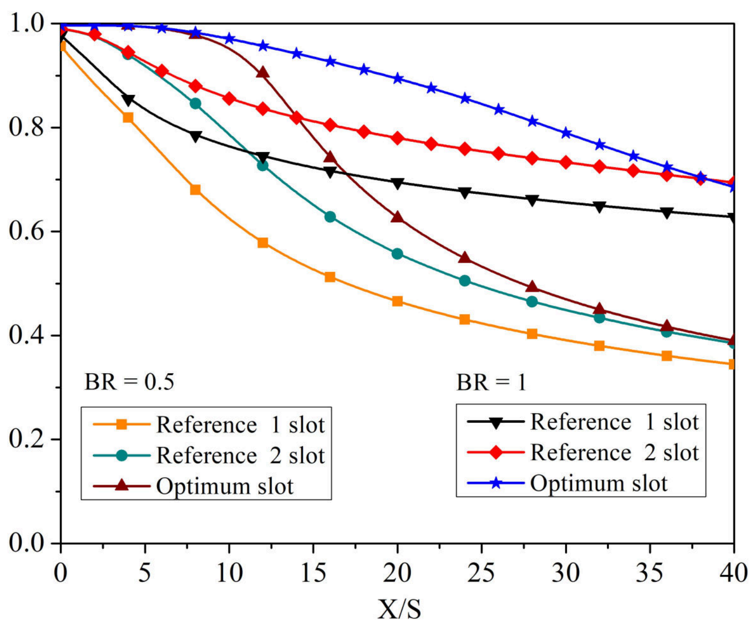

(a)

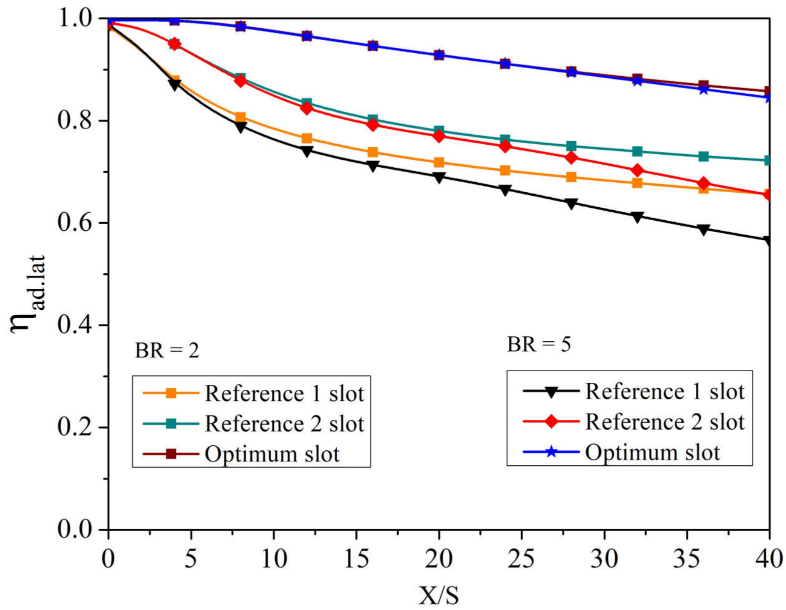

(b)

Figure 6.13: Comparison of centerline adiabatic effectiveness between reference and optimum configurations obtained numerically at various blowing ratios (a) BR = 0.5, 1 (b) BR = 2, 5

However, in the far field (X/S = 32 to 40), the effectiveness of the optimum configuration is reduced to the reference -1 configuration. This reduction is because of the lower momentum of the coolant due to the large diameter for the optimum configuration compared to the reference configurations.

Furthermore, with an increase in the blowing ratio from 2 to 5, the η_{ad} is enhanced throughout the streamwise distance compared to the reference configurations. Even in the far-field (X/S = 40), a maximum η_{ad} of 0.88 is observed for BR = 2.

Figure 6.14 shows the performance index (ψ) of the optimum configuration compared to reference 1 and reference 2 configurations. From the figure, it is evident that the ψ is more than 1 at all the blowing ratios. However, the enhancement is small at the blowing ratio of 0.5 due to low coolant flux. Compared with reference 1, the optimum configuration has a maximum ψ of 2.45 and a minimum ψ of 1.1. Similarly, a maximum ψ of 2.95 and a minimum ψ of 1.05 are observed compared to reference 2 across the range of blowing ratios considered in the study. Hence, this behavior indicates that the optimum configuration is robust and performs well at all the blowing ratios.

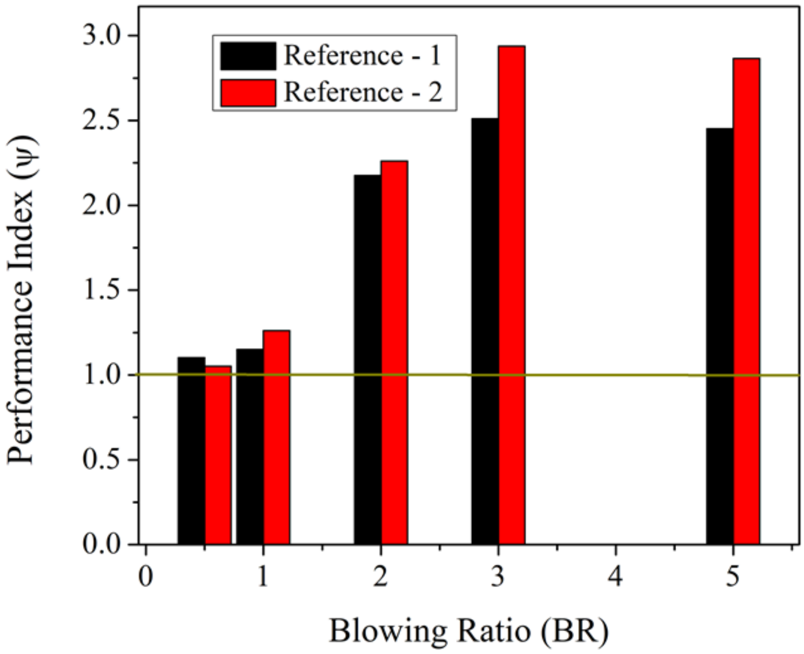

Figure 6.14: Performance index (ψ) of optimum configuration compared to reference -1 and reference -2 configurations

6.2.7 Experimental testing of optimum configuration

The optimum configuration is then tested experimentally under laboratory conditions (low temperature and pressure) to check the reliability of its performance. Figure 6.15 shows the variation of laterally averaged adiabatic effectiveness ($\eta_{ad.lat}$) of the optimum configuration along the streamwise distance and compared with reference -1 configuration for blowing ratios (BR) 1 and 2. In addition, a numerical study is also conducted alongside the experimental study to verify the reliability of the cooling performance of the optimum configuration.

From Figure 6.15, one can see that there is reasonably good agreement between the numerical and experimental studies for both reference 1 and optimum configurations. In addition, it is observed that the optimum slot configuration performs better than the reference 1 slot configuration.

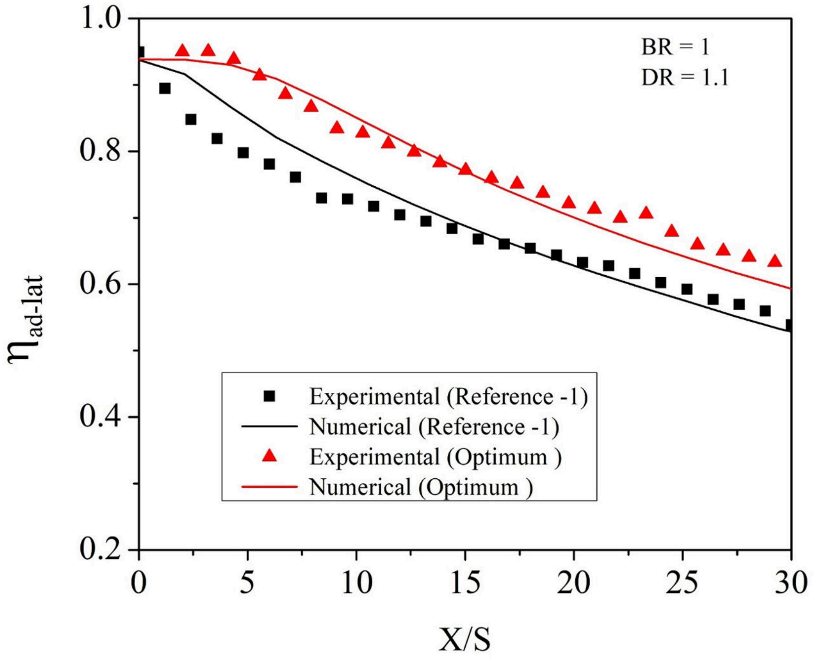

(a)

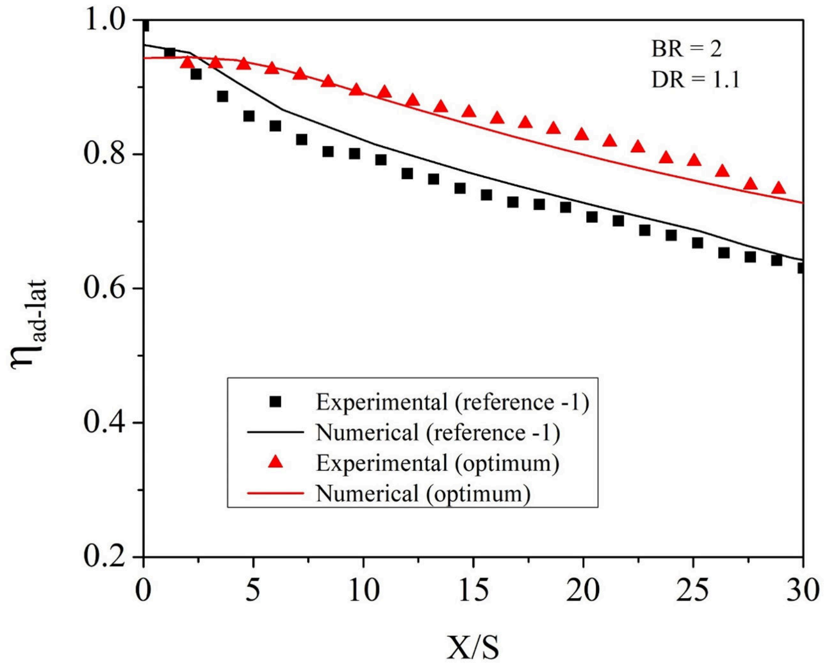

(b)

Figure 6.15: Comparison of laterally averaged adiabatic effectiveness between reference -1 and optimum configurations obtained experimentally and numerically at various blowing ratios (a) $BR = 1$ (b) $BR = 2$

For $BR = 1$, the adiabatic effectiveness distribution on the liner surface for a range of $-2.5 \leq Z/S \leq 2.5$ and X/S = 0 to 30 is shown in Figure 6.16. The film cooling effectiveness is significantly higher for the optimum configuration compared to the reference 1 configuration. Another interesting observation is that the undulating behavior of effectiveness is reduced, and its uniformity is enhanced in the case of optimum configuration. As described in the previous section, the uniform coolant at the slot exit and smooth interaction in the mixing zone contributed to the enhancement of $\eta_{ad.lat}$.

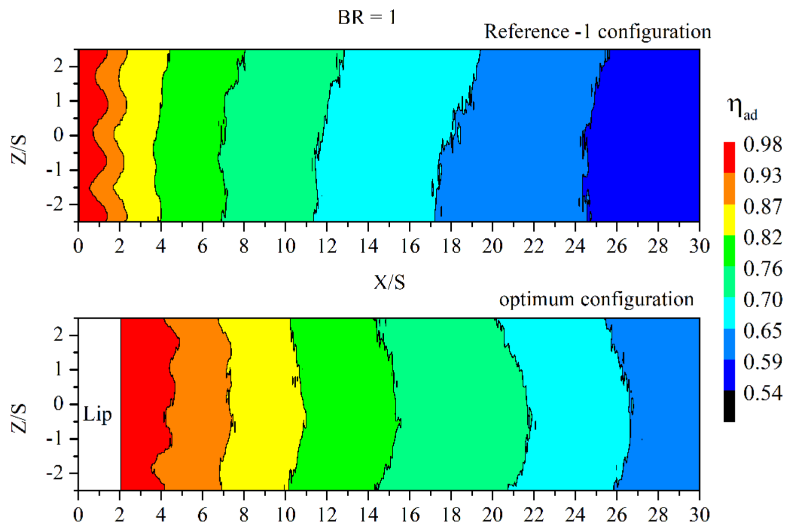

Figure 6.16: Comparison of experimentally measured adiabatic effectiveness contours between (a) reference -1 slot configuration (b) optimum slot configuration

6.3 INVESTIGATION ON THE SUBSEQUENT ROW OF LINERS

In an actual combustor, a series of concentric cooling ring liners (CR) are employed which are stacked horizontally, and the coolant is injected through the annular gaps (slots) between the liners. In the previous sections, the results of investigations conducted on a single liner were reported. In this section, the results of the numerical investigation conducted on two rows of subsequent liners are reported to understand the effect of film cooling of the first cooling ring on the film cooling effectiveness of the subsequent cooling ring. The study is conducted under actual engine conditions (high temperature and pressure). Furthermore, the number of cooling rings that can be reduced by replacing the reference 1 slot with the optimized slot is identified. In addition, the reduction of coolant mass flow rate for the entire combustor film cooling is reported. For this study, the reference 1 slot is considered due to its best performance out of existing slots in the combustor.

The schematic of the subsequent row of liners is shown in Figure 6.17. Two cooling rings (CR - 1 and CR - 2) with identical slots are stacked in a row with a dimensionless distance (G/S). The numerical domain consists of three slot jet holes with periodic boundary conditions.

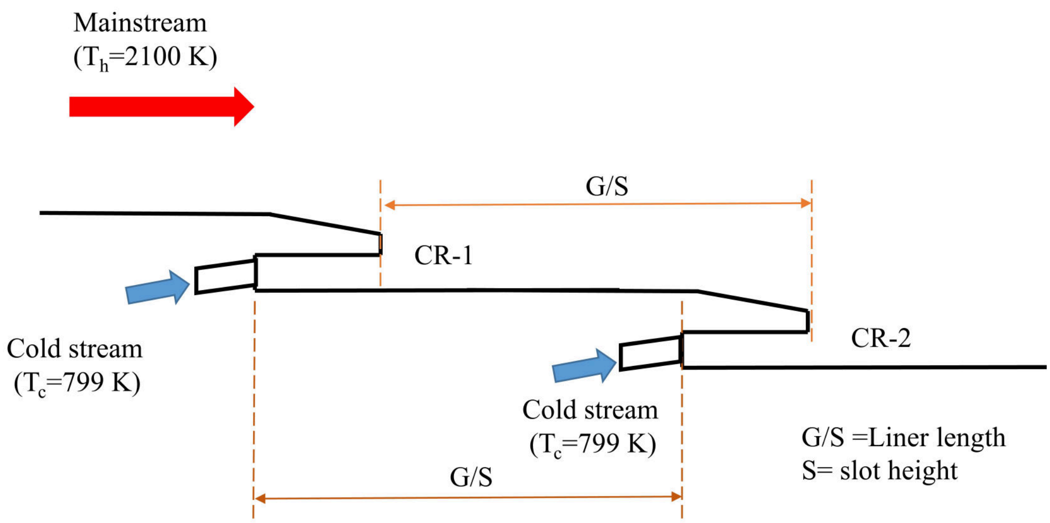

Figure 6.17: Schematic of the subsequent row of liners

For a better understanding, the numerical domain and meshing are compared for a single liner and two subsequent liners and shown in Figure 6.18. In the case of the subsequent row of liners, two cooling rings are arranged within the domain length of 89 S. Velocity boundary condition is imposed at the mainstream and coldstream inlets. Pressure outlet boundary condition with zero static pressure is defined at the domain outlet. All the walls are defined as zero heat flux adiabatic conditions.

The computational domain is discretized into a structured hexagonal grid using the commercially available software ANSYS ICEM CFD. Two grid-independent single-liner domains are merged for the numerical domain of the subsequent liners.

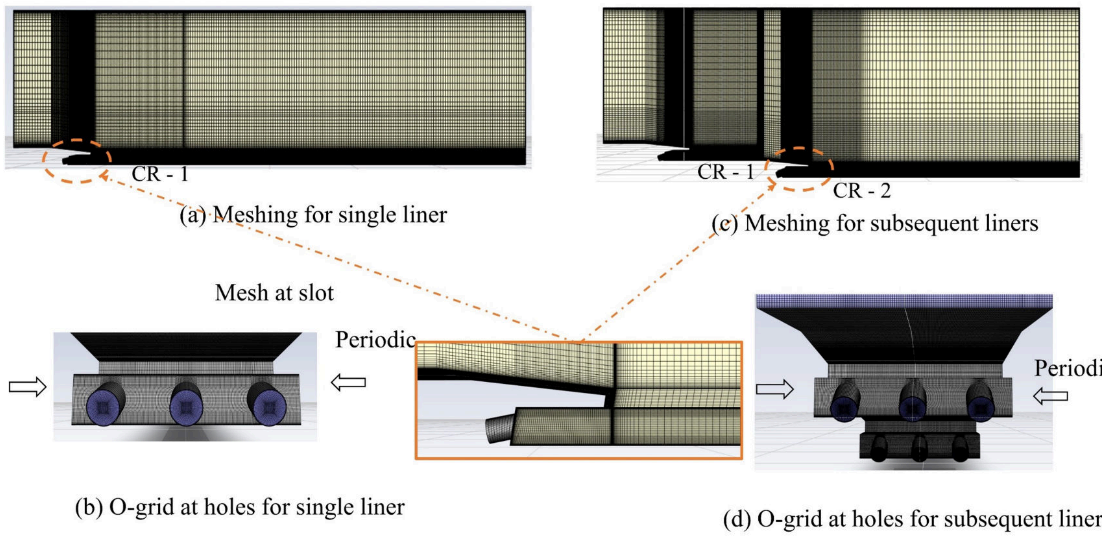

Figure 6.18: Comparison of the numerical domains for the single liner and two subsequent rows of liners

Figure 6.19 shows the adiabatic centerline effectiveness (η_{ad}) on the cooling rings CR 1 and CR 2 obtained with reference 1 slot configuration. The distance between the two liners G/S for the reference 1 configuration is 10.

In the case of CR 1, the η_{ad} is nearly one at the slot exit ($X/S = 0$) and decreases to 0.85 within the short span of $X/S = 10$. In contrast, the η_{ad} is significantly higher for CR 2. Even for far-field at location $X/S = 40$, where the liner length of CR 2 is 30, the η_{ad} is comparatively higher than for CR 1.

This behavior is well explained using the temperature contours on the mid-plane of the domain (see Figure 6.19). One can observe from the figure that the mainstream temperature for the CR 1 at the slot exit is nearly 2100 K. However, in the case of CR 2, the mainstream is diluted with the coolant used for film cooling of CR 1. As a result, the mainstream temperature is reduced, and the effectiveness is enhanced for CR 2.

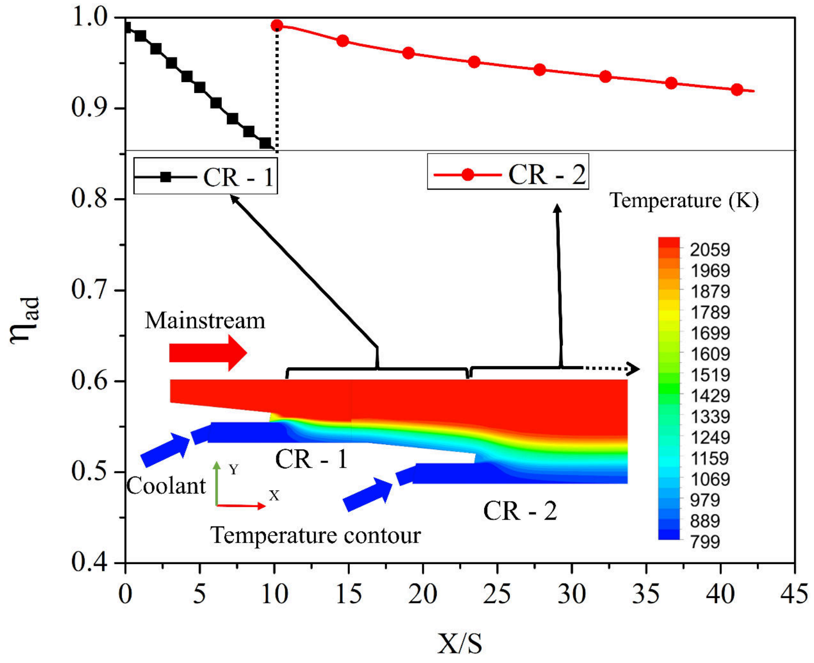

Figure 6.19: Centerline film cooling effectiveness at $BR = 1$ in the subsequent row of liners with reference 1 slot and temperature contours in the central x-y plane

Temperature contours on the two subsequent rows of liners (CR 1, CR 2) for BR of 1 are shown in Figure 6.20.

Figures 6.20a and 6.20b compare the reference 1 and optimum configurations at a fixed liner length (G/S) of 10. From the figure, it is apparent that the optimum configuration significantly cools the cooling ring(CR) 1 to low temperatures compared to the reference 1 configuration. Thus, the optimal configuration can protect the liner with $G/S > 10$ compared to the reference 1 slot.

In addition, for the optimum configuration, temperature contours for various liner lengths ranging from $G/S = 10$ to 28 are compared. This comparison helps one to determine the maximum liner length (G/S) for the optimum configuration that can be cooled equivalent to the reference -1 slot (see Figure 6.20b – e). From the figure, the temperature in the far field of CR 1 rises as G/S increases from 10 to 28. Hence, it is evident that the area-averaged effectiveness ($\eta_{ad.avg}$) of the liner obtained with the reference 1 configuration would be similar to the optimum configuration at some value in the range

$10 < G/S < 28$.

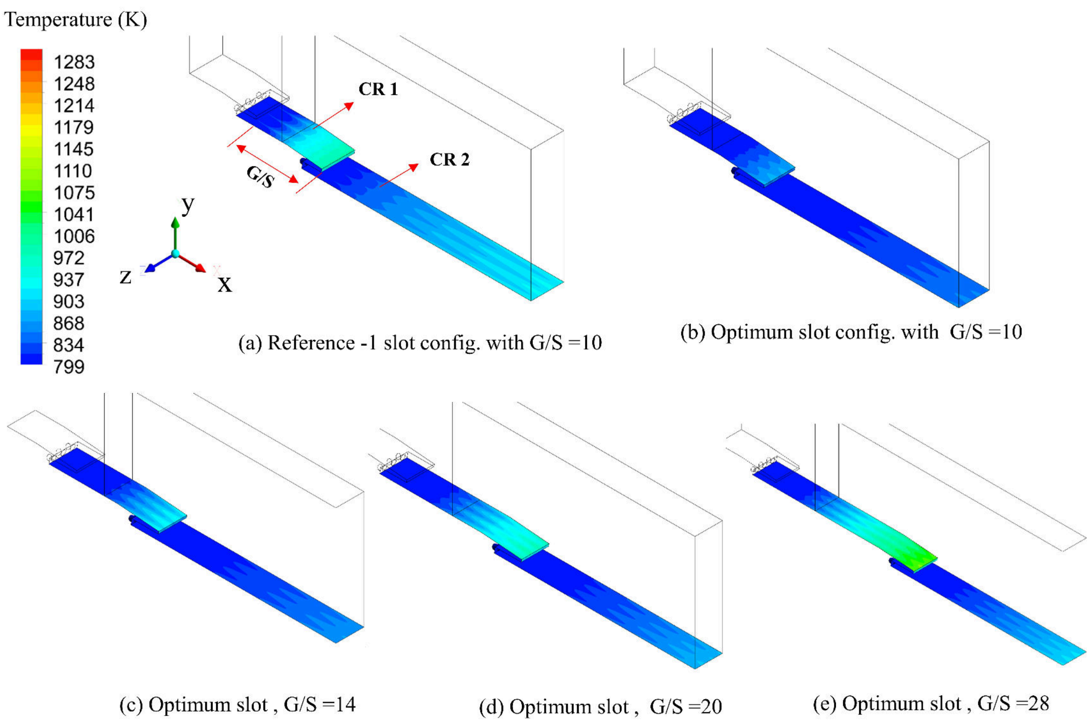

Figure 6.20: Comparison of temperature contours on the subsequent row of liners between reference -1 slot with G/S of 10 and optimum slot configurations with G/S ranging from 10 to 28

6.3.1 Reduction of coolant mass flux for the entire combustor

In this section, the reduction of coolant mass flux for film cooling of the entire combustor using the optimum slot configuration is reported. The total length of the baseline combustor (G/S_{total}) is 80, and it consists of 6 pairs of cooling rings (outer and inner) with varying liner lengths (G/S) ranging from 10 to 28. The smallest liner length (G/S) of 10, at which the maximum $\eta_{ad.avg}$ is achieved, is considered as the baseline liner length. An assumption is taken that the entire combustor has identical film cooling slots. For the optimum slot configuration, Figure 6.21 shows the variation of area-averaged effectiveness ($\eta_{ad.avg}$) and its corresponding standard deviation (σ_η) on the cooling ring (CR -1) against its length (G/S). In addition, the performance of the reference 1 slot configuration with G/S of 10 is also highlighted in the figure to compare it with the optimum configuration. For both blowing ratios 0.5 and 1, it is observed that the $\eta_{ad.avg}$ decreases, and the σ_η increases with an increase in liner length (G/S).

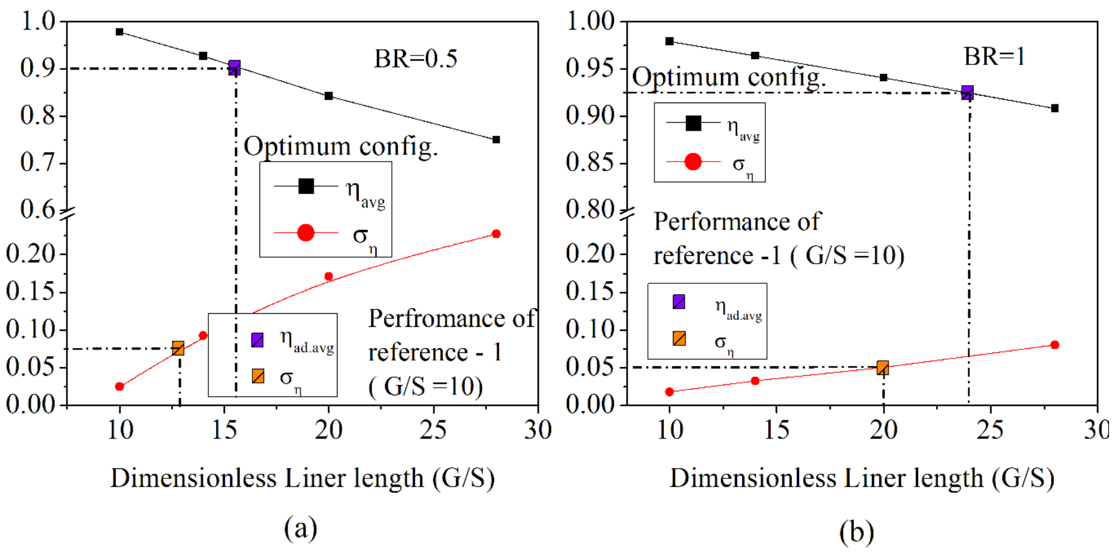

Figure 6.21: Performance of optimum configuration for various liner lengths (G/S) to identify the optimum liner length at (a) $BR = 0.5$ (b) $BR = 1$

From Figure 6.21a, for $BR = 0.5$, it is observed that the optimum slot configuration with a liner length (G/S_{opt}) of 15.5 has $\eta_{ad.avg}$ of 0.9, which is the same as the $\eta_{ad.avg}$ obtained for reference 1 slot configuration with G/S of 10. Here, the optimum configuration can cool an additional liner length (G/S) of 5.5. Similarly, the optimum slot configuration with G/S_{opt} of 12.8 has σ_η of 0.075, equivalent to σ_η of the reference 1 slot configuration with G/S of 10. Here, the optimum configuration can cool an additional liner length of G/S of 2.8. With some compromise on standard deviation, the optimum configuration can cool an additional liner length (G/S) of 5.5.

Similarly, in the case of $BR = 1$, optimum configuration with G/S_{opt} of 24 and 20 has similar $\eta_{ad.avg}$ and σ_η as the reference -1, respectively.

Considering the low blowing ratio (BR) of 0.5, the optimum configuration can cool an additional liner length (G/S) of 5.5 which results in a reduction of one pair of cooling rings. As a result, the total coolant mass flux required for the entire combustor is reduced by 16.66 %.

6.3.2 Experimental testing of subsequent liners

An experimental investigation is conducted under laboratory conditions (low temperature and pressure) to verify the reliability of the above numerical study on the subsequent rows of liners. The reference 1 slot with G/S of 10 and the optimum slot with G/S_{opt} of 15.5 are considered in the study. The experiments are conducted at blowing ratios (BR) of 0.5 and 1 and compared with the conjugate numerical study, which mimics the experimental setup. Figure 6.22 shows the schematic and photograph of the test plate for testing subsequent rows experimentally.

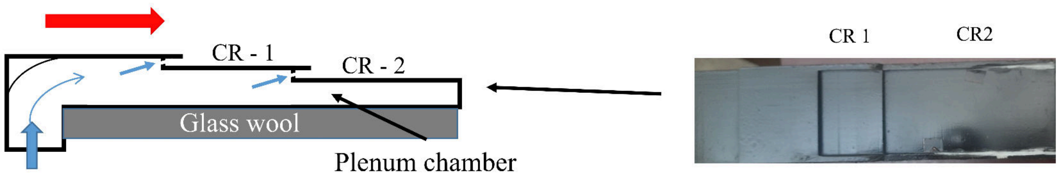

(a) Test section for subsequent cooling rings

(b) Picture of subsequent rings test plate used in the experiments

Figure 6.22: Test section for testing subsequent rows experimentally

The variation of overall effectiveness (η_{ov}) along the streamwise distance (X/S) for the reference 1 and optimum configurations is shown in Figures 6.23a and 6.23b, respectively. From the study, it is observed that there is reasonably good agreement between experimental results and numerical results.

Furthermore, for the reference 1 configuration at BR = 0.5, the overall effectiveness η_{ov} at X/S = 0 is close to 0.9, and it is reduced to 0.8 at X/S = 5. In addition, an interesting point is noted that the η_{ov} is enhanced between $5 \leq X/S \leq 10$. A similar trend of effectiveness is also observed for BR = 1. This behavior is attributed to the heat removal at the end of CR 1 (lip) by the coolant injected in the slot for CR 2. The schematic of heat removal from the lip is depicted in Figure 6.23 for better understanding.

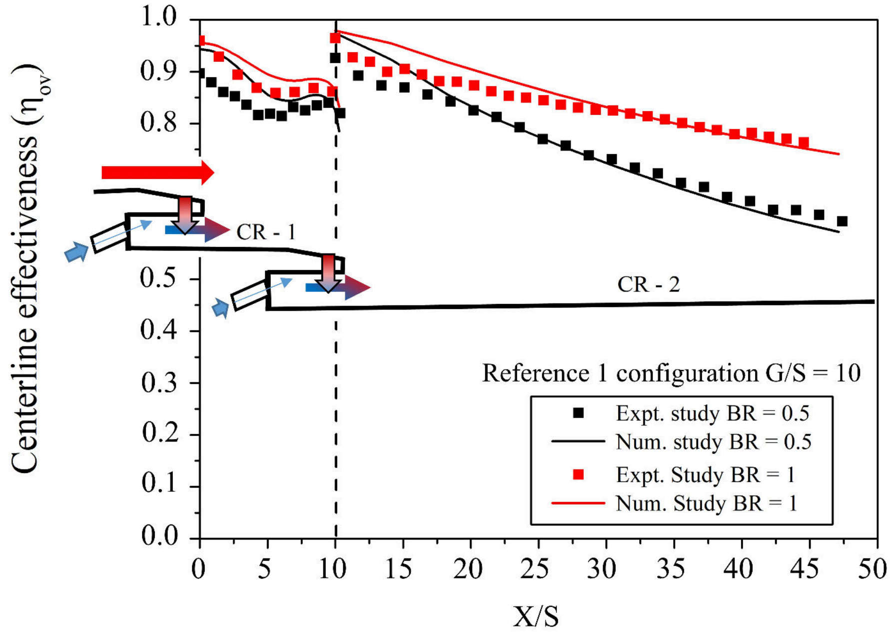

(a)

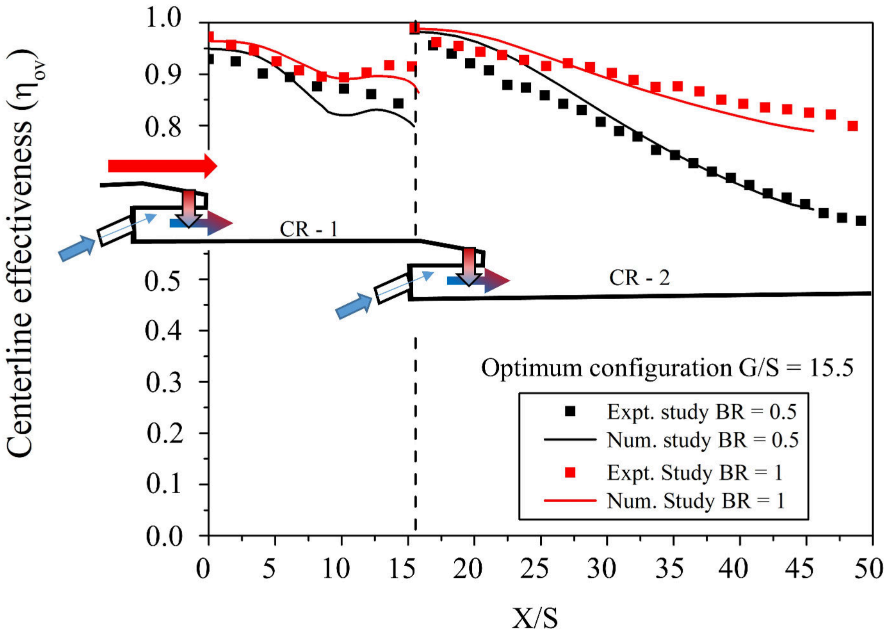

(b)

Figure 6.23: Comparison between experimentally and numerically obtained effectiveness for a subsequent row of liners at BR = 0.5 and 1 (a) Reference - 1 slot configuration with G/S = 10 (b) Optimum slot configuration with G/S_{opt} = 15.5

In the present domain, there are no cooling rings after CR 2. As a result, the η_{ad} deteriorates along the streamwise direction.

Another observation is that for $BR = 0.5$, the η_{ov} at the end of the CR 1 for reference 1 slot with G/S of 10 and optimum slot with G/S of 15.5 is approximately the same. In the case of $BR = 1$, the η_{ad} for the optimum slot is more than the reference 1 slot. This indicates that the optimum slot is able to cool better than the reference 1 considered.

6.4 PERFORMANCE ASSESSMENT OF A HYBRID FILM COOLING BY INCORPORATING THE OPTIMUM THREE-DIMENSIONAL SLOT

From the above study, an optimum three-dimensional slot configuration is identified that enhances film cooling performance. However, the fundamental drawback of slot cooling is that the film cooling effectiveness decays over the length of the liner due to the entrainment of coolant with the mainstream flow. This behavior is apparent in the baseline slot configurations as well as inevitable in the optimum three-dimensional slot. On the other hand, according to the studies carried out by Venkatesh *et al.* (2018), there was a deficiency in the coverage of coolant in the upstream location of the effusion configuration, resulting in reduced effectiveness. To address these limitations, researchers embarked on a combined approach known as hybrid slot cooling, which integrates both three-dimensional slot and effusion cooling techniques. A more extensive exploration of the fluid flow and heat transfer characteristics, along with the optimization of the hybrid slot cooling geometry, was carried out by Adapa (2022). In his investigations, the geometrical parameters of the effusion holes were optimized, keeping the three-dimensional slot as a reference 1. Furthermore, the baseline reference 1 slot was replaced with the optimized slot obtained in the previous section 6.2.3 to optimize the entire hybrid configuration. In view of obtaining the complete benefit of film cooling, the present study aims to show the enhancement of film cooling performance by substituting the baseline three-dimensional slot of the hybrid slot with the optimized slot obtained in section 6.2.3.

6.4.1 Geometric configuration

In this section, the details of the three-dimensional hybrid slot-effusion cooling configuration used in the present study are discussed. As previously mentioned, the hybrid configuration combines two distinct film cooling configurations: 1. Three-dimensional slot. 2. Effusion array. The three-dimensional slot configuration is derived from the reference 1 configuration that was extensively examined in previous chapters. Meanwhile, the effusion parameters are adapted from the research conducted by Hong Qu *et al.* (2017). A schematic of the hybrid configuration is shown in Fig. 6.24.

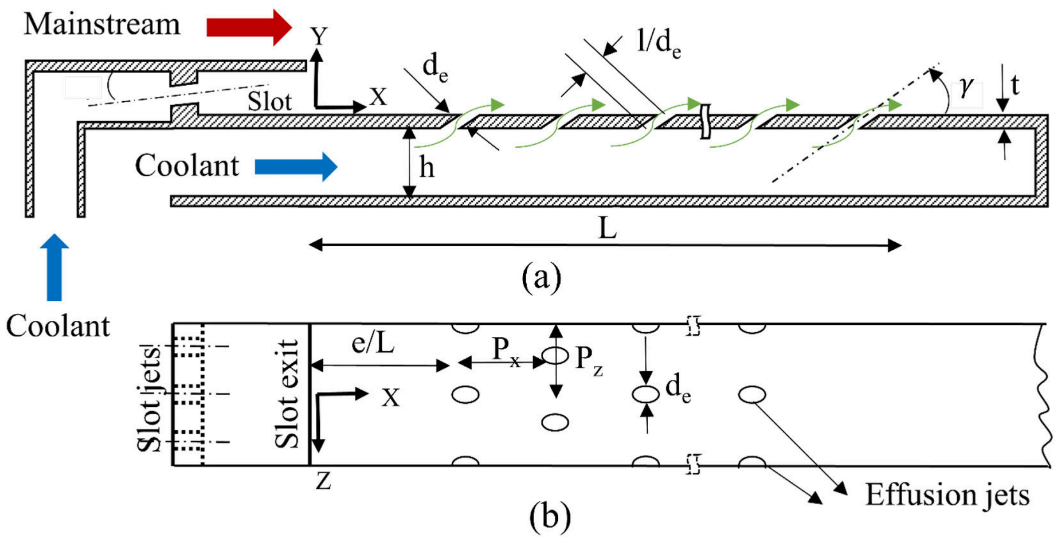

Figure 6.24: Schematic view of the three-dimensional hybrid slot-effusion cooling configuration used in the present study (Adapa (2022))

The details of the geometrical parameters of the hybrid configuration used by Adapa (2022) are provided in Table 6.8.

Table 6.8: Dimensions of the hybrid slot configuration

Parameter	Value
Refernce 1 three-dimensional slot	
Slot jet diameter, d_j (mm)	1.7
Pitch of slot jets, P_j/d_j	2.4
Lip taper angle, α^0	5
Lip length, L/d_j	4
Effusion array	
Diameter of effusion jets, d_e (mm)	1
Offset, e/L	0.25
Pitch of effusion jets, $P_x = P_z$ (mm)	6.28
No. of effusion rows	12
Forward inclination γ^0	30

A computer-aided design (CAD) model is developed using the values given in Table 6.8 and is shown in Fig. 6.25.

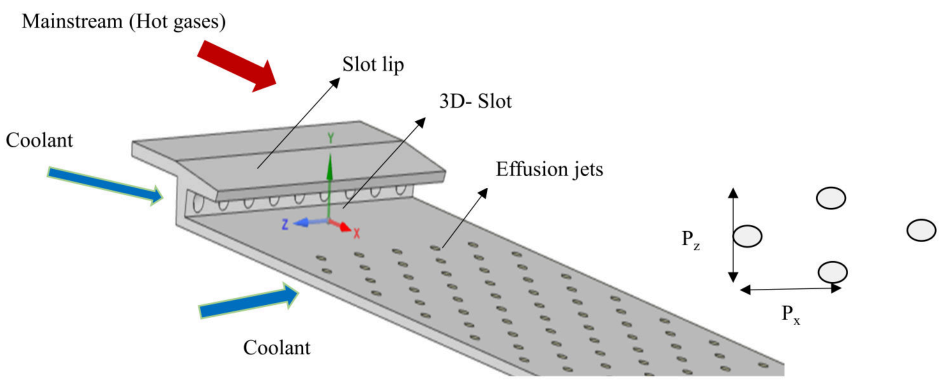

Figure 6.25: CAD model of the Hybrid configuration (Adapa (2022))

The method discussed in the previous section for optimizing the three-dimensional slot was implemented by Adapa (2022) for optimizing the effusion parameters of the hybrid slot configuration and then replaced the baseline reference 1 slot with the optimum slot. The geometrical variables of the final optimal three-dimensional hybrid slot-effusion configuration are given in Table 6.9.

Table 6.9: Geometrical variables of the final optimized three-dimensional hybrid slot-effusion configuration

Design variable	**Value**
Optimum Effusion array	
Effusion hole diameter (d_e in mm)	1.00
Offset, (e/L)	0.22
Aspect ratio (P_x/P_x)	1.13
Fraction of backward effusion rows	0.87
Optimum three-dimensional slot	
Slot jet diameter (d_j)	1.99
Pitch of slot jets (P_j/d_j)	2
Lip taper angle (α^0)	4.8^0
Lip length (L/d_j)	5

6.4.2 Dimensionless parameters

This section describes the dimensionless flow parameters involved in the present study. Here, the incorporation of new parameters necessitates a reiteration of the parameters discussed in the previous chapters.

Blowing Ratio

In film cooling, the blowing ratio is defined as the ratio of coolant mass flux to the mainstream mass flux. The blowing ratio represents the amount of coolant supplied with respect to the hot stream. From the definition, the blowing ratio can be written mathematically as follows:

$$BR = \frac{\rho_s U_s}{\rho_h U_h} \tag{6.4}$$

Coolant Mass Flow Ratio

In the present study, the cooling performance of the baseline three-dimensional slot and the hybrid configurations are compared at a fixed coolant mass flow rate. For a fixed value of slot blowing ratio (BR_{sl}) in the three-dimensional slot configuration, there exists a certain amount of coolant mass flow rate, $\dot{m}_c$. This $\dot{m}_c$ is split into two components as mass flux from the slot ($\dot{m}_{sl}$) and mass flux from the effusion array ($\dot{m}_{eff}$) for the hybrid slot-effusion configuration using the parameter coolant *Mass Flow Ratio*.

$$MFR = \frac{\dot{m}_{sl}}{\dot{m}_{eff}} \tag{6.5}$$

Therefore, the total coolant mass flow rate ($\dot{m}_c$) is the sum of two components, $\dot{m}_{sl}$ and $\dot{m}_{eff}$.

$$\dot{m}_c = \dot{m}_{sl} + \dot{m}_{eff} \tag{6.6}$$

6.4.3 Comparison of film cooling performance between baseline three-dimensional slot, optimum three-dimensional slot, and optimum hybrid slot

In this section, a grand comparison is elucidated at a fixed mass flow rate of coolant at BR=1 and MFR =5 for the case of hybrid cooling to understand the benefit of the final optimum hybrid slot over the optimum three-dimensional slot and the baseline three-dimensional slot (reference-1). Figure 6.26 shows the comparison of the lateral averaged adiabatic film cooling effectiveness along the streamwise distance (X/S) for baseline reference 1 slot, optimum slot, and optimum hybrid slot. From the figure, it is seen that the optimum hybrid configuration outperformed the baseline reference 1 and optimum slot configurations, and film cooling effectiveness is improved significantly in the far field where X/S = 40. However, up to X/S = 28, there is no significant relative improvement of the hybrid slot because of the superior performance of the optimum three-dimensional slot.

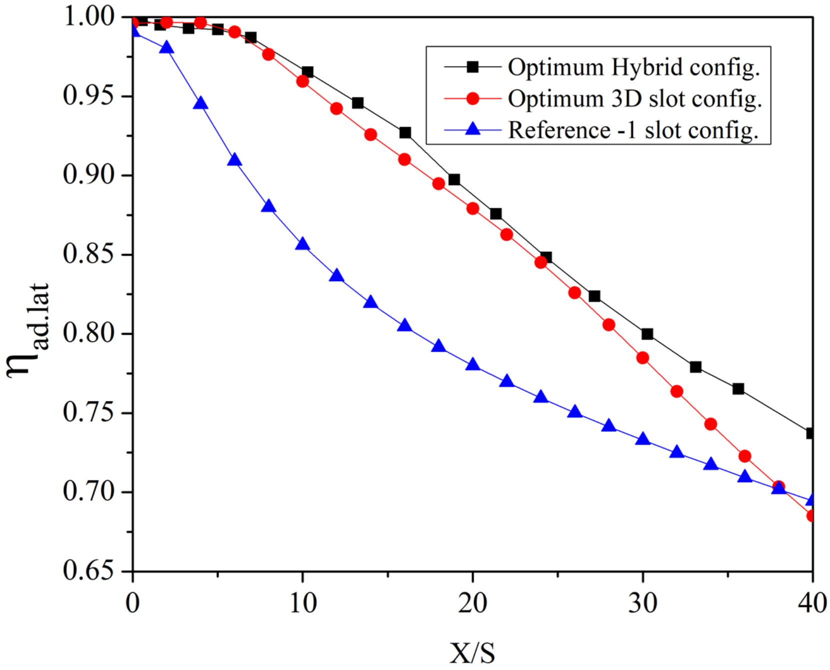

Figure 6.26: Comparison of the lateral averaged adiabatic film cooling effectiveness along X/S for baseline reference -1 three-dimensional slot, optimum three-dimensional slot, and Optimum hybrid slot

Figure 6.27 shows the temperature contours on the liner surface for the reference 1 slot, optimum slot, and optimum hybrid slot configurations. From the figure, it is apparent that the optimum three-dimensional slot outperformed the baseline three-dimensional slot. The temperature on the optimum three-dimensional slot is much lower compared to the baseline three-dimensional slot. However, in the far field, the effectiveness is deteriorated. This negative effect is reduced with the optimum hybrid cooling. The effusion array cooled the far field of the liner to low temperatures.

The area-averaged film cooling effectiveness ($\eta_{ad.avg}$) and its standard deviation (σ_η) for reference-1 slot, optimum slot, and hybrid slot are elucidated in Table 6.10.

Table 6.10: Comparison of adiabatic film cooling performance between reference 1, optimum three-dimensional-slot and optimum hybrid slot configurations

Parameter	Reference - 1 slot	Optimum slot	Optimum hybrid slot
$\eta_{ad.avg}$	0.81	0.875	0.89
σ_{η}	0.102	0.095	0.088

In addition, Figure 6.28 shows the enhancement of film cooling performance in percentages. It is clear from the figure that the optimum three-dimensional slot has 8% enhancement in $\eta_{ad.avg}$ and 6.5% reduction in σ_{η} compared to the baseline three-dimensional slot (reference 1). The optimum hybrid slot has approximately 9.5% enhancement in $\eta_{ad.avg}$ and 13.5% reduction in σ_{η} compared to the baseline three-dimensional slot (reference 1).

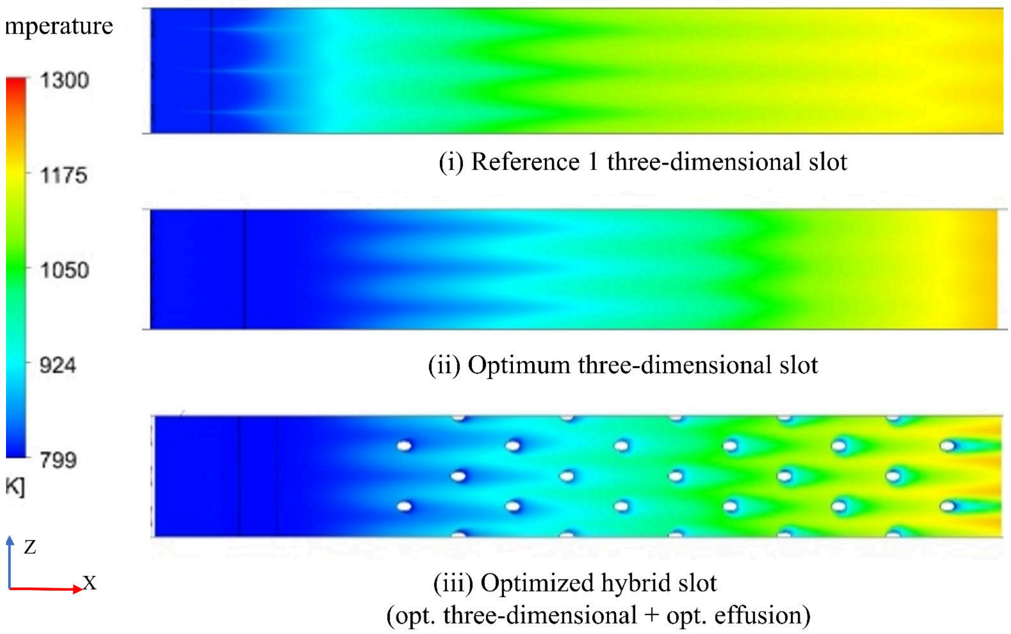

(a)

Figure 6.27: Comparison of temperature contours of the liners

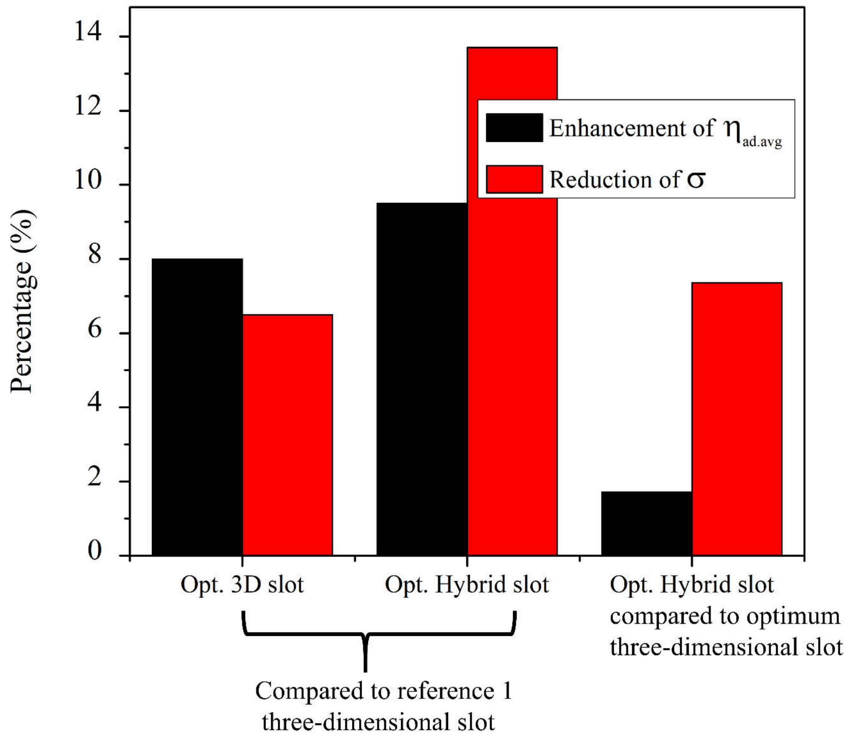

Figure 6.28: Comparison of enhancement of the film cooling performance with the hybrid slot cooling

The optimum hybrid configuration slightly enhances $\eta_{ad.avg}$ and there is a significant reduction in σ_η which is approximately 7.5% compared to the optimum three-dimensional slot. Hence, the optimum hybrid slot is the best configuration that enhances the film cooling effectiveness and reduces the non-uniformity of effectiveness on the liner surface.

6.5 CONCLUSIONS

In the chapter, the results of the combined experimental and numerical investigations to estimate the performance of a three-dimensional film cooling slot configuration were reported followed by an elucidation of the optimization procedure using an evolutionary-based genetic algorithm. For the purpose of optimization, a surrogate model was developed for which a Latin hypercube sampling technique was used to create the design space. Using the validated numerical model, each design point was numerically solved under actual engine conditions (high pressure and temperature). An optimum configuration is identified using the surrogate model and genetic algorithm. Additionally, a numerical study was conducted under actual engine conditions on two rows of subsequent liners to understand the influence of film cooling of the first liner on the effectiveness of the subsequent liner. The optimum length of each cooling ring and reduction of coolant mass flow rate is determined for the entire combustor. In addition, the baseline three-dimensional slot of an improvised hybrid slot configuration is replaced with the optimized three-dimensional slot configuration to get the complete benefit of film cooling. The salient conclusions from the present study are:

1. RANS simulations combined with the kriging technique as a surrogate model and using the evolutionary-based genetic algorithm for optimization, an optimum slot configuration is identified .

2. The optimum slot configuration outperformed both reference configurations. The average adiabatic effectiveness ($\eta_{ad.avg}$) is enhanced by 19.8 % with respect to reference 2 slot configuration. The optimum configuration performs well at all the off-design blowing ratios from 0.5 to 5. In addition, it outperformed reference configurations in terms of adiabatic as well as overall performances.

3. With a compromise on standard deviation, the optimum slot configuration requires a 4 to 24 % less coolant mass flux compared to the reference 1 slot and 4 to 40 % less coolant mass flux compared to reference 2, which are operated at a BR of 1.

4. By considering the least blowing ratio of 0.5, the optimum slot cools an additional length of 5.5 compared to reference 1 for the same coolant mass flux, which contributes to a reduction of one pair of cooling rings. As a result, the coolant mass flux is reduced by 16.66% for the entire combustor. The optimum slot configuration for film cooling of the entire combustor is recommended with five pairs of cooling rings, with each cooling ring of length G/S = 15.5.

5. The numerically obtained performance of the optimum and baseline configurations for the single liner and the subsequent row of liners shows a reasonably good agreement

with the in-house experimental results under laboratory conditions.

6. The final optimal hybrid configuration enhances the area averaged effectiveness ($\eta_{ad.avg}$) by 9.5% and reduces the standard deviation (σ_η) by 13.5% compared to the baseline reference-1 configuration. In addition, the optimum configuration slightly enhances the $\eta_{ad.avg}$ and significantly reduces σ_η by 7.5 % compared to the optimum three-dimensional slot. Hence, hybrid slot cooling enhances film cooling effectiveness and its uniformity on the liner surface and is considered to be the best film cooling configuration for longer liner lengths.

6.6 CLOSURE

In this chapter, a three-dimensional film cooling slot configuration was optimized. A combined experimental, numerical, and machine-learning approach was employed for the modeling, simulations, and optimization. In addition, the optimum liner length required by implementing the optimum slot configuration for the entire combustor was reported. Finally, the optimum slot configuration with the single liner and subsequent liner were experimentally tested and compared with the baseline configuration for robustness. In the next chapter, the effect of gas radiation and thermal barrier coating on the three-dimensional slot film cooling is presented.

[1]

[1]This chapter is drawn from the following publication: **Revulagadda A.P**, Ramapada Rana, Batchu Suresh, Balaji C, Pattamatta A, "A Multiobjective Optimization of 3D - Slot Jet Configuration for Enhancement of Film Cooling in an Annular Combustor Liner", International Journal of Heat and Mass Transfer, 218(2024), p.(124745), doi.org/10.1016/j.ijheatmasstransfer.2023.124745.

CHAPTER 7

EFFECTS OF GAS RADIATION AND THERMAL BARRIER COATING ON THE FILM COOLING PERFORMANCE

7.1 INTRODUCTION

In a gas turbine, the combustion temperatures would be approximately 2100K. At these high combustion temperatures, the radiative heat transfer which increases as the difference in the fourth power of temperature between the body and surroundings cannot be neglected. To simplify the complexity of the present problem, the study was conducted without considering the effect of combustion gas in the previous chapters. However, it would be prudent to investigate the effect of combustion gas radiation on film cooling performance and quantify the effect. In addition, it is required to test the robustness of the optimum three-dimensional film cooling slot discussed in Chapter 6.

In this chapter, the effect of combustion gas radiation on the film cooling performance of the three-dimensional wall jet slot (reference 1) is estimated numerically under actual engine conditions (high pressure and temperature). In addition, the effect of radiation on the flow characteristics and the effect of liner surface emissivity on film cooling performance is reported. Finally, the effect of thermal barrier coating (TBC) to reduce the thermal load on the liner surface is discussed.

The schematic and nomenclature of the three-dimensional wall jet slot considered in the study are shown in Figure 7.1. For this investigation, the reference -1 slot configuration is considered, and the details of the geometry are given in Table 7.1. A nickel-based superalloy is used as the liner material, and Yttria-stabilized Zirconia is used for the thermal barrier coating. The thermophysical properties of the liner are taken from Li *et al.* (2023) and those of TBC are Li and Yang (2019) and Vassen *et al.* (2004). The material properties considered for the liner and TBC are given in Table 7.2.

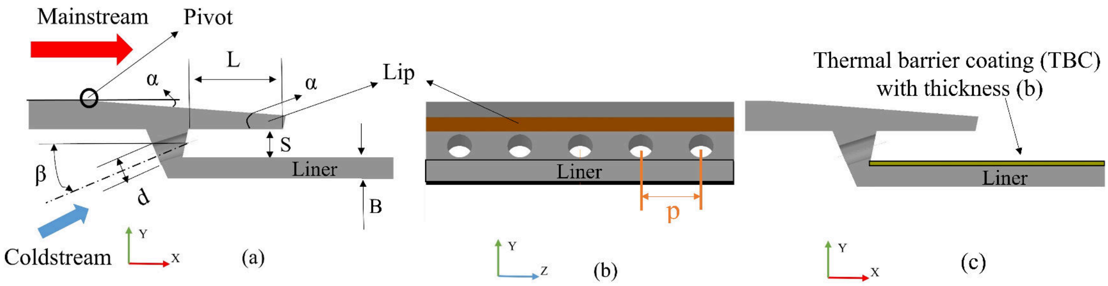

Figure 7.1: Schematic of the three-dimensional slot : S = slot height, d = Slot jet diameter, p = Slot jet pitch, L = lip length, α = Lip taper angle, β = Slot jet injection angle, B = Thickness of the liner, b = Thickness of the thermal barrier coating, (a) side view of the slot (b) front view of the slot (c) Liner with thermal barrier coating

Table 7.1: Dimensions of the practical three-dimensional slot considered in the present study

S (mm)	d (mm)	p/d	L/d	α	β	B (mm)	b (mm)
2.5	1.7	2.45	4.4	5^o	20^o	2.5	0.5

Table 7.2: Thermo-physical properties of the liner and thermal barrier coating

Property	Units	Liner	TBC
Density	Kg/m^3	8100	6000
Specific heat (C_p)	J/kg K	550	500
Thermal conductivity	W/mK	16	1
Surface emissivity	-	0.8	0.8

In the present study, conjugate heat transfer is considered in the domain. As a result, the film cooling effectiveness obtained with the temperature of the liner surface that is of interest and relevance is the overall film cooling effectiveness. This is also called liner film cooling effectiveness and is given as

$$\eta_{ov}(x,z) = \frac{T_h - T_w(x,z)}{T_h - T_c} \tag{7.1}$$

If the wall temperature is measured on the top surface of the TBC then the effectiveness obtained is considered as the thermal barrier coating effectiveness (τ). The expressions for the overall laterally averaged ($\eta_{ov.lat}$) and overall area-averaged effectiveness ($\eta_{ov.avg}$) of the measured overall effectiveness are given in Equation 7.2 and 7.3.

$$\eta_{ov.lat} = \frac{1}{L}\int_{-p/2}^{p/2} \eta_{ov}(z) d(Z/S) \tag{7.2}$$

$$\eta_{ov.avg} = \frac{1}{A}\int_{0}^{40}\int_{-p/2}^{p/2} \eta_{ov}(x,z) d(Z/S) d(X/S) \tag{7.3}$$

7.2 NUMERICAL METHODOLOGY

To reduce the complexity of the problem, radiative heat transfer was not modeled in the preceding chapters. However, to investigate the effect of combustion gas radiation, radiation is modeled along with conduction and convection in the present study. Here, the governing equations, particularly the conservation of energy equation, are modified as necessary. As a result, for the sake of completeness, the details of the numerical methodology and its validation are presented in the ensuing sub-section.

7.2.1 Governing equations

In the numerical study, a conjugate heat transfer method is considered for energy transport in which the fluid and solid regions are solved simultaneously. The fluid flow is three-dimensional, incompressible, turbulent, and steady. The species transport model is utilized to simulate the multicomponent combustion gases in the domain. Reynolds averaged equations (RANS) are used to model the turbulent fluid flow, and commercially available software ANSYS Fluent V20.1 is used to solve them with a proper turbulence closure. The governing equations used for continuity, momentum, and energy equations for the fluid and solid domains are given in Equations 7.4 - 7.7, respectively.

$$\frac{\partial \rho}{\partial t} + \nabla \cdot (\rho \vec{u}) = 0 \tag{7.4}$$

$$\frac{\partial \rho \overrightarrow{u}}{\partial t} + \nabla \cdot (\rho \overrightarrow{u} \overrightarrow{u}) = -\nabla p + \nabla \cdot (\bar{\bar{\tau}}) + \rho \overrightarrow{g} + \overrightarrow{F} \tag{7.5}$$

$$\frac{\partial (\rho E)}{\partial t} + \nabla \cdot (\overrightarrow{u}(\rho E + p)) = -\nabla \cdot \left(k\nabla T - \sum_j h_i \overrightarrow{J_i} + (\bar{\bar{\tau}} \cdot \overrightarrow{u}) \right) + S_h \tag{7.6}$$

$$\frac{\partial \rho h}{\partial t} = \nabla \cdot (k\nabla T) \tag{7.7}$$

Where ρ, $\overrightarrow{u}$, and k represent the density, velocity, and thermal conductivity of the fluid, respectively. In addition, p represents pressure, t represents time, $\bar{\bar{\tau}}$ represents the stress tensor, $\overrightarrow{F}$ represents volume force, E represents the internal energy, i represents the i-th component, h represents enthalpy, J represents the diffusion term and S_h represents the source term.

The non-reactive multicomponent species transport equation is given as Equation 7.8.

$$\frac{\partial \rho Y_i}{\partial t} + \nabla .(\rho \overrightarrow{u} Y_i) = \nabla \overrightarrow{J_i} \tag{7.8}$$

Where, Y_i represents the local mass fraction of each species, $\overrightarrow{J_i}$ is the diffusion flux of species i, and for turbulent flows, it is defined in Equation 7.9.

$$\overrightarrow{J_i} = -(\rho D_{i,m} - \frac{\mu_t}{Sc_t})\nabla Y_i - D_{T,i}\frac{\nabla T}{T} \tag{7.9}$$

Here, $D_{i,m}$ and $D_{T,i}$ represent the mass diffusion coefficient for species i in the mixture and the thermal diffusion coefficient, respectively. In addition, Sc_t represents the Schmidt number.

The numerical method incorporates the discrete ordinate method for modeling the radiation, wherein the radiative transfer equation is solved for a finite number of solid angles. Each solid angle is represented with a direction vector $\overrightarrow{s}$ in the cartesian system. The governing equation of the radiative transfer equation for a gray gas in the direction

$\overrightarrow{s}$ is given in Equation 7.11.

$$\frac{dI\left(\overrightarrow{r},\overrightarrow{s}\right)}{ds}+(a+\sigma_s)\,I\left(\overrightarrow{r},\overrightarrow{s}\right)=an^2\frac{\sigma T^4}{\pi}+\frac{\sigma_s}{4\pi}\int_0^{4\pi} I\left(\overrightarrow{r},\overrightarrow{s}'\right)\phi\left(\overrightarrow{s},\overrightarrow{s}'\right)d\Omega' \quad (7.10)$$

where a represents absorption coefficients, σ_S represents scattering coefficient, n represents refractive index, σ represents Stefan-Boltzmann constant, $\overrightarrow{s}'$ represents scattering direction vector, s represents path length, T represents temperature, ϕ represents the phase function and Ω' represents the solid angle.

The working fluid is air, and the thermo-physical properties of air are acquired from Lemmon *et al.* (2018). Pure air is considered as a coldstream, and combustion gases are considered as the mainstream. The combustion gas components in the mainstream are CO_2, CO, H_2O, H_2, N_2. The gases H_2O, CO_2, CO participate in the radiation heat exchange whereas H_2, N_2 are transparent to the radiation. Nitrogen gas is considered the most abundant and is set to be the last species. Scattering of the radiation is not considered in the study.

The properties of the nonreactive multicomponent gas mixture, such as thermal conductivity (k), specific heat (C_p), and dynamic viscosity (μ), are calculated based on mass-weighted-mixing law. The thermal conductivity of the mixture is calculated as $k = \sum_{i=0}^{I} Y_i k_i$. Similarly, the specific heat and viscosity of the mixture are calculated as $c_p = \sum_{i=0}^{I} Y_i c_{pi}$, $\mu = \sum_{i=0}^{I} Y_i \mu_i$, respectively. In addition, the weighted sum gray gases model (WSGGM) model is used to estimate the emissivity of the gas. The WSGGM is a compromise between a totally gray gas model and a completely non-gray model. The model is widely implemented in studies in which multi-component gases contain CO_2 and H_2O. In WSSGM, the total emissivity over the distance s can be represented as:

$$\varepsilon = \sum_{i=0}^{I} W_{\varepsilon,i}(T)(1 - e^{-a_i p s}) \quad (7.11)$$

Where, $W_{\varepsilon,i}$ is the emissivity weighting factor for the ith fictitious gray gas, $(1 - e^{-a_i p s})$ is the ith gray gas emissivity, a_i is the absorption coefficient of the ith gray gas, P is the partial pressure of all absorbing gases, and s is the path length. The values of $W_{\varepsilon,i}$ and a_i

are adopted from studies conducted by Smith *et al.* (1982) and Coppalle and Vervisch (1983). The liner wall is a nickel-based alloy and is considered opaque. The liner absorbs some portion of incident radiation flux, and the rest is reflected. A complete diffuse reflection is assumed in the present study. Since it is difficult to determine the emissivity of the combustor liner walls accurately, the emissivity of the liner is considered 0.8 following Wang *et al.* (2011).

The governing equations are discretized using second-order upwind interpolation, and pressure-velocity coupling is implemented using a coupled solver. For turbulence closure, a realizable k-epsilon turbulence model with improved wall treatment (RKE-ewt) is used. As described in the previous chapters, Enhanced Wall Treatment (ewt) is imposed in the near-wall, and the dimensionless first grid node distance from the wall (Y^+) is maintained at less than 5 to capture the viscous sub-layer. For accurate predictions, viscous dissipation effects are considered. The simulations are carried out until the scaled residuals for the energy equation reach 10^{-10} and for the remaining equations, 10^{-5}, respectively.

7.2.2 Computational domain

The computational domain of the film cooling and its meshing used in the present numerical study are shown in Figures 7.2a and 7.2b respectively.

To reduce the computational cost, the domain is made of a single slot jet hole with periodic boundary conditions on the side walls. The length (l) of the domain from the slot exit is 48 S. The height of the mainstream section and the coolant plenum are 16 S and 10 S, respectively. The velocity and mass flow boundary conditions are imposed at the mainstream and coldstream inlets, respectively. Pressure outlet boundary conditions are imposed on the mainstream and cold stream outlets. The exit of the coolant plenum is given with a certain back pressure, resulting in the mass split for film cooling from the secondary annular stream.

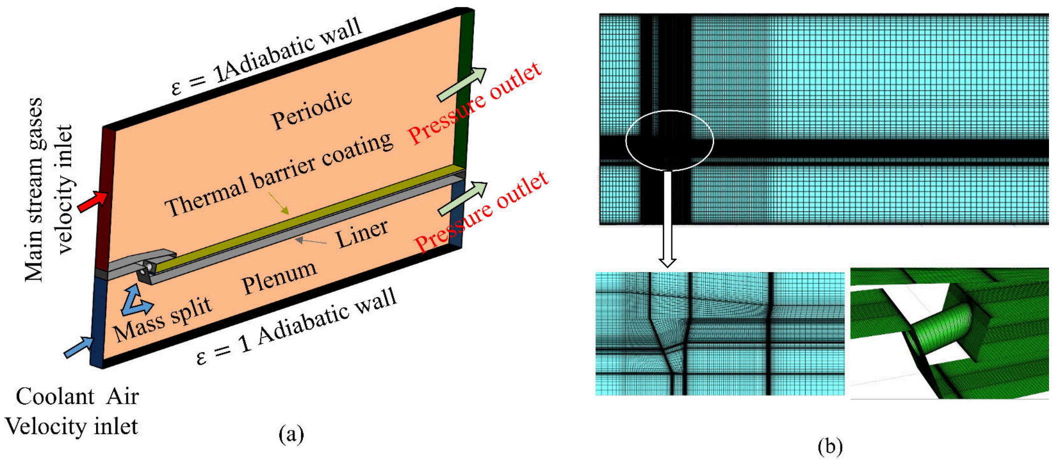

Figure 7.2: (a) Computational domain with boundary conditions (b) Details of the Meshing

In the present study, the blowing ratio is fixed at 0.5. The top and bottom walls are given zero heat flux adiabatic condition. Following Wang *et al.* (2011), the emissivity of the top and bottom walls of the domain is set to 1, and external radiation is also accounted for by setting an emissivity of 0.5 to all the inlet and outlet faces. The liner surface emissivity (ε_L) is fixed at 0.8. The study is conducted at actual engine conditions which was presented in the previous chapters. The inlet temperature of the coldstream is 799 K, and the mainstream is 2100K. An operating pressure of $2{\times}10^5$ Pa which exists in actual engine conditions, is considered. Further details of the actual engine operating conditions considered in the present study are given in Table 7.3.

Table 7.3: Actual engine operating conditions

DR	BR	u_h (m/s)	u_c (m/s) (plenum inlet)	Operating pressure pa	P_h (pa) (Gauge) (mainstream outlet)	P_c (pa) (Gauge) (coldstream outlet)
2.6	0.5	59	40	200000	0	3000

A structured hexagonal grid is generated in the computational domain using the commercially available software ANSYS ICEM CFD (see Figure 7.2b). To improve the quality of the orthogonal mesh, the O-grid is generated in the slot jet holes. A grid independence study is conducted to identify an optimum mesh to estimate accurate results with less computational cost. Grid resolutions between 1.8 to 5 million nodes are considered for the study. From this study, it was observed that the η_{ov} remains constant beyond the grid a with 2.8 million nodes. Hence, the computational domain with a total of 2.8 million nodes is considered to be optimum and used in the subsequent simulations.

7.2.3 Validation of the numerical study

The numerical study is validated with in-house transient experiments for the case without gas radiation and also with the literature for the case with gas radiation. For the case without gas radiation, Figure 7.3 shows a comparison of adiabatic effectiveness between in-house experiments conducted under laboratory conditions and the numerical study conducted under actual engine conditions(without gas radiation). In both cases, the blowing ratio (BR) and the density ratio (DR) are fixed at 1 and 2.6, respectively.

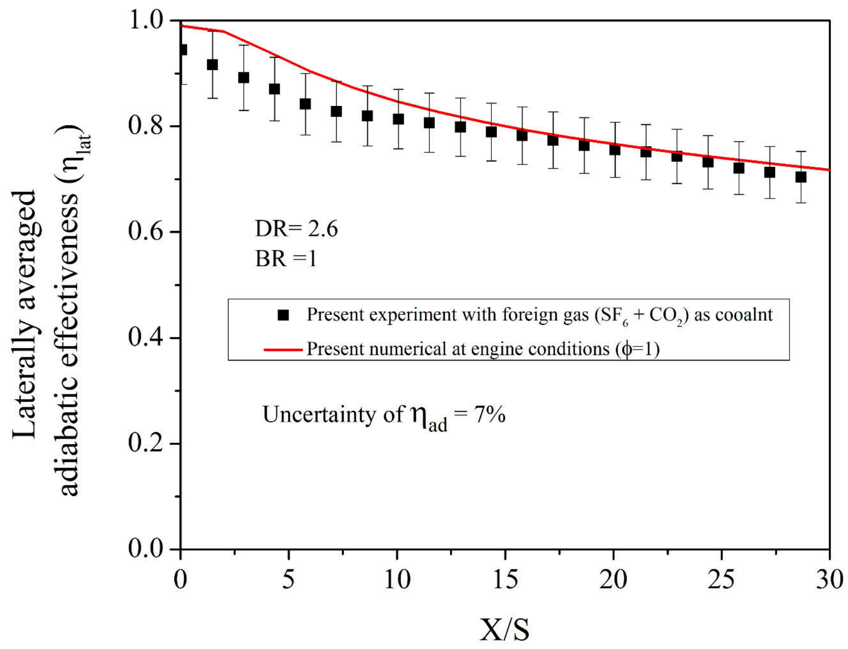

Figure 7.3: Validation of the present numerical study with in-house experiments (without gas radiation) under laboratory conditions

Under laboratory conditions, the mainstream (air) inlet temperature is 60^oC, the cold stream temperature is 30^oC, and the operating pressure is 101325 Pa. A high-density foreign gas made of SF_6 and CO_2 is used as coldstream to mimic the density ratio of 2.6 that exists in the actual engine conditions.
In the simulations, the multispecies composition of stoichiometric combustion is considered mainstream, and the air is used as a cold stream. The inlet temperatures of main and cold streams are 2100K and 799K, respectively, and the operating temperature is $2 \times 10^5 Pa$. Combustion gas radiaiton is neglected. From the figure, it is observed that the adiabatic film cooling effectiveness obtained with the numerical study under actual engine conditions is in reasonably good agreement with the experimental data obtained under laboratory conditions conducted at a density ratio of 2.6.

In addition, the present numerical study is also validated by considering the gas radiation effects with the experimental and numerical study conducted on the turbine blade film cooling by Wang *et al.* (2011). For this purpose, the dimensions of the computational domain and operating conditions are mimicked with Wang *et al.* (2011). Following Li *et al.* (2023), the domain is made of a single hole to reduce the computational cost, and a periodic boundary condition is imposed on the side faces. The mainstream velocity is 15.5 m/s, and the coldstream inlet velocity at the plenum is 10 m/s. Pressure outlet boundary condition is given to both mainstream and coldstream outlet faces. The combustion gases of the mainstream are CO_2, H_2O, O_2, N_2 and their mass fractions are 6.97, 7.92, 13.73% and the balance is N_2 respectively. Pure air is considered a cold stream. The species transport model is utilized to simulate the multicomponent combustion gases in the mainstream. The emissivity of the liner surface is set to 0.8, and for all the inlet and outlet faces the emissivity is set to 0.5. Figure 7.4 shows a comparison of the centerline temperature for the top and bottom faces of the liner between the present numerical study and the experimental and numerical study of Wang *et al.* (2011).

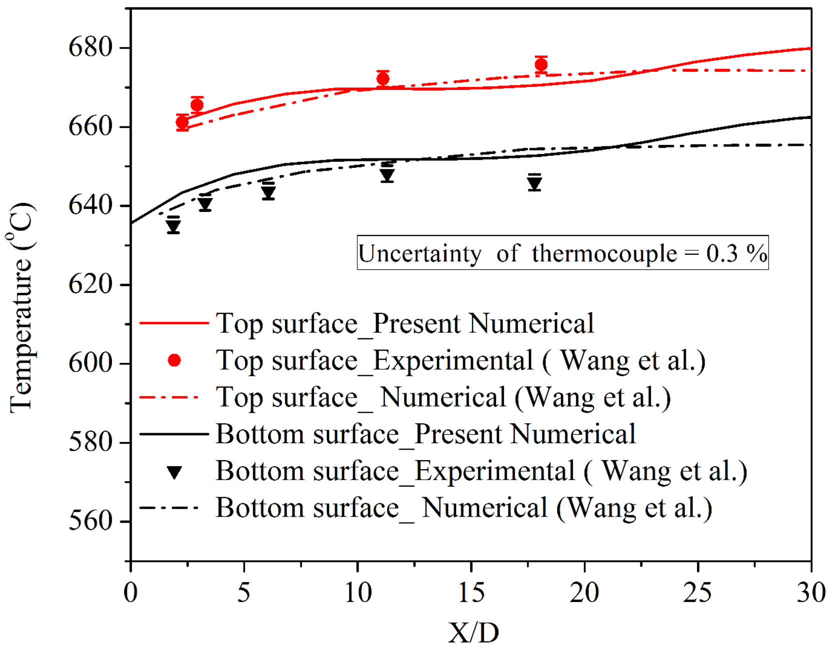

Figure 7.4: Validation of the present numerical study with Experimental study by Wang *et al.* (2011) (With gas radiation)

One can observe from the figure that there is reasonably good agreement between the present numerical data and the experiment and numerical data from the literature. From both validations, it is evident that the realizable k-ϵ turbulence model with enhanced wall treatment (RKE-ewt) is reasonably accurate, and the simulation settings used for considering the gas radiation are reliable and this model used in the subsequent simulations.

7.3 EFFECTS OF GAS RADIATION AND THERMAL BARRIER COATING ON THE FILM COOLING PERFORMANCE

In this section, the results of the numerical investigation to study the effect of combustion gas radiation on the performance of a three-dimensional slot film cooling are discussed. The influence of the combustion gases obtained for various equivalence ratios (ϕ), the emissivity of the liner surface, and thermal barrier coating on the film cooling performance are investigated. Finally, the robustness of the optimum three-dimensional slot configuration obtained in Chapter 6 is verified.

7.3.1 Effect of combustion gas radiation on the film cooling effectiveness

According to Mark and Selwyn (2016), the air available for the combustion of the fuel varies within the combustor zones as well as the flight conditions such as take-off and cruising. The availability of air-to-fuel combustion can be characterized by a term called equivalence ratio (ϕ) which is defined as the ratio of the mass flow rate of the actual fuel to air to the stoichiometric fuel to air.

The radiation from these combustion gases at high combustion temperatures and the effect of equivalence ratios cannot be neglected and also observed by Wang *et al.* (2011) in his study on film cooling of turbine blades.

As a result, the effect of the equivalence ratio (ϕ) on the film cooling effectiveness is investigated with and without gas radiation. The radiation effects are simulated by setting the surface emissivity (ε_L) of the liner surface to 0.8 on both the cold and hot stream sides. A kerosine-based aviation fuel JP-8 is used to estimate the equivalence ratio (ϕ) in the study.

According to Starik (2010), the approximate chemical formula of the JP-8 is $C_{11}H_{21}$. The effect of combustion gases in the mainstream obtained for lean, stoichiometric, and rich mixtures on the film cooling effectiveness is investigated. The equivalence ratio (ϕ) of lean, stoichiometric, and rich combustion are 0.6, 1, and 1.5, respectively. The mole fractions of combustion gases for these equivalence ratios are estimated using the procedure described by Turns (2012) and are shown in Table 7.4.

Table 7.4: Mole fractions of the combustion products for JP - 8 ($C_{11}H_{21}$) for various types of combustion

Combustion products	Lean mixture	Stoichiometric mixture	Rich mixture
Equivalence ratio	ϕ = 0.6	ϕ = 1	ϕ = 1.5
Fuel- Air ratio	0.00411	0.0685	0.1028
CO_2	0.08199	0.13317	0.05545
CO	0	0	0.12131
H_2O	0.07826	0.12712	0.11595
H_2	0	0	0.05277
O_2	0.08075	0	0
N_2	0.75901	0.73971	0.65453

Figure 7.5(a) shows the effect of equivalence ratio (ϕ) and gas radiation on the film cooling effectiveness along the streamwise direction (X/S) of the combustor liner for a blowing ratio of 0.5. The overall film cooling effectiveness ($\eta_{ov.lat}$) is seen to be unaffected by the change in equivalence ratio for both gas radiation and without gas radiation. The reason behind this is that the density ratio and blowing ratio remain approximately constant for all the mixtures. Even when gas radiation is considered, the effectiveness is not significantly affected. According to Maurente and Alves (2019), the major contribution of radiative heat transfer in a combustor is H_2O. However, in the present case, the change in mole fraction of the H_2O for the considered equivalence ratios is minimal. As a result, the influence of the equivalence ratio (ϕ) on ($\eta_{ov.lat}$) is not significant under gas radiation as well.

Another interesting point to be noted here is that the film cooling effectiveness is reduced drastically when the radiation effects are considered. The area-averaged film cooling effectiveness deteriorated by 23.5% due to the gas radiation. Hence, radiation effects cannot be neglected in the estimation of the film cooling performance accurately and for a fail-safe design.

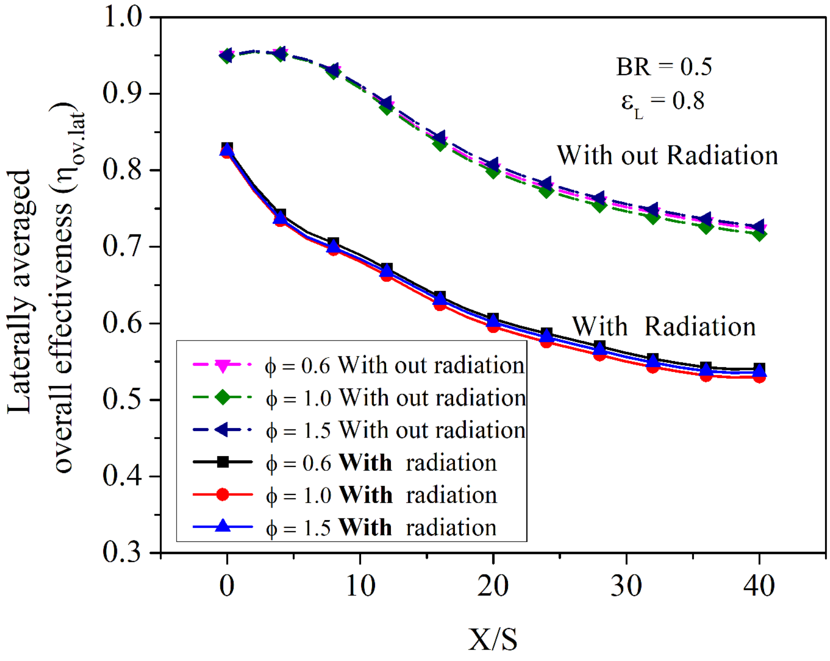

(a)

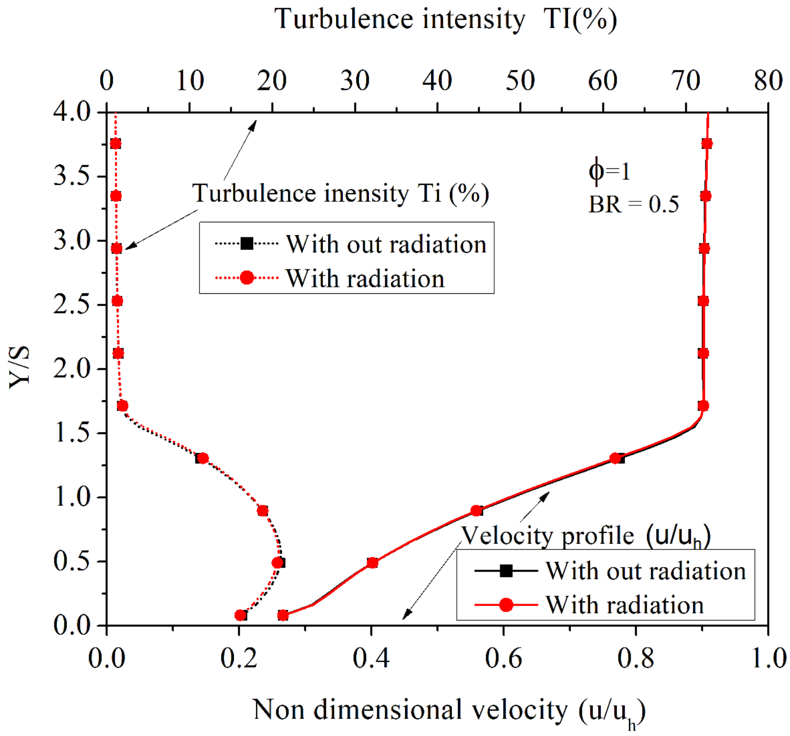

(b)

Figure 7.5: (a) Effect of equivalence ratio and gas radiation on film cooling effectiveness (b) Effect of radiation on the velocity profile and its turbulence intensity TI(%) at $X/S = 20$

Along with the influence of gas radiation on film cooling effectiveness, the effect on the flow characteristics is also investigated. As there is no effect of equivalence ratio (ϕ) on the $\eta_{ov.lat}$, flow characteristics are investigated only for the case stoichiometric mixture ϕ = 1 and BR = 0.5. Figure 7.5(b) depicts the non-dimensional x-component velocity (u/u_h) and its corresponding local turbulence intensity TI(%) in the direction (Y/S) normal to the liner surface at X/S = 20. One of the observations is that for a blowing ratio of 0.5, the coolant mass flux coming out of the slot is relatively less than the mainstream, resulting in a velocity deficit from Y/S = 0 to 1.5. In addition, the corresponding turbulence intensity (TI) is significantly high in the velocity deficit zone due to the entertainment of the mainstream. The TI is maximum at the interaction of the main and cold streams due shearing of both streams. Furthermore, it is observed that there is no significant effect of gas radiation on both the velocity profile and its corresponding turbulence intensity TI%.

7.3.2 Effect of liner emissivity on the film cooling effectiveness

The radiative heat transfer depends on the emissivity of the surface. A highly polished surface does not absorb or emit radiation significantly. On the other hand, a rough surface has more surface area to absorb or emit radiation.

In addition, the combustor and hot gas path components may be subjected to soot deposition on the surface and enhance the emissivity of the surface. Hence, the effect of emissivity (ε_L) of the liner surface on the film cooling effectiveness is investigated in this section.

Figure 7.6 shows the effect of liner emissivity on the laterally averaged overall effectiveness ($\eta_{ov.lat}$) along the streamwise distance (X/S). From the figure, it is seen that the $\eta_{ov.lat}$ of the liner without radiation is the maximum and the $\eta_{ov.lat}$ is minimum for the case with the gas radiation and ε_L = 0.8.

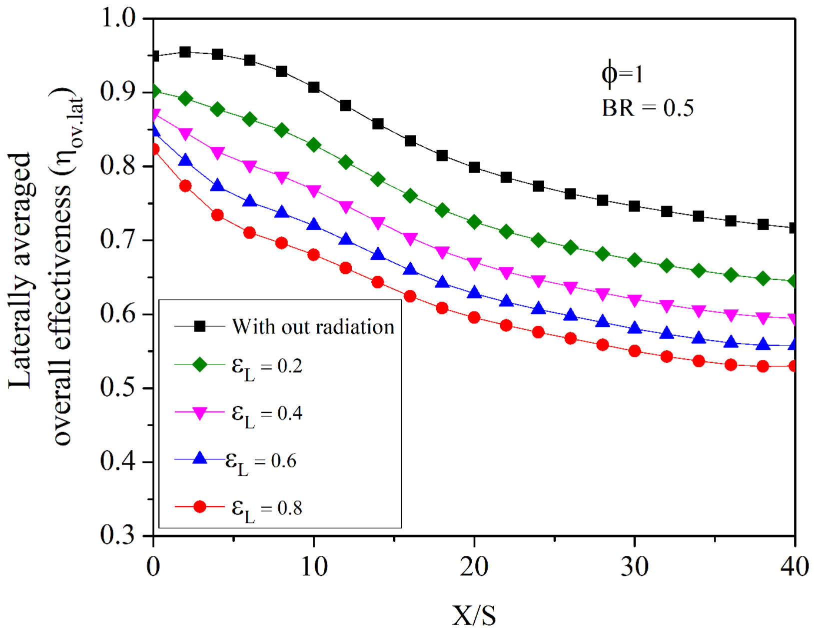

Figure 7.6: Effect of surface emissivity on Laterally averaged effectiveness along the streamwise distance (X/S)

The effectiveness ($\eta_{ov.lat}$) is enhanced as the ε_L is reduced from 0.8 to 0.2. Hence, it is clear that the effectiveness is highly dependent on the emissivity of the liner, and the radiative heat transfer can be impeded by reducing the emissivity of the liner surface. In addition, the deterioration of $\eta_{ov.lat}$ due to radiation mentioned in the previous section corresponds to the ε_L = 0.8, and it changes with the liner emissivity. Figure 7.7 shows a comparison of temperature contours of the liner surface for the cases with and without gas radiation. Figure 7.7 (i) shows the liner temperature for the case without gas radiation. One can observe that a maximum temperature of 1100 K is obtained at the end of the liner. In addition, for the case with gas radiation, figures 7.7 (ii to v) show the temperature contours on the liner with ε_L ranging from 0.2 to 0.8. It is observed that the temperature of the liner is increased drastically with an increase in emissivity, and the maximum temperature is found to be approximately 1400 K for the case of ε_L = 0.8. At these high temperatures, the liner might not withstand prolonged periods of operation which can lead to the possible failure of the combustor.

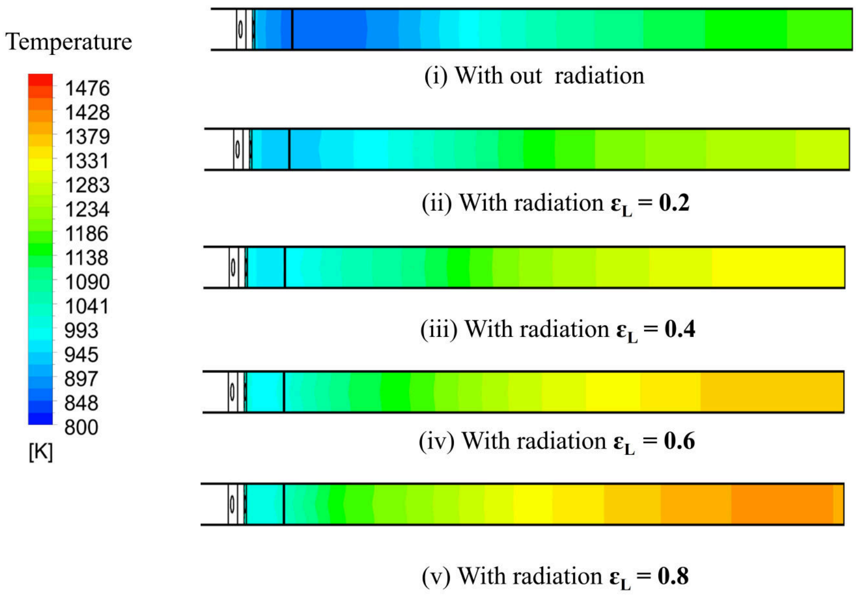

Figure 7.7: Effect of surface emissivity on temperature distribution on the liner surface

7.3.3 Effect of the thermal barrier coating on film cooling effectiveness

In addition to film cooling, the liner can also be protected from high-temperature combustion gases using a thermal barrier coating (TBC) on its surface. The TBC has a low thermal conductivity and high-temperature resistance. As a result, it reduces the heat flux on the liner surface and permits the combustor to run at high temperatures. The TBC coating considered in the study is Yttria-stabilized Zirconia (YSZ). Thermal and physical properties of YSZ available in the literature Li and Yang (2019) and Vassen *et al.* (2004) are considered in the study and elucidated in Table 7.2. Figure 7.8 depicts the temperature contours on the liner surface with and without TBC.

For the case of the liner without considering the gas radiation and without TBC (see Figure 7.8(a), the maximum temperature is approximately 1100K, which increases to 1400K with gas radiation (see Figure 7.8(b). However, from Figure 7.8(c), it is observed that the temperatures are reduced to a safe value of temperature of 1200K with TBC. The temperature is approximately reduced by 200K. Figure 7.8(d) shows the temperature on the top surface of the thermal barrier coating (TBC), and it is the maximum of all the cases because of its low thermal conductivity.

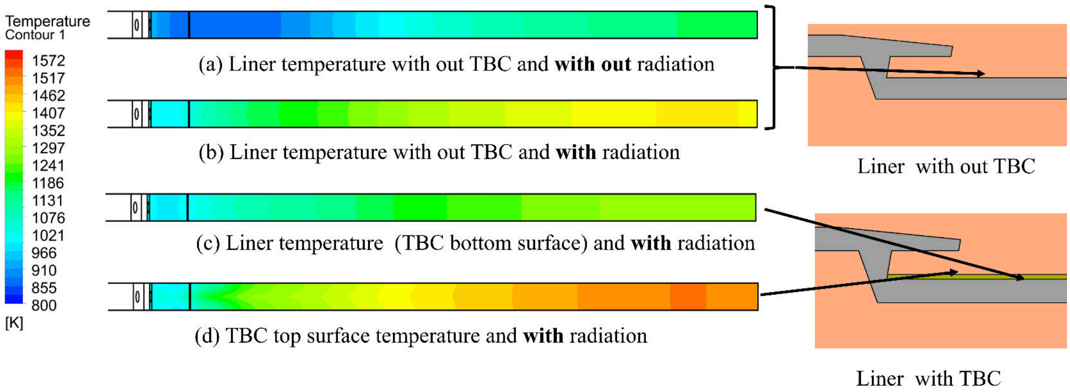

Figure 7.8: Temperature contours on (a-b) liner surface with and without radiation (c) liner surface with radiation and with TBC (d) top surface of TBC with radiation

Figure 7.9 shows the effect of TBC on the laterally averaged overall effectiveness ($\eta_{ov.lat}$). The $\eta_{ov.lat}$ of the liner surface is significantly enhanced with the application of TBC compared to the case without TBC.

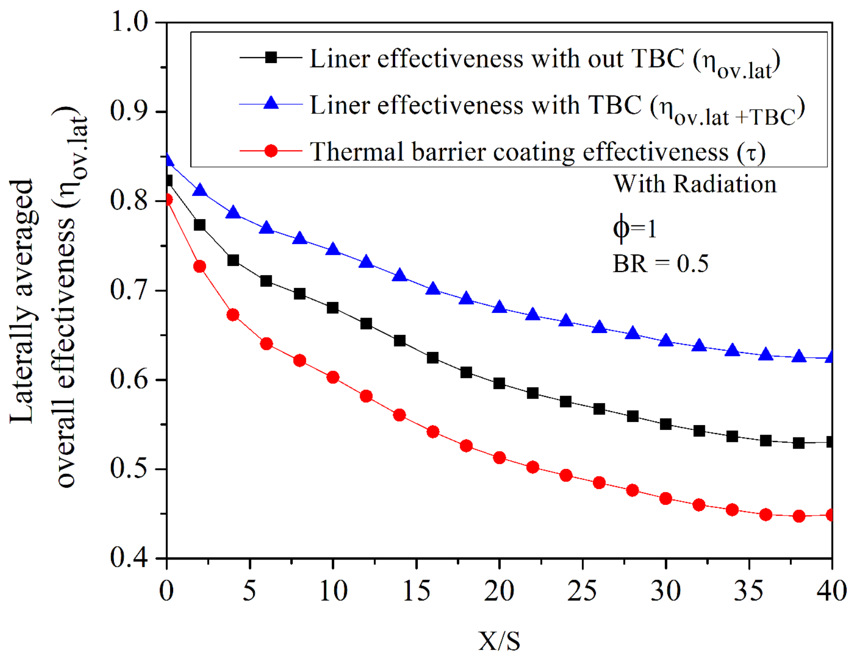

Figure 7.9: Effect of TBC on laterally averaged overall effectiveness along the streamwise distance (X/S)

Furthermore, the film cooling effectiveness on the top surface of the thermal barrier coating, called thermal barrier coating effectiveness (τ), is very low due to its low thermal conductivity. However, the TBC can withstand high temperatures.

Figure 7.10 shows a comparison of area-averaged overall effectiveness ($\eta_{ov.avg}$) between the cases following (i) No gas radiation and (ii) with gas radiation.

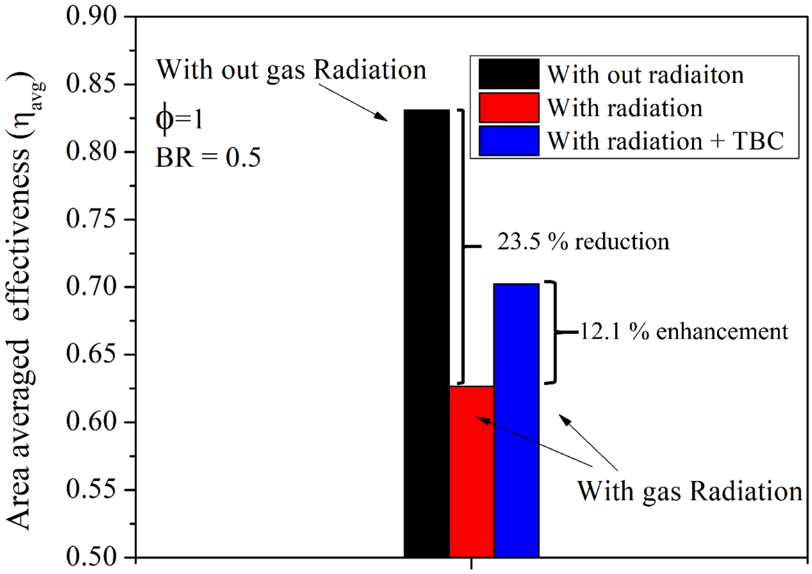

Figure 7.10: Comparison of area averaged overall effectiveness between the cases (i) No gas radiation and (ii) with gas radiation (iii) with gas radiation and TBC

For the case of gas radiation, the $\eta_{ov.avg}$ is shown for both with and without TBC. As already discussed, the $\eta_{ov.avg}$ is reduced by 23.5% due to radiation. However, with the application of TBC, the $\eta_{ov.avg}$ is enhanced by 12%. As a result, the $\eta_{ov.avg}$ is enhanced from 0.62 to 0.7 with the TBC. The enhancement in the effectiveness is due to the reduction in heat transfer to the liner surface by the low thermally conductive TBC.

7.4 PERFORMANCE OF OPTIMUM SLOT CONFIGURATION UNDER GAS RADIATION

In the previous sections, the effect of gas radiation and thermal barrier coating on the film cooling performance of the reference 1 slot configuration in a baseline combustor was extensively investigated. In this section, the robustness of the optimum configuration obtained without considering the gas radiation in previous chapter 6 is verified by considering the effects of gas radiation. For this purpose, the cooling performance of the optimum configuration is compared to two reference configurations considered from the baseline combustor. The dimensions of these configurations are elucidated in Table 7.5.

Table 7.5: Dimensions of reference and optimum configurations

Parameter	unit	Reference - 1	Reference - 2	Optimum configuration
slot jet diameter (d)	mm	1.7	1.5	1.99
Slot jet pitch (p)	mm	4.19	4.19	4
Lip taper angle (α)	^{o}	5	0	4.8
Lip length (L)	mm	7.5	5.1	11.3

Figure 7.11 shows the variation of overall film cooling effectiveness of reference and optimum configurations at BR = 1 along streamwise distance (X/S) when gas radiation is considered.

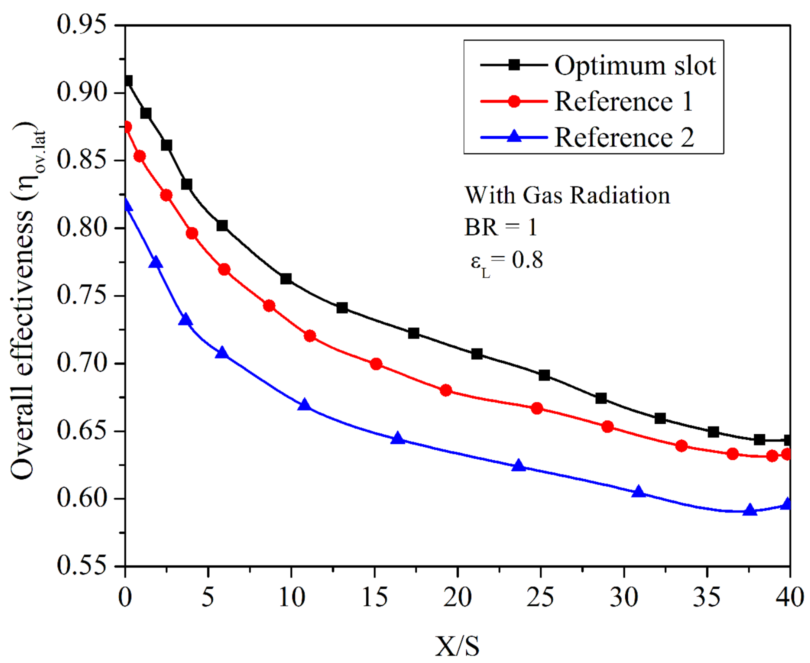

Figure 7.11: Variation of overall film cooling effectiveness along X/S (with gas radiation)

From the figure, the film cooling effectiveness of the optimum configuration is seen to be higher than the reference configurations of the baseline combustor. In addition, Figure 7.12 depicts the percentage enhancement of the area-averaged cooling performance at different conditions, such as adiabatic effectiveness without gas radiation ($\eta_{ad.avg}$), overall effectiveness without gas radiation ($\eta_{ov.avg}$), and overall effectiveness with gas radiation ($\eta_{ov\_rad.avg}$).

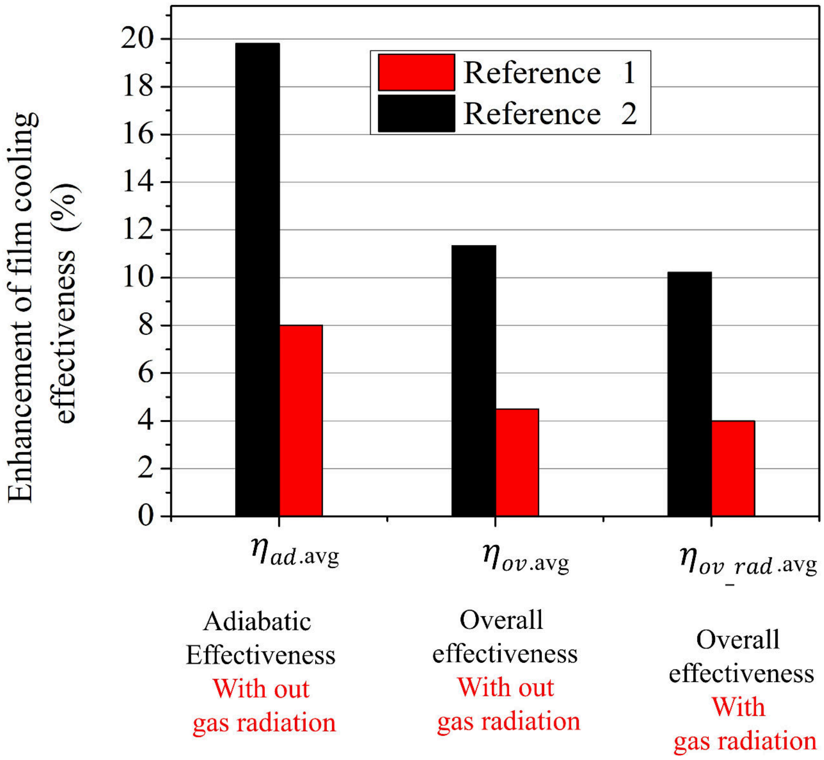

Figure 7.12: Percentage enhancement of η_{avg} for optimum configuration compared to reference slot configurations

Under adiabatic conditions, the film cooling effectiveness is enhanced by 8 % and 19.8 % compared to references 1 and 2, respectively. Under these conditions, the cooling effectiveness obtained is the sole effect of coolant from the slot and its mixing with the mainstream. However, in the case of overall effectiveness, the liner is additionally cooled by the air in the annular spacing. The optimum three-dimensional slot configuration also has a better overall film cooling performance in the case of without gas radiation as well as with gas radiation. In the case of gas radiation, the overall effectiveness is enhanced by approximately 4 and 10% compared to reference 1 and 2 configurations, respectively. Hence, the optimum configuration is robust and performs well under actual engine conditions, even when the effects of gas radiation are taken into consideration.

7.5 CONCLUSIONS

In this chapter, the results of numerical investigations to study the characteristics of fluid flow and heat transfer by the combination of conduction, convection, and radiation in the film cooling of a combustor liner were reported. The conjugate effects are accounted for by solving fluid and solid domains simultaneously. In addition, radiation from the high-temperature combustion gases was accounted for by employing the discrete ordinate model in the numerical scheme to solve the radiative heat transfer equation (RTE). Furthermore, the influence of a ceramic-based thermal barrier coating known as Yttria-stabilized Zirconia on the film cooling effectiveness was explored. The salient conclusions of the study are:

1. Gas radiation shows a significant effect on the overall film cooling effectiveness η_{lat}. The area-averaged effectiveness (η_{avg}) reduces by 23.5% for a particular liner emissivity of 0.8 compared to the case without gas radiation while the equivalence ratio(ϕ) has minimal effect on the film cooling effectiveness.

2. Gas radiation shows a very minimal effect on flow characteristics such as velocity and its corresponding turbulence intensity profiles.

3. The emissivity of the liner surface plays a significant role in the radiative heat transfer. The temperature on the liner surface is reduced as the surface emissivity decreases from 0.8 to 0.2.

4. The thermal barrier coating (TBC) enhances the area averaged effectiveness (η_{avg}) by 12% compared to the case without TBC and helps to maintain the surface of the liner at safe temperatures under high heat fluxes.

5. The optimum three-dimensional slot configuration obtained based on adiabatic

performance is robust and performs well under actual engine conditions, even when the effects of gas radiation are taken into consideration.

7.6 CLOSURE

In this chapter, the results of the numerical investigation to study the effects of gas radiation and thermal barrier coating on film cooling performance were reported. In addition, the robustness of the optimum three-dimensional slot configuration obtained under adiabatic conditions was verified. In the next chapter, the major conclusions of the entire study and the scope for future work are presented.

[1]

[1]This chapter is drawn from the following publication: **Revulagadda A.P**, Ramapada Rana, Batchu Suresh, Balaji C, Pattamatta A "Effects of Gas Radiation and Thermal Barrier Coating on the Film Cooling Performance in an Annular Combustor" 17th International Heat Transfer Conference (Presented).

CHAPTER 8

CONCLUSIONS AND SCOPE OF THE FUTURE WORK

8.1 INTRODUCTION

Modern gas turbine demands high turbine inlet temperature to increase cycle efficiency. Over the last few decades, the demand for the turbine inlet temperature has increased from approximately 1100 K to 2100 K. The hot-gas path components, such as combustors, guide vanes, and turbine blades, cannot withstand high-temperature combustion gases. From the material engineering point of view, these components would fail due to creep and thermal fatigue. To overcome these problems, the hot gas path components are cooled to safe temperatures using relatively low-temperature bleed air from the compressor through multiple internal passages. In the present work, the cooling of a typical annular combustor liner using various three-dimensional film cooling techniques is investigated extensively.

First, an experimental investigation was carried out on a three-dimensional slot film cooling under laboratory conditions (low pressure and low temperatures) to study the flow behavior and cooling performance for a wide range of blowing and density ratios. The experimental results were used to validate the numerical study obtained under laboratory conditions (low temperature and pressure). Using the validated RANS-based numerical model, a numerical study was conducted to investigate the film cooling performance at actual engine conditions (high pressure and high temperatures) with a view to understanding the effect of the operating conditions on the film cooling performance. Following this, detailed parametric studies were conducted using the RANS approach to understand the influence of flow and geometrical parameters on the film cooling effectiveness. An artificial neural network-based mathematical model was developed to predict the film cooling effectiveness, given the blowing ratio and geometrical parameters.

In addition, a unique combination of experimental studies, numerical modeling, and machine learning algorithms was used to optimize the film cooling three-dimensional slot configuration. A surrogate model is developed to predict the film cooling performance based on the geometrical parameters of the slot. An optimum configuration is identified within the surrogate model using an evolutionary-based Genetic algorithm. The key objective of the optimization is to maximize the area-averaged effectiveness ($\eta_{ad.avg}$) and minimize its standard deviation (σ_η) at a fixed coolant mass flux. An optimum liner length was also identified to reduce the cooling rings for the entire combustor. The optimum configurations were tested using in-house experiments under actual engine conditions (low temperature and pressure). In addition, the baseline three-dimensional slot of a hybrid slot configuration investigated in a separate collaborated study is replaced with the optimized three-dimensional slot configuration obtained in the present study to get the complete benefit of film cooling.

Finally, numerical investigations were conducted to estimate the effect of the combustion gas radiation on the film cooling performance. The effect of equivalence ratio (ϕ) and the impact of emissivity on the liner surface were investigated. The effect of a thermal barrier coating on the film cooling performance was reported. In addition, the optimized slot configuration obtained was tested for its robustness under gas radiation, and its performance was compared with the reference slot configurations in the baseline combustor.

8.2 MAJOR CONCLUSIONS OF THE PRESENT STUDY

Based on the numerical and experimental studies and machine learning-assisted optimization, the major conclusions of the present study are:

- In practical three-dimensional slot film cooling, velocity profiles along the streamwise direction exhibit self-similar behavior for blowing ratio (BR) ≥ 2.

- Under laboratory conditions (DR = 1.1), the film cooling effectiveness increases between $0.5 \leq BR \leq 2$. However, the effectiveness reduces from $3 \leq BR \leq 5$ due to a significant increase in turbulence intensity caused by the shearing of main and cold streams in the mixing zone. Moreover, similar trends of effectiveness are observed under actual engine conditions (DR = 2.6). Hence, to save the amount of coolant, it is not recommended to operate the film cooling beyond BR = 2.

- In practical slots, the density ratio significantly affects film cooling effectiveness. For a fixed blowing ratio (BR), film cooling effectiveness obtained for a DR of 2.6 is higher than that obtained for a DR of 1.1.

- Using RANS simulations and the kriging technique, a surrogate model is developed at BR = 1, and the optimum configuration is identified using the genetic algorithm.

- The optimum slot configuration outperformed both reference configurations. A maximum $\eta_{ad.avg}$ of 19.8 % is enhanced with optimum configuration on comparison with reference 2 slot configuration. The optimum configuration performs well at all the off-design blowing ratios from 0.5 to 5. In addition, it outperforms reference configurations in terms of adiabatic as well as overall performances.

- With a compromise on standard deviation, the optimum slot configuration requires a 4 to 24 % less coolant mass flux compared to the reference 1 slot and 4 to 40 % less coolant mass flux compared to reference 2, which are operated at a BR of 1.

- By considering the least operable blowing ratio of 0.5, the optimum slot cools an additional length of 5.5 compared to reference 1 for the same coolant mass flux, which contributes to a reduction of one pair of cooling rings. As a result, the coolant mass flux is reduced by 16.66% for the entire combustor. The optimum slot configuration is recommended for film cooling of the entire combustor using five pairs of cooling rings, with each cooling ring of length G/S = 15.5.

- A comparison of optimized hybrid and reference 1 three-dimensional slot configurations for BR = 1 shows an enhancement of 9% in the area averaged effectiveness and 13.5% reduction in its standard deviation under actual engine conditions.

- Gas radiation significantly affects the overall film cooling effectiveness. The area-averaged effectiveness ($\eta_{ov.avg}$) reduces by 23.5% for a particular liner emissivity of 0.8 compared to the case without gas radiation. The equivalence ratio(ϕ) has a minimal effect on the film cooling effectiveness.

- The emissivity of the liner surface plays a significant role in the radiative heat transfer. The temperature on the liner surface reduces as the surface emissivity decreases from 0.8 to 0.2.

- The thermal barrier coating (TBC) enhances the area averaged effectiveness (η_{avg}) by 12% compared to the case without TBC and helps to maintain the surface of the liner at safe temperatures under high heat fluxes.

- The optimum three-dimensional slot configuration obtained based on adiabatic performance is robust and performs well under actual engine conditions, even when the effects of gas radiation are considered.

A grand overview of the entire study is presented in Fig. 8.1.

Experimental and Numerical Investigation of the three-dimensional Slot Film Cooling of an Annular Combustor Liner

⬇

Development of an experimental test facility to test the film cooling performance of a combustor liner

⬇

Experimental testing of the baseline configuration (Heat and fluid flow characteristics)

⬇

Validation of numerical study with in-house experiments under laboratory conditions

⬇

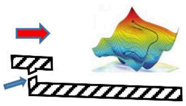

Numerical investigation on the performance of the baseline three-dimensional slot configuration under actual engine conditions.

⬇

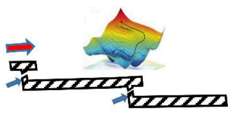

Optimization of the three-dimensional slot configuration, hybrid configuration and pitch between subsequent rows to optimize the number of cooling rings in the combustor under actual engine conditions numerically.

⬇

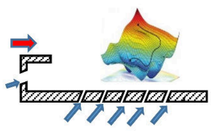

Experimental testing of optimum configurations under laboratory conditions

⬇

Outcomes:

- The optimum slot configuration requires 4 to 24 % less coolant mass flux compared to the reference 1 slot and 4 to 40 % less coolant mass flux compared to reference 2, for the same effectiveness.
- With implementation of optimum slot, one pair of cooling rings can be reduced in the combustor

⬇

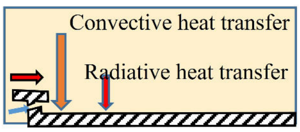

- Investigation on effect of gas radiation and thermal barrier coating on cooling performance
- Testing the robustness of the optimized three-dimensional slot configuration under effects of gas radiation

⬇

Outcomes:

- Gas radiation shows a significant adverse effect on film cooling performance, however, the optimum configuration outperforms baseline configurations even when the effects of gas radiation are considered.
- Thermal barrier coating reduces the heat transfer to the liner, thereby enhances the effectiveness by 12 %

Figure 8.1: Grand overview of the present study

8.3 SUGGESTIONS FOR THE FUTURE WORK

Studies on combustors concern several conditions and parameters, and in view of this, it is challenging to include all of them in a single study. Hence, the problem was simplified by limiting the number of liners to one or two in this work. However, the studies can be further extended as follows:

- The current studies can be scaled up to the full combustor and the effect of parameters such as primary holes, intermediate holes, dilution holes, and liner-to-liner effects on film cooling can be investigated. The problem can be initiated with simple hot and cold streams and extended to complete combustion studies. The complete combustor studies need to include the effect of swirler, fuel injection, atomization, evaporation, fuel combustion, primary holes, intermediate holes, dilution holes, three-dimensional slot film cooling, and hybrid cooling of the combustor.

- The full-scale combustion studies on the baseline and optimized liner (by replacing the whole combustor with optimum geometry) to estimate the advantage of using the optimum slot configuration.

- Investigation of the multi-liner hybrid cooling rings would help to optimize the pitch between the rings and also the total number of cooling rings required for the entire combustor.

- Investigation of hybrid cooling by combined conduction, convection, and radiation under actual engine operating conditions would reveal the realistic fluid flow heat transfer characteristics .

- Investigation of film cooling using large eddy simulations to explore the flow structures as the RANS approaches have their limitations with accuracy compared to LES.

8.4 CLOSURE

This chapter gave an overview of the various problems considered in this thesis. Following this, the major conclusions of the study and the scope for future work were highlighted.

LIST OF PUBLICATIONS

I. REFEREED JOURNALS BASED ON THESIS

Revulagadda A.P, Adapa B.R., Balaji C, Pattamatta A, "Fluid Flow and Heat Transfer Characteristics of Three-Dimensional Slot Film Cooling in an Annular Combustor", International Journal of Heat and Mass Transfer ,211(2023),p.(124211), doi.org/10.1016/j.ijheatmasstransfer.2023.124211.

Revulagadda A.P, Ramapada Rana, Batchu Suresh, Balaji C, Pattamatta A, "A Multiobjective Optimization of 3D - Slot Jet Configuration for Enhancement of Film Cooling in an Annular Combustor Liner", International Journal of Heat and Mass Transfer, 218(2024), p.(124745), doi.org/10.1016/j.ijheatmasstransfer.2023.124745.

Adapa B.R, **Revulagadda A. P.**, Pattamatta A., and Balaji C., (2022). "Film Cooling Studies on Combined Three-dimensional Slot and Effusion Jet Configuration of an Annular Combustor Liner", International Journal of Fluid Mechanics Research,49 (3) (2022), pp. 61-80. DOI: 10.1615/InterJFluidMechRes.2022043245.

Revulagadda A.P, Adapa B.R., Balaji C, Pattamatta A, "Performance Assessment and Optimization of Three-Dimensional Hybrid Slot-Effusion Jet Cooling Configuration of an Annular Combustor Liner", Applied Thermal Engineering, 240(2024), 122198, https://doi.org/10.1016/j.applthermaleng.2023.122198.

II. PUBLICATIONS IN CONFERENCE PROCEEDINGS

Revulagadda A.P, Adapa B.R., Pattamatta A, and Balaji C, "A Numerical Investigation on the Effect of Lip Geometry with Tangential Film Cooling on an Annular Combustor", Proceedings of the National Aerospace Propulsion Conference, Springer Nature Singapore (2023), pp. 527-542. https://doi.org/10.1007/978-981-19-2378-4_30.

Revulagadda A.P, Ramapada Rana, Batchu Suresh, Balaji C, Pattamatta A "Effects of Gas Radiation and Thermal Barrier Coating on the Film Cooling Performance in an Annular Combustor" 17th International Heat Transfer Conference (Presented).

Adapa, B. R., **Revulagadda, A. P.**, Pattamatta, A., and Balaji, C., "Numerical Investigations on Combined Slot and Effusion Film Cooling of an Annular Combustor Liner", Proceedings of the 26th National and 4th International ISHMT-ASTFE Heat and Mass Transfer Conference December 17-20, 2021, IIT Madras, India. Begel House Inc. DOI: 10.1615/IHMTC-2021.1380.

III. PRESENTATIONS IN CONFERENCES

Sangamesh C.Godi, **Revulagadda A.P.**, Pattamatta, A., and C. Balaji, ”Heat Transfer Characteristics of a Single Row of Three-Dimensional Wall Jets, 2nd National Aero Propulsion Conference”, IIT Kharagpur, West Bengal, India, 17 - 19 December 2018.

APPENDIX A

CALIBRATION CURVES

A.1 DETAILS OF THE K-TYPE THERMOCOUPLES CALIBRATION USED IN THE PRESENT STUDY

Table A.1: Data collected for thermocouple calibration.

$T_{set}(^oC)$	$T_{ref}(^oC)$	$T_{measured}(^oC)$	$T_{set}(^oC)$	$T_{ref}(^oC)$	$T_{measured}(^oC)$
25	24.8	24.6	60	60.1	59.8
30	30.1	29.7	65	65	64.7
35	34.8	34.5	70	70.1	69.8
40	39.9	39.7	75	75.2	74.9
45	45.0	44.7	80	80.4	80.1
50	49.9	49.7	85	85.4	85.1
55	55.0	54.7	90	90.5	90.3

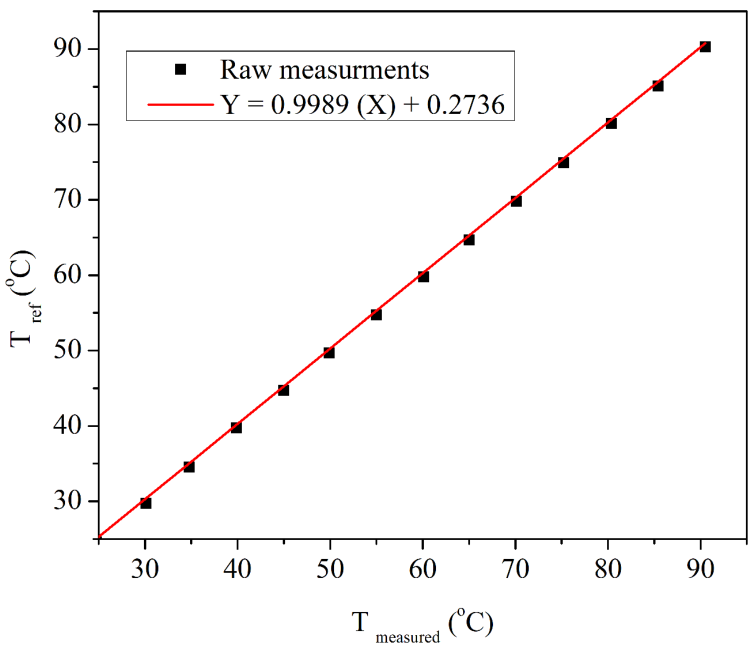

Figure A.1: Calibration curve for the K-type thermocouple

A.2 CALIBRATION OF THE BOUNDARY LAYER PROBE OF THE HOTWIRE ANEMOMETER

Table A.2: Data utilized for calibration of the boundary layer probe of the hotwire anemometer

S. No	Velocity U(m/s)	Voltage E (V)	*S. No*	Velocity U(m/s)	Voltage E (V)	*S. No*	Velocity U(m/s)	Voltage E (V)
1	0	1.282	21	7.559	1.859	41	16.903	2.096
2	1.316	1.501	22	7.785	1.868	42	17.358	2.103
3	1.861	1.562	23	8.004	1.874	43	18.043	2.117
4	2.279	1.6	24	8.528	1.891	44	19.069	2.113
5	2.632	1.618	25	8.629	1.894	45	20.386	2.161
6	2.942	1.639	26	9.021	1.908	46	21.622	2.179
7	3.223	1.658	27	9.305	1.915	47	22.792	2.197
8	3.482	1.678	28	9.67	1.925	48	23.54	2.207
9	3.722	1.685	29	10.022	1.935	49	24.442	2.221
10	3.948	1.703	30	10.527	1.948	50	25.312	2.234
11	4.364	1.724	31	11.01	1.961	51	26.318	2.248
12	4.745	1.747	32	11.547	1.974	52	27.915	2.269
13	5.096	1.765	33	12.06	1.99	53	29.424	2.291
14	5.426	1.775	34	12.69	2.006	54	31.527	2.318
15	5.736	1.793	35	13.159	2.015	55	32.233	2.327
16	6.03	1.802	36	14.111	2.036	56	33.549	2.343
17	6.311	1.813	37	14.888	2.054	57	34.816	2.356
18	6.58	1.823	38	15.289	2.063	58	36.037	2.371
19	6.838	1.834	39	15.846	2.073	59	37.219	2.381
20	7.086	1.843	40	16.224	2.081	60	38.814	2.399

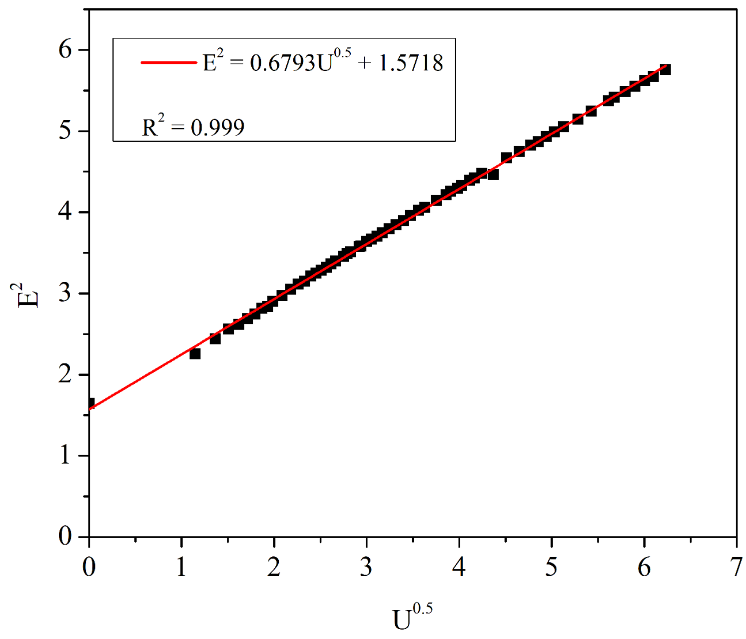

Figure A.2: Calibration curve for the anemometer

The procedure to estimate mean velocity of the flow and its fluctuations is described below.

$$E^2 = a + bU^{0.5} \tag{A.1}$$

where, E is the mean voltage and U is mean velocity. The velocity is then estimated from the mean voltage as:

$$U = \left(\frac{E^2 - a}{b}\right)^2 + bU^{0.5} \tag{A.2}$$

where,

E= $\frac{E_{measured}}{DC\ gain}$

$U_{inst} = Mean\ value + Fluctuation\ value = U + u_{rms}$

$U_{inst} = E + e$

Where, $e = \frac{e_{measured}}{AC\ gain} = \frac{Estd}{DC\ gain \times AC\ gain} = \frac{bu}{4E\sqrt{U}}$

$\Rightarrow RMS\ velocity,\ \mathrm{u}_{rms} = \frac{e}{S}\ Where\ S = \frac{b}{4E\sqrt{U}}$

BIBLIOGRAPHY

1. **Adapa, B. R.** (2022). ” an improvised hybrid slot-effusion configuration for cooling enhancement in an annular combustor liner. *Indian Institute of Technology Madras*, **Masters of Science Thesis**.

2. **Akwaboa, S.**, **P. Mensah**, and **R. Diwan** (2010). Effects of Thermal Radiation on Air Plasma Spray (APS) Coated Gas Turbine Blade. **Volume 4: Heat Transfer, Parts A and B**, 627–633. URL `https://doi.org/10.1115/GT2010-23660`.

3. **Andreini, A.**, **G. Caciolli**, **B. Facchini**, **L. Tarchi**, **D. Coutandin**, **A. Peschiulli**, and **S. Taddei**, Density ratio effects on the cooling performances of a combustor liner cooled by a combined slot/effusion system. *In Turbo Expo: Power for Land, Sea, and Air*, volume 44700. American Society of Mechanical Engineers, 2012.

4. **Andrews, G.** and **F. Bazdidi-Tehrani**, Small diameter film cooling hole heat transfer: the influence of the number of holes. *In ASME 1989 International Gas Turbine and Aeroengine Congress and Exposition*. American Society of Mechanical Engineers Digital Collection, 1989.

5. **Andrews, G.**, **F. Bazdidi-Tehrani**, **C. Hussain**, and **J. Pearson**, Small diameter film cooling hole heat transfer: The influence of the hole length. *In ASME 1991 International Gas Turbine and Aeroengine Congress and Exposition*. American Society of Mechanical Engineers Digital Collection, 1991.

6. **Andrews, G.**, **I. Khalifa**, **A. Asere**, and **F. Bazdidi-Tehrani**, Full coverage effusion film cooling with inclined holes. *In Turbo Expo: Power for Land, Sea, and Air*, volume 78811. American Society of Mechanical Engineers, 1995.

7. **ANSYS Fluent** (2013). *ANSYS Fluent Theory Guide 15.0*. ANSYS, Inc., Canonsburg, Pennsylvania, United States.

8. **Asok Kumar, N.** and **S. Kale** (2002). Numerical simulation of steady state heat transfer in a ceramic-coated gas turbine blade. *International Journal of Heat and Mass Transfer*, **45**(24), 4831–4845. ISSN 0017-9310. URL `https://www.sciencedirect.com/science/article/pii/S0017931002001904`.

9. **Ben Haj Ayech, S.**, **S. Habli**, **N. Mahjoub Saïd**, **P. Bournot**, and **G. Le Palec** (2016). A numerical study of a plane turbulent wall jet in a coflow stream. *Journal of Hydro-environment Research*, **12**, 16–30. ISSN 1570-6443. URL `https://www.sciencedirect.com/science/article/pii/S1570644316000186`.

10. **Bittlinger, G.**, **A. Schulz**, and **S. Wittig**, Film cooling effectiveness and heat transfer coefficients for slot injection at high blowing ratios. *In ASME 1994 International Gas Turbine and Aeroengine Congress and Exposition*. ASME Digital Collection, 1994.

11. **Ceccherini, A.**, **B. Facchini**, **L. Tarchi**, **L. Toni**, and **D. Coutandin**, Combined effect of slot injection, effusion array and dilution hole on the cooling performance of a real combustor liner. *In Turbo Expo: Power for Land, Sea, and Air*, volume 48845. 2009.

12. **Cho, H. H.** and **J. K. Ham** (2001). Influence of Injection Type and Feed Arrangement on Flow and Heat Transfer in an Injection Slot . *Journal of Turbomachinery*, **124**(1), 132–141.

13. **Click, A.**, **P. M. Ligrani**, **M. Hockensmith**, **J. Knox**, **C. Larson**, **A. Fairbanks**, **F. Liberatore**, **R. Patel**, and **Y.-H. Ho** (2021). Louver slot cooling and full-coverage film cooling with a combination internal coolant supply. *Journal of Turbomachinery*, **143**(3), 031004.

14. **Coppalle, A.** and **P. Vervisch** (1983). The total emissivities of high-temperature flames. *Combustion and Flame*, **49**(1), 101–108. ISSN 0010-2180. URL `https://www.sciencedirect.com/science/article/pii/0010218083901542`.

15. **Dávalos, J. O.**, **J. C. García**, **G. Urquiza**, **A. Huicochea**, and **O. D. Santiago** (2018). Prediction of film cooling effectiveness on a gas turbine blade leading edge using ann and cfd. *International Journal of Turbo Jet-Engines*, **35**(2), 101–111.

16. **Ekkad, S. V.**, **S. Ou**, and **R. B. Rivir** (2004). A transient infrared thermography method for simultaneous film cooling effectiveness and heat transfer coefficient measurements from a single test. *Journal of Turbomachinery*, **126**(4), 597–603.

17. **Facchini, B.**, **F. Maiuolo**, **L. Tarchi**, and **D. Coutandin**, Combined effect of slot injection, effusion array and dilution hole on the heat transfer coefficient of a real combustor liner: Part 1—experimental analysis. *In Turbo Expo: Power for Land, Sea, and Air*, volume 43994. 2010.

18. **Godi, S. C.**, **A. Pattamatta**, and **C. Balaji** (2019). Effect of the Inlet Geometry on the Flow and Heat Transfer Characteristics of Three-Dimensional Wall Jets. *Journal of Heat Transfer*, **141**(11). ISSN 0022-1481.

19. **Godi, S. C.**, **A. Pattamatta**, and **C. Balaji** (2020*a*). Heat transfer from a single and row of three dimensional wall jets-a combined experimental and numerical study. *International Journal of Heat and Mass Transfer*, **159**, 119801.

20. **Godi, S. C.**, **A. Pattamatta**, and **C. Balaji** (2020*b*). Heat transfer from a single and row of three dimensional wall jets - a combined experimental and numerical study. *International Journal of Heat and Mass Transfer*, **159**, 119801. ISSN 0017-9310.

21. **Hayes, S. A.**, **A. C. Nix**, **C. M. Nestor**, **D. T. Billups**, and **S. M. Haught** (2017). Experimental investigation of the influence of freestream turbulence on an anti-vortex film cooling hole. *Experimental Thermal and Fluid Science*, **81**, 314–326.

22. **Hong Qu, L.**, **J. zhou Zhang**, and **X. ming Tan** (2017). Improvement on film cooling

effectiveness by a combined slot-effusion scheme. *Applied Thermal Engineering*, **126**, 379–392.

23. **Huang, Z.**, **Y.-B. Xiong**, **Y.-Q. Liu**, **P.-X. Jiang**, and **Y.-H. Zhu** (2015). Experimental investigation of full-coverage effusion cooling through perforated flat plates. *Applied Thermal Engineering*, **76**, 76–85.

24. **Johnson, J. J.**, **P. I. King**, **J. P. Clark**, and **M. K. Ooten** (2013). Genetic Algorithm Optimization of a High-Pressure Turbine Vane Pressure Side Film Cooling Array. *Journal of Turbomachinery*, **136**(1). ISSN 0889-504X.

25. **Kline, S.** and **F. Mcclintock** (1953). Describing Uncertainties in Single-Sample Experiments . *Mechanical Engineering*, **75**, 3–8.

26. **Kumar, G.**, **M. Rettig**, **H. Mongia**, and **C. Chauvette**, *Automated cooling design methodology for combustor walls*. 1998. URL `https://arc.aiaa.org/doi/abs/10.2514/6.1998-836`.

27. **Lawal, A. I.** and **M. A. Idris** (2020). An artificial neural network-based mathematical model for the prediction of blast-induced ground vibrations. *International Journal of Environmental Studies*, **77**(2), 318–334.

28. **Lee, K.-D.** and **K.-Y. Kim** (2011). Surrogate based optimization of a laidback fan-shaped hole for film-cooling. *International Journal of Heat and Fluid Flow*, **32**(1), 226–238.

29. **Lefebvre, A. H.** and **D. R. Ballal**, *Gas turbine combustion: alternative fuels and emissions*. CRC press, 2010.

30. **Lemmon, E. W.**, **I. H. Bell**, **M. L. Huber**, and **M. O. McLinden** (2018). NIST Standard Reference Database 23: Reference Fluid Thermodynamic and Transport Properties-REFPROP, Version 10.0, National Institute of Standards and Technology. URL `https://www.nist.gov/srd/refprop`.

31. **Li, G.-R.** and **G.-J. Yang**, Chapter 7 - structure evolution of multiscaled thermal barrier coatings during thermal exposure. *In* **G.-J. Yang** and **X. Suo** (eds.), *Advanced Nanomaterials and Coatings by Thermal Spray*, Micro and Nano Technologies. Elsevier, 2019. ISBN 978-0-12-813870-0, 221–255. URL `https://www.sciencedirect.com/science/article/pii/B9780128138700000073`.

32. **Li, H.**, **M. Wang**, **R. You**, and **Z. Tao** (2023). Impact of thermal radiation on turbine blades with film cooling structures. *Applied Thermal Engineering*, **221**, 119832.

33. **Li, S.** and **H. Mongia**, An improved method for correlation of film-cooling effectiveness of gas turbine combustor liners. *In 37th Joint Propulsion Conference and Exhibit, Salt Lake City, Utah, USA*. AIAA, July, 2001.

34. **Li, X.**, Numerical simulation on fluid flow and heat transfer of film cooling with backward

injection. *In International Heat Transfer Conference*, volume 49408. 2010.

35. **Mark, C. P.** and **A. Selwyn** (2016). Design and analysis of annular combustion chamber of a low bypass turbofan engine in a jet trainer aircraft. *Propulsion and Power Research*, **5**(2), 97–107.

36. **Maurente, A.** and **C. G. Alves** (2019). Radiation heat transfer in a gas slab with properties characteristics of a jet engine combustor. *International Journal of Heat and Mass Transfer*, **145**, 118734. ISSN 0017-9310.

37. **McKay, M. D.**, **R. J. Beckman**, and **W. J. Conover** (1979). A comparison of three methods for selecting values of input variables in the analysis of output from a computer code. *Technometrics*, **21**(2), 239–245. ISSN 00401706.

38. **Moeini, A.** and **M. Zargarabadi** (2018). Genetic algorithm optimization of film cooling effectiveness over a rotating blade. *International Journal of Thermal Sciences*, **125**, 248–255. ISSN 1290-0729.

39. **Moffat, R. J.** (1988). Describing the uncertainties in experimental results. *Experimental Thermal and Fluid Science*, **1**(1), 3–17. ISSN 0894-1777.

40. **Mongia, H.**, *Engineering Aspects of Complex Gas Turbine Combustion Mixers Part I: High Delta-T*. 2012.

41. **Nina, M.** and **J. H. Whitelaw** (1971). The effectiveness of film cooling with three-dimensional slot geometries. *Journal of Engineering For Gas Turbines and Power*, 425–430.

42. **Park, K. H.**, **K. M. Yang**, **K. W. Lee**, **H. H. Cho**, **H. C. Ham**, and **K. Y. Hwang** (2009). Effects of injection type on slot film cooling for a ramjet combustor. *Journal of Mechanical Science and Technology*, **23**(7), 1852–1857.

43. **Pattamatta, A.** and **G. Singh** (2012). Assessment of turbulence models in the prediction of flow field and thermal characteristics of wall jet. *Frontiers in Heat and Mass Transfer (FHMT)*, **3**(2).

44. **Pu, J.**, **T. Zhang**, **W. li Zhou**, **J. hua Wang**, and **W. long Wu** (2022). Overall thermal performances of backward film cooling with simulated surface thermal barrier coatings at various walls. *Case Studies in Thermal Engineering*, **32**, 101876. ISSN 2214-157X. URL `https://www.sciencedirect.com/science/article/pii/S2214157X22001228`.

45. **Rao, K. V. L. N.**, **B. V. S. S. S. Prasad**, and **C. H. K. Babu** (2022). Investigations of combustor inlet swirl on the liner wall temperature in an aero engine combustor. *International Journal of Turbo Jet-Engines*, **39**(1), 89–102. URL `https://doi.org/10.1515/tjj-2019-0035`.

46. **Rastogi, A.** and **J. Whitelaw** (1973). The effectiveness of three-dimensional film-cooling slots—i. measurements. *International Journal of Heat and Mass Transfer*, **16**(9), 1665–1672.

47. **Sakai, E.**, **T. Takahashi**, and **H. Watanabe** (2014). Large-eddy simulation of an inclined round jet issuing into a crossflow. *International Journal of Heat and Mass Transfer*, **69**, 300–311.

48. **Sargent, S. R.**, **C. R. Hedlund**, and **P. M. Ligrani** (1998). An infrared thermography imaging system for convective heat transfer measurements in complex flows. *Measurement Science and Technology*, **9**(12), 1974.

49. **Schulz, A.** (2000). Infrared thermography as applied to film cooling of gas turbine components. *Measurement Science and Technology*, **11**(7), 948. URL `https://dx.doi.org/10.1088/0957-0233/11/7/311`.

50. **Scrittore, J. J.**, **K. A. Thole**, and **S. W. Burd** (2007). Investigation of velocity profiles for effusion cooling of a combustor liner. *Journal of Turbomachinery*, **129**(3), 518–526.

51. **Seo, H. J.**, **Y. J. Kang**, **H. C. Lee**, **J. S. Kwak**, **J. S. Park**, and **K. Lee** (2019). Optimization of the configuration of the laidback fan-shaped film cooling hole with a lateral expansion angle of 10 degrees. *Applied Thermal Engineering*.

52. **Shan, Y.**, **J. zhou Zhang**, and **C. xiong Pan** (2013). Numerical and experimental investigation of infrared radiation characteristics of a turbofan engine exhaust system with film cooling central body. *Aerospace Science and Technology*, **28**(1), 281–288.

53. **Singh, K.**, **B. Premachandran**, and **M. Ravi** (2017). Experimental and numerical studies on film cooling with reverse/backward coolant injection. *International Journal of Thermal Sciences*, **111**, 390–408.

54. **Singh, K.**, **B. Premachandran**, and **M. R. Ravi** (2018). Effect of Thermal Barrier Coating and Gas Radiation on Film Cooling of a Corrugated Surface. *Journal of Heat Transfer*, **140**(9).

55. **Sinha, A.**, **D. Bogard**, and **M. Crawford** (1991). Film-cooling effectiveness downstream of a single row of holes with variable density ratio. *Journal of Turbomachinery*, **113**(3), 442–449.

56. **Sivasegaram, S.** and **J. Whitelaw** (1969). Film cooling slots: the importance of lip thickness and injection angle. *Journal of Mechanical Engineering Science*, **11**(1), 22–27.

57. **Smith, T. F.**, **Z. F. Shen**, and **J. N. Friedman** (1982). Evaluation of Coefficients for the Weighted Sum of Gray Gases Model. *Journal of Heat Transfer*, **104**(4), 602–608. ISSN 0022-1481. URL `https://doi.org/10.1115/1.3245174`.

58. **Song, J.**, **K. W. Lee**, **K. M. Kim**, and **H. H. Cho** (2012). Slot film cooling performance in

combustor with flame holders. *Energy*, **37**(1), 533–539. ISSN 0360-5442. URL https://www.sciencedirect.com/science/article/pii/S0360544211007183. 7th Biennial International Workshop "Advances in Energy Studies".

59. **Srikanth, R.**, **P. Nemani**, and **C. Balaji** (2015). Multi-objective geometric optimization of a PCM based matrix type composite heat sink. *Applied Energy*, **156**(C), 703–714.

60. **Starik, A.**, *Kinetics of gaseous hydrocarbon fuel combustion and thermally nonequilibrium effects*. 2010. ISBN 978-5-94588-071-9, 55–76.

61. **Sturgess, G.**, Film cooling optimization for minimum cooling airflow in aircraft gas-turbines. *In Combustion in Advanced Gas Turbine Systems*. Elsevier, 1968, 347–376.

62. **Sturgess, G.** (1980). Account of film turbulence for predicting film cooling effectiveness in gas turbine combustors. *Journal of Engineering For Gas Turbines and Power*, **102**, 524–534.

63. **Tinga, T.**, **J. F. van Kampen**, **B. de Jager**, and **J. B. W. Kok** (2006). Gas Turbine Combustor Liner Life Assessment Using a Combined Fluid/Structural Approach. *Journal of Engineering for Gas Turbines and Power*, **129**(1), 69–79. ISSN 0742-4795.

64. **Tu, Z.**, **J. Mao**, and **X. Han** (2017). Numerical study of film cooling over a flat plate with anisotropic thermal conductivity. *Applied Thermal Engineering*, **111**, 968–980.

65. **Turns, S. R.**, *An introduction to combustion: Concepts and applications*. McGraw-Hill, 2012.

66. **Vassen, R.**, **X. Cao**, **F. Tietz**, **D. Basu**, and **D. Stöver** (2004). Zirconates as new materials for thermal barrier coatings. *Journal of the American Ceramic Society*, **83**(8), 2023–2028.

67. **Venkatesh, V.**, **J. Sriraam**, **K. Subhash**, **R. K. Velamati**, **A. Srikrishnan**, **B. Ramakrishnananda**, and **S. Batchu** (2018). Studies on effusion cooling: Impact of geometric parameters on cooling effectiveness and coolant consumption. *Aerospace Science and Technology*, **77**, 58–66.

68. **Wang, C.**, **J. Zhang**, **C. Wang**, and **X. Tan** (2020). Multi-optimization of a specific laminated cooling structure for overall cooling effectiveness and pressure drop. *Numerical Heat Transfer, Part A: Applications*, **79**(3), 195–221.

69. **Wang, C.**, **J. Zhang**, **J. Zhou**, and **S. A. Alting** (2015). Prediction of film-cooling effectiveness based on support vector machine. *Applied Thermal Engineering*, **84**, 82–93. ISSN 1359-4311.

70. **Wang, T.**, **S. Chintalapati**, **R. S. Bunker**, and **C. P. Lee** (2000). Jet mixing in a slot. *Experimental Thermal and Fluid Science*, **22**(1), 1–17. ISSN 0894-1777. URL https://www.sciencedirect.com/science/article/pii/S0894177700000108.

71. **Wang, T.** and **X. Li** (2008). Mist film cooling simulation at gas turbine operating conditions. *International Journal of Heat and Mass Transfer*, **51**(21), 5305–5317. ISSN 0017-9310.

72. **Wang, W.**, **P. Sun**, **J. Ren**, and **H. Jiang** (2011). Radiative Effectiveness on the Aero- and Thermodynamics in a Highly Thermally Loaded Film Cooling System. **Volume 5: Heat Transfer, Parts A and B**, 325–334.

73. **Wang, X.**, **H. Xu**, **J. Wang**, **W. Song**, and **M. Wang** (2019). Multi-objective optimization of discrete film hole arrangement on a high pressure turbine end-wall with conjugate heat transfer simulations. *International Journal of Heat and Fluid Flow*, **78**, 108428.

74. **Wang, Y.**, **S. Qian**, **Y. Sun**, **W. Wang**, and **J. Cui** (2023). Fast prediction and uncertainty analysis of film cooling with a semi-sphere vortex generator using artificial neural network. *AIP Advances*, **13**(1), 015303.

75. **Wei, J.**, **J. Zhang**, **S. Li**, and **F. Wang** (2015). Numerical study on impinging-film hybrid cooling effect with different geometries. *International Journal of Thermal Sciences*, **92**, 199–216.

76. **Wikipedia** (2007). URL `https://en.wikipedia.org/wiki/File:Jet_engine.svg`.

77. **Wing, M.** (1981). The Protection of Gas Turbine Blades. *Platinum Metals Rev*, **25**(3), 94.

78. **Wolfshtein, M.** (1969). The velocity and temperature distribution in one-dimensional flow with turbulence augmentation and pressure gradient. *International Journal of Heat and Mass Transfer*, **12**(3), 301–318.

79. **Yang, C.** and **J. Zhang** (2012). Influence of multi-hole arrangement on cooling film development. *Chinese Journal of Aeronautics*, **25**(2), 182–188.

80. **Yang, W.**, **X. Liu**, **G. Li**, and **J. Zhang** (2012). Experimental investigation on heat transfer characteristics of film cooling using parallel-inlet holes. *International Journal of Thermal Sciences*, **60**, 32–40. ISSN 1290-0729.

81. **Zhang, H.**, **Q. Wang**, **Z. Chen**, **X. Su**, and **X. Yuan** (2020). Effects of compound angle on film cooling effectiveness considering endwall lateral pressure gradient. *Aerospace Science and Technology*, **103**, 105923. ISSN 1270-9638.

82. **Zhang, J.**, **C. Yuan**, **P. Ji**, **J. Wei**, and **X. He** (2018). Experimental investigation on the overall cooling effectiveness of t-type impinging-film cooling. *Applied Thermal Engineering*, **128**, 595–603.

83. **Zhou, M. D.** and **I. Wygnanski** (1993). Parameters governing the turbulent wall jet in an external stream. *AIAA Journal*, **31**(5), 848–853.

CURRICULUM VITAE

NAME	Revulagadda Ananda Prasanna
DATE OF BIRTH	06 April 1993

EDUCATION QUALIFICATIONS

2014 **Bachelor of Engineering**

Institution	Sir C R Reddy College of Engineering
Specialization	Mechanical Engineering

2016 **Masters of Technology**

Institution	Gayatri Vidya Parishad College of Engineering (A)
Specialization	Thermal Engineering

Doctor of Philosophy

Institution	IIT Madras
Specialization	Thermal Engineering

Registration Date 02 Jan 2018

DOCTORAL COMMITTEE

Chairperson	Dr. SHAMIT BAKSHI Professor Department of Mechanical Engineering
Guide(s)	Dr. ARVIND PATTAMATTA Professor Department of Mechanical Engineering
	Dr. CHAKRAVARTHY BALAJI Professor Department of Mechanical Engineering
Member(s)	Dr. BALAJI S.SRINIVASAN Professor Department of Mechanical Engineering
	Dr. RINKU MUKHERJEE Associate Professor Department of Applied Mechanics
	Dr. SHALIGRAM TIWARI Professor Department of Mechanical Engineering